Synthesis of nanostructured materials in deep eutectic solvents

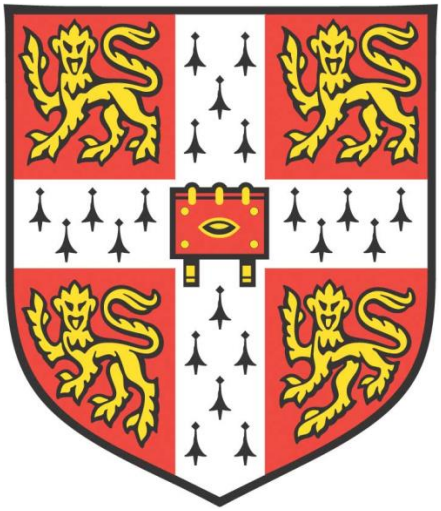

Sukanya Datta

Churchill College, Cambridge, UK

Department of Chemical Engineering and Biotechnology, University of Cambridge

This dissertation is submitted for the degree of Doctor of Philosophy

February 2020

Declaration

This dissertation is the result of my own work and includes nothing which is the outcome of work done in collaboration except as declared in the Preface and specified in the text. It is not substantially the same as any that I have submitted, or, is being concurrently submitted for a degree or diploma or other qualification at the University of Cambridge or any other University or similar institution except as declared in the Preface and specified in the text. I further state that no substantial part of my dissertation has already been submitted, or, is being concurrently submitted for any such degree, diploma or other qualification at the University of Cambridge or any other University or similar institution except as declared in the Preface and specified in the text. It does not exceed the prescribed word limit (65,000) for the Engineering Degree Committee.

Sukanya Datta

February 2020

Abstract

Synthesis of nanostructured materials in deep eutectic solvents
Sukanya Datta

Deep eutectic solvents (DES), a new generation of non-toxic, eco-friendly and biodegradable solvents discovered in 2001 consist of a variety of cations and anions. These new sub-category of ionic liquids present interesting properties due to the hydrogen bonding between their components and are being currently explored for a number of applications such as nanomaterial synthesis, electrodeposition, metal processing etc. Particularly interesting is their use as solvents for the synthesis of nanomaterials. The DES are especially attractive due to the lack of toxic emissions because of their negligible vapour pressure in comparison to the volatile organic compounds. However there is a lack in the understanding on the role played by DES to produce nanomaterials.

Herein, the role of reline, an eutectic mixture of choline chloride and urea, one of the most popular DES, is elucidated during the synthesis of different families such as gold (noble metal), vanadium pentoxide (transition metal oxide), ceria and zirconia (ceramic oxides). The work focuses on gaining a holistic understanding on the interaction of reline with different precursors. It is found that reline can act as an 'all in one' platform such as template reagent, reducing agent, solvent platform and morphology directing agent in the synthesis of nanomaterials. It is important to highlight that there is no addition of any external additives in contrast to previously published work.

It is demonstrated here that reline can actively form gold nanoparticles by reducing a salt precursor and simultaneously stabilize the nuclei, delaying their growth, leading to highly monodispersed small gold particles. In the case of metal oxides, the templating role of reline is elucidated to produce different morphologies of vanadium pentoxide upon altering the water ratio in reline. Reline has been also shown to direct the growth of 1D ceria-zirconia nanorods. The effect of reline on the crystal phase of the zirconia nanomaterial is also investigated herein.

Contents

List of Figures

List of Tables

Nomenclature

Abbreviations and acronyms

AC-STEM	Aberration corrected-scanning transmission electron microscopy
BET	Brunauer–Emmett–Teller
DES	Deep eutectic solvent
DLVO	Derjaguin, Landau, Vervey and Overbeek (DLVO) theory
Ea	Activation energy
EDX	Energy-dispersive X-ray spectroscopy
ESI-MS	Electrospray ionization- mass spectroscopy
FWHM	Full width at half maximum
GC-MS	Gas chromatography-mass spectroscopy
HAADF	High angle annular dark field
HBD	Hydrogen bond donor
HR-TEM	High resolution transmission electron microscopy
ICP-OES	Inductively coupled plasma optical emission spectroscopy
ID	Internal diameter
IL	ionic liquid
JCPDS	Joint Committee on Powder Diffraction Standards
MFC	Mass flow controllers
NMR	Nuclear magnetic resonance
OA	Oriented attachment
pXRD	Powder X-ray diffraction
PEMFC	Proton exchange membrane fuel cell
PTFE	Poly tetra fluoroethylene
SAXS	Small angle X ray scattering
SEM	Scanning electron microscopy
SERS	Surface enhanced raman spectroscopy

TPR	Temperature programmed reduction
TCD	Thermal conductivity detector
TOF	Turnover frequency
VOCs	Volatile organic compounds
XPS	X-ray photoelectron spectroscopy
{}	Curly parenthesis denoting crystal phases

Chemical formulae

Au	Gold
Au/CeO_2	Gold nanoparticles supported on ceria
Au/CeO_2-ZrO_2	Gold nanoparticles supported on ceria-zirconia
Au/ZrO_2	Gold nanoparticles supported on zirconia
$[BMim]^+$	n-butylmethylimidazolium
$[BPy]^+$	N-butylpyridinium
$Ce(NO_3)_2.6H_2O$	Cerium nitrate
CeO_2	Ceria
$C_6H_8O_6$	Ascorbic acid
$C_5H_{14}ClNO$	Choline chloride
ChCl	Choline chloride
$C_5H_{14}BrNO$	Choline bromide
CZ	Ceria-Zirconia support
CO	Carbon monoxide
$CO(NH_2)_2$	Urea
DMF	Dimethyl formamide
$[EMIM]^+$	1-ethyl-3-methylimidazolium
$FeCl_3$	Iron chloride
KOH	Potassium hydroxide
$HAuCl_4$	Chloroauric acid
NH_3	Ammonia
NaOH	Sodium hydroxide

PVP	Polyvinylpyrrolidone
$[Py_{1,4}]^+$	Pyrrolidinium
SiC	Silicon carbide
$SnCl_2$	Tin chloride
$[Tf_2N]^-$	bis(trifluoromethylsulfonyl)amide
$[TfO]^-$	trifluoromethanesulfonate
V_2O_5	Vanadium pentoxide
$VO(acac)_2$	Vanadyl acetylacetonate
ZrO_2	Zirconium di oxide
m-ZrO_2	monoclinic zirconia
c-ZrO_2	cubic zirconia
$ZrO(NO_3)_2 \cdot (H_2O)_6$	Zirconyloxynitrate hexahydrate
$ZnCl_2$	Zinc chloride

Acknowledgement

I am deeply indebted to my family, my dad, mom and sister for always believing in me and supporting my dreams. I would not have been able to come so far without their guidance and moral support.

I am extremely fortunate and blessed to have Dr Laura Torrente as my advisor, who has been a tremendous mentor for me. I am deeply grateful for her unwavering support, guidance, and advice both for my research and career pursuits. Her patience allowed me to grow as a researcher, at my own pace. I very much appreciate her for her generosity with her time, and providing constant advice and encouragement. I enjoyed and learnt a lot from working with her and other members in her group. I would like to express my gratitude to Prof Cate Ducati for her immense support and valuable mentorship. I am immensely thankful to Schlumberger foundation for funding my PhD and providing me this wonderful opportunity to study at the University of Cambridge.

It is truly an honour and pleasure to have been working with the Torrente research group, notably Yunhu, Collin and Joseph for the scientific discussions we shared. I am immensely grateful to our wonderful postdocs (both former and present) Bruno, Antonio, Herme, Florian, Reza, Mauro and Kejun for their generous and helpful suggestions. I am indebted to the CEB technical support team and especially to Peter Claxton, Chris Bawden and Phil Salway for helping me out on numerous occasions during my lab work. I am thankful to Stuart Fordham and Ian Pattison who always processed my purchase orders promptly.

I am grateful to Dr Heather Greer at the Department of Chemistry for sharing her expertise and supporting me endlessly during my electron microscopy sessions. I would like to thank Christopher Amey and Adam Brown at the Maxwell centre for helping with the characterization measurements. My humble appreciation for Dr Jeremie Asselin for assisting me with the Raman measurements.

I am deeply indebted to Dr Emanuela Liberti at the University of Oxford, UK for providing me with the aberration corrected-scanning transmission electron microscopy measurements and for taking deep interest in my research work. I am grateful to my collaborators Dr Karen Edlen, Dr Changshin Jo, Dr Iva Manasi, Ms Christina Boukouvala, Dr Michael De Volder and Dr Emilie Ringe for their help and guidance. I am grateful to Dr Shaoliang Guan at Harwell and Swansea facilities for the XPS and ESI-MS measurements. I am grateful to Dr Rittick Barua for his useful feedback on thesis editing.

My heartiest thanks to the entire team of Nanodoctoral training centre program for their continued support and providing a lot of opportunities to grow as a researcher during my PhD.

I would take this opportunity to thank my mentors Dr Antoine Barbier and Dr Shabnam Johry who have always supported me and encouraged me with their dynamic vision and unending support.

I would like to thank my friends and family for their love and continuous support. I am grateful to Hirak, Aazraa, Shreyashi, Tahmida, Ram and Sayanti for making my stay in Cambridge truly memorable and exciting. I am thankful to my dear friends in India Shweta, Kritika and Jassjot for their un-ending support and always being there for me.

Finally, my heartfelt thanks to Baridhi for his patience, encouragement and unending support.

Dissemination of research

The research presented in this thesis has been disseminated throughout the course of the project through presentations at international and national conferences and departmental events along with publications in relevant scientific journals.

Publications

- Sukanya Datta, Changshin Jo, Michael De Volder and Laura Torrente-Murciano, Morphological control of nanostructured V_2O_5 by deep eutectic solvent, *ACS Applied Materials and interfaces*, 2020, 12, 18803-18812.
- Zhigang Hu, Julien Mahin, Sukanya Datta, Tamsin E. Bell and Laura Torrente-Murciano, Ru-based catalysts for H_2 production from ammonia: effect of 1D support, *Top. Catal*., 2019, 62, 1169–1177.
- Sukanya Datta and Laura Torrente-Murciano, Nanostructured faceted ceria as oxidation catalyst, *Current Opinion in Chemical Engineering*, 2018, 20, 99-106.

Oral presentations

- *Elucidating the role of deep eutectic solvent to synthesize gold nanoparticles,* ACS Fall 2019 National meeting and exposition, San Diego, USA, August 2019.
- *The role of deep eutectic solvents towards the synthesis of nanomaterials*, Department of Chemical Engineering and Biotechnology, Graduate Conference, Cambridge, UK, June 2019.
- *Continuous synthesis of nanostructured materials*, Department of Chemical Engineering and Biotechnology, Graduate Conference, Cambridge, UK, May 2017.

Poster presentations

- *Engineering nanostructured materials in deep eutectic solvents,* NanoCDT external advisory board conference, Cambridge, UK, March 2019.
- *Synthesis of nanostructured materials in deep eutectic solvents*, Department of Chemical Engineering and Biotechnology, Graduate Conference, Cambridge, UK, April 2018.
- *Use of deep eutectic solvents toward the synthesis of ceramic oxides*, UK-India Newton Bhabha researcher's link workshop, Kolkata, India, December 2017.
- Synthesis of nanostructured ceria in green, environment-friendly deep eutectic solvents, RSC 13th International conference on Material science, Liverpool, UK, July 2017.

Chapter 1: Introduction

Nanotechnology finds its applications in a number of areas such as health care[1], diagnostics[2], catalysis[3], sensors[4], and agriculture[5] as shown in Figure 1 due to its attractive properties like high surface area to volume ratio and the unique quantum confinement effects that comes into play at the nanoscale. The physical and chemical properties of nanomaterials are strongly dependent on their size and morphology and this aspect is particularly relevant for the above mentioned applications[6]. Hence, the choice of synthesis routes to develop nanomaterials is extremely crucial to achieve desirable morphology-activity relationships[7,8,6].

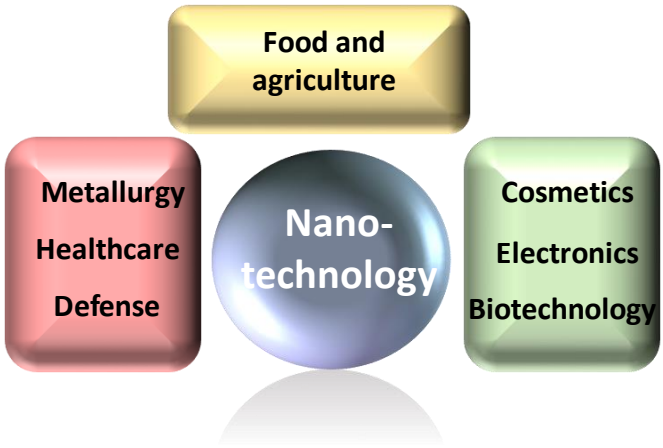

Figure 1: Summary of the different applications of nanotechnology.

In this regard, deep eutectic solvent (DES) is an emerging class of green, eco-friendly and biodegradable solvent discovered by Abbott *et al.* in 2001[9] which have shown to fulfil multiple roles in the synthesis of nanomaterials[10]. DES are formed by mixing two solids with high melting points in a particular ratio to form a free flowing liquid. Reline which is formed by combing choline chloride and urea in the molar ratio of 1:2 is one of the most popular DES reported till date in the literature towards the synthesis of nanomaterials. However there is a lack in the understanding on the role of reline in the synthesis of

nanomaterials. In this thesis, the multiple roles played by reline in the development of the nanomaterials are investigated. Another DES known as asline formed by the combination of choline chloride and ascorbic acid in the molar ratio of 2:1 is also reported herein to elucidate the capping ligand action of the DES.

A range of physical methods (atomic layer deposition, molecular beam epitaxial, spray pyrolysis, pulsed layer deposition) and chemical routes (microemulsion routes, sol-gel, sonochemical, solvothermal and metal salt reduction and photochemical process) are available for the synthesis of nanomaterials[11]. Due to the simplicity and better control in size and morphologies of the nanostructures by the wet chemical synthesis method[12], this thesis has employed the wet chemical routes for nanomaterial synthesis.

By carefully selecting the main components of a chemical synthesis process such as solvent, reducing agent, nature of precursor and capping ligand/surfactant, it is possible to tune the morphology and size of nanomaterials. The present state of nanomaterial synthesis rely heavily on the addition of external additives in solvents as shape directing agents and stabilizers to control the crystal growth and sizes of these materials[13]. However most of the commonly used surfactants, reducing agents and solvents have several environmental hazards associated with them as presented in Table 1[14].

Table 1: Environmental hazards associated with some of the common capping ligands, reducing agents and solvents[14].

Toxicities	Capping ligands	Reducing agents	Solvents
Harmful	PPI, PEI, CTAB	EG, Vitamin C	Ethanol, toluene, ODE
Irritant	PEG,PAA, linoleic acid, TOPO, TOP, OA, ODA	Citric acid	
Corrosive	PAA, TOP, OAm, DDA	Citric acid, $NaBH_4$, OAm	OAm
Toxic	PAA, PAMAM, OA	Formaldehyde, CO,N_2H_4, $NaBH_4$	Ethanol, DMF, toluene
Flammable	-	Ethanol, N_2H_4	Ethanol, toluene
Extremely flammable	-	CO	-
Non eco-friendly	CTAB, OAm, DDA	N_2H_4, $NaBH_4$, OAm	OAm

PPI: poly(propyleneimine), PEI: polyetherimide, CTAB: cetyltrimethylammonium bromide, PEG: polyethylene glycol, PAA: polyacrylic acid, TOPO: trioctyl-phosphine oxide, TOP: tri-n-octylphosphine,

OA: oleic acid, ODA: octadecylamine, OAm: oleylamine, DDA: dodecylamine, PAMAM: poly(amidoamine), EG: ethylene glycol, ODE: 1-octadecence.

Hence, it is important to look for alternative sustainable routes such as DES for the synthesis of nanomaterials to minimize the use of these external additives in the reaction medium so that the overall ecological footprint is reduced minimizing chemical wastage. The addition of these auxiliary additives also hampers the nanoparticle surface and passivates them for catalysis reactions[15].

In wet chemical synthesis, solvents are extremely crucial as they not only constitute almost 80% by mass in a chemical reaction but also possess the potential to replace surfactants and reducing agents to act 'all-in-one' platform in the chemical reaction[16].

However there is a lack in the development and understanding of the solvent systems which have the potential to fulfil multiple roles in the synthesis of nanomaterials[17].

The main motivation of this PhD thesis is to understand the role of the DES reline in the synthesis of nanomaterials to reveal how the interaction of the components of the eutectic mixtures can act and thus substitute the use of multiple auxiliary additives such as reducing agents, templating ligands and morphology directing compounds as summarized in Figure 2.

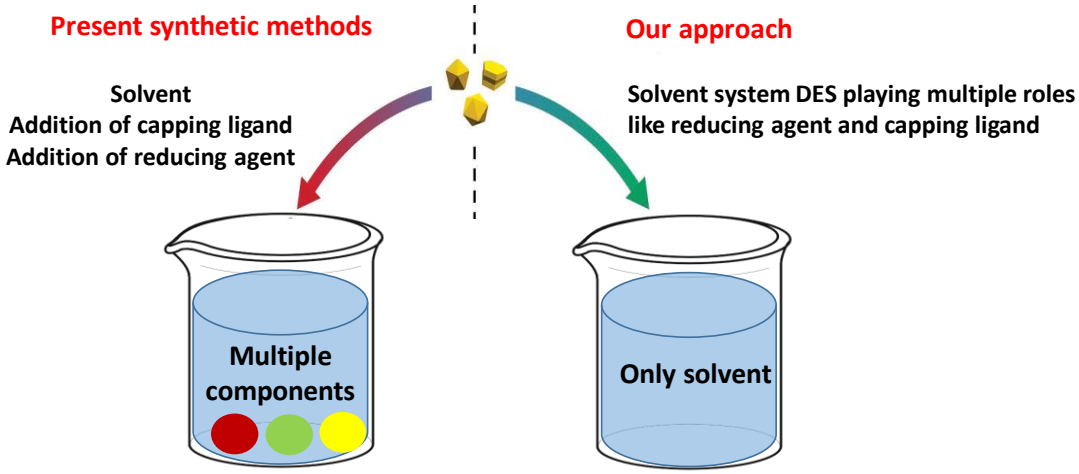

Figure 2: Schematic representation of the PhD aim to replace the present nanomaterial synthesis route employing multiple components in the reaction medium with only DES to play various roles.

1.0 Aims and objectives of the thesis

The overall aim of this PhD thesis is to elucidate and understand the role of deep eutectic solvents towards the synthesis of nanomaterials. In order to achieve this aim, the following objectives are carried out:

- Development and mechanistic understanding of synthesis route for three different classes of nanomaterials: Au (noble metal), V_2O_5 (transition metal oxide), CeO_2 and ZrO_2 (ceramic oxides). These three different classes of materials are chosen in order to elucidate the role of DES and its chemistry with different materials (Figure 3).
- Understand the effect of DES/water ratios on the crystal structure, morphology and consequently physical and chemical properties by advanced characterization of these nanomaterials.
- Study of the morphology-activity relationship of these nanostructured materials for applications like carbon monoxide (CO) oxidation (ceria-zirconia, gold on ceria-zirconia support and gold on zirconia support), Li-ion batteries (vanadium pentoxide) and plasmonics (gold nanomaterials) as model reactions.

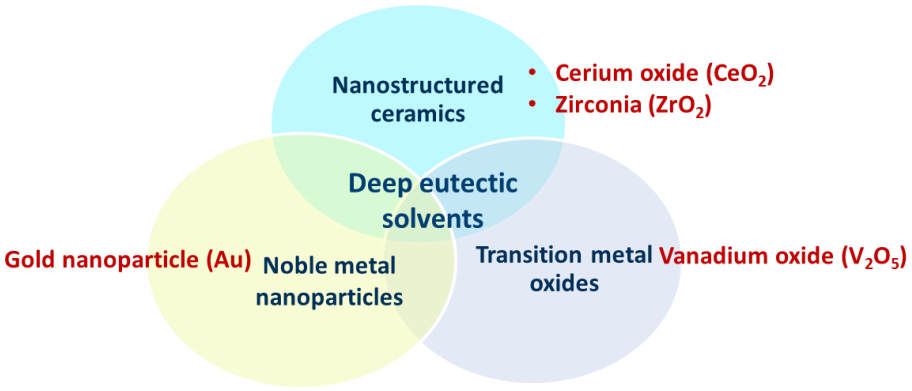

Figure 3: Range of different materials chosen for this PhD thesis.

1.1 Impact of the thesis

The ability of the DES system to produce nanomaterials within a sustainable framework on account of its green, biodegradable and eco-friendly affiliation offers a huge potential to create a meaningful impact to generate nanomaterials in an environmental-friendly manner.

The conventional use of aromatic solvents for organic or nanomaterial synthesis is hazardous due to the volatile and toxic emissions which also destroys the ozone layer[18]. This challenge is mitigated by the use of DES due to the lack of associated vapour emissions because of negligible vapour pressure in comparison to the volatile organic compounds.

The need to develop external additives-free solvent platforms for the synthesis of nanomaterials is of great importance to reduce the overall ecological footprint. The addition of external additives to tune morphology or size of nanomaterials in the solvents add to the operational production cost and also presents several detrimental effects to the environment.

1.2 Thesis structure

This thesis is divided into the following chapters:

Chapter 1: Introduction

Chapter 2: Literature review

This chapter reviews the current state of art on the synthesis of nanomaterials by DES routes and the available synthesis methods to produce gold (Au), vanadium pentoxide (V_2O_5), ceria (CeO_2) and zirconia (ZrO_2). In addition, the structure-property relationship of these materials are also presented. This chapter concludes by identifying potential gaps present in the literature and how this thesis work can address these gaps.

Chapter 3: Experimental methodologies

This chapter provides detailed experimental protocols on the synthesis of nanomaterials in DES, characterization tools and catalytic measurements for CO oxidation.

Chapter 4: The role of DES in the synthesis of gold nanomaterials

This chapter unravels the role of DES reline and asline as a reducing agent, stabilizer and capping ligand towards the synthesis of gold nanomaterials without the addition of any external additives. The as-synthesized gold nanomaterials are further used for plasmonic applications (surface enhanced Raman spectroscopy) for rhodamine B dye.

Chapter 5: Elucidating the role of DES reline towards the synthesis of nanostructured V_2O_5

This chapter elucidates the template role of reline/water mixtures to produce different morphologies of V_2O_5 (nanoballs, nanosheet and nanofleece) upon changing the water ratio in DES in the solvothermal synthesis. The structure-property relationships of these different V_2O_5 nanostructures have been studied for Li-ion battery applications.

Chapter 6: Synthesis of ceria-zirconia nanomaterials in DES reline

This chapter devises the synthesis of CeO_2/ZrO_2 nanomaterials in reline. Advanced characterization of these CeO_2/ZrO_2 nanomaterials are further carried out. CO oxidation is

used as a model reaction to test the catalytic activities of the CeO_2/ZrO_2 nanomaterials. These CeO_2/ZrO_2 nanomaterials are also used as supports for gold nanoparticles as catalysts for CO oxidation.

Chapter 7: Synthesis of nanostructured ZrO_2 in DES reline

This chapter presents the synthesis of nanostructured ZrO_2 in reline and aqueous NaOH solutions. These two different synthesis routes are carried out to study the effect of the solvent environment on the final crystal phase. Building on the methodology of gold nanoparticle synthesis in DES from chapter 4, Au/ZrO_2 catalysts are synthesized and tested for CO oxidation reaction.

Chapter 8: Conclusions and future work.

This chapter presents the main conclusions of this work as well as future directions in the field.

Chapter 2: Literature review

The primary aim of this research project is to underpin the actual role of the deep eutectic solvent (DES) reline (formed from choline chloride and urea in the molar ratio of 1:2) and asline (formed by combining choline chloride and ascorbic acid in the molar ratio of 2:1) in the synthesis of nanomaterials. This literature review evaluates the current state of art on areas relevant to this research work. Initially, the properties of DES are explained, highlighting their uses for nanomaterial synthesis. Subsequently, the common synthesis routes of the metal and metal oxide materials (Au, V_2O_5, CeO_2 are ZrO_2) that are employed in this work are evaluated along with their structure-property relationships. Previously reported synthesis methods in DES and ionic liquid (IL) available for these materials are discussed as well. The mechanism for CO oxidation reaction for un-doped and doped support is reviewed herein. Finally the conclusions from this chapter has addressed those areas where more work is required to fill the gaps highlighting the scientific challenges.

2.1 Introduction to deep eutectic solvents (DES)

In 2001, Abbott and co-workers at the University of Leicester, UK first coined the term 'deep eutectic solvent' or DES to describe a class of solvents that are formed by mixing two kinds of solids with high melting points in a particular ratio to form a free flowing liquid[9]. DES are composed of Brønsted and Lewis acids/bases and contain a number of cations and anions[19]. DES are popularly considered to be an alternative and sustainable sub-category of ionic liquid (IL) based solvents. However there are some differences between IL and DES. IL primarily comprise of one kind of cation and anion whereas DES contains a mixture of cations and anions[19]. Preparation of DES is easier than IL as IL often requires an oxygen-free environment. The 'green affiliation' of the IL are questionable due to the nature of the starting materials to make the IL at the first place and the related

toxicity issues along with poor biodegradability of the IL are pointed out in certain reports as well[20]. To overcome these challenges faced by the IL, DES are explored to synthesize nanomaterials in a solvent-driven approach.

The historic development of IL (which in the later years gave rise to DES) started in 1914 when Paul Walden synthesized the first IL ethylamine nitrate (melting point 14 °C) by protonating ethylamine with nitric acid[21]. It is imperative to revisit this legendary work of Paul Walden as this laid the first foundation of IL as we now know it. Even though the work is more than 100 years old, the principles and concepts behind association and dissociation of salt solutions to create liquid solvents (with melting points lower than 100 °C) are still relevant today[22]. Since the discovery of the first IL in 1914, it took several years before scientists achieved major milestones toward developing different generations of IL. These developments ultimately led to the formation of DES in the recent years[23].

The properties of IL and DES depend heavily on the choice of cations and anions. Over the years, properties from the 1st generation of IL to the DES have been significantly altered by employing more bio-renewable ions. The earlier generations of IL were toxic and air-moisture sensitive in comparison to their later generations which are more air/moisture stable and less toxic[24].

2.1.1 DES formation and lowering in melting point

Frederick Guthrie, a British physicist and chemist coined the word 'eutectic' in 1884. Eutectic systems are defined as homogeneous mixtures formed by two or more components that melts or solidifies at temperatures lower than the melting point of either constituents. Thermodynamically, a eutectic point in a binary mixture is referred to as that temperature when both the solid phases are in equilibrium with the liquid phase. There are some theories available in the literature to explain the eutectic fusion of components to produce a liquid. Savchenko proposed that due to the overlapping of energy levels and electron sharing, a eutectic mixture is formed[25]. A different theory of eutectic mixture formation was put forward by Petrucci who suggested a vapour phase mechanism of eutectic fusion[25]. According to Petrucci's theory, whenever two solids are mixed, there will be certainly a vapour phase present which is in equilibrium with the solid components, even if the volatility of the solids are low. Below eutectic temperatures, the solids

vaporizes independently and a mixed vapour is formed. At the eutectic temperature, this vapour phase comes into equilibrium with a liquid phase, the eutectic liquid. The first trace of the eutectic liquid results from the condensation of the vapours produced on mixing solid A and solid B. As can be seen from Figure 4**,** the eutectic point of a mixture is achieved at a particular molar ratio (also known as eutectic ratio) between the solid compounds which gives the lowest melting point.

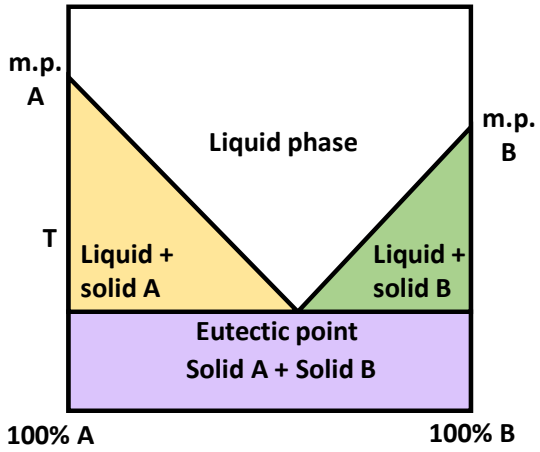

Figure 4: Phase diagram of a eutectic mixture.

The melting point of a DES system is significantly lower in comparison to its components due to a decrease in the lattice energy. According to Born Lande's equation, the lattice energy is inversely proportional to the radius of the ion. Consequently, in a DES, on account of hydrogen bonding between the parent compounds, the size of the ion increases leading to a decrease in lattice energy. The Born Lande's equation is shown as follows in eq.1.

$$\Delta H_{lattice} = \frac{-e^2 z^+ z^-}{4\pi\varepsilon_o r_o} \times M \times N_A \times \left(1 - {}^1/_n\right) \qquad (1)$$

Where e is the elementary charge, 1.602177× 10^{-19} C, ε_o is permittivity of vacuum, 8.85419× 10^{-12} Fm^{-1}, N_A is the Avogadro constant, 6.02214× 10^{23} mol^{-1}, M is the Madelung constant, n is the Born's exponent, z^+ and z^- are the magnitudes of ionic charges and r_o is the cation-anion inter-nuclear distance.

Due to the hydrogen bonding between the hydrogen bond donor (HBD) molecule and the chloride anion of choline chloride, there is an increase in the radius of the ion. As a result, the net lattice energy of the system decreases. As the lattice energy of an ionic substance is defined as the energy required to dissociate a solid into gaseous ions hence higher lattice energies result in higher melting points and lower lattice energies results in lower melting points.

2.1.2 Categories of DES

DES are broadly divided into four major categories depending on the nature of the parent constituents as follows:

a) **Type I**: These have the general formula $Cat^+X^-_zMX$ and are formed from quaternary ammonium salts ($Cat^+X^-_z$) and metal halides MX (M= Zn, Sn, Fe, Al, Ga, In, X is a halide anion)[19]. The metal halide should have a melting point of less than 300 °C to form room temperature eutectic mixtures[19]. $ZnCl_2$, $FeCl_3$ and $SnCl_2$ are the most commonly investigated metal halide salts with choline chloride (ChCl) as the quaternary ammonium moiety. It is interesting to note that although $ZnCl_2$, $FeCl_3$ and $SnCl_2$ are metal halides, their eutectic compositions are different (e.g. $ZnCl_2$:ChCl=2:1 and $SnCl_2$:ChCl=2.5:1) because formation of a eutectic mixture strongly depends on factors such as nature of the Lewis acidity and bonding strength of the constituent metal salts with choline chloride[26].

b) **Type II**: In type II DES, the metal salts from type I DES are replaced with hydrated metal salts as the anionic complexing species with the formula $Cat^+X^-MX\cdot yH_2O$. Type II DES are a combination of quaternary ammonium salts and hydrated metal chlorides. For example, hydrated chromium chloride ($CrCl_2.6H_2O$) forms a eutectic mixture with choline chloride; however, anhydrous chromium chloride with the addition of 6 molecules of water externally does not lead to the formation of an eutectic mixture, indicating the importance of water coordination around the chromium centres[26].

c) **Type III**: Type III DES are composed of a quaternary ammonium salt and a hydrogen bond donor (HBD) with the general formula Cat^+X^-RZ (Z= $CONH_2$,

COOH, OH). This is the most popular family of DES formed by a cation, an anion and a HBD species. Some of the most common HBD are polyalcohols, polyamides and carboxylic acids. The reduction in the overall lattice energy leading to the formation of the eutectic mixture is due to the complexation of the HBD species to the anion and withdrawing the electron density of the anion from the cation[10]. Weaker anion-cation interaction results in weakening of these bonds. The two most important factors that determine the lowering in melting point of a system containing a quaternary ammonium salt and HBD are their individual lattice energies and extent to which HBD interacts with the quaternary ammonium salt[27].

d) **Type IV**: Type IV DES have the general formula $MCl_{x-1}^{+}\cdot RZ$ (MCl is the metal chloride and RZ is the HBD). In type IV DES, the metal chloride replaces the quaternary ammonium salt moiety and complexes with a HBD. Metal halides like $ZnCl_2$ and HBD like urea and acetamide constitute type IV systems[28].

The use of choline chloride (hydroxyethyltrimethylammonium chloride) as the quaternary ammonium salt is the most common hydrogen bond acceptor (HBA) because it is a small molecule that has an asymmetric quaternary ammonium salt with a polar functional group. These factors reduce the melting points of the resultant system[26]. When salts of symmetrical cations such as H_4NCl and Me_4NCl are used, no liquid formation is observed below 200 °C whereas on using salts containing asymmetric ions such as Me_3NEt^{+}, it is possible to achieve larger depressions in the freezing points of the eutectic mixtures[9]. Choline chloride is used as pro-vitamin B_4 and as chicken feedstock which makes it one of the eco-friendly starting components to be used in the DES.

2.1.3 Reline

Reline is one of the most popular type III DES which is a combination of a quaternary ammonium salt (choline chloride) and a HBD (urea) in a molar ratio of 1:2 respectively. The melting point of choline chloride and urea are 303 °C and 133 °C respectively. On mixing them in the molar ratio of 1:2 (choline chloride: urea), the net DES reline is a liquid at room temperature which has a melting point of just 12 °C. The chemical structure of reline is shown in Figure 5. For each 1 (choline chloride): 2 (urea) moities in reline, 8 hydrogen from the urea moiety are available for every 14 hydrogen from the choline

molecule. The most accepted theory behind the deep eutectic behaviour is the interaction of the chloride anion (from choline chloride) with the hydrogen bond donor, urea[29,30]. Out of the several possible hydrogen bond networks possible in reline, O-H—O=C are stronger than N-H—O=C and N-H—Cl hydrogen bonds[31]. Ineleastic neutron scattering studies have shown that the choline cation skeleton is conserved and urea loses its planarity (i.e. shifts from its regular sp^2 hybridization state to an intermediate stage between sp^2 and sp^3)[31]. The loss of urea's planarity leads to greater flexibility in reline's network pertaining to the formation of several intermolecular contacts with varying strengths. The eutectic mixture is formed on account of charge delocalization between the halide anion with the amide moiety[32]. It is important to mention that the ab-initio studies by Zahn *et al.* have recently disputed the widely cited charge delocalization theory between urea and chloride anion in reline[33]. It was found that the negative charge transfer occurred from the chloride anion to the choline moiety and urea remained primarily uncharged.

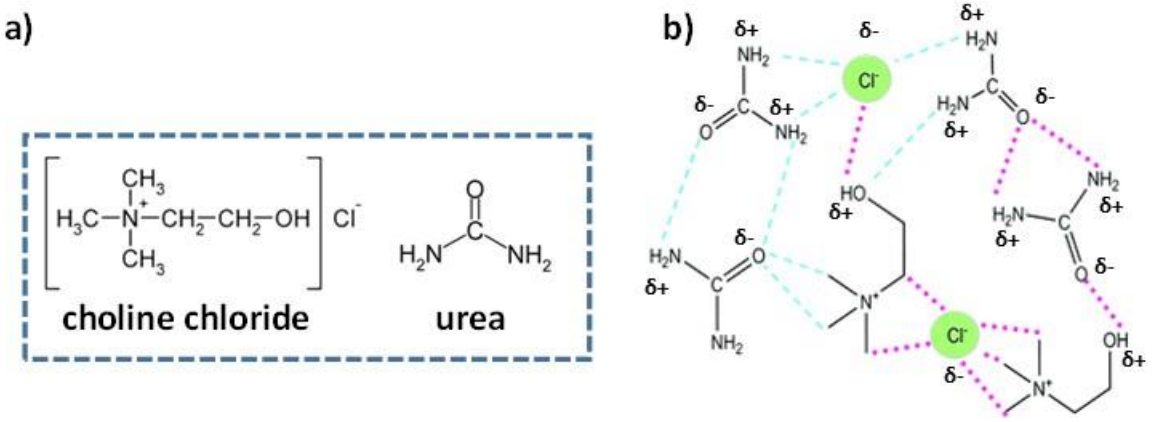

Figure 5: a) Parent components of reline- choline chloride and urea; b) Schematic representation of the various hydrogen bonds possible in reline system showing a 2 ChCl: 4 urea cluster (blue dashed lines are the intermolecular forces, the pink dotted lines and black solid lines are already present in the parent solids) Adapted from Perkins *et al.*[31]. The pink dotted lines represent intermolecular H bonding and black lines represent the C-N and C-C bonds in the solid. Partial charges are depicted on the atoms to indicate the direction of hydrogen bonding.

Reline presents a number of unique chemical characteristics. Some of the facts on the intermolecular and intramolecular hydrogen bonding in reline are as follows[34]:

1) Urea is the HBD, with strong hydrogen bonding between urea and the chloride anion present. However, the self-diffusion coefficient of urea is greater than choline and consequently their motions are not fully aligned, with the urea molecules having greater mobility than chlorine anion.
2) Urea has a smaller size and low molar mass than choline chloride leading to a higher number of urea molecules interacting with the anions compared to the choline cations interacting with urea molecules.
3) Urea presents specific hydrogen interactions with chloride anions. While hydrogen atoms (cis and trans) maintain their original configuration, H_{trans} is more likely to form hydrogen bond with anions than H_{cis}.
4) Hydrogen bonds between NH---Cl^- are stronger than NH---O=C hydrogen bonds, so the former are preferred. The trans NH group can form a bifurcated double hydrogen bond as in the urea crystal, and so trans NH----Cl^- hydrogen bonds are favoured over cis.

2.1.4 Asline

Asline, a new type III DES was recently discovered in 2018, formed from choline chloride as the quaternary ammonium salt and ascorbic acid as the HBD moiety[35]. A range of molar ratios between choline chloride and ascorbic acid (1.2:1, 2:1 and 2.5:1) produces the eutectic liquid (asline) that has a melting point of 85 °C. Out of all the eutectic ratios possible for asline, the eutectic ratio of 2:1 (choline chloride: ascorbic acid) exhibits the highest decomposition temperature and hence the highest thermal stability. The main reason of formation of asline is attributed to the strong hydrogen bond present between the halide anion of choline chloride and ascorbic acid. Due to the recent discovery of asline, there are no published reports in the literature yet on the detailed molecular structure and nature of hydrogen bonding present.

2.1.5 Physico-chemical properties of reline and asline

The main physico-chemical properties like melting point, density, viscosity, ionic conductivity and solubilities of certain metal oxides in reline and asline are summarized in Table 2 as follows:

Table 2: Physico-chemical properties of reline and asline.

Property	Reline	Asline
Melting point	12 °C[19]	85 °C[35]
Density[36]	1.25 gcm^{-3}	Not available
Viscosity at 60 °C (mPa.s)	69[37]	1852
Ionic conductivity at 30 °C[38]	0.199 mS cm^{-1}	-
Solubilities of certain metal oxides (in ppm)[39]	ZnO-1894, V_2O_5-4593, Cu_2O-219	-

- Not available.

2.1.6 Use of DES in nanotechnology

The increasing interest in DES due to their excellent solvation properties, readily biodegradable and eco-friendly components makes them adoptable for a number of applications in nanotechnology. The role of DES to synthesize nanomaterials are broadly studied in six major areas[40]: a) shape-control of nanomaterials, b) electrodeposited films, c) metal-organic frameworks, d) colloidal assemblies, e) hierarchically porous carbons and f) DNA/RNA architectures. Although there has been an accelerated interest in the use of DES as a solvent media for nanomaterial synthesis, yet employing DES for synthesis of materials at the nanoscale is still in its infancy as the first research article on the use of DES to synthesize nanomaterials was published only in 2008[41].

2.2 Gold nanoparticles

Gold nanoparticles play a crucial role in several technological advancements in an array of applications related to catalysis, plasmonics and therapeutics amongst others due to its exceptional physical and chemical properties at the nanoscale[42]. Au nanoparticles offers several properties such as high surface to volume ratio, excellent biocompatibility, ease of preparation and unique optoelectronic properties in comparison to the bulk counterparts[43]. The physico-chemical properties of the nanomaterials are dictated strongly by the size and morphologies which in turn affects the final applications.

Size is a crucial factor because smaller particles have a greater fraction of surface atoms which possess higher binding energies than their bulk atoms[44]. The high reactivity of the

surface atoms is due to fewer number of neighbouring atoms and thus more number of unsatisfied bonds which makes the surface atoms less stable than their bulk counterparts. As can be seen from Figure 6, the % of surface atoms to bulk is about 50% for metal nanoparticle of sizes less than 3 nm and less than 10% for sizes more than 50 nm[45].

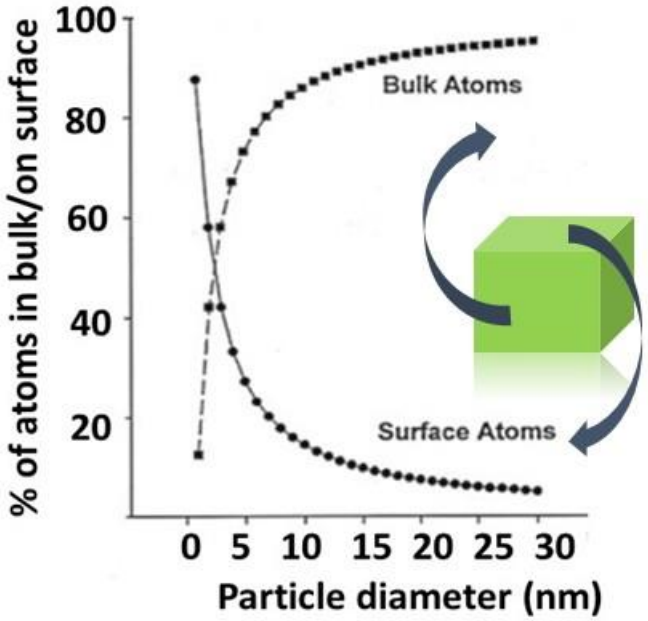

Figure 6: Calculated % of atoms present in bulk to surface ratio as a function of different particle size (Adapted from Klabunde *et al.* [45]).

In addition to size, morphology plays a key role in the final applications due to the selective exposure of surface active planes in metal and metal oxide nanocrystals[46]. For example in the case of metal nanoparticles, anisotropic shapes of gold such as nanoplates and branched structures are particularly attractive because of the sharp edges and high electric field localization at the corners which are suitable for plasmonic properties[47]. Plasmonic properties are the interactions arising between the free electrons and the incident light due to the collective oscillation of electrons upon excitation by electromagnetic radiation. For metal oxide nanocrystals such as in CeO_2, selective exposure of different crystallographic planes exhibit different reactivities towards CO oxidation due to differences in surface energies of the phases[6].

2.2.1 Synthesis of gold nanomaterials

Proper scientific investigation on gold nanoparticles started in 1850s when Michael Faraday prepared colloidal gold by reducing gold chloride with phosphorus in carbon disulphide in a biphasic system[48]. Due to facile fabrication and easy tuneability of size and shape by changing the components in the wet chemical colloidal synthesis method[49], in this thesis, the synthesis of gold nanoparticles is carried out by wet chemical synthesis technique. This section will focus on some of the important concepts like colloidal stability, size and shape control in such synthesis as discussed below before reviewing the state of art available to synthesize gold nanomaterials.

2.2.1.1 Colloidal stability of gold nanoparticles

Colloidal nanoparticles refers to the formation and uniform dispersion of nanoparticles in a colloidal state. A colloidal system is considered to be unstable if the nanoparticles agglomerate with each other. Colloidal nanoparticles tend to aggregate due to the attractive van der waals forces acting between their surfaces[50]. In 1940s, Derjaguin, Landau, Vervey and Overbeek (DLVO) proposed a theory to explain colloidal stability by looking at the balance between these two opposing forces: electrostatic repulsion (electrolytic double layer forces) and Van der Waals attraction. According to the DLVO theory, a colloidal system will be stable if the electrostatic repulsive forces are stronger than the attractive forces so that the particles repel each other and hence, there will be no coagulation[51]. However, if the attractive forces are dominant, then the colloidal particles will attract each other and form aggregates. A colloidal solution of nanoparticles are usually stabilized in two ways:

1) Electrostatic stabilization is achieved by the formation of an electrical double layer around the nanoparticles[52]. The nature of charge on the colloidal nanoparticles depends on the charges by the ions of the dispersing medium adsorbed on their surfaces. For example, Au nanoparticles prepared by the most common citrate reduction method are negatively charged due to the adsorption of citrate anions and Cl^- ions from the gold precursor[53]. Positive counter ions surround the negative charged particle surface as shown in Figure 7a. An electrical double layer is formed subsequently where these ions adsorb to the metal

nanoparticle surface due to the attraction of opposite charged ions. This electrical double layer is neutral in charge. The main components of the electrical double layer are as follows:

a) Surface charge: The charge on the colloidal nanoparticle due to surface adsorption of the ions present in the dispersion medium.
b) Stern layer: Layer comprising of opposite charges (counter-ions) adhering to the surface charges by electrostatic forces.
c) Diffuse layer: A film of the solvent surrounding the nanoparticle. This layer contains a mixture of cations and anions which move freely.

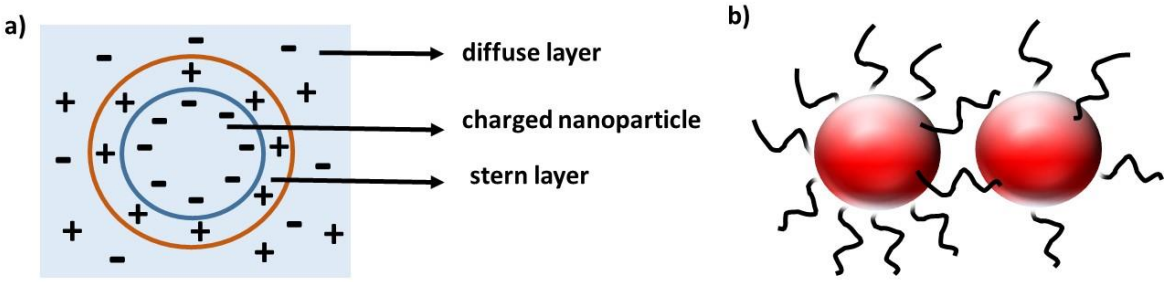

Figure 7: a) Schematic representation of the electrical double layer surrounding the metal nanoparticle according to the DLVO theory; in this case, the nanoparticle surface is negatively charged, the stern layer comprises of oppositely charged ions and the outer diffuse layer contains a medley of cations and anions that are moving freely, b) steric stabilization present between two nanoparticles due to the adsorption of polymers.

However there are certain limitations to electrostatic stabilization of colloidal nanoparticles such as these concepts are applicable to dilute systems only, neglects the possibilities of chemical reaction between the solvent and the nanoparticle and assumes uniform surface charge density on the nanoparticle.

2) Steric stabilization: Steric stabilization is a stabilization process where the particles are coated with an adsorbed layer of stabilizers to prevent their agglomeration. By adding stabilizers such as capping ligands and surfactants, coagulation of colloidal nanoparticles can be prevented as shown in Figure 7b. The adsorbed layers of these polymeric materials

repel each other and this kind of repulsion is known as steric repulsion[54]. For example, amphiphilic stabilizers such as PVP (poly vinyl pyrrolidone) is one of the popular steric stabilizers owing to its amphiphilic nature where both the hydrophilic and hydrophobic component remains attached to the nanoparticles[55].

2.2.1.2 Size control of gold nanoparticles

In order to develop an understanding on size control of gold nanoparticles, it is crucial to understand the mechanism of growth of nanocrystals in the solution in the first place[56]. The growth of nanocrystals in solution is explained by the La Mer scheme which was originally developed in 1950s to explain the growth of colloidal sulphur sols[57] but over the years, La Mer model has been used extensively to explain the growth mechanistic of nanoparticles. The La Mer mechanism is divided into two processes: first nucleation followed by the growth of nanocrystals. The entire process of nucleation and growth is divided into three stages as shown in Figure 8: (I) rapid increase in the concentration of free monomers in the solution, (II) burst-nucleation of the monomers decreasing the concentration of free monomers in the solution and (III) growth of nuclei due to diffusion of monomers.

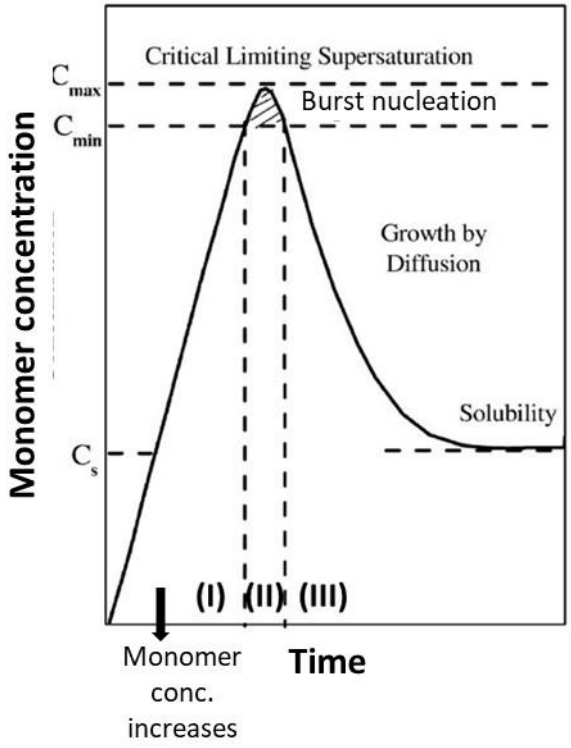

Figure 8: La Mer's schematic representation (Adapted from Thanh *et al.* [58]).

It is desirable to obtain monodisperse uniform size distribution for nanoparticles due to their strong property-size relationship[59]. In solutions of relatively higher monomer concentration, small nanoparticles grow faster than the larger ones (size focussing) leading to monodisperse size distribution. By arresting the reaction at the nucleation stage such as by supplying more reactants to maintain the saturation, a critical radius r_{crit} can be maintained to ensure monodispersity. Critical radius for a particle is defined as the minimum size at which the particle will survive in the solution without getting dissolved[58]. When the monomer concentration is low or gets consumed in due course because of particle growth, the smaller particles ($r < r_{crit}$) are depleted and the larger ones ($r > r_{crit}$) grow (size defocussing) that leads to broad size distribution. The growth of the larger particles at the cost of smaller particles is known as Ostwald ripening.

The growth condition of the critical radii r_{crit} is strongly dependent on the saturation ratio, *S*, which is the ratio of C/C_0, where *C* is the concentration of the solute and C_0 is the equilibrium concentration. The relation is given by Eq.2[58]

$$r_{crit} = \frac{2\gamma V}{k_b T ln S} \qquad (2)$$

where V is the molecular volume of the precipitated species, γ is the surface free energy per unit surface area, kb is the Boltzmann constant, and T is the temperature.

A large body of literature is available on methods to tune the size of gold nanoparticles from 1-100 nm either by using surfactants like oleylamine[60], PVP[61] and tannic acid[62] or by employing surfactant-free synthesis in which the reaction medium itself such as the solvent play dual roles of reducing the precursor and size control[63]. Under aqueous conditions, gold nanoparticles of sizes 12-64 nm are produced by the pioneering work of Frens *et al.* by changing the concentration of sodium citrate or sodium borohydride in the reaction medium where the citrate and borohydride play dual roles of controlling the nanoparticle size and acting as reducing agent[64,65]. In the presence of a strong reducing agent like sodium borohydride, small sized gold nanoparticles are formed due to faster rates of reduction whereas in weak reducing agents like citric acid, large gold nanoparticles are obtained because of slower reduction rates. In non-aqueous medium, the popular work of Brust in the synthesis of gold nanoparticles show that it is possible to synthesize gold nanoparticles of size 1-4 nm depending on the reaction conditions when the tetrachloroaurate ions are transferred to the toluene phase by using tetra-alkylammonium bromide followed by reduction with sodium borohydride in the presence of thiols[66]. In Brust synthesis, sodium borohydride reduces the gold precursor and thiols act as capping ligands to control the growth of gold nanoparticles.

2.2.1.3 Shape control of gold nanoparticles

Although there has been an explosion of research articles on the growth of gold nanocrystals in solutions, our understanding on the shape evolution of metal nanocrystals is still rudimentary[67]. Some of the main factors that are responsible for effective shape control are: a) the growth of a particular crystal morphology due to the adsorption of capping ligands like PVP on particular crystal facets[68] or the presence of small amounts of different salts that can greatly alter the final morphology by selective adhesion to particular facets of the crystal for example small amounts of silver nitrate salt present in the solution

during the growth of gold nanoparticles has a prominent effect on the morphology because deposition of silver monolayer on the surface of Au nanoparticles acts as a strong binding agent that prohibits crystal growth in some dimensions such as {110} facets[47] and b) a strong relation is present between the final morphology and the crystalline structure of the seed for example, nanoparticles exhibiting regular decahedral geometry grow from seeds with pre-formed decahedral geometry[69]. There are two major categories of the shapes of gold nanoparticles; spherical and non-spherical. The most common gold nanoparticle synthesis routes like Turkevich[70], Frens[71] and Brust[66] provide spherical gold nanoparticles (as discussed in the previous Section 2.2.1.2).

There has been an increasing interest to develop non-spherical or anisotropic gold nanoparticles due to several attractive features offered by them such as rod shaped gold nanoparticles are beneficial to enhance the surface plasmon resonance properties due to their sharp geometries (i.e. ends of rods) which leads to high electric field gradients[72]. Gold nanomaterials with spiky edges are also desirable for the generation of hot electrons which is useful for surface enhanced Raman spectroscopy (SERS)[73]. SERS is a surface sensitive technique that enhances Raman scattering by molecules adsorbed on plasmonic nanoparticles. A vast amount of literature is available on the anisotropic growth of gold nanomaterials in aqueous conditions. Branched gold nanostructures like bipod, tripod and tetrapod are prepared by adding capping surfactants like CTAB (cetyltrimethylammonium bromide) to solutions containing $HAuCl_4$ and ascorbic acid[74,75]. The use of other capping agents like SDS (sodium dodecyl sulfate) and PVP (poly vinyl pyrrolidone) are also carried out to synthesize branched Au nanostructures[76]. Dimethylformamide (DMF) is a versatile solvent which acts as a reductant, solvent and ligand to synthesize metal nanoparticles[77]. DMF acts both as a solvent and capping ligand by tuning shape morphologies like triangles, decahedra, octahedrons or spheres[78] .

2.2.2 Structure-activity relationship of Au

Structure functionality studies show that the optimum size and shape required for the gold nanoparticles is strongly dependent on the final applications for e.g. the optical properties of gold nanomaterials rely heavily on shape because the refractive index sensitivities (i.e. change in localized surface plasmon resonance wavelength per unit refractive index)

changes with morphology[79]. The index sensitivities increases with an increase in elongation and as the axes becomes sharper such as for nanorods and nanobipyramids due to an increase in the electromagnetic field at the sharper edges[80] whereas for nanocubes and nanospheres, the index sensitivities are much smaller[81]. Anisotropic gold nanostructures like nanostars, nanothorns and snowflakes are also effective for catalytic activities such as electrocatalysis owing to a high density of stepped atoms[41].

One of the most commonly studied catalytic reaction for gold nanoparticles to gain more insights on the structure-activity relationship is the oxidation of CO[82]. The unique physico-chemical properties of gold which makes it suitable for a range of applications such as catalysis are highly dependent on the size of nanoparticles for e.g. small gold nanoparticles of sizes 2-4 nm are two times more reactive towards CO oxidation than 20-30 nm size because Au atoms at the steps and corners of the smaller particles have lower coordination numbers and d states closer to the Fermi level resulting in a stronger interaction between the Au atoms and CO molecules[83].

2.2.3 Synthesis of gold nanomaterials in DES

Over the last decade, a number of studies[84,85,86,87] have been published on the wet chemistry synthesis of gold nanoparticles in reline by adding external reducing agents like ascorbic acid and sodium borohydride. Sun *et al.*[41], Stassi *et al.*[87] and Barcenas *et al.*[85] reported the synthesis of multiple twinned gold nanostructures such as stars and snowflakes by reducing $HAuCl_4$ in reline using ascorbic acid as a reducing agent. The effect of different reaction parameters such as amount of water, reactant concentration and temperature on the resulting gold nanostructures are investigated by them. In these studies, ascorbic acid acts both as a reducing agent and an anisotropic template directing agent due to its preferential adsorption on particular crystalline facets directing the anisotropic crystal growth process[49].

The reduction of $HAuCl_4$ by ascorbic acid involves its deprotonation and thus the presence of water in the system accelerates the synthesis of gold nanoparticles[88]. Although the varying amounts of water lead to different shapes, the exact contribution of water towards the tuning of varied morphologies is yet to be fully understood in detail. Similarly, gold

nanowire networks have been synthesized by Chirea *et al.* by reducing $HAuCl_4$ by sodium borohydride in reline at 40 °C[86]. It was shown here that urea molecules in reline stabilizes the resulting gold nanowire network during the fast reduction of Au^{3+} by sodium borohydride due to the formation of an intermediate adduct between choline chloride, urea and $AuCl_4^-$. The different morphologies of Au nanocrystals were tuned in reline by changing the amount of water and the applied potential during electrodeposition by Li *et al.*[89]. The change in morphologies upon varying the water content occur mostly because of the following reasons: a) on increasing water content in the DES reline, the rate of ionic migration and electrochemical reduction happens faster leading to a rapid nucleation and growth of Au nanocrystals; b) in the absence of water, a large number of choline cations are available in the solvent but on increasing the amount of water, the availability of choline cations to participate in the reaction to tune the shape decreases which affects the final morphologies. A summary of the different gold nano morphologies synthesized in reline with different reducing agents are listed in Table 3.

Similar results on the synthesis of gold nanoflowers in the DES formed by a mixture of choline chloride, gallic acid and glycerol is reported where the carboxyl and hydroxyl groups present in gallic acid act as the reducing and stabilizing agent to synthesize gold nanostructures[90].

Table 3: Summary of the synthesis of gold nanomaterials in DES with the addition of external reducing agents.

Ref	DES	Reducing agent	Gold Morphologies
[85]	Reline (choline chloride and urea)	Ascorbic acid	Nanoflowers (30 °C) Urchin like structures (60 °C) Star shaped (90 °C) Agglomerates of stars (120 °C)
[87]	Reline (choline chloride and urea)	Ascorbic acid	Nanostars (room temperature)
[41]	Reline (choline chloride and urea)	Ascorbic acid	Snowflakes (no water) Nanostars (5000 ppm water) Nanothorns (10000 ppm water)
[89]	Reline (choline chloride and urea)	Electrodeposition	Nanostars (pure reline) Sea-urchin (80% water in reline) Spherical (50% water in reline) Amorphous (pure water)
[86]	Reline (choline chloride and urea)	$NaBH_4$	Nanowires
[90]	Choline chloride, gallic acid and glycerol	-	Nanoflowers

2.3 Metal oxide nanomaterials

Metal oxides constitute an important class of materials in various areas such as catalysis, energy storage, medicines and sensor applications[91]. At the nanoscale, metal oxides are attractive because of their unique electrical, chemical and physical properties for example, the electrical and ionic conductivity properties of metal oxides like SnO_2 makes it attractive for sensor applications due to change in conductivity on account of band bending produced by adsorption of molecules[92]. There are a wide range of different morphologies of metal oxide nanomaterials available such as 1D nanowires and nanotubes, 2D nanosheets, 3D shapes and nanoparticles. As discussed in Chapter 1, out of several physical and chemical methods available for the synthesis of nanomaterials, the focus of the thesis is on two methods; solvothermal/hydrothermal routes and wet chemistry reduction of the precursor salt method because of their simplicity and good control of size and shape at the nanoscale[93,94].

2.3.1 Wet chemical synthesis of metal oxide nanomaterial

Hydrothermal synthesis

Hydrothermal synthesis of nanomaterials involves their growth at high temperature and autogeneous pressure (> 100 °C, > 1 atm) in aqueous conditions. The mechanism consists of the hydrolysation of the metal nitrate salt normally used as precursor to form metal hydroxides. Metal hydroxides are then precipitated as metal oxides through dehydration as shown in eq. 3 and 4[95,96].

$$M(NO_3)_x + xH_2O \rightarrow M(OH)_x + xHNO_3 \qquad (3)$$

$$M(OH)_x \rightarrow MO_{x/2} + {}^{x}/_{2}\, H_2O \qquad (4)$$

Solvothermal synthesis

Solvothermal synthesis of nanomaterials is similar to the hydrothermal synthesis; however, the main difference between the two methods is that in solvothermal synthesis, the solvent is non-aqueous. This synthesis involves operating pressures ranging from more than 1 atm and temperatures between 100 °C and 300 °C[97]. The main factors governing the solvothermal reactions are the solvent nature and the thermodynamic parameters[98]. Solvent

selection is important as it determines the mechanism of formation and thus the resulting product. It is possible to tune the shape and size of the nanomaterials by controlling the other factors in solution such as nature of solvent, precursor, temperature, reaction time and pH[99]. In solvothermal synthesis, supersaturation is the phenomenon that controls the overall nucleation rate and crystal growth[99]. Supersaturation is defined as the condition when a solution has more amount of the dissolved material than could be dissolved by the solvent under normal conditions. The solute starts precipitating into clusters of crystals whenever the solution reaches its supersaturation stage. Soon following nucleation, these crystals grow in larger sizes and shapes following mostly two processes i.e. transport of units through solution and attachment of these units to the growth sites as seen in Figure 9 [100].

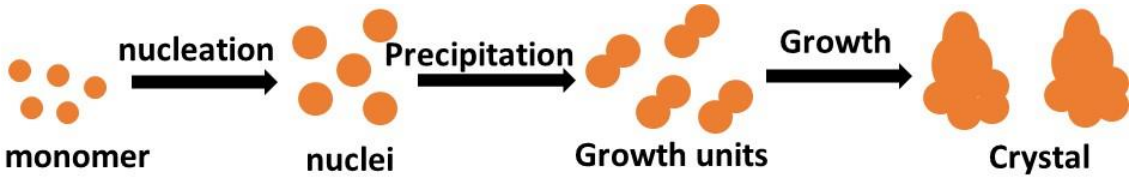

Figure 9: Schematic representation of the growth of nanomaterials in solvothermal synthesis conditions (Adapted from Li *et al.* [100]).

Main advantages of solvothermal processes for the synthesis of nanomaterials are better control over shape and size, growth of single crystals at low temperatures and ceramics preparation from metastable states[101]. However one of the disadvantages of this synthesis technique is the inability to monitor the reaction in-situ because the ordinary autoclaves (reaction vessels employed for solvothermal synthesis) are usually opaque.

The growth of metal oxide nanomaterials is broadly governed by four possible processes taking place in the solution phase: nucleation, particle growth, Ostwald ripening[102] (where some of the nanoparticles grow at the expense of other nanoparticles which dissolve) and dissolution kinetics of nanoparticles[103]. The concepts of nucleation and particle growth are explained with the help of La Mer diagram shown in Section 2.2.1.2.

2.3.2 Mechanistic strategies to control shape of metal oxide nanomaterials

Before the current state of art is reported for the wet chemical synthesis of metal oxide nanomaterials, it is vital to understand how the nanocrystal surfaces of metal oxides can be manipulated to tailor shape and sizes of the products. Shape control of the nanomaterials is an interplay between thermodynamic parameters (e.g. relative stabilities of the crystal faces) and kinetic limited processes like diffusion of reactants in the mixture and surface adhesion of surfactants[104]. The three major strategies for metal oxide shape control are as follows:

1) **Oriented attachment (OA)**: It is the growth mechanism process where the nanoparticles with common crystallographic axes are combined together directly to form larger particles[105]. The mechanism of the growth of anisotropic nanomaterials by OA route is by either collisions of aligned nanoparticles in solution or rotation of non-aligned nanoparticles that are in contact to obtain low-energy morphologies[106]. Nanorods of TiO_2 grows in hydrothermal conditions by OA mechanism due to the collision amongst the nanocrystals and formation of rod like morphology possessing minimum surface area[107].

2) **Effect of surface energy and selective adhesion**: Surfactants having different affinities for different crystal phases lead to excellent shape control due to selective adhesion. For example, in the absence of surfactants, TiO_2 grows as arrow shaped nanocrystals with fast growth along {001} face followed by a bipyramid shaped base terminated by {001} and {101} crystal faces. When lauric acid is used as a surfactant, there is a reduction in the growth along {001} direction resulting in the formation of nanorods[108].

In addition to surfactants, dopants (traces of impurity elements) play an important role in shape control by stabilizing specific phases of the crystallographic lattice. An example of this can be seen from the conversion of CeO_2 nanopolyhedra into nanospheres by doping with Ti^{4+}[109]. Introduction of dopants in the crystal lattice increases the number of electric dipoles present which in turn affects the nucleation and growth process, hence influencing the final shape and size of the nanocrystals[110].

3) **Control of the growth regime**: Isotropic growth of nanomaterials is favoured in the presence of a sufficient supply of thermal energy and low flux of monomers whereas anisotropic growth is favoured by a high flux of monomers[104]. An example of the effect of growth regime can be seen from the evolution of Co_3O_4 crystals under different reaction times. During early stages, Co_3O_4 nanocubes are formed by the specific growth of {111} facets but upon exceeding the reaction time, the initial monomer concentration gradually depletes to a level that is lower than required for nanocube formation. Thus, the cubic shape evolves into spherical shape which is the most stable phase by the growth of {100} faces because of the differences in the chemical potential of these two faces[111].

2.3.3 Surfactant-free processes to synthesize nanomaterials

One of the aims of this PhD thesis is to investigate the use of DES to synthesize nanomaterials in a solvent-controlled approach without the addition of any external additives in the reaction medium, hence it is imperative to mention other solvents that are reported in the literature that fulfil the surfactant-free approach to develop nanomaterials. Benzyl alcohol is a versatile solvent as more than 53 different types of metal oxides are synthesized by reacting their respective precursors in it[112]. Oxides of metals such as iron, indium, gallium and zinc are produced by reaction of the respective metal acetyalacetonates with certain amines like benzylamine which play dual roles of reactant and solvent[113,114]. A series of reactions involving the solvolysis of metal acetylacetonates followed by C-C bond cleavage to produce N-benzylacetamide and enolate ligands upon reaction with benzylamine produces metal oxide nanoparticles[114]. Glycothermal routes employing glycols like ethylene glycol, 1,4- butanediol and 1,5- butanediol as solvents also fulfils multiple roles such as strong oxidizer and bidentate ligands which can bind to the metal ions to form metal complexes that serve as molecular templates in directing chemistry at the nanoscale to synthesize metal oxides[115,116,117].

In ionothermal syntheses, IL are the reaction media and also provides template cations around which inorganic frameworks grow[118]. The ‘all-in one’ properties of IL are due to several factors[119]. On one side, the extensive hydrogen bonding system in IL is highly structured and hence affects the resulting products and on the other side, IL are immiscible with a number of organic solvents, thus desirable bi-phasic synthesis reactions can be

designed. IL also stabilizes nanomaterials by forming a protective layer of counter-ions around the metal nanoparticles that prevent these from agglomeration[120].

2.4 Ceria

Ceria (CeO_2) is a stable pale yellow oxide known to crystallize in a fluorite structure (space group Fm3m), where Ce^{4+} ions occupy the face centre and cubic positions, the oxide ions occupy the tetrahedral sites whereas the octahedral sites remain vacant as shown in Figure 10[121].

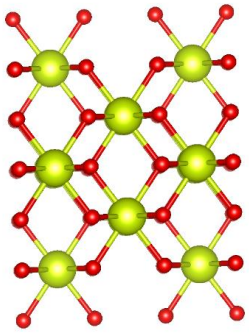

Figure 10: Fluorite crystal structure of ceria, green spheres: cerium atoms, red spheres: oxygen atoms.

Ceria forms non-stoichiometric oxides of the formula CeO_{2-x} under reducing atmospheres ($0<x<0.5$) due to the capability of the cerium atom to cycle between +3 and +4 oxidation states. By increasing the reducing temperature, the ceria lattice undergoes an expansion due to the reduction of Ce^{4+} to Ce^{3+} (ionic size of Ce^{3+}(101 pm) is larger than Ce^{4+}(87 pm))[122]. These non-stoichiometric phases formed during the reduction process can be easily oxidized to CeO_2 under mild oxidizing conditions. This ability of CeO_2 to store and release oxygen due to the Ce^{3+}/Ce^{4+} redox couple is known as oxygen storage capacity (OSC)[123] and depends on the ambient oxygen partial pressure and temperature as seen in eq. 5.

$$\boldsymbol{CeO_2 \rightarrow CeO_{2-x} + \frac{x}{2} O_2 \ (0 < x < 0.5)} \qquad \boldsymbol{(5)}$$

OSC is an important property of the catalytic materials to store oxygen in an oxygen rich environment and to release oxygen in an oxygen deficient environment. Owing to its high OSC, CeO_2 has attracted the attention of the scientific community for decades due to its applications in a wide range of catalytic areas such as in three way catalytic converters, fluidised catalytic cracking, removal of soot from diesel engine exhaust, oxidation of pollutants and in fuel cell technology[124,125].

2.4.1 Synthesis of nanostructured faceted CeO_2

A wide range of methods are reported for the synthesis of nanostructured ceria including electrochemical deposition[126], sol-gel[127] and hydrothermal methods[7]. Amongst these, the hydrothermal method being the simplest and one of the most economical routes, has attracted considerable interest as discussed in Section 2.3.1. Table 4 provides an overview of the main solvothermal methods used for the synthesis of nanostructured ceria, including the synthesis conditions and the resulting morphology.

Table 4: Overview of the main solvothermal methods for the synthesis of nanostructured ceria.

Ref	Ceria precursor	Solvent	Surfactant	T / °C	Time	Morphology
[7]	$Ce(NO_3)_3.6H_2O$	Water / NaOH	No surfactant	70	10 h	Nanoparticles
				100		Nanorods
				180		Nanocubes
[128]	$CeCl_3 \cdot 7H_2O$	Water / ethanol	Octadecylamine	160	72 h	Nanorods
			SDS	160	72 h	Nanoparticle
			NaOT	160	72 h	Nanoparticle
[129]	$Ce(NO_3)_3.6H_2O$	Water / ethanol NaOH	Oleic acid	180	24 h	Nanospheres
		Water / n-butylalcohol NaOH				Nanocubes
[130]	$Ce(NO_3)_3.6H_2O$	Water	Ethylene glycol	300	10 min	Aggregates of nanoparticles
				350		Nanoflowers
				380		Nanoflowers
[131]	$Ce(NO_3)_3.6H_2O$	Urea / Water		150	0.5	Rods
				150	24	Prism
				150	72	Polygon
[132]	$Ce(NO_3)_3.6H_2O$	Ethylene glycol	-	180	48 h	Palm leaves using glass slides as substrates

[133]	$[(NH_4)_2Ce(NO_3)_6]$	Aq. NH_3 solution NaOH	Ethylene glycol	50 (microwave)	30 min	nanoparticle
[134]	$CeCl_3 \cdot 7H_2O$	Toluene	hexadecylamine	80	24 h	Nanocubes
[135]	$CeCl_3.7H_2O$	Aq. H_2SO_4, NH_3 solution	CTAB	80	4 days	Nanorods
[136]	$Ce(NO_3)_3 \cdot 6H_2O$	Water / Diethyleneglycol	PVP	180	24 h	Nanospheres
[137]	$Ce(CH_3CO_2)_{3.x}H_2O$	1,4-butanediol/ ethylene glycol, octanoic acid		300	2 h	Plates
[138]	$CeCl_3.7H_2O$	Ethanol / peroxyacetic acid		160	9 h	Hollow nanocubes
[139]	$CeCl_3.7H_2O$	Water / formamide / H_2O_2	PVP	180	24 h	Hollow nanospheres
[140]	$Ce(NO_3)_3.6H_2O$	Urea / water / Glycerine		100	24 h	Nanospindles
[141]	$Ce(NO_3)_3.6H_2O$	Hexanol / Ammonia		180	24 h	Micropillows
[142]	$Ce(NO_3)_3.6H_2O$	Water	PVP	140	24 h	Spherical nanocrystallite
[143]	$Ce(NO_3)_3.6H_2O$	Water / Urea		150	12 h	Nanospindles
[144]	$Ce(NO_3)_3.6H_2O$	Water / Carbamide	CTAB	150	16 h	Triangular microplates

Synthesis conditions play a key role to determine the resulting ceria morphology and size. For example by systematically varying the concentration of base (NaOH) and temperature during hydrothermal synthesis; nanoparticles, nanorods and nanocubes are selectively synthesised as the temperature and NaOH concentration increases[7] due to changes in the dissolution/recrystallization kinetics. Alternatively, templating agents and/or surfactants are also used to control the morphology. Surfactants like octadecylamine, CTAB and PVP are able to tune the morphology of ceria into nanorods and even affecting the size distribution[128,135,142], while others such as SDS and NaAOT fail to produce 1D morphologies[128]. The choice of solvent and precursor also plays a crucial role in affecting the morphology of the resulting ceria materials. In specific cases, the solvent is not only a

platform for the dissolution of the ceria precursor but also plays dual role as a surfactant. Oleic acid acts as a surfactant to produce nanospheres when water/ethanol is used as the solvent and nanocubes when water/n-butylalcohol is used[129]. Other factors such as the presence of alcoholic groups in organic compounds, e.g. glycerine, are responsible for the linkage of nanoparticles, forming nanospindles[140]. Alkaline conditions favour the synthesis of a mixture of quadrangular and hexagonal nanoparticles whereas acidic conditions induces the formation of hexagonal shaped nanoparticles[131].

2.4.2 Structure-activity relationship of nano CeO_2

Experimental[145] and theoretical[146] studies show that the physico-chemical properties of the nanoceria exhibit surface-structure dependent characteristics because different morphologies selectively expose different crystal planes[6]. Ceria nanoparticles preferentially expose {111} and {100} facets, ceria rods are known to enclose {110} and {100} surface planes, and ceria cubes, {100} planes. Figure 11 shows the atomic configurations of each of the ceria facets. Ab-initio calculations show that {100} phase is the most reactive surface as it presents a high surface energy of 2 eV followed by the {110} surface of 1.50 eV and finally the {111} surface exhibits the lowest surface energy of 1.21 eV and hence is the most stable surface[147,148]. The oxidation activities are inversely proportional to the phase stabilities and thus, the most reactive crystal surfaces are {110} and {100} facilitating the formation of oxygen vacancies and exhibiting higher reducibility at lower temperatures along with larger OSC[7]. Experimental results show that the migration of lattice oxygen from bulk to surface is highest for these two {100} and {110} surfaces[149] while for the (111) surface, surface oxygen vacancies are immobile at room temperature[150]. Hence, the reducibility of nanoceria increases in the order of rods > particles > cubes[7].

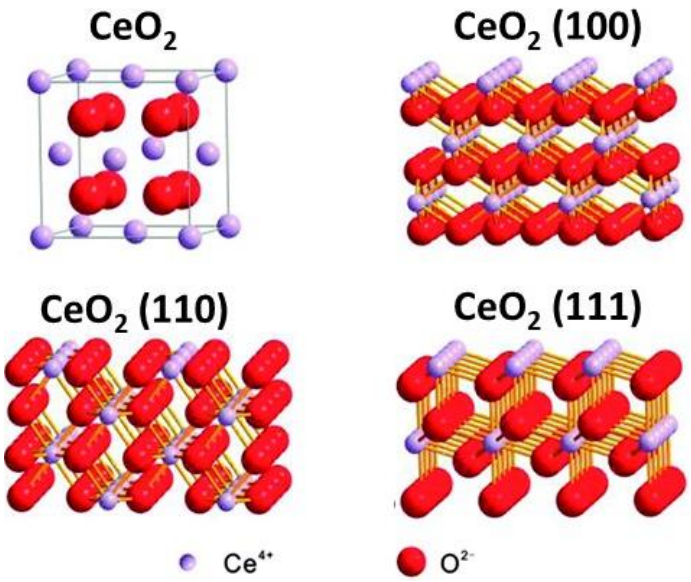

Figure 11: Atomic configurations of the unit cell and the {001}, {111}, and {110} facets of CeO_2 (Adapted from Li *et al.* [46]).

In addition to morphology effects, the OSC of ceria is known to depend strongly on the particle size such as 5-10 nm particles show a higher surface oxygen concentration than the 30 nm particles[151]. The presence of this surface oxygen is of key importance specially in oxidation reactions where it can easily react with reacting species[151]. Thus, a good morphological control and selective exposure of crystal phases is extremely important for various oxidation catalytic reactions (e.g. VOCs and CO) on nanostructured ceria because theoretical calculations predict strong CO chemisorption on the higher energetic {100} and {110} surface planes in comparison to the {111} plane[152].

2.4.3 Use of IL and DES to synthesize nanostructured CeO_2

Despite the easy scale-up of most of these hydrothermal methods, they often involve the use of harsh, toxic and corrosive alkaline agents like NaOH. Some works using IL to engineer different morphologies of nanostructured ceria like nanospheres, rod, ribbons and flowers have been reported by manipulating the nature of cation such as aromatic, pyrridinium, pyrrolidinium and alkyl chain based in the IL[153]. In these IL, different cations influence differently towards mechanisms like electrostatic attractions, self-assembly, hydrogen bonds and π-π stacking to influence the growth of CeO_2 in IL resulting in

different morphologies. Monodisperse spherical aggregates of nanocrystalline ceria were developed using IL both as the solvent and template source[154].

In addition to IL, DES also presents a sustainable and non-toxic alternative towards novel solvothermal routes. To date, reline and another DES composed of CTAB and acetic acid are the only DES that are used to successfully synthesise nanostructured ceria[155,156]. Liquid-phase neutron diffraction measurements show that the solvent plays the role of a latent supramolecular catalyst leading to a solvent-driven pre-organisation of reactants, allowing the low-temperature synthesis of nanostructured ceria. Significant control over the morphology, size and porosity can be achieved by controlling the reline/water ratio[155]. DES composed of CTAB and acetic acid is shown to stabilize ceria nanoparticles and prevent these against agglomeration[156]. CTAB is a common surfactant and hence its incorporation in the DES serves dual roles of surfactant and solvent along acetic acid.

2.5 Zirconia

ZrO_2 exists in three crystallographic phases: monoclinic, tetragonal and cubic phase[157]. Monoclinic phase exists below 1170 ℃, tetragonal between 1170 ℃ and 2370 ℃ and cubic phase above 2370 ℃ as shown in Figure 12.

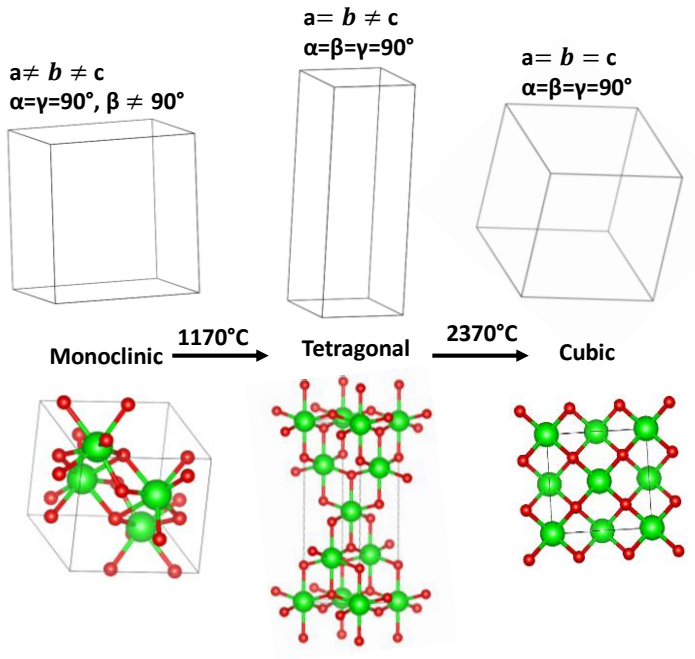

Figure 12: Crystallographic phases of ZrO_2: monoclinic, tetragonal and cubic (Adapted from Brog *et al.* [158]).

Zirconia, ZrO_2 is used extensively in a wide range of applications such as nanoceramics, reinforced ceramic composites, bio-material for dental implants and coatings for ceramic fibres[159]. The use of ZrO_2 as a technologically important metal oxide is due to its intrinsic properties such as high melting point, resistance to acids and alkali, hardness and shock wear. Factors like low thermal conductivity and high thermal coefficient expansion makes ZrO_2 a suitable candidate to be used as thermal coatings[160].

2.5.1 Synthesis of nanostructured ZrO_2

Several methods are reported in the literature to synthesize nanostructured zirconia such as co-precipitation, hydrothermal synthesis, sonochemical, microemulsion and sol-gel[161]. Hydrothermal route is one of the most popular route to synthesize ZrO_2 nanomaterial due to easy preparation methods and good control over morphology and size as mentioned previously in Section 2.3.1. An overview on the synthesis of ZrO_2 in hydrothermal conditions to develop different phases and morphologies is shown in Table 5.

Table 5: Overview of the main solvothermal methods for the synthesis of nanostructured zirconia.

Ref	Zirconia precursor	Solvent	Surfactant	T(°C)	Time (h)	Morphology/ Phase
[162]	$ZrO(NO_3)_2.xH_2O$	NaOH (5M), ethanol	-	200 250	24 24	Nano rice^{m} Hexagonal nanodiscs^{m}
[163]	Commercial ZrO_2	NaOH (10M)	-	150	85	Spherical^{t,m,c}
[164]	$ZrOCl_2.8H_2O$ $Zr(OH)_2(C_2H_3O_2)_2$ $ZrO(NO_3)_2.xH_2O$	H_2O H_2O H_2O	-	170 210 210	- - -	Spherical^{m} Circular^{m} Irregular^{m}
[165]	$ZrO(NO_3)_2.xH_2O$	H_2O	-	250	24	Nanocrystal^{m}
[166]	$ZrO(NO_3)_2.xH_2O$	Urea/ H_2O Urea/CH_3OH	-	140 140	20 20	Nanocrystal^{m} Nanocrystal^{t}
[167]	$Zr(NO_3)_4.5H_2O$	$N_2H_4.H_2O$ NaOH	-	150 150	24 24	Nanocrystal^{tmaj} Nanocrystal$^{m\ maj}$
	$ZrOCl_2.8H_2O$	$N_2H_4.H_2O$ NaOH	-	150 150	24 24	Nanocrystal$^{t\ maj}$ Nanocrystal$^{m\ maj}$
[168]	$ZrOCl_2.8H_2O$	Aq. NH_3 solution	Diethanolamine Triethanolamine Glycerol Dichloromethane Ethyl bromide Ethyl iodide Trimethylamine Dimethylamine	180	24	Ellipse^{t} Ellipse^{t} Sphere^{t} Spindle^{m} Ellipse^{m} Spindle^{m} -$^{t+m}$ -$^{t+m}$
[169]	Commercial ZrO	NaOH (15,20,25M)	-	200	7 days	Nanobars^{m}
[170]	ZrB_2	H_2O_2	-	170	24	Nanorod^{m}
[171]	$Zr(NO_3)_4.5H_2O$	NH_4F	-	180	72	Nanorods
[172]	$ZrOCl_2.8H_2O$	NH_4OH	-	200	12	Nanoparticles^{t}
[173]	$ZrCl_4$	$LiOH.H_2O$ NaOH KOH $(CH_3)_4NOH$	-	110	7	Nanoparticle^{cmaj} Nanoparticles^{c} Nanoparticles$^{c\ med,\ m\ small}$ Nanoparticles$^{m\ med,\ c\&t\ minor}$
[174]	$ZrOCl_2.8H_2O$	Na_2CO_3 NaOH Na_2SO_4 HNO_3 NH_4F	-	450	50	Twinned^{m} Twinned^{m} Powder^{m} Powders^{m} Plate crystals^{m}
[175]	$ZrO(NO_3)_2.xH_2O$ (0.25M) $ZrO(NO_3)_2.xH_2O$ (0.38M)	H_2O H_2O	-	250 250	24 0.5	Nanoparticle^{m} Nanoparticle^{m+t}
[176]	$ZrOCl_2.8H_2O$	NH_3 solution	CTAB	250	18	Nanoparticles^{t}

[177,178]	$ZrOCl_2.8H_2O$	NaOH	Lauric acid, SDS	160	12	Lamellar

- No surfactants used.

m, t, c, maj, min, med represents monoclinic, tetragonal, cubic, major phase, minor phase and medium phase respectively.

From Table 5, it can be seen that the final ZrO_2 phase is closely dependent on the synthesis conditions such as the nature of solvent. Unlike monoclinic (m-zirconia), tetragonal (t-zirconia) and cubic (c-zirconia) are unstable at room temperatures and transform to m-zirconia in the presence of moisture[179,180]. However, by systematically varying the nature of the alkaline base and solvent during the hydrothermal treatment or by introducing dopants like alkali metals and yttria[181], selective tuning of zirconia phases (monoclinic, tetragonal, cubic) can be achieved due to changes in the dissolution/recrystallization kinetics. Pure phases of t-ZrO_2 and m-ZrO_2 are obtained when methanol and water are used respectively as solvents with urea[166]. This shows that solvents play a crucial role towards phase control because water transforms the hydrous intermediate metastable t-ZrO_2 precipitates into more stable m-ZrO_2 by dissolution and precipitation, whereas methanol removes the water molecules from the precursors by the reaction with urea to maintain the tetragonal phase of the ZrO_2 intermediates[166]. Synthesis of t-ZrO_2 and m-ZrO_2 are also achieved by using hydrazine and NaOH respectively because hydrazine not only acts as the solvent but also as a coordinating ligand with the Zr precursor[167]. The use of additives like polyhydric alcohols (glycerol) act as good chelating agents to Zr centres in order to tune t-ZrO_2 phase whereas alkyl halides favour the formation of m-ZrO_2 but the exact reason for the phase stabilities by these alcohols and alkyl halides is still poorly understood[168]. Phase determination depends largely on the nature of the cation present in the base as well[173]. Mineralizers such as LiOH and NaOH, which have a smaller cationic radii, favour the formation of cubic phase whereas monoclinic phase is favoured in solvents like trimethylamine which have a larger radii. The larger cationic radii of the mineralizer causes a decrease in the crystallization rate which provides sufficient time to the nucleation reaction to arrive at the thermodynamically stable monoclinic phase[182].

Templating agents and/or surfactants are also used to control the morphologies of nanomaterials as discussed previously. Surfactants such as CTAB, SDS and lauric acid are able to produce nanoparticles and lamellar structures and even affecting the size

distribution[177,176]. The choice of solvent and precursor also plays a crucial role in affecting the morphology of the resulting ZrO_2 materials. In specific cases, the solvent is not only a platform for the dissolution of the precursor but also acts as a surfactant. For example, changing the solvent from water/NaOH to water/ethanol mixtures, the resultant morphology modifies from nano-rice to hexagonal nanodiscs[162]. Other factors such as the presence of OH groups in organic compounds, e.g. glycerol, leads to the formation of nanospheres whereas additives like those containing amine groups such as triethanolamine and diethanolamine form nano-ellipses due to the difference in the growth rate of different crystallographic planes[168]. Acidic conditions induce the formation of a mixture of nanoplates and nanoparticles whereas alkaline conditions favour the synthesis of micrometer sized twinned particles due to the differences in the dissolution process, formation of intermediate metal-additive species and nucleation growth steps[174].

2.5.2 Structure-activity relationship of ZrO_2

Selective exposure of the crystallographic phases in ZrO_2 plays a significant role in a wide range of applications such as nanostructured ceramics, sensors, solid oxide fuel cells and catalyst support due to high oxygen ion conductivity, good mechanical and electrical properties[163]. The three different ZrO_2 polymorphs: monoclinic, tetragonal and cubic; exhibit different catalytic activities, selectivities and adsorption phenomenon due to the variations in the densities of the hydroxyl group, lewis acid/base strength of cation/anion pair sites and Brønsted acid and base sites on their surfaces[183]. Experiments have shown the difference in the total number of acid sites and base sites on the surface of m and t-ZrO_2[184]. The total number of acid sites for m-ZrO_2 and t-ZrO_2 are 1.88 and 1.55 nm^{-2} respectively. Whereas the total number of base sites are 0.93 and 3.23 nm^{-2} respectively. In order to understand the crystal phase-activity relationship of ZrO_2 polymorphs, several catalytic reactions have been reported in the recent past, allowing the study and comparison of the activity of different phases. For example, monoclinic ZrO_2 presents a higher activity than c-ZrO_2 and t-ZrO_2 in the photocatalysis of methyl orange due to the presence of more surface hydroxyl groups, lewis acid sites, better adsorption properties and more defects[185]. The formation of carbonate-like complexes via strong binding of CO is suggested as potential reaction pathway for t-phase whereas formate intermediate species

are created on m-phase[184]. Due to the larger number of acid and base sites on monoclinic zirconia, Cu/m-ZrO_2 and Au/m-ZrO_2 are more effective than the tetragonal phase towards methanol synthesis from CO/H_2 and water gas shift reactions respectively[186,187]. V_2O_5/m-ZrO_2 is more active for alkylation of phenol due to high acidity on account of anionic concentration on monoclinic surface[188]. However, the presence of a lower number of lewis acid sites on the surface of tetragonal phase is beneficial for other applications like liquid phase hydrogenation of benzene to cyclohexene (Rh-B/t-ZrO_2)[189] and Cu/t-ZrO_2 for CO hydrogenation as Cu is displaced better on the t-phase[190]. Higher hydrocarbon formation occurs for the tetragonal/cubic phase due to a greater number of basic sites in comparison to monoclinic zirconia. Tetragonal sulphated ZrO_2 is found to be more effective in bimolecular reactions like n- butane isomerization due to the stabilities of intermediate transition state complex species to the O_2^- that is tetra-coordinated on the surface[191]. These results show that a solid understanding on the development of a particular phase is essential for final applications.

2.5.3 Use of IL and DES to synthesize nanostructured ZrO_2

Tetrafluoroborate based IL with different cations (1-butyl-3-methylimidazolium (BMim) and N-butylpyrridinium (Bpy) are used to synthesize ZrO_2 nanowires to study the role of cation in the synthesis as the solvent[192]. It is observed that ZrO_2 nanowire formation does not takes place in the absence of IL however BMim IL produces more uniform nanowires suggesting the surfactant role of IL towards the formation of ZrO_2 nanowires. A combination of BMim IL and water is used to synthesize spherical ZrO_2 nanoparticles using the technique of microemulsion in order to replace the highly volatile xylene phase with the negligible vapour pressure of BMim IL[193]. Tetragonal phase of ZrO_2 is synthesized in the microemulsion technique and the BMim IL also help in preventing the agglomeration of ZrO_2. There are no reports published so far in the synthesis of nano ZrO_2 in DES. Synthesis of 2D open framework zirconium phosphates in DES via solvothermal synthesis based on tri- and tetra methyl alkyl groups along with oxalic acid as the HBD moiety play dual roles of both the solvent and template to synthesize zirconium phosphates by getting incorporated in the Zr framework[194,195,196,197]. These examples show the

potential of novel chemistries based on IL and DES to synthesize nanomaterials in solvothermal reactions.

2.6 Vanadium pentoxide (V_2O_5)

Vanadium, the chemical element with an atomic number of 23 is named so after the Scandinavian goddess of beauty and fertility (*Vanadis*) by Nils Gabriel Sefström who discovered various chloride salts of vanadium in 1830s. Out of several possible oxides of vanadium from +2 to +5, vanadium pentoxide (V_2O_5) is the most important oxide due to its wide usage in various technological applications such as cathode materials for Li-ion batteries[198], electrochemical capacitors[199] and biological sensors[200]. In particular, orthorhombic V_2O_5 is an attractive cathode material for battery applications as its theoretical and real capacity upon two Li ion insertions/extractions is higher (294 $mAhg^{-1}$) than conventional cathode materials[201]. One of the most common oxide of vanadium, V_2O_5 belongs to the orthorhombic crystal class with a space group of P*mmn*, (D_{2h}^{13}) and lattice parameters a = 11.510 Å, b = 3.563 Å, c = 4.369 Å with distorted square pyramidal coordination symmetry[202] as shown in Figure 13. This distorted polyhedral structure forms $(V_2O_4)_n$ zigzag double-chains along the {001} direction which are cross-linked along {100} through shared corners[203]. The layered structure of V_2O_5 are held together by weak V-O bonds comprising of VO_5 square pyramids sharing edges and corners[204].

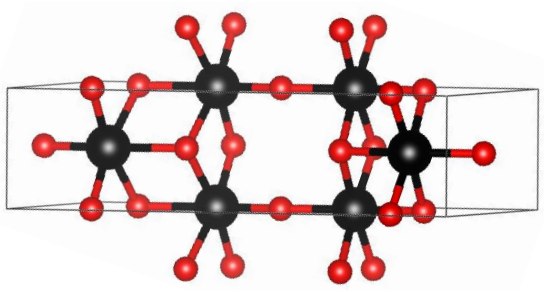

Figure 13: Orthorhombic phase of V_2O_5; black spheres: vanadium atoms, red spheres: oxygen atoms.

2.6.1 Synthesis of nanostructured V_2O_5

Various strategies are employed to synthesize nanostructured V_2O_5 such as sol-gel processing, thermolysis, reverse micelle and hydrothermal synthesis[205]. Out of these methods, due to the advantages offered by the hydrothermal route such as rapid and facile preparation, cheap and scalable synthesis (as discussed in the previous Section 2.3.1), several reports are published in the past towards the synthesis of different nanostructured morphologies of V_2O_5 by hydrothermal routes[199,206,207,208]. Different morphologies of nanostructured V_2O_5 such as nanowires, nanowaxberries and nanoflowers are synthesized by using different concentrations of PVP under hydrothermal conditions[207].

PVP is an excellent crystal growth modifier that tunes the formation of superstructures in solutions by its preferential adsorption to certain crystalline facets, leading to different shapes of V_2O_5. Similarly, ethylene glycol has been used as an additive to synthesize V_2O_5 nanoflowers[209] by its coordination with vanadium ions forming nanorods which then self-assemble into nanoflowers. In the absence of ethylene glycol, nanobelts and nanoparticles are synthesized. Different acids such as acetic acid and nitric acid are used in aqueous and ethanol solvents to obtain nanoflowers, nanoballs, nanowires and nanorods[208]. As can be seen from the above examples, it is possible to obtain various morphologies from different solvents such as acids and alcohols due to the adsorption abilities of the functional groups present in these solvents to adhere on the nanocrystal facets[210].

High aspect ratio $V_2O_5.xH_2O$ nanobelts and nanorolls are synthesized under hydrothermal conditions by using strong and weak acids like sulphuric acid and acetic acid respectively[211]. On altering the hydrothermal conditions like temperature and synthesis time, the amount of water intercalated between the nanostructures in the reaction mixture plays an important role to tune various morphologies of nanostructured $V_2O_5.xH_2O$ nanowires and nanorods[206]. At lower temperatures, more flexible structures like nanowires are obtained whereas nanorods are obtained under high temperature conditions i.e. in the less hydrated forms[206].

2.6.2 Structure-activity relationship of V_2O_5

Various V_2O_5 nanostructured morphologies like nanowires, nanowaxberries and nanoflowers have been tested for Li-ion battery electrode applications[207]. The best stability is shown by the nanoflowers and highest Li-ion diffusion coefficient in comparison to other nanostructures because the nanoflowers are usually composed of nanoflakes, which increases the surface area of the materials that facilitates the easy diffusion of ions. The structure-activity relationship is evident on studying the electrochemical behaviours using cyclic voltammetry and galvanostatic charge-discharge curves on four different morphologies of V_2O_5 including nanoflowers, nanoballs, nanowires and nanorods[208]. V_2O_5 nanorods exhibits the best electrochemical behaviour in terms of storage capacity, electrochemical kinetics and charge discharge capabilities due to its rod-like structure which facilitates the diffusion and migration of Na^+ ions during ion insertion while using Na_2SO_4 electrolyte. Microspheres of V_2O_5 with different interiors such as hollow, yolk-shelled, multi-shelled and single-shelled structures have been tested to understand the role of these complex interior structures for Li-ion battery applications[212]. The unique yolk-shell structures facilitate an efficient penetration of the electrolyte and a good contact area between the electrolytes and electrode due to the void space present within the microspheres and porous shell.

2.6.3 Use of IL and DES to synthesize nanostructured vanadium based compounds

Two IL $[Py_{1,4}][Tf_2N]$ and $[EMIM][Tf_2N]$ with different cations $[Py_{1,4}]^+$ and $[EMIM]^+$ have been used to synthesize V_2O_5 nanoparticles and study the effect of cations in the synthesis[213]. V_2O_5 nanoparticles with poor surface areas and crystallinity are obtained in $[EMIM]Tf_2N$ because the positive charge is delocalized in the aromatic imidazolium ring and is not available for donation in comparison to pyrrolidinium where the charge is available for donation[213]. Imidazolium based IL have been used as both solvents and intercalating agents to synthesize 1D nanorods by a facile solvothermal synthesis route[214]. V_2O_5 nano/micro rods are synthesized by using two types of IL [EMIM][TfO] and $[EMIM][Tf_2N]$ by ultrasound irradiation technique to study the effect of different anions

$[TfO]^-$ and $[Tf_2N]^-$ on the V_2O_5 morphologies[215]. Due to the steric hindrance of $[Tf_2N]^-$ anion in comparison to $[TfO]^-$, the micro/nanorods of V_2O_5 are less aggregated. Lamellar and clubbed morphologies of vanadium phosphate catalysts by using sodium metavanadate and peroxyphosphoric acid as the initial raw precursors are synthesized in reline as the template agent[216]. It is believed that the breakdown of the urea portion from reline releases the expected template species to synthesize other compounds such as vanadium oxyfluorides[217]. There have been no reports published in the literature so far on the use of any DES to synthesize nano V_2O_5.

2.7 CO oxidation

Catalytic CO oxidation to form CO_2 is one of the most widely studied reactions due to its applicability in a large number of industrial processes to oxidize CO in the automotive industry sector, petrochemical industries and fuel production. CO oxidation is commonly used as a model reaction to compare oxidation catalytic activities. Research towards the development of catalysts that can facilitate CO oxidation at lower temperatures is attractive in order to enable the catalytic converters in the automobiles to convert CO during the cold start period[218]. An increased interest in gold nanoparticles for low temperature CO oxidation began when an unexpected high catalytic activity of gold was reported by Haruta *et al.* and Hutchings *et al.* towards the oxidation of CO at temperatures as low as -70 °C[219,220]. Gold is attractive for CO oxidation reactions due to the high propensity of oxygen to adhere to the surface of gold nanoparticles particularly at the low coordinated sites and defects[221]. CO is a strong σ- donor and a good π- acceptor ligand. The bonding of CO to the metals comprises of two components. The first component is the donation of 2 electrons from the lone pair on carbon into a vacant metal d-orbital by the formation of a σ bond (formed by the overlap of sp hybridized electron pair on carbon with the d, s and p orbitals on the metal). This electron donation make the metals more electron rich and subsequently a filled metal d orbital interacts with an empty π* orbital on the carbon atom from the CO molecule (known as back-bonding) to decrease the added electron density. As the π* orbital of the carbon gets filled from the back-donation of electrons from the metal d

orbital, the carbon-oxygen bond is weakened whereas the metal-carbon bond is strengthened.

The catalytic activity of gold is strongly dependent on the nature of support (reducible or non-reducible) and the active sites present at the interface between the gold nanoparticle and the support[222]. Ceria is one of the most popular supports for Au nanoparticles to study CO oxidation reactions due to its high OSC[6].

Mars-Van-Krevelen model is one of the most popular mechanisms available to explain the CO oxidation on both (with and without gold nanoparticle) ceria based supports. Figure 14a presents a schematic representation of the CO oxidation for only ceria based catalyst (without any gold nanoparticle) comprising of three key steps; i) reaction of CO molecule with the lattice oxygen of ceria to form CO_2 and leaving a surface oxygen vacancy site; ii) Adsorption of gas phase oxygen into the vacancy site and iii) second CO molecule reacting with the adsorbed oxygen.

The mechanism of oxidation of CO by ceria/Au system is depicted in Figure 14b showing the following steps[223]: i) CO is activated on the metal nanoparticle surface and react with oxygen atoms coming from the ceria based support. Oxygen transport from the support to the metal depends on the availability and mobility of oxygen and vacancies at the surface and the interface between the metal nanoparticle/support. Gas-phase oxygen are adsorbed on the two electron defect sites at the metal nanoparticle-oxide border and are consumed by the adsorbed CO; ii) consumption of lattice oxygen by the adsorbed CO to produce CO_2 and iii) replenishment of the surface oxygen vacancies by gas-phase O_2. Metal nanoparticles on ceria support systems are more effective than pure ceria towards CO oxidation due to the preference of CO adsorption on Au nanoparticle surface rather than the oxide[224].

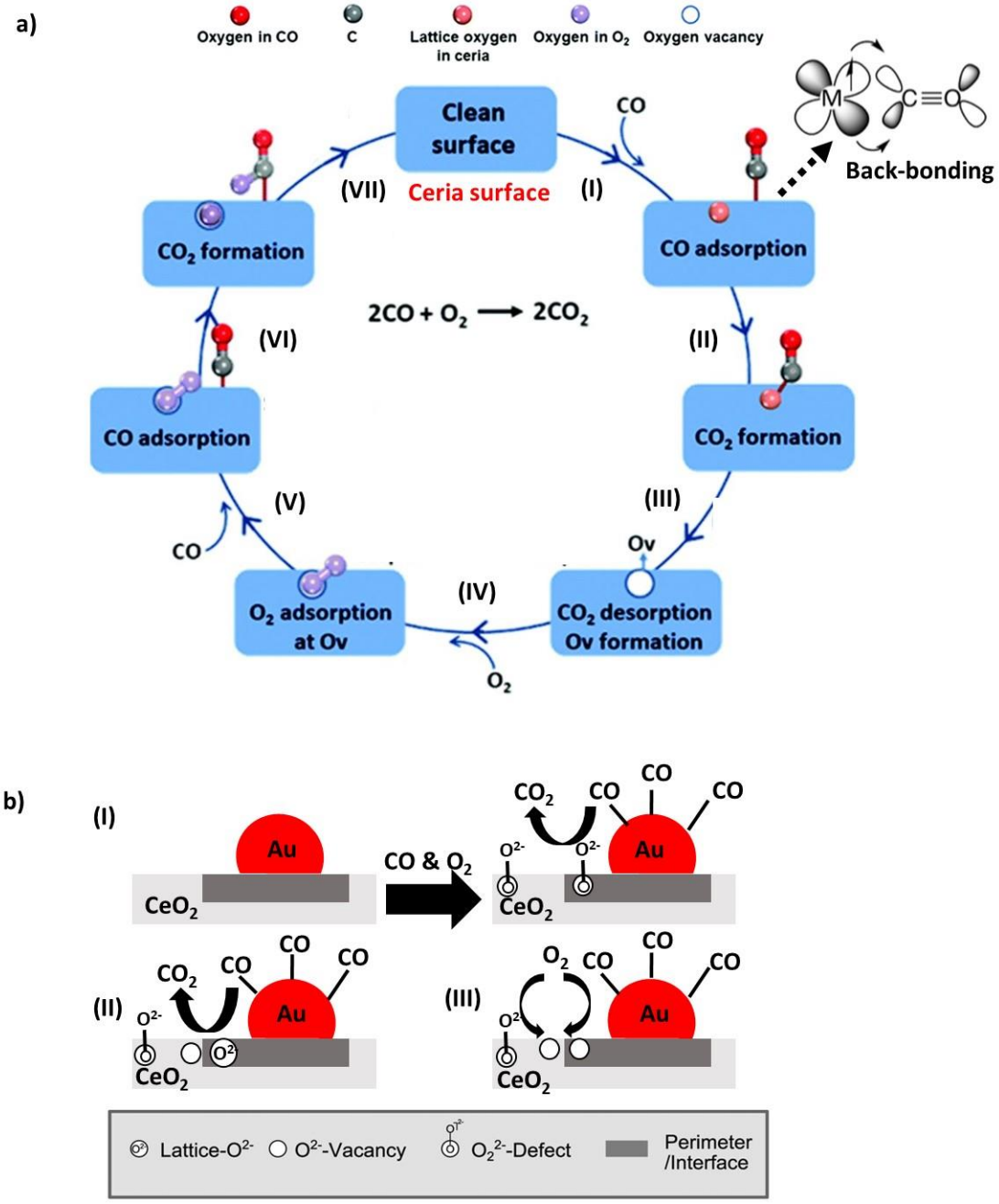

Figure 14: Schematic representation of CO oxidation mechanism on a) only ceria-based support (Adapted from *Liu et al.* [225]) and b) Au supported ceria catalysts (Adapted from Lohrenscheit *et al.* [223]).

2.8 Literature review conclusions

In this thesis, the use of deep eutectic solvent(s) as an alternative route to the use of surfactants and corrosive bases is explored and indeed, initial studies are reported in the literature showing the ability of DES to control the size and morphology of nanomaterials within the framework of a solvent-controlled approach. As the DES are a class of green and eco-friendly solvents hence there is an overall decrease in the ecological footprint on using these for nanomaterial synthesis replacing the addition of external additives in the reaction.

Since the discovery of DES in 2001, it is only from 2008 onwards that research groups have started exploring the potential of DES to synthesize nanomaterials. However, full understanding of the mechanism of formation and/or the actual role of the different DES components is not clear, limiting the development of new solvent systems. The use of DES towards the synthesis of metal oxides is extremely limited. Although DES systems have been employed to synthesize metal nanoparticles like copper, platinum and gold, yet the exact role on the interaction of the eutectic solvent with the materials is not completely understood.

This literature review has considered previous work on various surfactant assisted and other surfactant-free approaches for the synthesis of metal oxide (CeO_2, ZrO_2 and V_2O_5) and gold nanomaterials. These metal oxides and Au are used for various applications such as catalysis, Li-ion batteries and plasmonics which are strongly dependent on the structure-property relationship of the nanomaterials.

It is highlighted herein that synthesis reaction conditions are important to influence the final shape and size of the nanomaterials. In order to synthesize nanomaterials of desirable morphologies and sizes, several reagents such as surfactants and capping ligands are employed in the wet chemical synthesis method. In addition to the use of surfactants, conventionally the use of aqueous NaOH and KOH as the solvent medium is common to prepare nanomaterials in spite of their corrosive and harsh nature.

This PhD thesis fulfils the gaps presented in the literature so far to develop external additives free systems based on DES to synthesize nanomaterials and use them for various

applications. This research also elucidates the mechanism on how these DES platforms serve several roles such as reducing agent, template delivery component and exfoliating agent.

Chapter 3: Experimental methods

This chapter reports the experimental methodologies followed to synthesize nanomaterials in the DES (Chapters 4, 5, 6 and 7). The different nanomaterials are synthesized by two routes- solvothermal and colloidal synthesis. Gold nanomaterials are synthesized by colloidal route and the metal oxides (transition and ceramic) based nanomaterials are synthesized by the solvothermal routes.

3.1 Solvothermal synthesis

The solvothermal approach involves the heating of the reactants in a sealed stainless-steel vessel, commonly known as the autoclave. The autoclave comprises of a polytetrafluoroethylene (PTFE) liner inside a stainless steel unit. The reaction mixture is poured in the PTFE liner followed by the sealing of the autoclave using the rupture disc and top ring discs and then heated inside the air-circulating oven. Throughout this thesis, Parr PTFE liners of capacity 125 mL and autoclave model 4748 are used. The components of the autoclave and the air-circulating oven are shown in Figure 15.

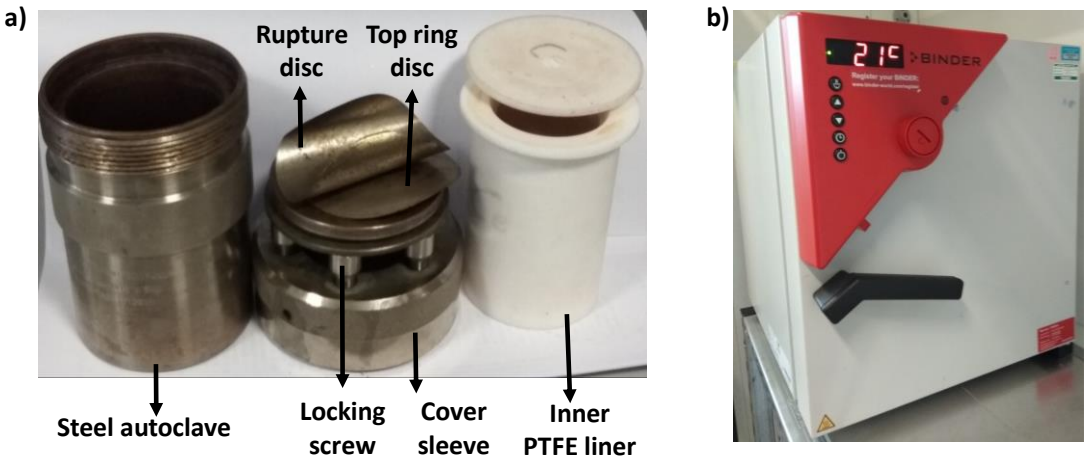

Figure 15: Experimental set-up arrangement of the solvothermal synthesis process: a) various components of the autoclave; b) air-circulating oven for heating the autoclave.

3.2 Colloidal synthesis

In this thesis, gold nanomaterials are synthesized by batch colloidal synthesis method under ambient pressures using heat-up technique as shown in Figure 16. The typical experimental setup for the colloidal synthesis of nanomaterials comprises an oil (or water bath), magnetic hot plate and a thermocouple to maintain the reaction temperature.

Solvothermal[226,227,228] and colloidal[229,230] synthesis routes are widely reported as reproducible and feasible techniques in the literature to synthesize nanomaterials of controllable morphologies and sizes. Applying the framework of these synthesis techniques, this thesis provides the detailed experimental methodologies to synthesize different nanomaterials as explained in Sections 3.3 - 3.9. The use of solvothermal and colloidal synthesis of nanomaterials demonstrates the reproducibility and robustness of these techniques to produce the nanomaterials for the different experiments. The quality of the nanomaterials were tested by techniques like X-ray diffraction (XRD) and scanning electron microscopy (SEM).

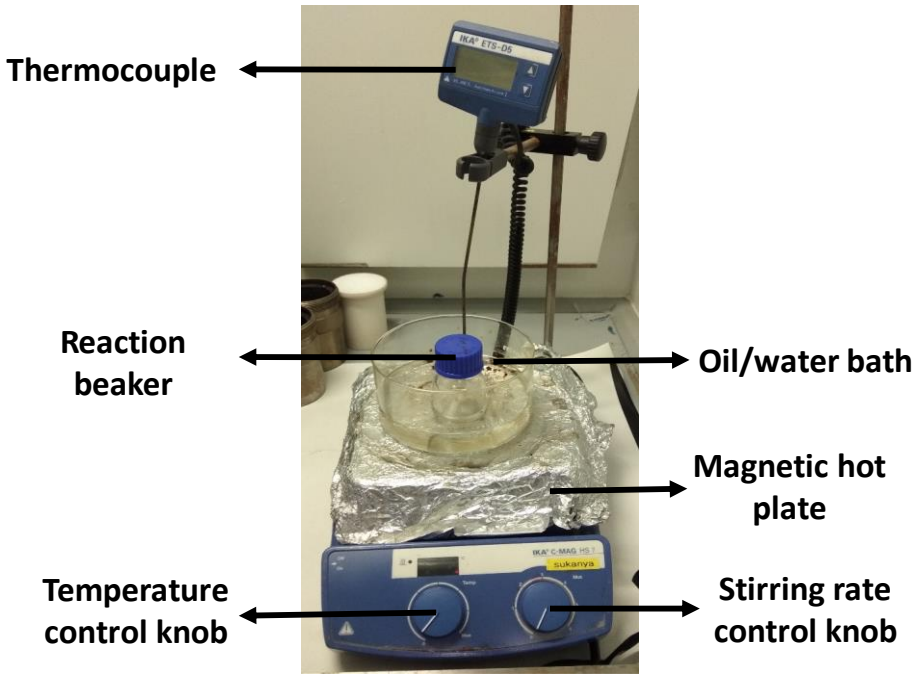

Figure 16: Typical experimental setup of a colloidal nanomaterial synthesis approach in the laboratory.

3.3 Preparation of deep eutectic solvents (DES)

3.3.1 Reline

The deep eutectic solvent reline is prepared following a previously reported method[155] using choline chloride and urea as received from Alfa Aesar. The components are mixed in the molar ratio of 1:2 respectively and allowed to stir for 4 h at a temperature of 80 °C till a clear liquid is formed. In order to prepare reline/water mixtures, water is added in the requisite molar quantity after the preparation of reline. The water content of pure reline was found to be ~2250 ppm by Karl Fischer titration technique. Due to the hygroscopic nature of the starting precursor (choline chloride; >98% pure), it might be expected that it may contribute to the traces of water in the deep eutectic solvent formation.

3.3.2 Asline

The deep eutectic solvent asline is prepared following a previously reported method[35] using choline chloride and ascorbic acid as received from Alfa Aesar and Acros Organic respectively. The components are mixed in the molar ratio of 2:1 respectively and allowed

to stir for 4 h at a temperature of 100 ℃ till a clear liquid is formed. In order to prepare asline/water mixtures, water is added in the requisite molar quantity after the preparation of reline.

3.4 Synthesis of gold nanoparticles in DES

This section discusses the synthesis of gold nanomaterials using DES (reline and asline).

3.4.1 Synthesis of gold nanoparticles in pure reline and reline/water mixtures

Gold nanoparticles are synthesised in reline-based solvents. In a typical synthesis procedure, 10 mL of freshly prepared reline (or reline/water (1:10 molar ratio respectively) mixture) is heated in an oil bath to the required reaction temperature under stirring. Once the required temperature (30 ℃, 60 ℃, 100 ℃ and 140 ℃) is achieved, 10 µL of $HAuCl_4$ solution (Sigma Aldrich, 4.82 mM) precursor is added. The reaction is left to proceed under constant stirring for a number of h depending on the reaction temperature. After the synthesis, the solution is cooled down to room temperature. In this reaction, as different oxidation states of gold exhibits different colours hence it is possible to stop the reaction at that stage to isolate a particular oxidation state by quenching the reaction in ice-cold water; for e.g. Au in +3, +1 and 0 oxidation state shows yellow, colourless and ruby red solution colours.

3.4.2 Synthesis of gold nanoparticles in pure asline and asline/water mixtures

Gold nanomaterials are synthesised in asline-based solvents. In a typical synthesis procedure, 10 mL of freshly prepared asline or asline: water (1:5 and 1:10 molar ratio respectively) in a closed glass bottle is heated in an oil bath to the reaction temperature under stirring. Once the required temperature (30 ℃, 60 ℃ and 100 ℃) is achieved, 100 µL of $HAuCl_4$ solution (Sigma Aldrich, 48.2 mM) precursor is added. The reaction is left to proceed under constant magnetic stirring for 1h. After the synthesis, the solution is cooled down to room temperature. The solutions are alternately washed with water and

ethanol repeatedly and centrifuged for 10 min at 4200 rpm to remove the asline. The products are dried overnight in vacuum oven at 80 ℃.

3.5 Synthesis of divananadium pentoxide (V_2O_5) nanomaterials in reline

V_2O_5 nanostructures are synthesized using a solvothermal route. In a typical synthesis, 80 mL of pure reline, reline/water mixture (1:2, 1:10 and 1:20 by molar ratio respectively) or pure water is added to a PTFE autoclave liner. V_2O_5 (1.8 g) is added to the solution and stirred at 80 ℃ for two h. The liner is then placed inside a stainless steel autoclave which is heated inside an air-circulating oven for 10 h at 180 ℃. After this time, the autoclave is cooled down naturally to ambient temperature. The resulting black reaction mixture is washed repeatedly with water and ethanol, centrifuged at 4200 rpm for 10 min and dried in a vacuum oven at 80 ℃ overnight. This dried black solid is then calcined at 500 ℃ for 4 h at a rate of 10 ℃/min to yield a bright yellow V_2O_5.

3.6 Synthesis of nano ceria (CeO_2) in reline and reline/water mixtures

80 mL of reline/water (1:10) molar ratio is added to a PTFE liner autoclave. $Ce(NO_3)_3.6H_2O$ (1.5g), purchased from Sigma Aldrich is added to the vessel and homogeneously mixed before sealing it. The liner is then placed inside a stainless steel autoclave which is heated inside an air-circulating oven at 140ºC for 10 h. Once the synthesis is finished, the autoclave is cooled down naturally to ambient temperature. The resulting solid product is washed repeatedly with water and ethanol, centrifuged at 4200 rpm for 10 min and dried in a vacuum oven at 80 ℃ overnight. This dried solid is then calcined at 500 ℃ for 4 h at a rate of 10 ℃/min to produce a pale yellow CeO_2.

3.7 Synthesis of nano ceria/zirconia (CeO_2-ZrO_2) in reline and reline/water mixtures

A range of ceria-zirconia nanostructure synthesis are carried out by the solvothermal synthesis approach in reline/water system using $Ce(NO_3)_2.6H_2O$ and $ZrO(NO_3)_2.6H_2O$ as the initial precursors. These samples are referenced as pure ceria, CZ 80/20 (80% CeO_2 and 20% ZrO_2), CZ 60/40 (60% CeO_2 and 40% ZrO_2), CZ 50/50 (50% CeO_2 and 50% ZrO_2), CZ (80% CeO_2 and 20% ZrO_2) and pure ZrO_2. The percentages denote the molar ratios between the initial precursor i.e. $Ce(NO_3)_2.6H_2O$ and $ZrO(NO_3)_2.6H_2O$. To maintain the desirable molar ratios, following quantities of the starting precursors were added: pure ceria (1.5g $Ce(NO_3)_2.6H_2O$), CZ 80/20 (1.5g $Ce(NO_3)_2.6H_2O$ and 0.28g $ZrO(NO_3)_2.6H_2O$), CZ 60/40 (1.5g $Ce(NO_3)_2.6H_2O$ and 0.72g $ZrO(NO_3)_2.6H_2O$), CZ 50/50 (1.5g $Ce(NO_3)_2.6H_2O$ and 1.11g $ZrO(NO_3)_2.6H_2O$), CZ 40/60 (1.5g $Ce(NO_3)_2.6H_2O$ and 1.64g $ZrO(NO_3)_2.6H_2O$) and CZ 20/80 (1.5g $Ce(NO_3)_2.6H_2O$ and 4.42g $ZrO(NO_3)_2.6H_2O$). 80 mL of reline/water (1:10) molar ratio is added to a PTFE liner autoclave. Suitable amounts of $Ce(NO_3)_3.6H_2O$ and $ZrO(NO_3)_2.6H_2O$ are added to the vessel to form the CZ samples and homogeneously mixed before sealing it. The liner is then placed inside a stainless steel autoclave which is heated inside an air-circulating oven at 140 ℃ for 10 h. After this time, the autoclave is cooled down naturally to ambient temperature. The resulting reaction mixture is washed repeatedly with water and ethanol, centrifuged at 4200 rpm for 10 min and dried in a vacuum oven at 80 ℃ overnight. This dried solid is then calcined at 500 ℃ for 4 h at a rate of 10 ℃/min to yield CeO_2-ZrO_2 samples.

3.8 Synthesis of zirconia (ZrO_2) in reline/water mixtures and NaOH

ZrO_2 nanoparticles are synthesized using a solvothermal route. In a typical synthesis, 80 mL of different ratios of reline/water solutions or pure water is added to a PTFE liner. Detailed studies are done mostly for reline/water (1:10 molar ratio) but other reline/water ratios such as 1:2 are used to understand the synthesis mechanism better. $ZrO(NO_3)_2.6H_2O$

(3.51 g) is added to the solution and stirred for two h. The liner is then placed inside a stainless steel autoclave which is heated inside an air-circulating oven for 10 h at 140 ℃ and 180 ℃. After this time, the autoclave is cooled down naturally to ambient temperature. The resulting white product is then washed alternately with water and ethanol to remove any traces of deep eutectic solvent and centrifuged at 4200 rpm for 10 min and dried in a vacuum oven at 80 ℃ overnight. The same synthesis protocol is also repeated with 80 mL of NaOH (1M, 5M and 15 M) (instead of reline solutions) to study the effect of the solvent on the resulting ZrO_2 crystalline phase.

3.9 Catalyst preparation – Au/CeO_2-ZrO_2

The catalytic activities of Au/CeO_2-ZrO_2 are tested in the model CO-oxidation reactions. In 10 mL of pure reline, appropriate amount of $HAuCl_4$ precursor is added (2.8 wt% and 5.6 wt% theoretical Au loading) and the solution is stirred at 80 ℃ for 5 min till the solution turns homogeneously pale yellow. 200 mg of the ceria-zirconia (or pure ceria or zirconia) is added to the reaction mixture and stirred constantly for 3 h at 80 ℃ till the solution turns colourless. After this, the reaction is quenched by putting it under ice-water bath and allowed to cool overnight. The resulting reaction mixture is washed repeatedly with water and ethanol, centrifuged at 4200 rpm for 10 min and dried in a vacuum oven for overnight.

3.10 Material characterization

A complete and detailed characterization of the prepared materials is extremely crucial to obtain a full understanding on the physical and chemical properties of these materials which in turn provides fundamental insights on the material's activity and provides feedback in designing better samples with improved performances.

3.10.1 X-ray diffraction (XRD)

XRD is an analytical technique carried out for the phase identification of samples. The principle behind XRD is the interaction of the monochromatic light source (like Cu Kα or Mo Kα) with the atoms of the periodic lattice. As given by the Bragg's law, the scattering

of the X-ray atoms in the atomic lattice in a constructive interference manner is given by eq. 6.

$$n\lambda = 2d\ sin\Theta \qquad (6)$$

Where n represents the integral order of reflection, λ is the X-ray wavelength, d is the distance between the two lattice planes and Θ is the angle between the incoming X-rays and the normal to the reflecting lattice plane. Each phase has a particular diffraction pattern that helps the users to determine the crystal phase and crystallinity.

In this work, powder X-ray diffraction has been carried out for powder samples which are finely ground and homogeneous.

Crystal phase identification of the powder samples are carried on a Bruker D8 Advance powder X-ray diffractometer with a VANTEC-1 detector and Cu Kα radiation at 40 kV and 40 mA. For this purpose, a thin layer of vacuum grease is put on the plastic XRD mould and approximately 50 mg of sample is mounted on the holder.

The coherent diffraction domain size for the particles is given by the Scherrer equation is eq.7.

$$D = \frac{K\lambda}{\beta Cos\Theta} \quad (7)$$

Where D is the coherent diffraction domain size, λ is the wavelength of the X-ray source applied, β is the reflection width (2Θ) and K is the shape constant (usually 0.9). The Scherrer equation used to calculate the coherent diffraction domain size for the CZ samples is calculated from the peak centred at 28.5° (Chapter 6) and the peak centred at 28.2° is used for the zirconia samples (Chapter 7). Scherrer equation is a method to 'estimate' the particle sizes and the true sizes could be determined by using electron microscopy techniques like TEM. Contributions from the XRD instrument towards peak broadening could be calculated by peak modelling studies using Rietveld calculations[231]. However, in this thesis, in the absence of taking into consideration the instrumental errors towards peak broadening, the upper size limits for particles might be over-estimated by 1 nm[232].

3.10.2 Electron microscopy measurements

Electron microscopy is an invaluable technique for obtaining high resolution images at the nanoscale.

High-resolution transmission electron microscopy (HR-TEM) measurements are recorded at an electron beam energy of 200 kV on a Talos TEM. For TEM, the samples were dispersed in 5mL of ethanol and directly drop-casted on carbon/copper TEM grids. The particle size distribution are calculated by using the ImageJ software and the particle sizes are expressed as average ± standard deviation. Several micrographs are taken from different areas of the TEM grid to calculate the lateral size diameter of the particles.

High angle annular dark field (HAADF-STEM) measurements are carried out using a Tecnai F20 using an accelerating voltage of 200 kV.

Aberration-corrected scanning transmission electron microscopy (AC-STEM) measurements are carried out by our collaborator Dr Emanuela Liberti at the University of Oxford. The samples are imaged on a probe corrected JEOL ARM200F at the electron Physical Science Imaging Centre (ePSIC) operated at 200 kV. A probe convergence semi-angle of 24 mrad and a probe current of 13 pA are used for the simultaneous acquisition of annular dark-field (ADF) and bright-field (BF) images. For ADF, an inner collection semi-angle of 55 mrad and outer collection semi-angle of 215 mrad are used, while BF images are recorded with a collection semi-angle of 15 mrad.

Scanning electron microscopy (SEM) measurements are performed on a MIRA3 FEG-SEM (Field emission gun scanning electron microscope) with a Schottky emitter for imaging the samples. The samples are mounted on a conductive carbon tape followed by a 10 nm Pt sputtering.

3.10.3 Electrospray ionization-mass spectroscopy (ESI-MS)

ESI-MS technique produces ions using an electrospray where a high voltage is applied to a liquid to produce an aerosol. The ionic species from the solution phase to the gas phase are transferred as follows: a) dispersal of the fine spray of charge droplets, b) solvent

evaporation (this refers to the solvent which is used to dilute deep eutectic solvent), c) ion ejection from the highly charged droplets.

ESI-MS spectra are recorded at the National Mass Spectrometry Facility at Swansea University using a Fourier Transform MS (FTMS or Orbitrap) by nanoelectrospray ionization (NSI). A very small aliquot (~ 2-4 µl) of each of the samples is diluted into 1 ml MeOH: H_2O (1:1) for nanoelectrospray analysis on the Thermo LTQ Orbitrap XL in both positive ion and negative ion modes. The Advion NanoMate inlet is used with a 96-well plate, corresponding transfer tips and 400-nozzle spray-chip at a flow rate of approximately 0.25 µL/min. The Orbitrap API source settings are as follows: source voltage +/- 1.4 KV; capillary temperature 200 ℃; capillary voltage +/- 47V; tube lens +150 V/-100 V. MS scan parameters: m/z 150 to 2000 and m/z 80 to 400 for internal lock mass accurate mass measurement of low m/z ions; resolution 100000.

ESI-MS studies are carried out to gain information on the alkylamine species formed in-situ in reline/water mixtures (Chapter 5). For this, the reline/water solutions (1:2 and 1:10 by molar ratio) are subjected to solvothermal synthesis in the autoclave at 180 ℃ for 10 h without the addition of any vanadium precursor. These samples are then sent to Swansea for the ESI-MS studies.

3.10.4 Nuclear magnetic resonance (NMR) studies

NMR is an analytical chemistry technique to identify structure and chemical environment of molecules in the solution phase.

For the gold samples, ^{13}C NMR and DEPT-135 (Distortionless enhancement by polarization transfer) are carried out in a 400 MHz Avance III HD Smart Probe spectrometer. For sample preparation, the colloidal samples are diluted with 750 µL of D_2O prior to analysis. The shift reference for ^{13}C and DEPT is actually the solvent itself. The NMR instrument uses a digital lock system, where the instrument consults a table of data to find where the 2H signal of a given solvent should appear, then adjusts the field of the magnet so the deuterium signal resonates at the expected frequency. The ^{13}C signal of the solvent should then be found at near the reference value. For ^{13}C experiments, the number of scans are 128, pulse lengths are 9.50 µs and recycle delay is 2 s.

^{51}V NMR measurements are carried out for the V_2O_5 samples in a 400 MHz Avance III HD Smart Probe spectrometer. For sample preparation, the colloidal samples are diluted with 750 µL of D_2O prior to analysis. Stock solutions of V(V) are prepared by dissolving the initial bulk V_2O_5 precursor (0.01M) in reline, reline/water (1:2 and 1:10 by molar ratio) and pure water solutions for analysis. An external reference comprising of a test solution of $V(OiPr)_3$ in C_6D_6 is used for ^{51}V NMR experiments and this is observed near the expected reference value of -634.5ppm. For ^{51}V experiments, the number of scans are 608, pulse lengths are 17.75 µs and recycle delay is 0.5 s.

3.10.5 Small angle X-ray scattering (SAXS)

Small angle X-ray scattering is a structural characterization technique which has enabled the scientific community to gain much more insights on nanoparticle research due to its ability to monitor reactions in real time and under native sample environment. In this thesis, SAXS technique is carried out to investigate the polydispersity and agglomeration of nanoparticles in solution.

In-situ SAXS measurements are performed on the I22 beamline at the Diamond Light source (Didcot, UK) by our collaborators Dr Iva Manasi and Prof Karen Edler at the University of Bath, UK. Small Angle X-ray Scattering (SAXS) measurements are carried out on the Au^+ (colourless) and Au^0 ruby red solutions prepared using the method described above in the experimental section to synthesize gold nanoparticles with initial concentration of $HAuCl_4$ at 4.82 mM and 9.64 mM. SAXS is carried out immediately after quenching the reaction using the XENOCS Nano-inXider SAXS/WAXS system and the Anton Paar SAXS/WAXS/GISAXS point system. Both of these use a Cu K-α source with wavelength 1.54 Å, giving a q-range of 0.004 $Å^{-1} < q < 0.4$ $Å^{-1}$. The scattering pattern so observed is fitted to spherical form factor with radius, *r*, and polydispersity, σ. The radius *r*, is calculated from the scattering factor q ($Å^{-1}$) where q is represented in eq. (8):

$$q = \frac{4\pi sin\Theta}{\lambda} \qquad (8)$$

$$r = \frac{\pi}{q}$$

Θ is the glancing angle between the incident X-ray beam and the sample, λ is the wavelength of X-ray beam.

3.10.6 Cyclic voltammetry

Cyclic voltammetry studies are carried out on colloidal nanoparticle systems (gold nanoparticle in reline in this case) to gain better understanding on the stability of the reaction products and the change in reduction potential values as a function of temperature.

Cyclic voltammograms are obtained for gold in pure reline samples utilizing a potentiostat (BioLogic VSP) connected to a three-electrode electrochemical setup consisting of a glassy carbon rod as the working electrode (Alfa Aesar, 3.14 mm^2 active area). Platinum wires are used as the counter and as the reference electrodes (Alfa Aesar, 99.997% metal basis). Before the beginning of each experiment, the glassy carbon electrode is cleaned with fresh aqua regia, rinsed with ultrapure water and subsequently washed with isopropanol and ultrapure water in a sonication bath. The platinum electrodes are cleaned with fresh aqua regia and rinsed with copious amounts of ultrapure water every time prior to use. The cyclic voltammograms are performed at different temperatures (30 ℃, 100 ℃ and 140 ℃) using an oil bath. Cyclic voltammetry measurements are carried out with the assistance of Dr Mauro Malizia, University of Cambridge.

3.10.7 Surface area measurements

Nitrogen adsorption and desorption studies are carried out at 77 K using an ASAP 2020 BET surface area analyser equipment from Micromeritics. Samples weighing approximately 100 mg are degassed prior to the analysis by heating at 120 ℃ under ultra-high vacuum. The specific surface area is calculated using the Brunauer-Emmett-Teller (BET) theory which takes into account the physical multilayer adsorption of gas molecules on a solid surface according to the given equation in eq. 9.

$$\frac{P}{V_a(P_o - P)} = \frac{1}{V_m C} + \frac{C - 1}{V_m C}\left(\frac{P}{P_o}\right) \qquad (9)$$

Va is the amount of gas adsorbed at pressure P, Po is the saturation pressure of the gas and C is a constant. In this equation, a straight line plot of $\frac{P}{V_a(P_o-P)}$ against $\frac{P}{P_o}$ with a slope of $\frac{C-1}{V_m C}$ and intercept of $\frac{1}{V_m C}$. V_m is calculated from slope and intercept.

Hence, the surface area is further calculated from V_m by using eq. 10.

$$Specific\ surface\ area\ (m^2 g^{-1}) = \frac{V_m \times N_A \times A_M}{W \times V_o} \quad (10)$$

N_A is the Avogadro's constant (6.023×10^{23});

A_M is the cross-sectional area of the adsorbate molecule, (for nitrogen, A_M=0.162 nm^2 at 77 K)

W is the weight of the sample

Vo is 22414 mL mol^{-1}.

3.10.8 X-ray photoelectron spectroscopy (XPS)

XPS is a surface sensitive technique that gives information on the elemental composition, oxidation states and electronic states for the material. The working of the XPS is based on the photoelectric effect. According to the photoelectric effect, when a photon of energy hν is absorbed by an atom, an electron either from the valence shell or core shell with binding energy E_b is ejected with kinetic energy E_k(eq. 11).

$$E_k = h\nu - \mathrm{E_b} - \phi \qquad (11)$$

ϕ is defined as the spectrometer work function

The instrument collects these photoelectrons to produce a spectrum between emission intensity and kinetic energies. This spectra can be further used for surface elemental analysis as the binding energies of the photoelectrons are characteristic of the elements from which these are emitted. XPS is used in this project to study the oxidation state of gold and ceria-zirconia nanomaterials synthesized in pure reline.

For gold, XPS spectra is recorded using a Thermo Scientific ESCALAB 250 Xi Spectrometer equipped with a monochromated Al K alpha source operating at 13.5 kV and 0.0205 mA. The pressure during the XPS analysis is 10^{-7} and 10^{-9} mbar. Three spot sizes

are recorded on each sample for analysis purposes. The spot size of each area is approximately 900 µm × 900 µm. The high resolution Au scans are done using a pass energy of 50 eV and step size of 0.1 eV. All the binding energies are corrected using the Au $4f_{7/2}$ peak at 84 eV. It takes approximately 5 min to acquire the XPS spectra for each sample. The XPS data is processed using Thermo avantage software package. The high resolution Au scans are done using a pass energy of 50 eV and step size of 0.1 eV. The samples for XPS measurement are prepared by dissolving $HAuCl_4$ in pure reline and heating the solution at 140 °C. The reaction is stopped at different time intervals in order to take out samples containing Au^{3+}, Au^{+} and Au^{0}. Thin layers of these samples are spin-coated on Si wafers. To ensure a homogeneous film, the substrate holder is rotated continuously at 0-5000 rpm over 2 s, at 5000 rpm for 60 s, 5000 to 0 rpm over 0.4 s after drop casting 1.5 mL of the samples on the Si wafers. The wafers are dried overnight in vacuum oven at room temperature prior to XPS analysis.

For ceria-zirconia samples, XPS Analysis is performed using a Thermo NEXSA XPS fitted with a monochromated Al kα X-ray source (1486.7 eV), a spherical sector analyser and 3 multichannel resistive plate, 128 channel delay line detectors. All data are recorded at 19.2 W and an X-ray beam size of 200 x 100 µm. Survey scans are recorded at a pass energy of 160 eV, and high-resolution scans are recorded at a pass energy of 20 eV. Electronic charge neutralization is achieved using a Dual-beam low-energy electron/ion source (Thermo Scientific FG-03). Ion gun current = 150 µA. Ion gun voltage = 45 V. All sample data are recorded at a pressure below 10^{-8} Torr and a room temperature of 294 K. Data is analysed using CasaXPS v2.3.19PR1.0. Peaks are fitted with a Shirley background prior to component analysis. Lineshapes of LA(1.53,243) are used to fit components. The X-ray photoelectron (XPS) data collection for the ceria-zirconia materials is performed at the EPSRC National Facility for XPS (“HarwellXPS”), operated by Cardiff University and UCL, under Contract No. PR16195.

3.10.9 Raman spectroscopy

Raman spectroscopy is a complimentary technique to XRD to study the phases of the samples. Raman spectroscopy is based on the ‘Raman effect’ which depends on the inelastic scattering of monochromatic light. Inelastic scattering means that when the

photons of the monochromatic light source interacts with the sample, their frequency changes. This shift in frequency or the 'Raman effect' provides information on the vibrational, rotational and other frequency transitions in the molecules. Raman spectroscopy is commonly used to characterize metal oxides because unlike XRD, which provides information only on the cationic lattice arrangement; Raman spectroscopy is sensitive to the position of the oxygen lattice vibrations as it is sensitive to the crystal symmetry[233]. In this thesis, Raman spectroscopy is used to study the phases of ceria/zirconia samples (synthesis of ceria/zirconia samples discussed in Section 3.7). For Raman measurements, sample amount equivalent to the fingertip is required. A LabRam 300 Horiba Raman microscope with a 50 x lens and a 532 nm excitation laser was used for the measurements.

3.10.10 Inductive coupled plasma - optical emission spectroscopy (ICP-OES)

ICP-OES is commonly used to determine the metal concentrations in dilute aqueous solutions with low ppm concentrations (~1 ppm). ICP-OES is used to analyse the gold content in the Au supported catalyst by acid digestion of the solid. For the acid digestion, aqua regia (1:3 mixture of 70 vol% HNO_3 and 36 vol% HCl is used) of volume 8 mL is used. These mixtures containing aqua regia solution are heated in an oil bath at 50 ℃ for 1 h and then the temperature is gradually increased to 70 ℃ and 90 ℃. The solutions are then allowed to cool overnight and then the necessary dilutions are carried out. A Perkin Elmer Optima 2100 DV spectrometer is used for the ICP analysis with argon as the torch gas. The obtained results are calibrated with the appropriate metal standards for gold (1 to 10 $mg \cdot L^{-1}$).

3.10.11 Temperature programmed reduction (TPR)

TPR is an analytical technique that is commonly used for the characterization of solid samples in order to determine the best reduction conditions. In this method, a reducing gas (hydrogen in our case) is passed over the oxidized sample which is subjected to a programmed temperature rise. The sample (approx.30 mg) is added in a U-shaped quartz reactor placed in a furnace fitted with a thermocouple. The sample is initially flushed with

an inert gas like argon or helium to remove any traces of air. After this, a reducing gas like hydrogen is passed through the sample while the temperature is raised. The composition of the exit gaseous mixtures are measured by the thermal conductivity detector (TCD). Whenever a reduction takes place at a particular temperature, hydrogen is consumed. TCD detects changes in conductivities related to the initial gas which can be related to hydrogen consumption.

TPR profiles of the samples are carried out using a Micromeritics Autochem 2920 with 20 mL/min of 5 vol% H_2 in argon from room temperature to 900 ℃ at a heating rate of 5 ℃/min. TPR profiles are analysed for the ceria/zirconia and Au based catalysts.

3.10.12 CO chemisorption

The activity of the catalytic materials greatly depends on the particle size of the metal nanoparticles on them as well as the metal dispersion % on these supports. For this purpose, CO pulse chemisorption is a common method employed to determine these factors. CO pulse chemisorption is carried out to determine the gold particle size on the ceria-zirconia catalytic supports. Prior to CO chemisorption, the specimen (approx. 30 mg) is reduced in-situ using 20 mL/min of 5% H_2 in argon at a heating rate of 5 ℃/min at a reduction temperature of 200 ℃ for 45 min. After the reduction is complete, the sample is cooled to -80 ℃ and held constantly at this temperature during the CO chemisorption analysis. The hemispherical diameter, d of the metal particle is calculated as follows[234]: The metallic surface area SA_{metal} is calculated first and then depending on the geometry, the diameter is found out in eq. 12 and 13.

$$SA_{metal} = \frac{V_{ads}}{22414} \times SF \times N_A \times A_{metal} \qquad (12)$$

$$SA_{metal} = \frac{A}{V.\rho} = \frac{2\pi r^2}{\frac{2}{3\pi r^3}.\rho} = \frac{3}{r.\rho} \qquad (13)$$

Where SF is the stoichiometric factor that depends on the species involved for the CO: metal interaction. For CO: Au chemisorption, SF is usually 1:1 for Au.

V_{ads} is total amount of CO adsorbed per mass of sample (cm^3/g)

N_A is Avogadro's constant

A_{metal} is the cross-sectional area of the metal (0.0869 nm^2 for gold)

A is the area of the particle, r is the particle radius

V is the volume of the particle, ρ is the density (19.3 g/cm^3 for gold)

The size distribution given by CO chemisorption is subjected to errors because of the following reasons[234]: the contact angle between the metal-support contact angle is not taken into consideration during particle size estimation, conventional assumption of semi-spherical nanoparticles may lead to wrong size estimation (in case the metal particle had some other shape like frustum, semi-octahedron and semi-truncated octahedron) and CO chemisorption provides an average particle size distribution.

3.10.13 Diffuse reflectance sphere solid UV measurements

UV-vis diffuse reflectance spectroscopy for zirconia powders (Chapter 7) is obtained in a UV-vis Shimadzu spectrometer with an integrating sphere reflectance accessory. The UV-vis absorption spectra is recorded in the spectral range of 190-900 nm.

3.10.14 Carbon monoxide (CO) oxidation catalytic rig

CO oxidation catalytic reaction is used as the model reaction to test the catalytic activity of the as-synthesized Au-ceria/zirconia, ceria-zirconia and Au/zirconia catalysts. The CO rig is designed and built by Dr Tamsin E. Bell, former PhD student at Torrente's group (Figure 17).

The description of the CO rig is as follows:

Mass flow controllers (MFCs) control the flow of the inlet gases. Four inlet gases are primarily used to study the CO oxidation reaction. These are: 5 vol% (CO/He); 5 vol% (O_2/He); 99.9 vol% (H_2) and 99.9 vol% (He). A Carbolyte tube furnace (30 cm in length) is used to heat the sample with openings at either end.

The catalyst is added in a U-shaped quartz reactor with an internal diameter of 0.4 cm with two bridges (one at the bottom and other at the top) to prevent the reactor against breaking while mounting the reactor in the rig. U-shape design of the reactor is usually preferred so

that the gases reach the set reaction temperature before arriving at the catalyst bed. The catalyst bed is prepared by first adding some quartz wool followed by 175 mg of fine silicon carbide, followed by a mixture of 25 mg of catalyst and 600 mg of coarse silicon carbide. Quartz wool is added on top to keep the catalyst bed in place. Two pressure indicators (P1 and P2) are present in the CO rig to monitor the pressure changes in the system and any kind of pressure drop across the catalyst bed.

The thermocouple data is obtained using a PICO TC-08 data logger and the gas analyser signal is recorded using a PICOLOG 1216 logger. The Picolog software records these signals after every 2 s. The gases are analysed by non-dispersive IR gas analyser (*ABB, EL3020-Uras 26*).

The rig is well equipped with handheld and portable CO and H_2 gas alarms in order to warn the rig user and other people working in the laboratory area. In addition to this, the CO line is fitted with a solenoid valve which turns off the gas line when the CO concentration exceeds 25 ppm in the laboratory area in case of an accidental leakage.

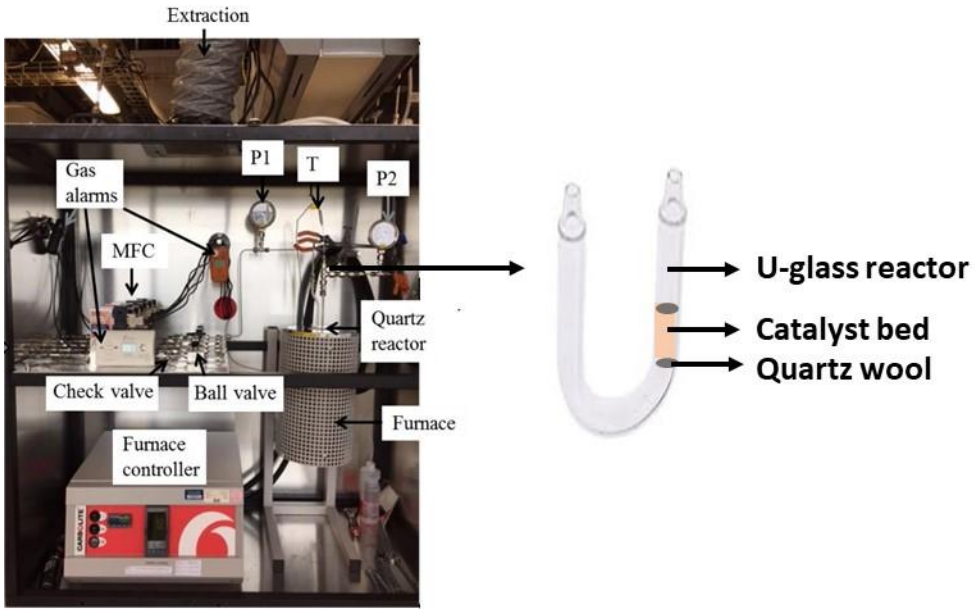

Figure 17: CO oxidation catalytic rig used in the lab (Adapted from Dr Tamsin E. Bell's PhD thesis)

Calibration: Two types of bubble flow meters are used to calibrate the MFC. Bubble flow meter with a capacity of 10 mL is used to calibrate the CO, H_2 and O_2 lines (as these have lower flow rates). Whereas 100 mL capacity bubble flow meter is used to calibrate the He inlet line as this has a higher flow rate. The gas analyser is also calibrated regularly to confirm the accurate flow rate. The calibration of the gas analyser is shown in Appendix A1.

During the catalytic test, the catalyst bed is pre-treated initially (by reducing in-situ by heating at 200 °C by flowing H_2 gas) followed by the CO oxidation reaction. The pre-reduction step is necessary for the Au supported catalysts to ensure that Au in the catalyst is properly reduced. A total flow rate of 300 mL/min is used, that is composed of 264 mL/min of He, 18 mL/min of 5 vol% of CO/He and 18 mL/min of 5 vol% O_2/He. These flow rates results in 3000 ppm of CO and 3000 ppm of O_2. According to the equation for CO oxidation (eq. 14), although only half as much as oxygen is required for CO, a 1:1 reagent ratio of CO to O_2 is used, representing an excess of O_2 according to the theoretical stoichiometry.

$$CO + \frac{1}{2}\ O_2 \rightarrow CO_2 \qquad (14)$$

Before reaction	F_a	F_b	0
During reaction	x	0.5x	x
After reaction	F_a-x	F_b-0.5x	x

$$CO\ concentration\ in\ the\ outlet\ stream = \frac{F_a - x}{F_a + F_b + F_{He} - 0.5x} = M$$

$$F_a - X = MF_a + MF_b + MF_{He} - 0.5xM$$

$$F_a - M(F_a + F_b + F_{He}) = (1 - 0.5M)x$$

$$x = \frac{F_a - M(F_a + F_b + F_{He})}{1 - 0.5M}$$

$$CO\ conversion = \frac{x}{F_a}$$

F_a, F_b, F_{He} are known flowrates of CO, O_2 and He in mol/s respectively. x is rate of CO consumed in mol/s.

For a standard catalytic reaction, the furnace temperature is ramped till 650 °C. These tests are repeated thrice to test the thermal stability of the catalyst.

The activation energies of the catalyst are calculated by using the Arrhenius equation where log conversion (y-axis) is plotted against the reciprocal temperature (1/T). The Arrhenius equation gives the dependence of the rate constant (k) on the absolute temperature T and pre-exponential factor A as follows in eq. 15.

$$k = Ae^{-\frac{E_a}{RT}} \qquad (15)$$

Upon taking the natural logarithm of the Arrhenius equation, Eq. 16 is obtained

$$ln\ k = \ln A - \frac{E_a}{RT} \qquad (16)$$

E_a is the activation energy and R is the ideal gas constant.

Chapter 4: The role of DES in the synthesis of gold nanomaterials

The first report on the synthesis of gold nanoparticles in DES, particularly reline, was published in 2008 by Sun *et al.* using ascorbic acid as an external reducing agent[41]. Since then, a number of studies[41,85,86,87] have been published on the wet chemistry synthesis of gold nanoparticles in DES reline by adding external reducing agents like ascorbic acid and sodium borohydride. Multiple twinned gold nanostructures such as stars and snowflakes were synthesized by Sun *et al.*[41], Stassi *et al.*[87] and Barcenas *et al.*[85] by reducing $HAuCl_4$ in reline using ascorbic acid as a reducing agent as discussed previously in the literature review (Chapter 2). In spite of several reports published on the synthesis of gold in reline, the actual role of reline in the synthesis of gold nanoparticles has not been known yet. Hence the aim of this chapter is to understand the role of reline in the synthesis mechanism of gold nanomaterials. Another DES known as asline is also studied herein to investigate the capping ligand roles offered by DES.

The usual pathway to synthesize nanoparticles by using the wet chemical reduction technique is to employ a reducing agent to reduce the precursor (normally a metal salt) in the presence of surfactants, capping ligands or stabilizers[235]. The reducing agents do not only act as mere sources of electrons but their ability to control factors like nucleation and growth indicates their importance in tuning the size and shape of the nanoparticles in the solution. This chapter is focussed to understand the roles played by DES as a reducing agent and capping ligand/stabilizer towards the synthesis of gold nanomaterials and to provide a platform to tune the morphology and size of gold at the nanoscale. Herein we have used two different types of DES: reline (choline chloride and urea) and asline (choline chloride and ascorbic acid) to act as solvent platforms to produce gold nanomaterials.

4.1 Synthesis of gold nanoparticles in pure reline

The gold precursor $HAuCl_4$ (4.82 mM) was heated in pure reline at 140 °C under continued stirring. The initial pale yellow colour of the gold precursor (Au^{3+}) turns to a colourless solution (Au^{+}) after 4 min followed by a pale ruby red colour (Au^{0}) after 7 min (or 11 min from the start of the reaction) (Figure 18). A dark reddish colour precipitate is observed later when the Au^{0} colloidal solution is left to stir further continuously. After the precipitation of the gold nanoparticles, a clear supernatant is seen. Each stage of synthesis is clearly observed as the reaction occurs in a step-wise manner from the reduction of Au^{3+} (yellow) to Au^{+} (colourless) and then to Au^{0} (ruby red) as seen in Figure 18.

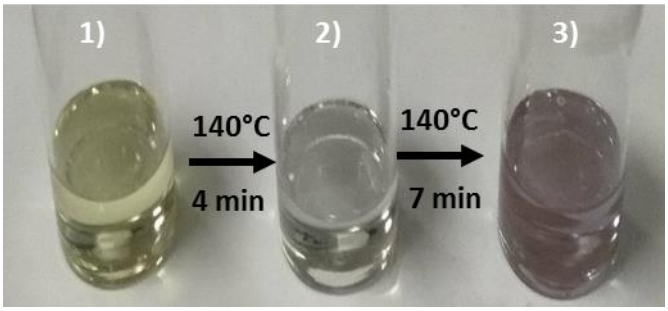

Figure 18: Different stages of gold nanoparticle formation in pure reline ($HAuCl_4$: 4.82 mM, 140 °C) 1) pale yellow solution at the beginning of the reaction; 2) colourless solution after 4 min and 3) ruby red colloidal solution after 11 min.

XPS measurements are employed to investigate the different oxidation states of gold species in pure reline during the synthesis process after quenching the reaction in ice cold water at different times. In the colourless gold colloidal stage that is obtained after 4 min (Figure 19a), both Au^{+} and Au^{0} states are identified. The doublets at 84.9 eV and 88.4 eV are related to $Au4f_{5/2}$ and $Au4f_{7/2}$ respectively for Au^{+}. Further, the doublet at 84.0 eV and 87.7 eV corresponds to $Au4f_{5/2}$ and $Au4f_{7/2}$ respectively for Au^{0}. From the XPS data, it is clear that in addition to the presence of +1 oxidation state in the colourless solution, reduced gold species are also present as indicated from the 0 oxidation state. This is in agreement with the high resolution-transmission electron microscopy (HR-TEM) micrographs (Figure 20a) where gold nanoparticles of size 1.6 ± 0.6 nm are observed in the

colourless samples. Earlier reports also state that colourless solution of gold nanoparticles are obtained when the particle sizes are about 1.9 ± 0.2 nm[236] which matches our observation of a colourless solution containing both the cationic gold (Au^+) species and the gold nanoparticles. It is well known that gold in +1 oxidation state gives rise to colourless solutions as well[237]. After 11 min from the start of the reaction, XPS spectra of the ruby red solution show doublets of $Au4f_{5/2}$ and $Au4f_{7/2}$ for Au^0 are observed at 84.0 eV and 87.7 eV respectively which is in agreement to the 0 oxidation state for gold (Figure 19b). The absence of the Au4f peak exhibiting a doublet at 85.8 eV and 89.5 eV corresponding to $Au4f_{7/2}$ and $Au4f_{5/2}$ respectively for Au^{3+} shows that Au^{3+} is reduced to Au^+ and Au^0.

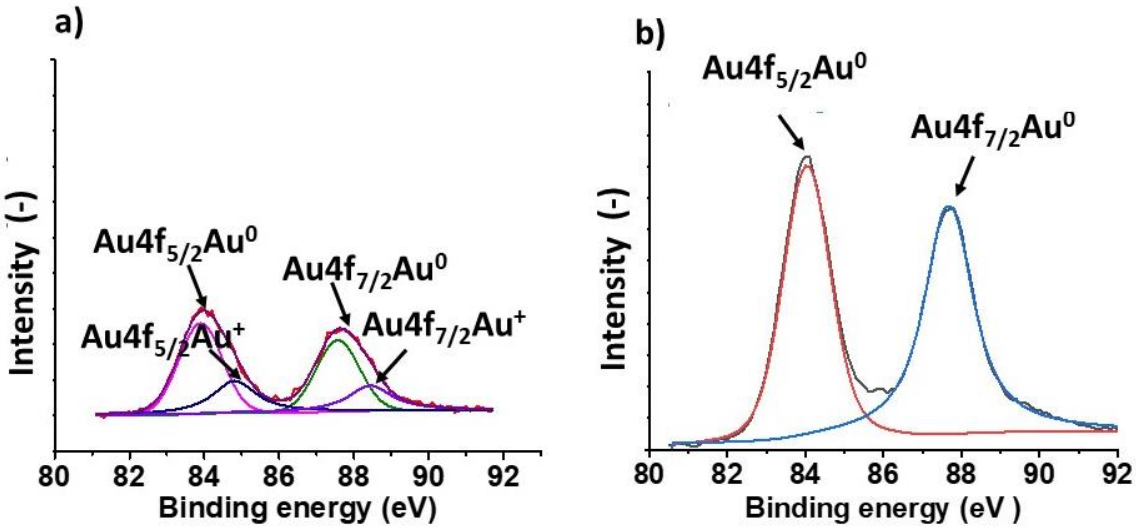

Figure 19: XPS spectra for the different stages of formation of gold nanoparticles in pure reline ($HAuCl_4$:4.82 mM, 140 °C) a) colourless solution after 4 min and b) ruby red solution after 11 min.

HR-TEM micrographs gives the particle size distribution of gold nanoparticles in the colourless solution and the ruby red solution in Figure 20. As mentioned before in the colourless solution (Figure 20a), mostly particle sizes around 1.6 ± 0.6 nm are present. From Figure 20b, it is clear that the particle size of Au nanoparticles in the ruby red solution phase is 2.6 ± 0.5 nm. In addition to the formation of the monodisperse small gold nanoparticles, some agglomerates of size approx. 50 nm are also observed as shown in Figure 20c-d.

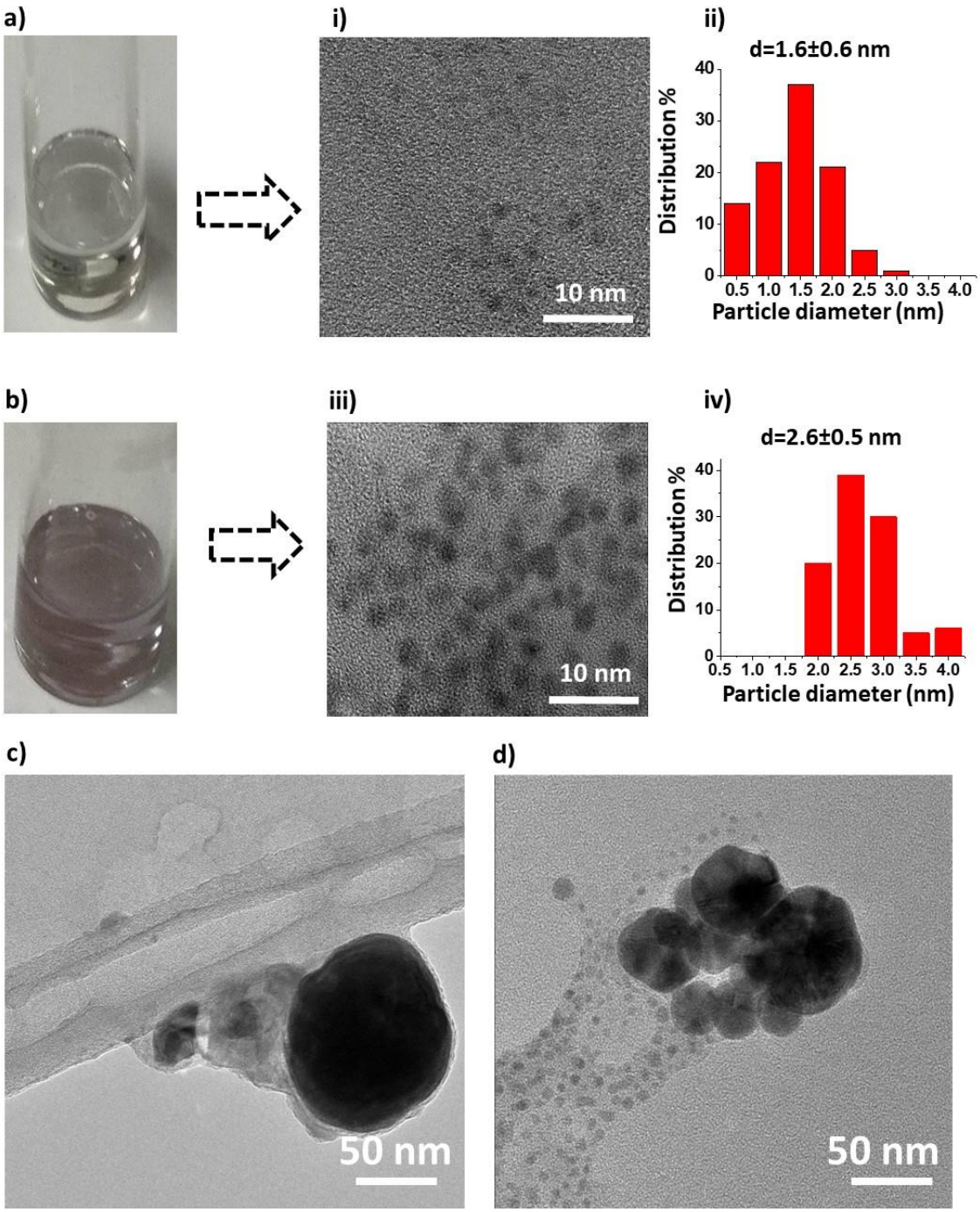

Figure 20: HR-TEM micrographs of gold nanoparticles in pure reline (i and iii); particle size distribution of the gold nanoparticles (ii and iv), a) colourless solution after 4 min; b) ruby red solution taken out after 11 min, c) gold agglomerates in colourless solution after 4 min; d) gold agglomerates observed in ruby red solution after 11 min. Both these samples are prepared at 140 °C, $HAuCl_4$: 4.82 mM.

SAXS measurements are carried out by our collaborators at University of Bath, UK (Dr Iva Manasi and Prof. Karen Edler).

In order to determine if the nanoparticle aggregates (as shown in the HR-TEM micrographs in Figure 20) are formed in the solution during the synthesis of the smaller gold nanoparticles or afterwards during the sample preparation for TEM measurements, in-situ SAXS analyses are performed for the samples (isolated at different stages of gold nanoparticle formation followed by quenching in ice-cold water) in pure reline at room temperature. SAXS is used as a complementary tool in addition to HR-TEM in order to gain understanding on the synthesis of gold nanoparticles in its liquid state itself i.e. in pure reline. Two different concentrations of $HAuCl_4$ (4.82 mM and 9.64 mM separately) are used to prepare the samples in pure reline at 140 °C for SAXS measurement. It is important to note that the concentration of $HAuCl_4$ for these SAXS measurements is 9.64 mM, double the concentration of 4.82 mM used in the rest of the experiments to avoid the signal to noise ratio masking the presence of small gold nanoparticles. In order to take out samples containing Au^+ and Au^0, the synthesis reaction is terminated at the same time intervals of 4 min and 11 min respectively.

When the initial $HAuCl_4$ concentration in the solution is 4.82 mM, nanoparticle agglomerates with a radius of 27.8 ± 1.6 nm and polydispersity of 28% is observed for the ruby red Au^0 solution (Figure 21a). The HR-TEM micrographs of the gold nanoparticle agglomerates in the ruby red solution are in agreement with the SAXS data (Figure 20a). However in the case of colourless Au^+ solution, it is noted that the signal to noise ratio is too weak and hence any scattering from ~1 nm particles is masked easily (Figure 21b).

For solutions containing initial $HAuCl_4$ concentration of 9.64 mM, two size populations are observed for the ruby red Au^0 solution: one distribution shows small nanoparticles with a radius of 1.02 ± 0.02 nm and a polydispersity of 12% (Figure 21c) and the second size population comprises of agglomerates with a radius of 31.1 ± 0.5 nm and polydispersity of 33%. For the colourless Au^+ solutions, Figure 21d, two size populations are observed: one with a radius of 0.93 ± 0.06 nm and polydispersity of 11% and the other one with a radius of 49.5 ± 10.5 nm and polydispersity of 25%. For the higher concentration of 9.64 mM, the SAXS data is in accordance with the HR-TEM values (Figure 20) as both these techniques

show the presence of two size populations (monodisperse and agglomerates). The presence of two population density components from the SAXS fit in Figure 21d is justified from the previous knowledge obtained from HR-TEM micrographs exhibiting two size distributions (monodisperse and agglomerates) for the gold nanoparticles.

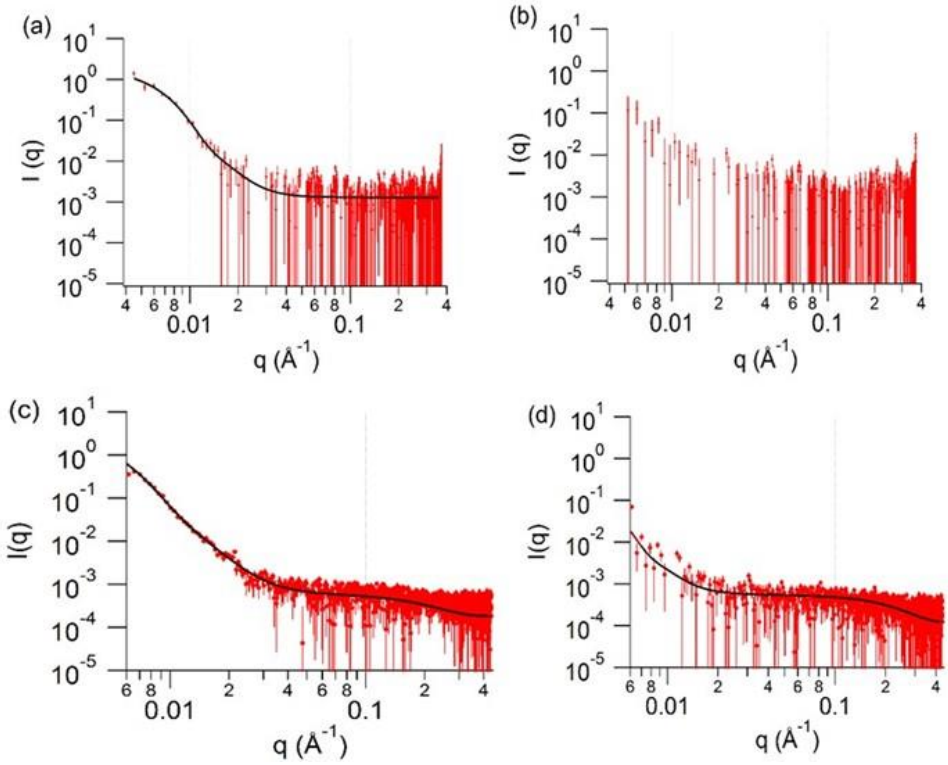

Figure 21: SAXS from Au^0 (ruby red) and Au^+ (colourless) solutions in pure reline. (a) SAXS from Au^0 solution with initial concentration of $HAuCl_4$ at 4.82 mM; (b) SAXS from Au^+ solutions with initial concentration of $HAuCl_4$ at 4.82 mM; (c) SAXS from Au^0 solutions with initial concentration of $HAuCl_4$ at 9.64 mM; (d) SAXS from Au^+ solutions with initial concentration of $HAuCl_4$ at 9.64 mM. The experimental SAXS intensity is shown in red with the spherical form factor fit to the data with black lines. All these solutions are prepared in pure reline at 140 °C and the reaction is stopped at 4 min and 11 min respectively for Au^+ and Au^0 state. Acknowledgement: Dr Iva Manasi.

From the SAXS data, it is found that for solutions with initial $HAuCl_4$ concentration as 4.82 mM which is also the original concentration used to synthesize gold nanoparticles, there are no agglomerates formed in-situ during the colourless Au^+ state because if there

are any agglomerates present then the SAXS will detect the signals as agglomerates are detected easily in comparison to small monodisperse nanoparticles. The agglomeration growth occurs gradually when the synthesis reaction proceeds towards the Au^0 ruby red state. The presence of small monodisperse gold nanoparticles are more evident when the initial gold concentration is 9.64 mM because the solution with 4.82 mM is too dilute to provide any scattering signals from these small sized gold nanoparticles.

4.1.1 Role of water in the synthesis of gold nanoparticle in reline

In order to understand the role of water in the reline system towards the synthesis of gold nanoparticles, reline/water mixtures with a 1:10 molar ratio is used as the reaction medium. As the synthesis reaction continues, the initial pale yellow colour of the gold precursor (Au^{3+}) changes to colourless (Au^{+}) state followed by a pale red colour (Au^0) at 140 °C (Figure 22). In comparison to pure reline, reduction of gold nanoparticles takes a longer time in the presence of water in reline as can be seen from Figure 22. It takes 30 min to reach the colourless state and 1.5 h to achieve the pale red stage. Differently to the pure reline system, the initial volume of the reaction solution is 10 mL but the volume decreases gradually as the reaction proceeds after the reaction times; the colourless vial has 5 mL and the pale red vial has 4 mL of the solution (Figure 22). The condensation of water droplets at the mouth of the vial containing the pale yellow solution indicates the loss of water from the solution as the reaction proceeds (Figure 22).

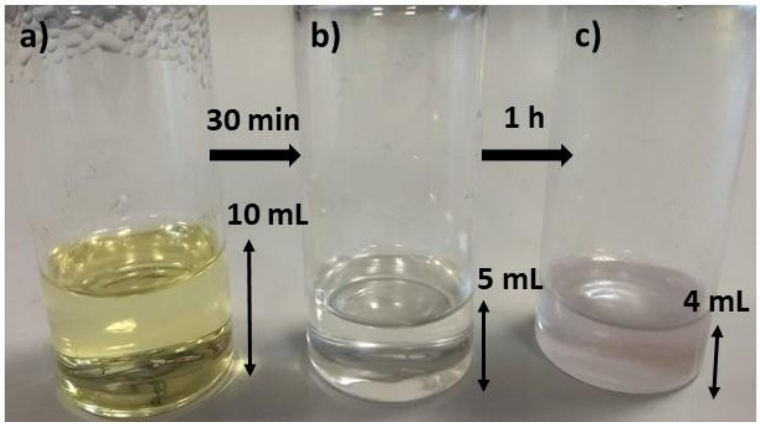

Figure 22: Different stages of the formation of gold nanoparticles in reline/water 1:10 molar ratio (140 °C) a) yellow solution taken at the beginning of the experiment; b) colourless solution after 30 min and c) pale ruby red solution after 1.5 h.

The estimated size of nanoparticles produced in reline/water mixtures (1:10) at 140 °C in the pale red solution is 2.5 ± 0.5 nm as seen in Figure 23a-b. Aggregates of gold nanoparticles of size 50 nm are also observed in the pale red solution as shown in Figure 23c.

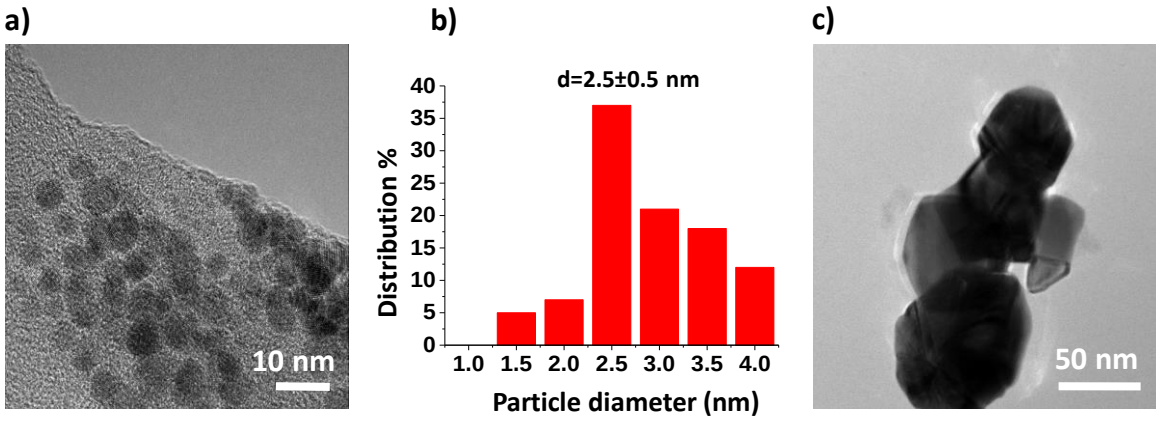

Figure 23: a) HR-TEM micrographs of Au^0 in reline/water 1:10 molar ratio, b) size distribution of the monodisperse gold nanoparticles and c) agglomerates of sizes greater than 50 nm. Initial $HAuCl_4$ concentration is 4.82 mM. The gold nanoparticles are prepared in reline/water (1:10 by molar ratio) at 140 °C.

4.1.2 Mechanism of the formation of gold nanoparticles in reline and reline/water systems

The following sections shed light on the role of reline and reline/water systems in the formation of gold nanoparticles.

Upon heating reline and reline/water mixtures at the synthesis temperature of 140 °C, gaseous compounds are released due to the *in-situ* decomposition of these solutions. A damp litmus test is carried out to identify the nature of these reducing gases and the litmus paper turns blue indicating the alkaline nature of these reducing gases. These gases are further identified by performing GC-MS analysis. GC-MS results of the gas sample taken during the heating of pure reline at 140 °C shows typical peaks for trimethylamine (m/z=59), $[CH_2=N=CH_2]^+$ (m/z=42)[238], $[(CH_3)_2N(CH_2)]^+$ [239] (m/z=58), traces of ammonia (m/z= 17), water vapour (m/z=18) , nitrogen (m/z = 28) and oxygen (m/z = 32) shown in Figure 24a. GC-MS results of the gas sample taken during the heating of reline/water mixtures at 140 °C shows typical peaks for ammonia (m/z=17), water vapour and NH_4^+(m/z=18), N_2 (m/z=28) and O_2 (m/z =32) (Figure 24b). It is observed that both the pure reline and reline/water mixtures release ammonia due to the hydrolysis of urea in eq.17. In pure reline, the hygroscopic nature of pure reline (trace amounts of water are present) and the aqueous solution of $HAuCl_4$ precursor (30 wt% of $HAuCl_4$ prepared in dilute HCl) are the potential water sources for urea hydrolysis.

$$NH_2CONH_2 + H_2O \rightarrow 2NH_3 + CO_2 \quad (17)$$

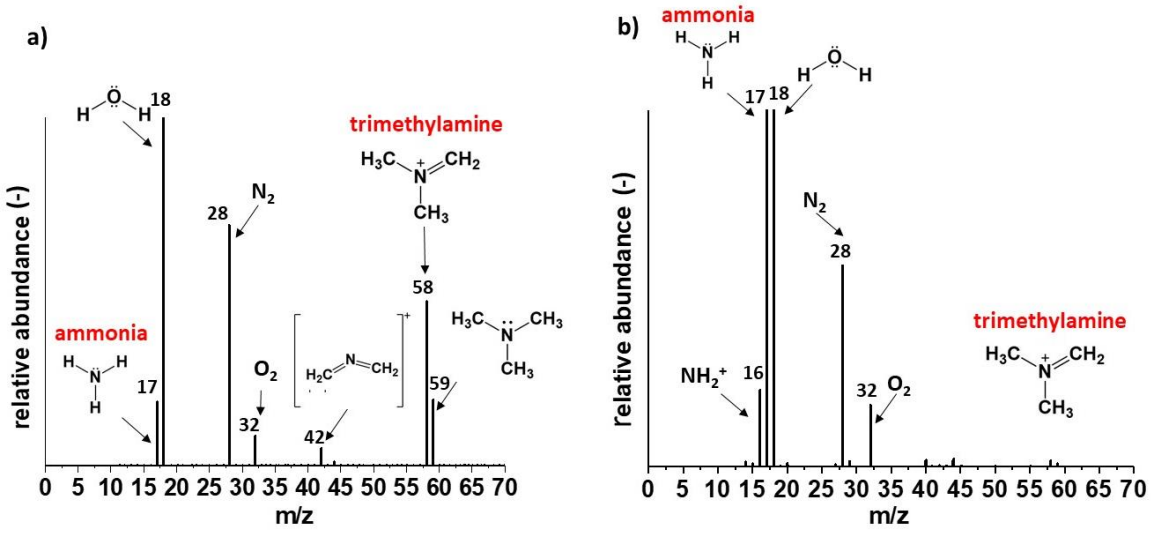

Figure 24: GC- MS (Gas chromatography mass spectroscopy) chromatograms of gas products on heating a) pure reline at 140 °C and b) reline/water (1:10 molar ratio) at 140 °C. No gold precursor is added in these.

The mechanism for the release of trimethylamine from choline chloride is illustrated in Figure 25. When the choline chloride is decomposed[240], an electron is provided to the choline cation by the chloride ion i.e. chlorine gas is formed upon the oxidation of chloride ion. The choline cation turns into an unstable radical due to the gain of an electron and further decomposes to produce trimethylamine and 2-hydroxyl ethyl radical species. Yue *et al.* presented this mechanism as they are able to detect chlorine gas upon the decomposition of choline chloride[241]. However, in our case, free chlorine gas is not detected by GC-MS analysis. The detection of free chlorine gas by GC-MS route is often not easy because its high reactivity to bind with other elements including internal parts of GC[242]. Electron spin resonance techniques can be used to detect unstable radicals in the system.

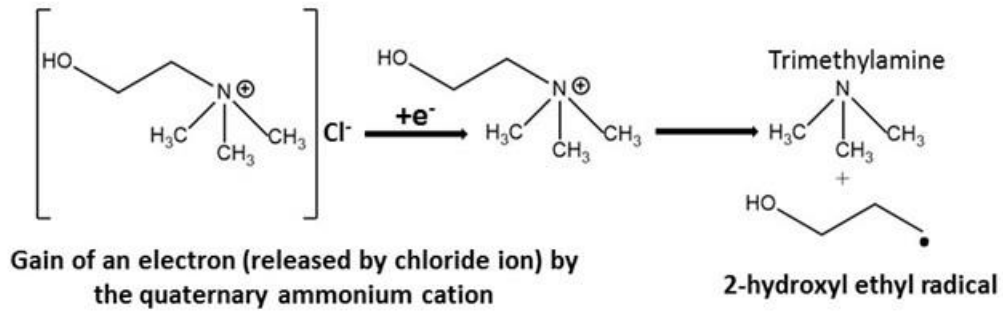

Figure 25: Possible decomposition mechanism of the choline chloride cation to release trimethylamine[241].

To gain additional insights on the reducing property of reline, ^{13}C NMR (Figure 26i, ii) and DEPT-135 (Figure 27) of pure reline, gold precursor ($HAuCl_4$) mixed with reline at room temperature and the supernatant remained after gold nanoparticle formation at 140 °C are carried out. It is also possible to use ^{1}H NMR analysis in addition to ^{13}C NMR as both these techniques provide information on functional groups. However data interpretation is more straightforward and easier in ^{13}C NMR analysis (atleast in our case here where we are interested to identify only the carbon atoms in the reline moiety). These data provides information related to the structural rearrangement (if any) in reline during the synthesis of gold nanoparticles. The lack of any structural rearrangement in reline such as oxidation of alcohol to aldehyde group during the synthesis of gold nanoparticles is confirmed from the NMR studies. 13C NMR spectra of pure reline shows peaks corresponding to urea 162.21 ppm and α-CH_2 68.20 ppm; β-CH_2 56.28 ppm, Me_3 54.40 ppm in the choline chloride. These carbon atoms are denoted as 1, 2, 3, 4 corresponds to the carbon atoms present in urea, α-CH_2, β-CH_2 and Me_3 in choline chloride respectively in Figure 26. An additional peak at 160 ppm (close to peak 1) is observed in (Figure 26i, a and b) which is attributed to the free uncoordinated urea[243] present in reline. This additional peak decreases in intensity compared to peak 1 in (Figure 26i, b) and gradually disappears in (Figure 26i, c) as the gold precursor is added. This peak disappearance is due to the coordination of urea with gold as discussed in later section (Section 4.1.5).

A minor downfield shift towards the left side is noted in the NMR peaks due to the acidic pH change upon the addition of the initial gold precursor $HAuCl_4$. It is common for acidic

protons to exhibit downfield shifts in NMR as these lack the electron cloud that is required to shield them from the instrument's magnetic field and hence these drift towards the downfield regime (in our case as $HAuCl_4$ is acidic). ^{13}C NMR spectra for urea interaction with the gold precursor (which is the zoomed version of the quartet peak around 162 ppm from Figure 26i) is shown in Figure 26ii. Prior to the addition of $HAuCl_4$, a quartet is observed centred at 162.21 ppm and after adding $HAuCl_4$ followed by heating, the quartet peak is disrupted and shifts downfield to yield a broadened peak at 162.4 ppm. In urea, coupling of carbon to one nitrogen delivers a 1:1:1 triplet, while the coupling to two nitrogen atoms should deliver a 1:2:3:2:1 quintet but due to the low coupling constant (^{13}C-^{14}N) and poor resolution, a quartet is observed instead of quintet. The equilibrium reactions of urea's coordination to gold is faster than the relaxation time of the measured protons leading to line broadening in ^{13}C NMR spectra as seen in in Figure 26ii. It is most likely that on adding $HAuCl_4$ to reline, interaction of urea with $HAuCl_4$ occurs and hence the quartet is disrupted. From the ^{13}C NMR data in Figure 26i, it could be suggested that the peaks labelled as 4 may also correspond to trimethylamine and not the carbon atoms in choline moiety. According to literature, ^{13}C NMR peaks for trimethylamine are usually centred at 47.5 ppm, but our peaks are at 78 ppm matches the reported values for carbon atoms in the choline chloride peak[244].

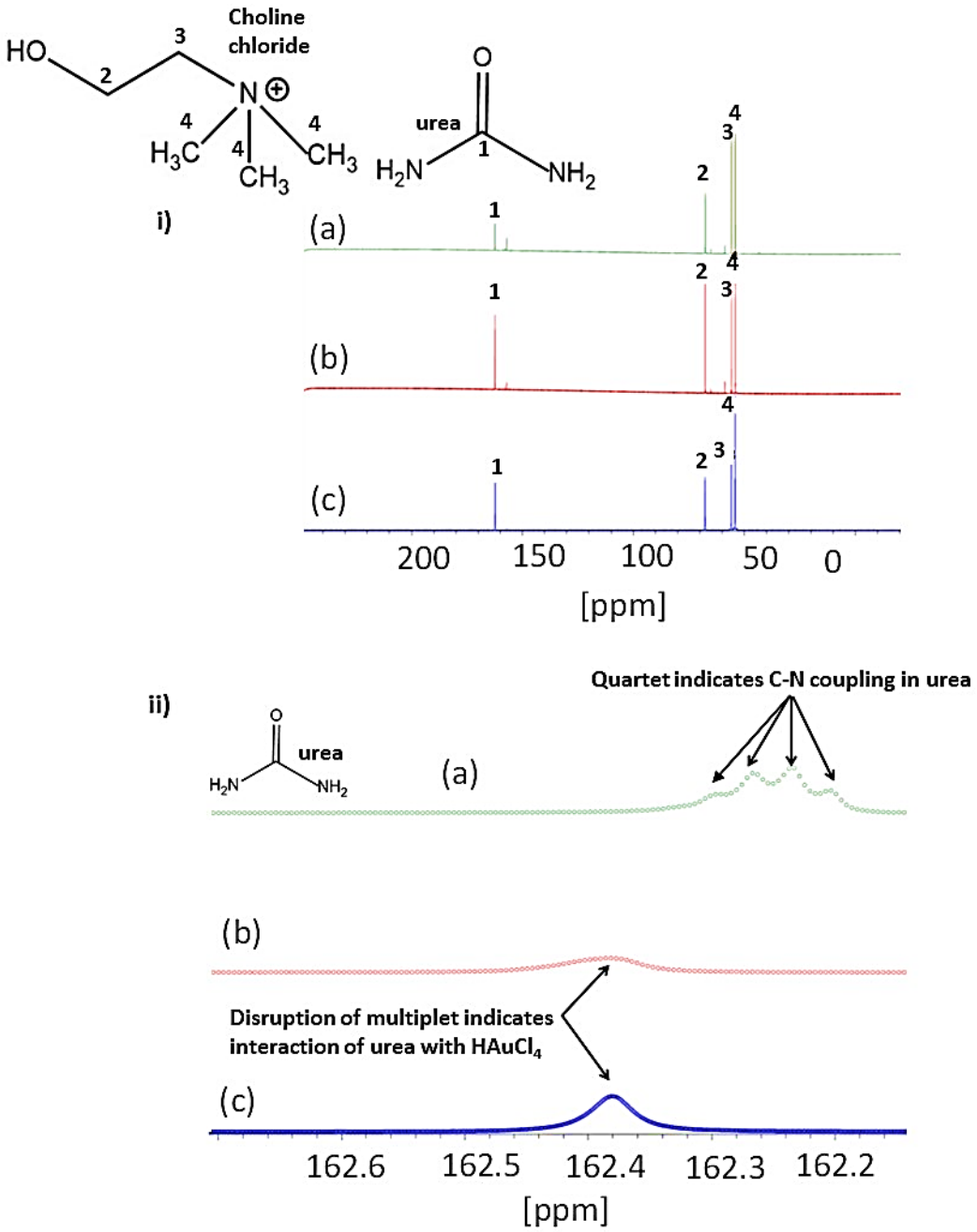

Figure 26: i) ^{13}C NMR spectra, ii) zoomed version of ^{13}C NMR in (i) indicating urea decoupling. Reaction conditions: (a) pristine reline, (b) $HAuCl_4$ (4.82mM)/reline mixture and (c) supernatant left after the precipitation of gold nanoparticles at 140 °C (within 2-3 h of $HAuCl_4$ addition).

Distortionless enhanced polarization transfer (DEPT-135) is an effective technique to know the number of protons that are attached to the carbon atoms. DEPT usually encompasses a polarization transfer from a proton to a carbon nuclei in order to increase its

signal strength of the carbon nuclei. The multiplicity i.e. the number of protons available for each carbon atom are determined in this case by using a 135 degree decoupler pulse. DEPT-135 spectra herein is phased to show the carbon atoms containing an odd number of protons (CH_3 and CH signals) in the positive or in the upward direction and those containing an even number of protons (CH_2) in the negative or in the downward direction (Figure 27). Since the carbon atom present in urea (denoted as 1) has no protons attached to it, hence no signal is observed. From the NMR and DEPT-135 data (Figure 27), it is clear that no additional peaks (for aldehyde or any other molecule) are observed from the parent peaks for reline. Only some shifts and disruption in the urea peak due to the change in pH and urea decoupling respectively are observed. Thus, the results from 13C NMR and DEPT-135 shows that structural rearrangement does not play any role towards the reducing nature of reline.

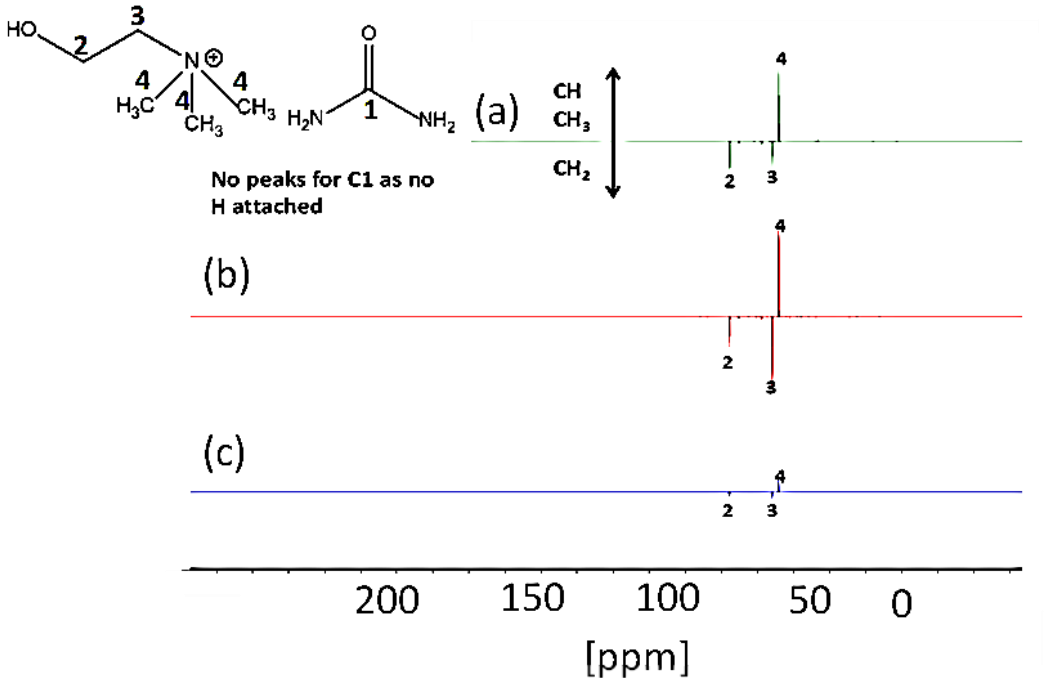

Figure 27: DEPT-135 spectra. (a) pristine reline, (b) $HAuCl_4$ (4.82mM)/reline mixture and (c) supernatant left after the precipitation of gold nanoparticles at 140 °C (within 2-3 h of $HAuCl_4$ addition).

4.1.3 Control experiments with individual components of reline

A number of control experiments are carried out in order to understand the contribution of the individual components present in reline i.e. choline chloride and urea, along with the release of trimethylamine and ammonia from these two components during the reduction of gold precursor.

When $HAuCl_4$ (4.82 mM) is added to the aqueous solution of choline chloride (formed by mixing water and choline chloride in 2:1 molar ratio similar to the composition between choline chloride and urea in reline) but without any urea in this aqueous choline chloride solution, and the reaction is heated under continuous stirring at 140 °C for 3 h, it is observed that the solution colour does not change from the initial pale yellow colour which shows that no reduction of the gold precursor occurs in the absence of urea. This observation indicates that neither choline chloride nor its thermal decomposition product trimethylamine play any role as reducing agents in the nanoparticle synthesis. This is because trimethylamine is a weaker reducing agent as the methyl groups attract the lone pair of electrons towards them and hence electrons are no longer available for donation to carry out the reduction process. However, when $HAuCl_4$ (4.82 mM) is added to the aqueous solution of urea (formed by mixing water and urea in 1:2 molar ratio similar to the composition between choline chloride and urea in reline) but without any choline chloride in the aqueous urea solution and the reaction is heated at 140 °C, the solution colour changes from pale yellow to ruby red within 1.5 h and upon continuous stirring, precipitation of gold is observed. These observations indicate that gold nanoparticle formation is possible in the aqueous solution of urea pointing to the fact that urea and/or ammonia are responsible for the subsequent formation of nanoparticles by reducing the gold precursor.

In order to find out exactly whether the reducing action is due to urea present in reline or ammonia released from urea upon heating, two additional synthesis of gold nanoparticles are carried out: one in aqueous urea solution and the second in pure reline at 30 °C.

As mentioned in the experimental section (Chapter 3), pure reline is always prepared by heating choline chloride and urea at 80 °C and cooled before using. The temperature of 30

℃ is chosen to test the synthesis of gold nanoparticles because hydrolysis of urea does not take place at 30 ℃ to release ammonia[245]. The pale yellow colour of the gold solution does not change in the aqueous urea solution but the solution turns colourless in pure reline at 30 ℃ when the reaction is continuously stirred for three days. These results indicate that during the synthesis of pure reline at 80 ℃, degradation of urea takes place to produce ammonium ion/ammonia which remains in the solution. This ammonium ion/ammonia is responsible for the reducing action of reline and not urea. A summary of the control experimental conditions is shown in Table 6.

Table 6: Summary of the control experiments carried out to identify the role of reline components to reduce gold precursor

Solvent	Experimental conditions	Observation	Reason
Aqueous choline chloride solution (without urea)	Addition of gold precursor (4.82 mM) followed by continued heating at 140 ℃ for 3 h	No reduction of gold precursor.	The decomposition product of choline chloride (trimethylamine) does not contribute to the reduction.
Aqueous urea solution (without choline chloride)	Addition of gold precursor (4.82 mM) followed by continued heating at 140 ℃ for 1.5 h	Reduction of gold precursor is observed.	The decomposition product of urea (ammonia) contributes to the reduction.
Aqueous urea solution (without choline chloride)	Addition of gold precursor (4.82 mM) followed by continued heating at 30 ℃ for 3 days	No reduction of gold precursor.	Hydrolysis of urea does not occur at 30 ℃ to produce ammonia, hence no reduction.
Pure reline	Addition of gold precursor (4.82 mM) followed by continued heating at 30 ℃ for 3 days	Reduction of gold precursor is observed.	Synthesis of reline initially at 80 ℃ already produces ammonia/ammonium ion which reduces the gold precursor.

Colorimetric studies show the presence of ammonium ion in pure reline that explains the reduction of gold without heating reline during the synthesis of gold nanoparticles. The commercial colorimetry kit purchased from Merck uses the Berthelot's reaction to detect ammonium ions in the solution as the reaction turns blue due to the formation of indophenol upon reaction with ammonium present in the liquid as seen in eq. 18. In the Berthelot's reaction, chloramine is initially produced when the ammonium ion interacts

with hypochlorite and subsequently quinonechloramine is obtained upon the reaction of chloramine with phenol. Indophenol is produced when phenol reacts with quinonechloramine (eq. 18). The absorption spectrum of indophenol blue 650 nm (Figure 28) matches with the literature[246].

During the preparation of pure reline at 80 ℃, urea decomposes to produce ammonium ions in the solution phase. Another experiment is carried out by adding liquid ammonia to the aqueous solution of urea at 30 ℃ in the presence of gold precursor and the solution colour changes from pale yellow to colourless within a minute indicating the reduction of Au^{3+} to Au^{+} indicating the reducing action of ammonia.

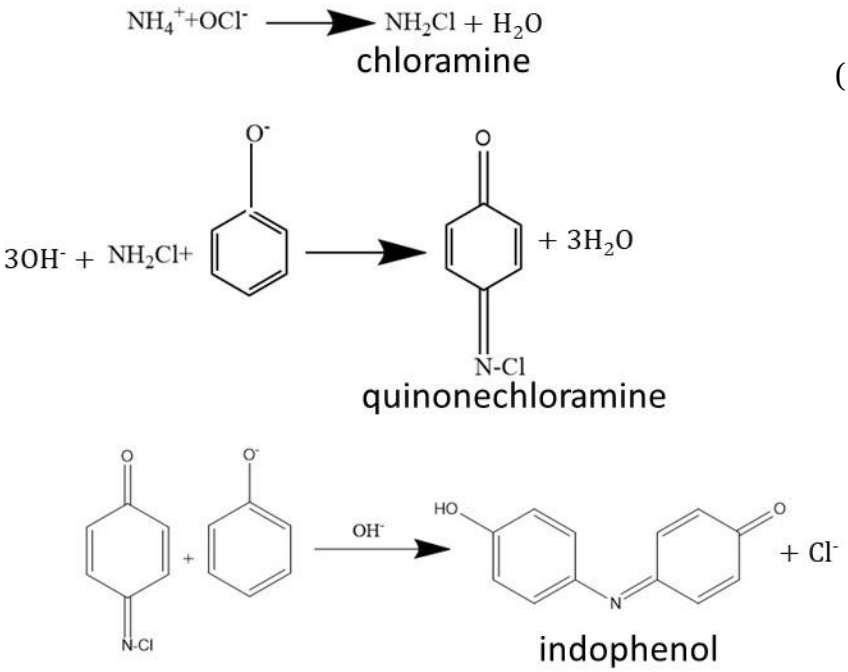

(18)

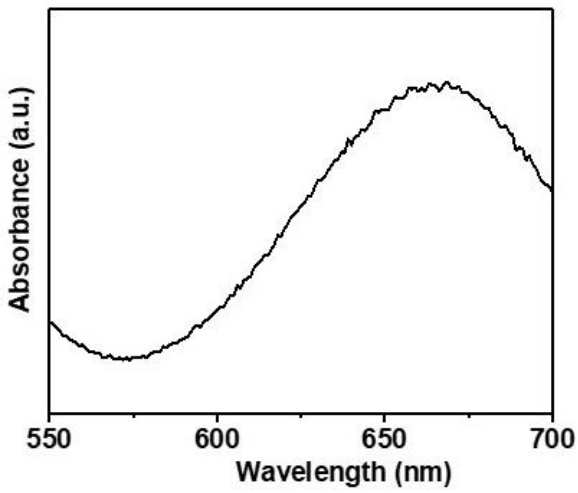

Figure 28: Absorbance spectra of indophenol formed as a result of Berthelot's reaction with ammonium ions in pure reline. Pure reline is prepared by combining choline chloride and urea in the molar ratio of 1:2 by heating at 80 °C for 2-3 h.

Ammonia is a stronger reducing agent compared to trimethylamine because in ammonia, the lone pair of electrons are readily available on nitrogen for donation. Ammonia is employed as reducing agent previously in certain reactions such as the selective catalytic reduction processes to reduce NO_x to N_2 and H_2O[247]. Ammonia is also used as reducing agent to produce ZnO, $CoFe_2O_4$ and silver nanoparticles from their precursors[248,249,250]. These control experiments show that the reduction of gold nanoparticles in reline is due to the reducing property of ammonia which is formed by the decomposition of urea.

4.1.4 Importance of hydrogen bonded framework in reline for nanoparticle synthesis

Along with the control experiments, it is crucial to note that the formation of gold nanoparticles is considerably quicker in reline (few min versus 1.5 h) compared to the aqueous urea or the reline/water 1:10 molar ratio solutions. This observation shows the importance of the extensive hydrogen bonded network present in reline between the urea and choline chloride moieties which is reported to be vital for controlling the growth and formation of regular, well-defined structures at the nanoscale[41]. The deep eutectic solvents

and ionic liquids are able to stabilize the intermediate transition states and also reduce the overall reaction barrier energy on account of this hydrogen bonded framework[251,252]. It is previously demonstrated by our group that reline acts as a supramolecular catalyst in reducing the activation energy barrier because the solvent structure of reline plays the role of an organic structuring framework to bring the reactants closer[155].

Theoretically, the reduction of gold nanoparticles in reline/water solutions should be quicker in comparison to pure reline because in reline/water 1:10 molar ratio, a greater quantity of ammonia is produced as water is present ten times more in the reline solution (as seen from the relative intensities of ammonia from the GC-MS chromatogram in Figure 24). However, reduction of gold nanoparticles takes hours in the presence of water in reline (Figure 22) instead of few minutes in pure reline system (Figure 18). The slower formation of gold nanoparticles in reline/water system in comparison to pure reline is observed because the structure of the reline is significantly altered when water is present as the intermolecular hydrogen bonded network is disrupted. Previous reports show that the parent components in reline are solubilized and the hydrogen bonds are hampered when water present in reline exceeds a certain concentration 25-41 wt%[38]. In our case, water present in reline/water 1:10 molar ratio is approx. 45 wt%. The eutectic nature of reline arises from the extensive hydrogen bond interactions present between the chloride anions in choline chloride with the hydrogen in urea and the hydroxyl groups in choline chloride[253]. As water is added, several bonds are disrupted such as the Ch^+-Ch^+ (choline-choline), Ch^+-Cl^- (choline-chloride) and Cl^--Cl^- (chloride-chloride) interactions because the Cl^- anions are preferentially hydrated by water in addition to the hydration of ammonium and hydroxyl ions of choline chloride[254]. Hence the molecular arrangement of reline drastically changes upon water addition and is best described as an aqueous solution of DES[255,254].

An additional experiment is carried out to shed light on the importance of hydrogen bonded matrix for the reduction of gold nanoparticles by using reline/water 1:2 molar ratio solution for the synthesis reaction at 140 °C. It is observed that this system takes 7 min and 30 min to reach the colourless Au^+ and ruby red Au^0 state respectively. These timescales are in between those of pure reline and reline/water 1:10 molar ratio indicating that as the

amount of water is increased in reline systems, the catalytic activity of these systems decreases.

4.1.5 Stabilization of Au^{+} and Au^{0} in pure reline

Reline and reline/water systems are overall weak reducing agents as reduction of gold nanoparticles takes minutes and hours respectively in these systems compared to other strong reducing agents like sodium borohydride, which are able to reduce gold in microseconds.

Strong reducing agents like sodium borohydride are able to generate small nanoparticles of size 1-2 nm due to faster rates of nucleation because whenever strong reducing agents are employed in the solution, the nucleation step itself consumes the monomers available in the solution to produce a larger number of nuclei instead of growing the existing nuclei[256]. However in the case of reline or reline/water systems as the reducing agent, small nanoparticles of sizes 1.6-3 nm are produced with a weaker reducing agent like ammonia. This is observed because reline systems also provide partial stabilization to the small gold nanoparticles as is evident from SAXS measurement in Figure 21.

The stability of Au^{+}/Au^{0} centres in reline can be explained on the basis of the DLVO theory for stabilization of metal nanoparticles in DES or IL. The Au centres are stabilized by the formation of the counter-ion layers from choline chloride around the gold nanoparticles in reline (Figure 29). The first layer of electrostatic stabilization is provided by the chloride ions and further steric stabilization is offered by the choline cation moiety. Along with these ionic layers, ammonia and urea aid towards the partial stabilization of the gold nanoparticles. Ammonia usually forms complex species in the reaction that in turn controls nucleation and agglomeration processes during the nanoparticle growth[257]. For example, in the stabilization of silver nanoparticles, ammonia is crucial as it forms $Ag[NH_3]_2^{+}$ complexes that deplete the availability of ionic silver in the medium and hence results in quasi-monodisperse silver nanoparticles[258,250].

Gold nanowire networks are stabilized by urea molecules in reline due to the formation of an intermediate adduct with the formula $[HO\text{-}CH_2\text{-}CH_2\text{-}N^{+}(CH_3)_3]AuCl_4^{-}.2(NH_2)_2CO$ between choline chloride, urea and $AuCl_4^{-}$[86]. Thus we propose a stabilization mechanism

where the gold centres are being stabilized by the counter-ions present in the DES, ammonia and urea in Figure 29.

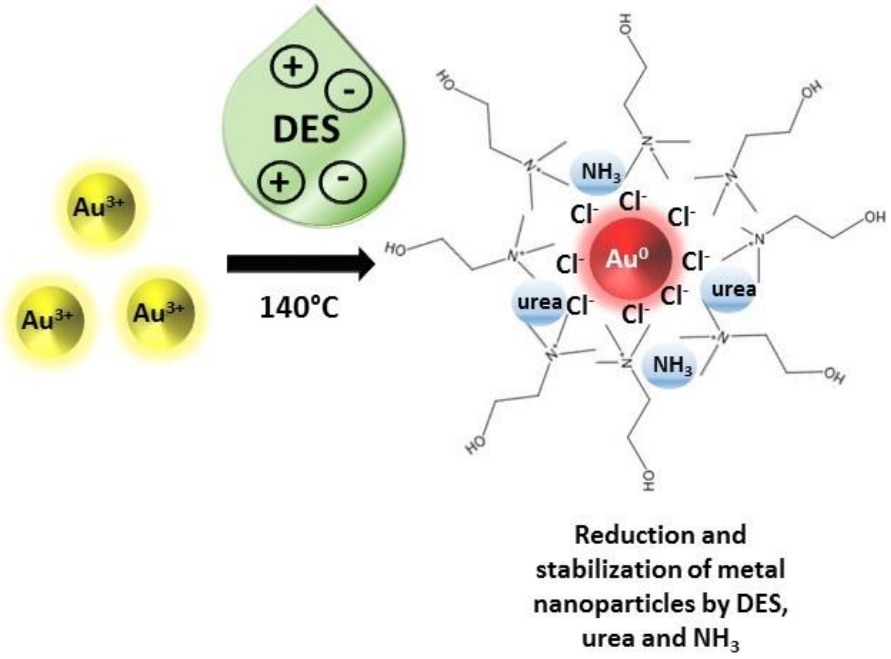

Figure 29: Stabilization of Au^0 centres by chloride ions and choline cations (from choline chloride). Counter-cations are present to provide charge balance and complete the electronic multilayer.

It has been reported previously that the smaller nanoparticles are usually protected by an IL layer which act as additives to prevent agglomeration by electrostatic or steric stabilization[120]. IL have emerged as a class of stabilizers to stabilize metal nanoparticles against agglomeration and because of this, they are popularly termed as 'entropic drivers' or the 'IL effect' due to the extensive hydrogen bonded network at the nanoscale of these IL that leads to spontaneous ordering of nanomaterials[259]. The IL prevents nanoparticle aggregation because they provide electrosteric (i.e. a combination of electrostatic and steric) stabilization to these nanoparticles[260,261]. The halide anion moiety of the IL usually provide the electrostatic stabilization and the tetra butyl ammonium cations offer steric stabilization to the nanoparticles as shown in Figure 30a. Stabilization in IL is achieved by the formation of an ion layer around the metal nanoparticles in these solvents[120]. The green coloured ions in Figure 30b represents the extensive hydrogen bonded network between the ions of the IL.

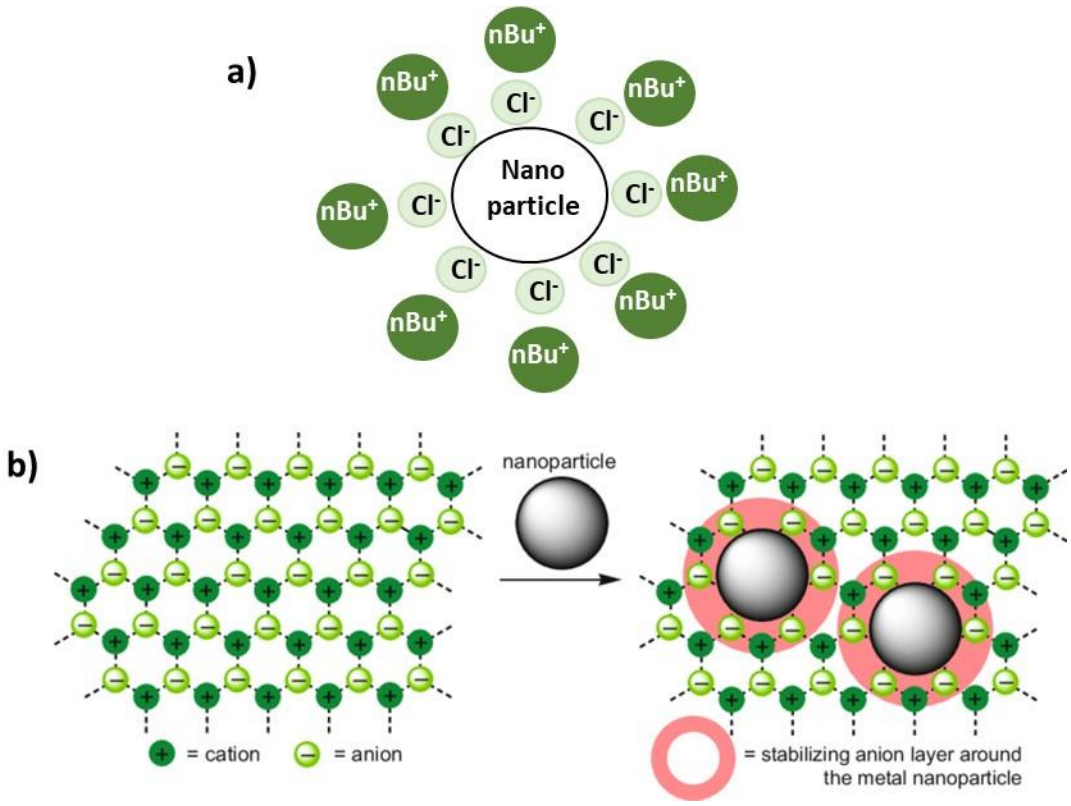

Figure 30: Stabilization of metal nanoparticles in ionic liquid by forming a) suggested primary anion layer around the metal nanoparticle (Adapted from Janiak[120]) and b) hydrogen bonded network present in IL (Directly reproduced from Ref. [262] with permission from the Royal Society of Chemistry).

4.1.6 Addition of polyvinylpyrrolidone to prevent agglomeration

Reline behaves as a weak stabilizer because agglomerates of sizes > 50 nm are observed in addition to the monodisperse gold nanoparticles both in the colourless and the ruby red solutions as seen in Figure 20c-d.

In order to prevent agglomeration of gold nanoparticles, PVP is added from the beginning of the synthesis at 140 °C and samples are isolated at 4 min (for the colourless stage) and 11 min (at the ruby red stage). Calculated particle size distributions of 3.0 ± 0.5 nm and 1.2 ± 0.4 nm are observed in the ruby red and colourless solution in pure reline respectively (Figure 31c,f). The particle size distribution of the gold nanoparticles with PVP matches the previous HR-TEM images for the gold nanoparticles without PVP (Figure 20). Aberration corrected scanning transmission electron microscopy (AC-STEM) (dark field and bright field) images show that there are no agglomerates after PVP addition both in

colourless and ruby red solution state (Figure 31b, e). PVP is a common stabilizer to prevent nanoparticle agglomeration due to its hydrophobic carbon chain that prevents the nanoparticles to come in contact with each other and hence avoids aggregation by steric hindrance[61].

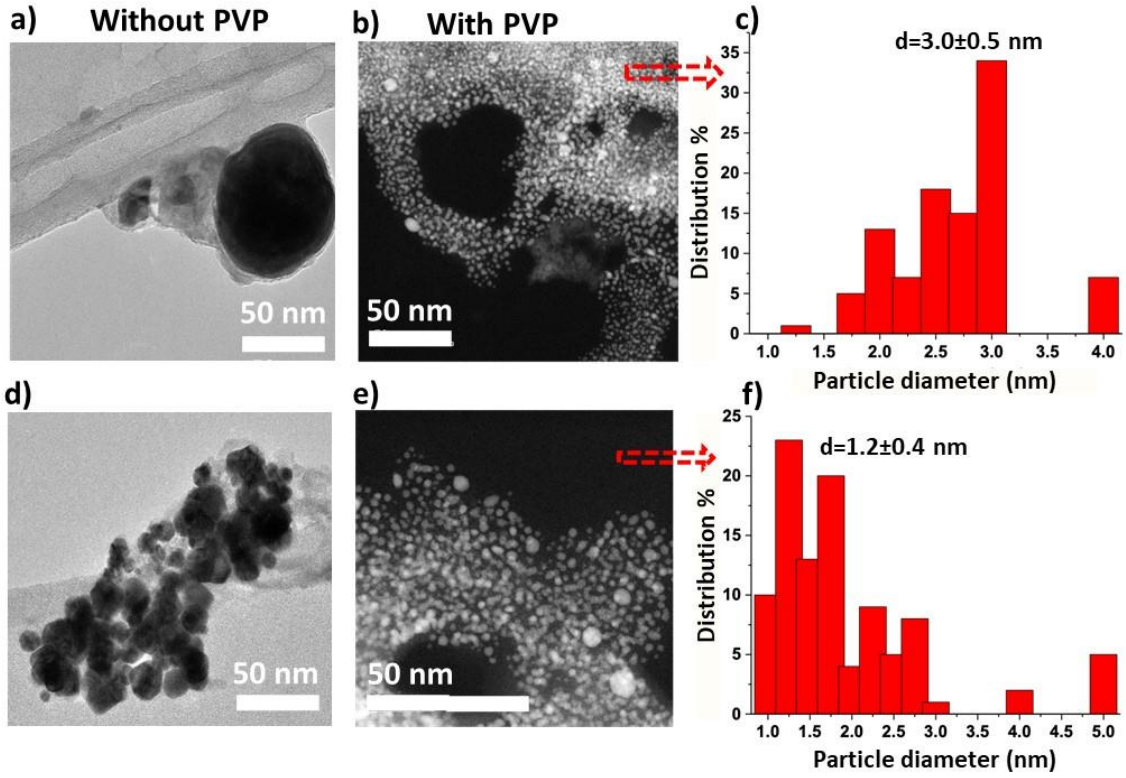

Figure 31: AC-STEM micrographs of a) agglomeration of gold nanoparticles in colourless solution after 4 min (without PVP), b) No agglomeration of gold in colourless solution after 4 min (with PVP added), c) particle size distribution of gold nanoparticles in colourless solution after 4 min (with PVP added), d) agglomeration of gold nanoparticles in ruby red solution after 11 min (without PVP), e) No agglomeration of gold in ruby red solution after 11 min (with PVP added) and f) particle size distribution of gold nanoparticles in ruby red solution after 11 min. The samples are prepared at 140 °C, $HAuCl_4$=4.82 mM.

Au nanoparticles in both the colourless and ruby red stage in pure reline shows decahedral and icosahedral face centred cubic (FCC) structures. In these images, the nanoparticles are oriented in the {110} zone axis (Figure 32 (a)), or aligned close to this orientation (Figure

32 (b), (c), Figure 33 (a), (b), (d)). Single atoms of Au are also observed in the images for both colourless and ruby red solutions.

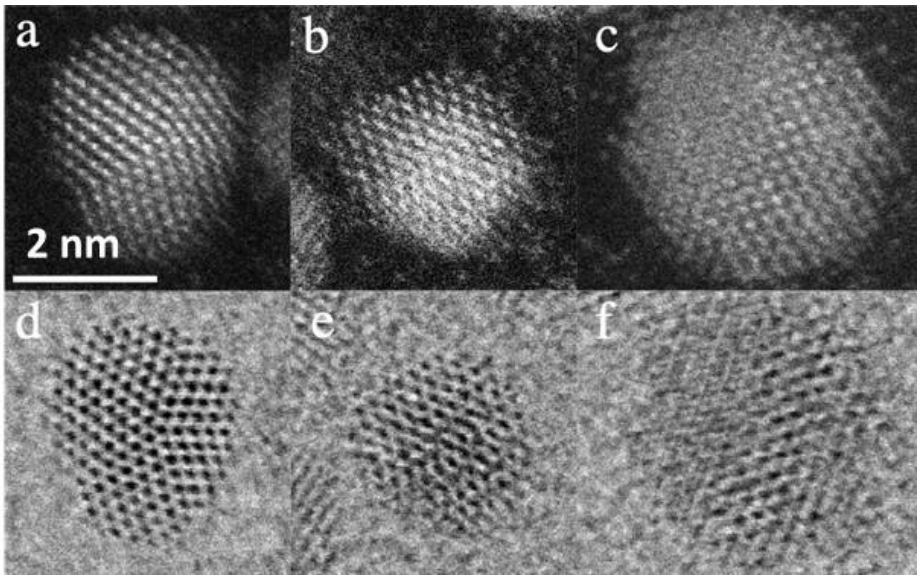

Figure 32: Simultaneously acquired high-resolution STEM ADF (a), (b), (c) and STEM BF (d), (e), (f) are representative of Au nanoparticles in colourless solution after 4 min. Scale bar is 2 nm. The samples are prepared at 140 °C, $HAuCl_4$=4.82 mM. Acknowledgement: Dr Emanuela Liberti.

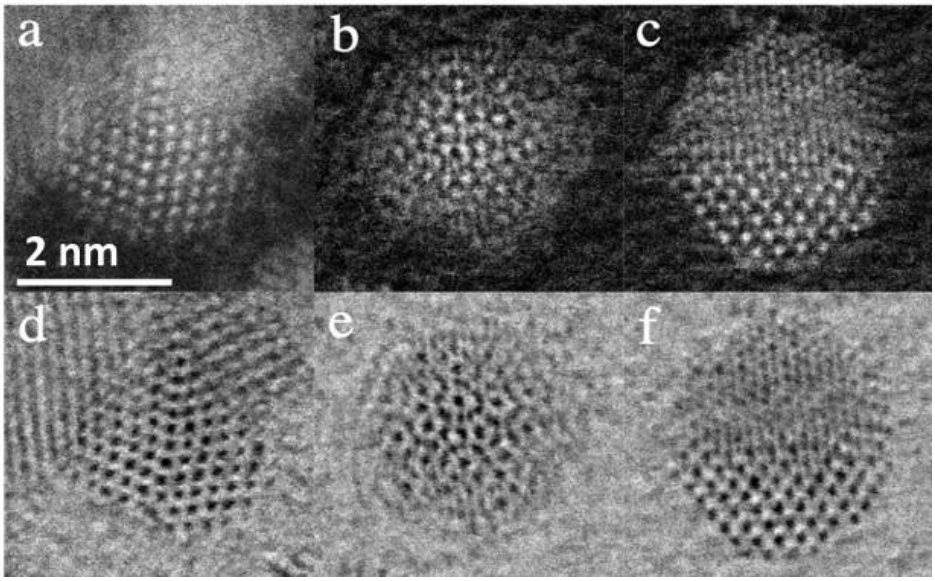

Figure 33: Simultaneously acquired high-resolution STEM ADF (a), (b), (c) and STEM BF (d), (e), (f) are representative of Au nanoparticles in ruby red solution after 11 min. Scale bar is 2 nm. The samples are prepared at 140 °C, $HAuCl_4$=4.82 mM. Acknowledgement: Dr Emanuela Liberti.

4.1.7 Effect of the reaction temperature on the synthesis of gold nanoparticles in pure reline

A series of experiments to investigate the reduction of gold precursor ($HAuCl_4$) in reline are carried out at different temperatures (30 ℃, 60 ℃, 100 ℃ and 140 ℃). As the temperature increases from 30 ℃ to 140 ℃, faster reduction of the gold precursor to synthesize gold nanoparticles is achieved as shown in Table 7. When the temperature is 30 ℃, it takes almost 3-4 days for the solution to reduce Au^{3+} to Au^{+} state (stage identification is possible due to change in colour from pale yellow to colourless) but at 140 ℃, it takes 4 min to reduce the +3 to 0 state (Table 7).

Table 7: Range of temperature conditions to synthesize gold nanoparticles in pure reline (4.82 mM $HAuCl_4$).

Temperature (°C)	Au^{3+} to Au^{+} [a] time	Au^{+} to Au^{0} [b] time
30	3-4 days	Not observed within 5 days
60	Within 2 days	Not observed within 3 days
100	Approx. 8-9 h	18 h
140	4 min	11 min

[a] Time taken to change from pale yellow to colourless state.

[b] Time taken to turn from colourless state to ruby red.

Electrochemical measurements are performed on pure reline system to gain a better understanding of the relationship between the reduction potentials and the reaction temperatures in these colloidal nanoparticle systems. Increasing the temperature shifts the reduction potentials to more anodic values (or positive values) for pure reline suggesting a favoured reduction process (Table 8). For example with an increase in temperature, the reduction potential shifts from -1.08 V at 30 ℃ to -0.71 V at 140 ℃ for pure reline.

Table 8: Reduction potential peaks at different temperatures for pure reline.

Temperature (°C)	Reduction potential peak (V vs Pt) $Au^{3+} \rightarrow Au^{0}$
30	-1.08
100	-0.82
140	-0.71

Conditions: 10 mL of pure reline $HAuCl_4$ (7.5mM), AuCl (8 mM) and 2 mL of as-prepared gold nanoparticles is added. All the three gold standards are added (Au^0, Au^+ and Au^{3+}) to ensure that all species are present in reline for proper peak identification. These gold standards are added in excess to make sure that all the species are identified in the solution.

The electrochemical reduction of $HAuCl_4$ in pure reline (Figure 34) presents two reduction peaks corresponding to the reduction of Au^{3+} and Au^+ respectively. It is important to note that the disproportionation of the gold precursor in pure water at 30 °C shows a single reduction peak (Figure 35) associated to the reduction of Au^{3+}, due to the lack of stability of Au^+ which rapidly disproportionates to Au^{3+} and Au^0 as shown in (19)[263]. It is clear from the electrochemical data that reline provides a certain level of stabilization for Au^+ species. The electrochemical measurements are carried out with the help of Dr Mauro Malizia, University of Cambridge.

$$Au^{+} \leftrightarrow Au^{3+} + Au^{0} \qquad (19)$$

The peaks in the ascending sweep corresponds to the oxidation of Au^0 and Au^+ species to Au^{3+} state in pure reline (Figure 34). Increasing the temperature shifts the oxidation potentials to less anodic values (or positive values) for pure reline suggesting a favoured oxidation process. The oxidation peak for pure water (Figure 35) corresponds to the oxidation of Au^0 to Au^{3+} because Au^+ is not stabilized in the aqueous systems.

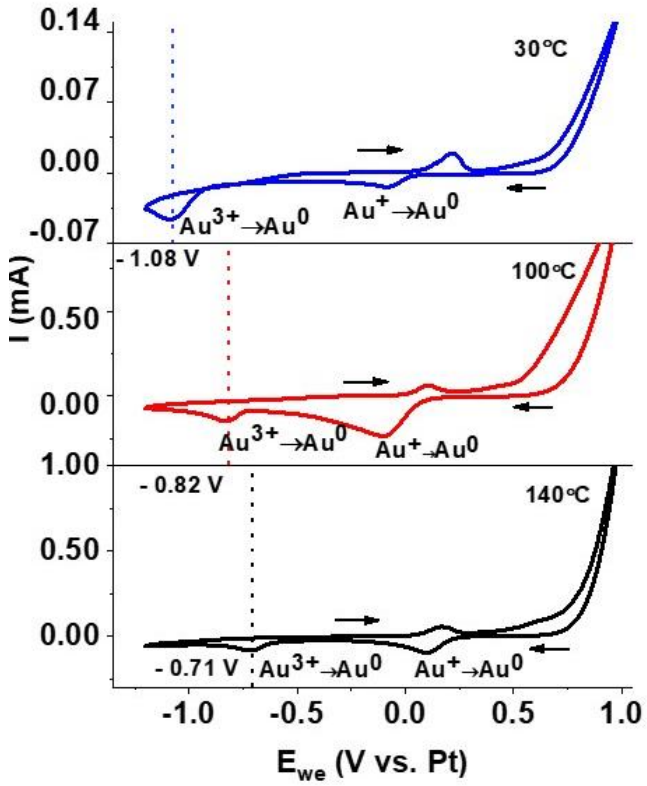

Figure 34: Cyclic voltammogram of $HAuCl_4$ in pure reline at different temperatures. Conditions: 10 mL of pure reline, $HAuCl_4$ (7.5 mM), AuCl (8 mM) and 2 mL of as-prepared gold nanoparticles is added. All the three gold standards are added (Au^0, Au^+ and Au^{3+}) to ensure that all species are present in reline for proper peak identification. These gold standards are added in excess to make sure that all the species are identified in the solution.

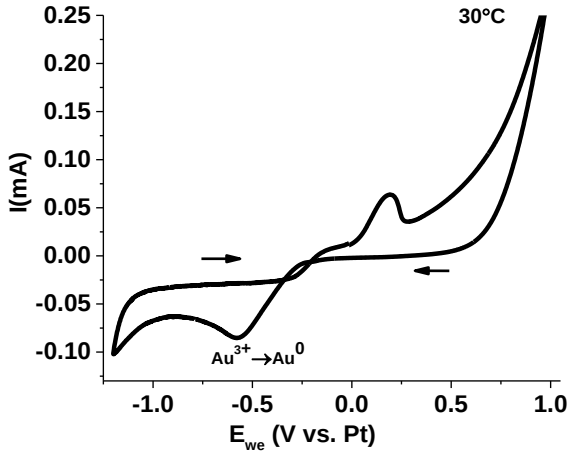

Figure 35: Cyclic voltammogram of Au^{+}, Au^{0} and Au^{3+} species in water. Conditions: 10 mL of water, $HAuCl_4$ (7.5 mM), AuCl (8 mM) and 2 mL of as-prepared gold nanoparticles was added at 30 °C. All the three gold species are added (Au^{0}, Au^{+} and Au^{3+}) to ensure that all species are present in water for proper peak identification. These gold standards are added in excess to make sure that all the species are identified in the solution.

4.1.8 Addition of ascorbic acid as an external additive in reline

From the above reported HR-TEM micrographs (Figure 20) it is observed that only spherical nanoparticles are produced whenever reline is used as the solvent platform. However for certain applications like plasmonics, morphology plays a crucial role due to the generation of 'hot-spots' for non-spherical nanoparticles or branched nanostructures where the electric field intensities are concentrated at the tips[264]. Hence, there is a growing interest to synthesize non-spherical morphologies that are beneficial for various plasmonic applications. The effect of increasing the concentration of $HAuCl_4$ in reline is studied by adding the gold precursor (48.2 mM) instead of previously used 4.82 mM separately to vials containing pure reline and reline/water 1:10 molar solutions at 140 °C under continuous stirring.

As can be seen from Figure 36, SEM images show highly polydisperse spherical gold nanoballs of sizes 100-250 nm in both reline/water solution and pure reline. These results show that even upon increasing the concentration of gold, there are no other morphologies observed except for the spheres. It is also observed that as the concentration of gold

precursor increases in reline, the reline is not able to offer stability to prevent the agglomeration of the particles. This experiment indicates only spherical morphologies are obtained in reline because neither choline chloride nor urea promotes anisotropic growth.

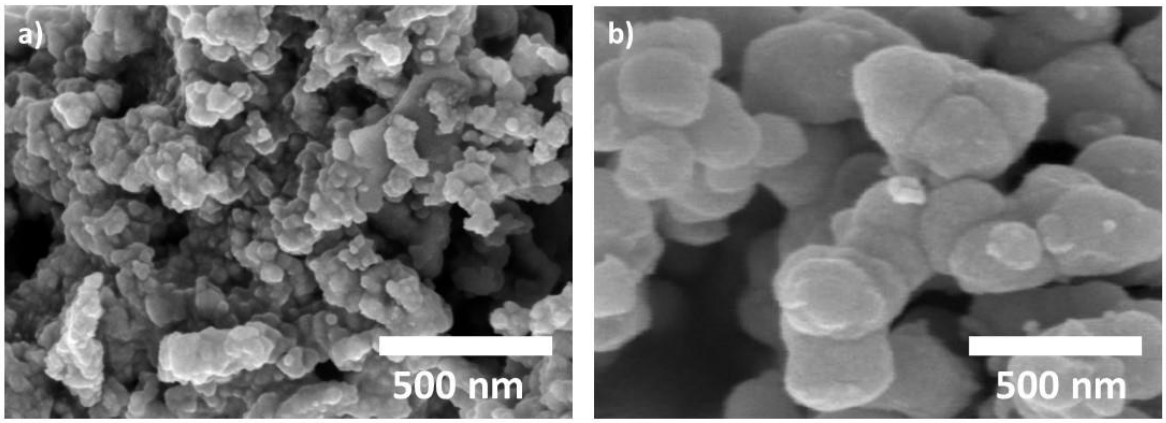

Figure 36: SEM micrographs of gold nanoparticles upon increasing the concentration of $HAuCl_4$ by ten times (48.2 mM) in a) pure reline and b) reline/water 1:10 molar ratio. Both the samples are prepared at 140 °C.

Different morphologies of gold nanostructures such as nanostars and snowflakes are synthesized in the past by adding ascorbic acid to reline[41,85,87] as discussed in the literature review in Chapter 2. Ascorbic acid is mostly used as a shape directing template due to its preferential adsorption on particular crystalline facets directing the anisotropic crystal growth process[84].

In our case, in order to produce non-spherical morphologies in reline, ascorbic acid is hence added to pure reline along with the gold precursor (48.2 mM) at a reaction temperature of 100 °C for 1 h. Flower like polydisperse structures of gold nanomaterials of 2 micron size are observed as shown by the SEM micrographs in Figure 37a under such reaction conditions because ascorbic acid promotes anisotropic growth[84].

Recently another newly reported DES composed of choline chloride and ascorbic acid combined in the molar ratio of 2:1 (known as asline)[35] is reported in the literature. Asline is used to study the effect of DES on the morphologies of gold because asline serves dual roles both as a solvent platform to dissolve the precursors and the reducing agent (ascorbic

acid) to reduce $AuCl_4^-$ to Au^0. To study the effect of mixture of asline and reline, 20 mL of pure reline/asline mixtures (10 mL each) are heated to 100 °C for 1 h with the gold precursor $HAuCl_4$ (48.2 mM). The gold nanostructures are highly polydisperse and their sizes range from 500 nm-2 micron as shown in Figure 37b. This result shows that asline plays a role to introduce anisotropy in the morphologies.

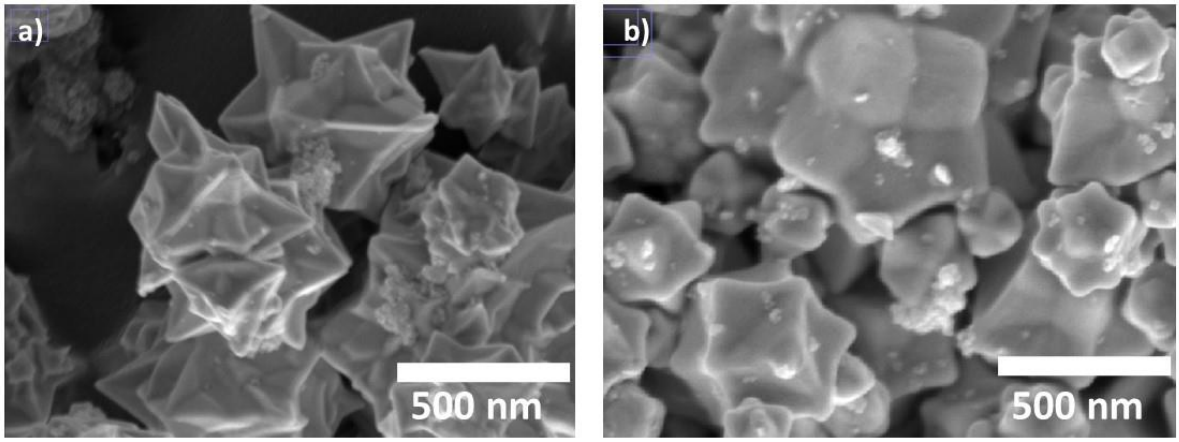

Figure 37: SEM micrographs of gold nanostructures synthesized in a) addition of external ascorbic acid in reline (100 °C, 1 h) and b) in reline/asline mixtures (50% each by volume), 100 °C, $HAuCl_4$ (48.2 mM) 1 h.

From here onwards, the synthesis of gold nanostructures in asline systems (without any reline) has been reported to study the effect of only asline in the formation of gold nanomaterials.

4.2 Use of asline to synthesize gold nanomaterials

Reduction of the gold precursor $HAuCl_4$ (48.2 mM) is carried out in batch in pure asline at 100 °C for 1 h in an oil bath under constant magnetic stirring. As the reaction continues, the initial pale yellow colour of the precursor (Au^{3+}) turns to dark red colour (Au^0) within 1 h indicating the reduction of Au^{3+} to Au^0. No colourless stage is observed in this reaction.

Figure 38 shows the corresponding SEM micrographs where the products are three dimensional nanoball structures of size 485 ± 45 nm. These structures appear as corrugated spheres or 'nanowalnut'.

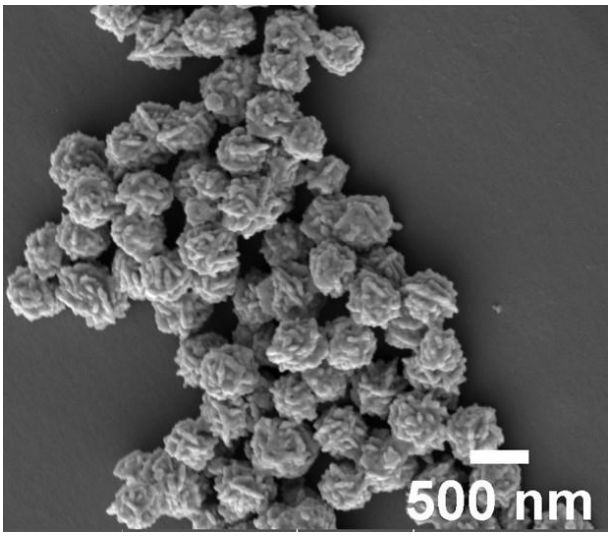

Figure 38: SEM micrographs of the gold nanowalnuts in pure asline, 48.2 mM $HAuCl_4$, 100 °C for 1 h.

In order to understand the formation mechanism of these gold nanowalnuts, the reaction is followed at different time intervals of 5 min, 15 min and 30 min (Figure 39a-e). The solution colour changes from pale yellow to dark red upon the addition of $HAuCl_4$ within 5 min indicating the formation of gold nanoparticles. As the reaction time increases from 5 min to 1 day, the solid product yield at the bottom of the vial decreases from 100% to 18% (Table 9). Nanostructures with pointed arm like morphology with a non-uniform size distribution of 300-600 nm are synthesized with arm lengths of 100-300 nm within 5 min of the reaction (Figure 39a). Within 5 min, anisotropic growth of Au takes place with 100% conversion of Au into solid product. As time increases, the morphology evolves into increasingly spherical structures leading to monodisperse balls of sizes 405 nm. Based on the above formation mechanism of the gold nanowalnuts in pure asline, the following mechanistic pathway is suggested in Figure 40.

A decrease in yield from 100% at 5 min to 40% at 1 h suggests that the morphology evolution takes place through digestive Ostwald ripening (Figure 39d). Much longer synthesis times of 1 day leads to random irregular structures (Figure 39e).

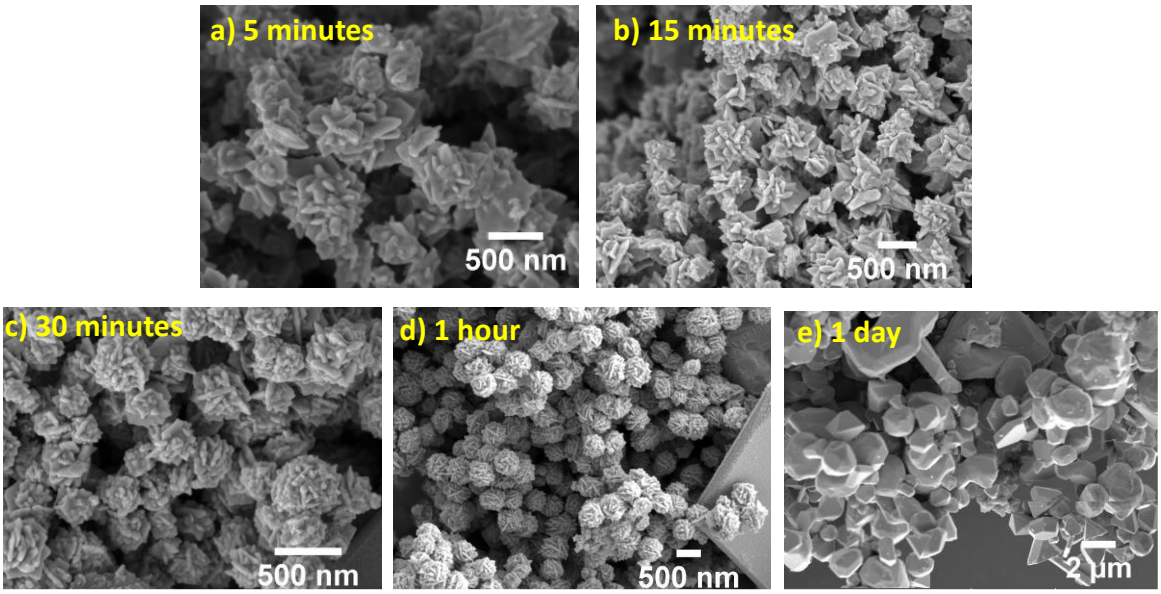

Figure 39: Formation mechanism of gold nanowalnuts in pure asline, 48.2 mM HAuCl4, 100 °C at different time intervals; a) 5 min; b) 15 min; c) 30 min; d) 1 h and e) 1 day.

Digestive Ostwald ripening and Ostwald ripening are two opposing phenomenon. Ostwald ripening is the phenomenon of the growth of large particles at the expense of the smaller particles when the small particles dissolve in the solution and their molecules are diffused in the bulk and these become deposited on the larger particles[265]. Unlike Ostwald ripening, in the case of digestive ripening, the large particles are re-dissolved to produce smaller particles which is observed in the supernatant in this case.

Table 9: Product yield % for the solid product deposited at the bottom of the reaction vial as a function of time.

Reaction time	% yield of the solid product	Particle size
5 min	100	300-600 nm
15 min	100	270-580 nm
30 min	89	245-520 nm
1 h	40	485 ± 45 nm
1 day	18	2-4 µm

Reaction conditions: pure asline, 100 °C, 48.2 mM $HAuCl_4$ as a function of time.

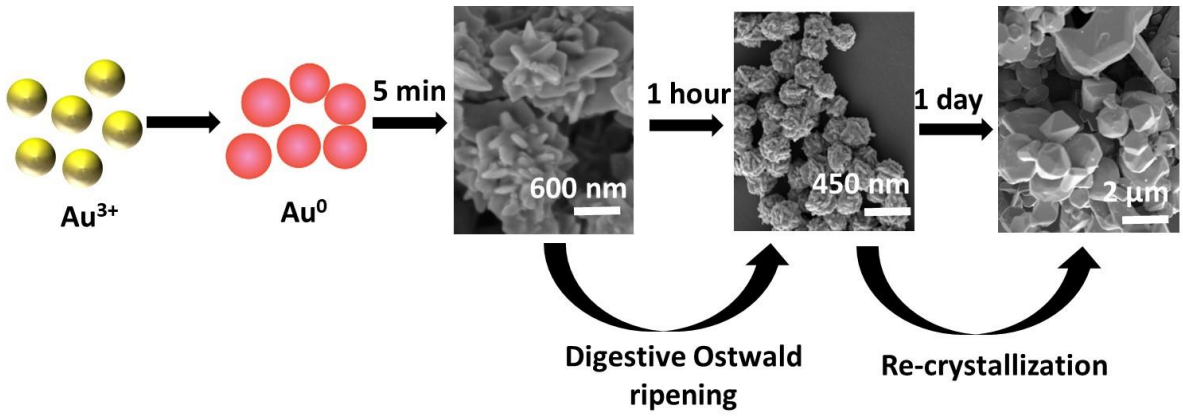

Figure 40: Mechanistic pathway of the production of gold nanowalnuts under pure asline conditions.

The presence of the gold nanoparticles in the supernatant (that is collected after 1 h of synthesis in pure asline/Au reaction at 100 °C) is verified by TEM (Figure 41) that shows a polydisperse distribution of gold nanoparticles of sizes 5-20 nm.

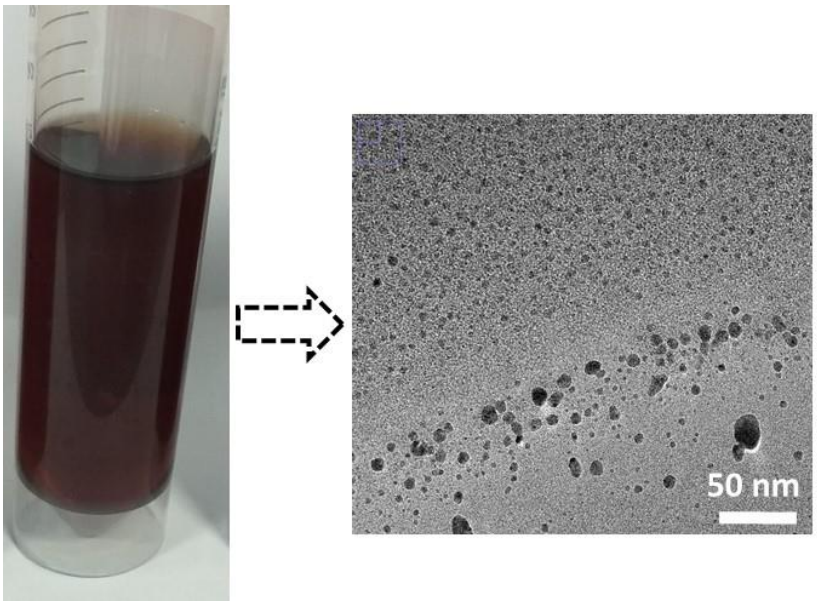

Figure 41: TEM micrograph of the gold nanoparticles remaining in the supernatant in 1 h of the synthesis of the gold nanomaterial synthesis in pure asline (48.2 mM $HAuCl_4$, 100 °C).

The monodisperse gold nanowalnuts gradually turn into polydisperse random gold nanostructures after one day when left at 100 °C as seen from Figure 39e. In order to understand the formation of these irregular structures, some additional syntheses are

carried out by initially synthesizing two separate batches of gold nanowalnuts in pure asline at 100 ℃ for 1 h (as shown in Figure 39d) followed by quenching this reaction in ice-cold water. After the reaction is quenched, one batch is left under continuous stirring at 30 ℃ for one day and the other batch is left at 60 ℃ stirring for one day. As can be seen from Figure 42a, the gold nanowalnuts are still observed even when the reaction is continued at 30 ℃ for one day. In Figure 42b, at 60 ℃, larger random aggregates are observed along with few nanowalnuts scattered on the bigger particles. These experiments indicate that as the temperature is increased, the nanowalnuts are depleted and large irregular structures are produced.

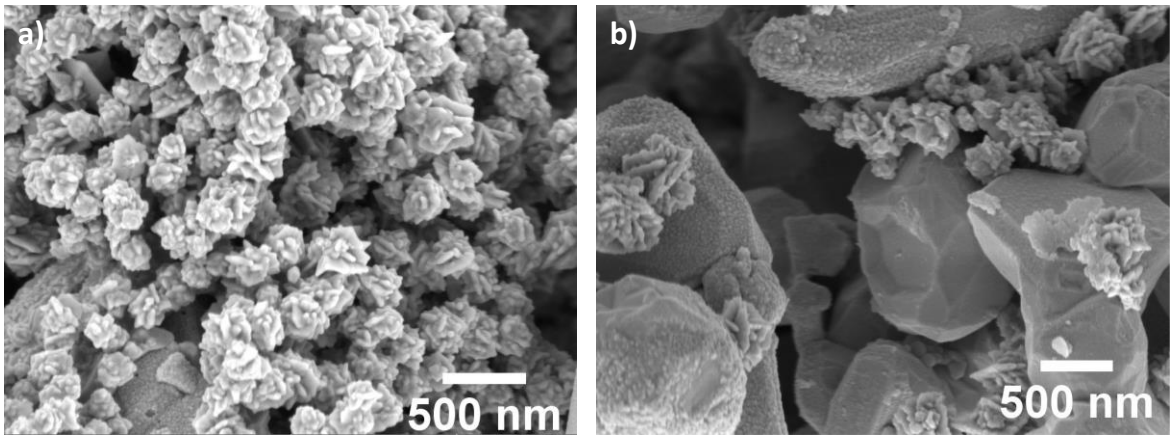

Figure 42: SEM micrographs of the solid product (at the bottom of the reaction vessel) after the reaction is quenched on completion of the reaction at 100 ℃ in pure asline (48.2 mM); the reaction is left under continuous stirring for 1 day at a) 30 ℃ and b) 60 ℃.

4.2.1 Effect of water and reaction temperature

Upon increasing the water ratio in pure asline, an evolution towards the production of random nanostructures from the well-defined gold nanowalnuts is observed (Figure 43). As the asline/water ratio becomes 1:5 and 1:10 respectively, the gold nanowalnuts are not formed and irregular shaped nanostructures of sizes more than 1 micron are obtained at all the temperatures (30 ℃, 60 ℃ and 100 ℃) as seen in Figure 43d-i. An exception to this observation is found only in the asline/water (1:5 by molar ratio) at 60 ℃ for one h, where a mixture of several plate-like and other geometrical shapes are observed like triangle, polyhedral and faceted-rod like structures of micrometer sizes (Figure 43e).

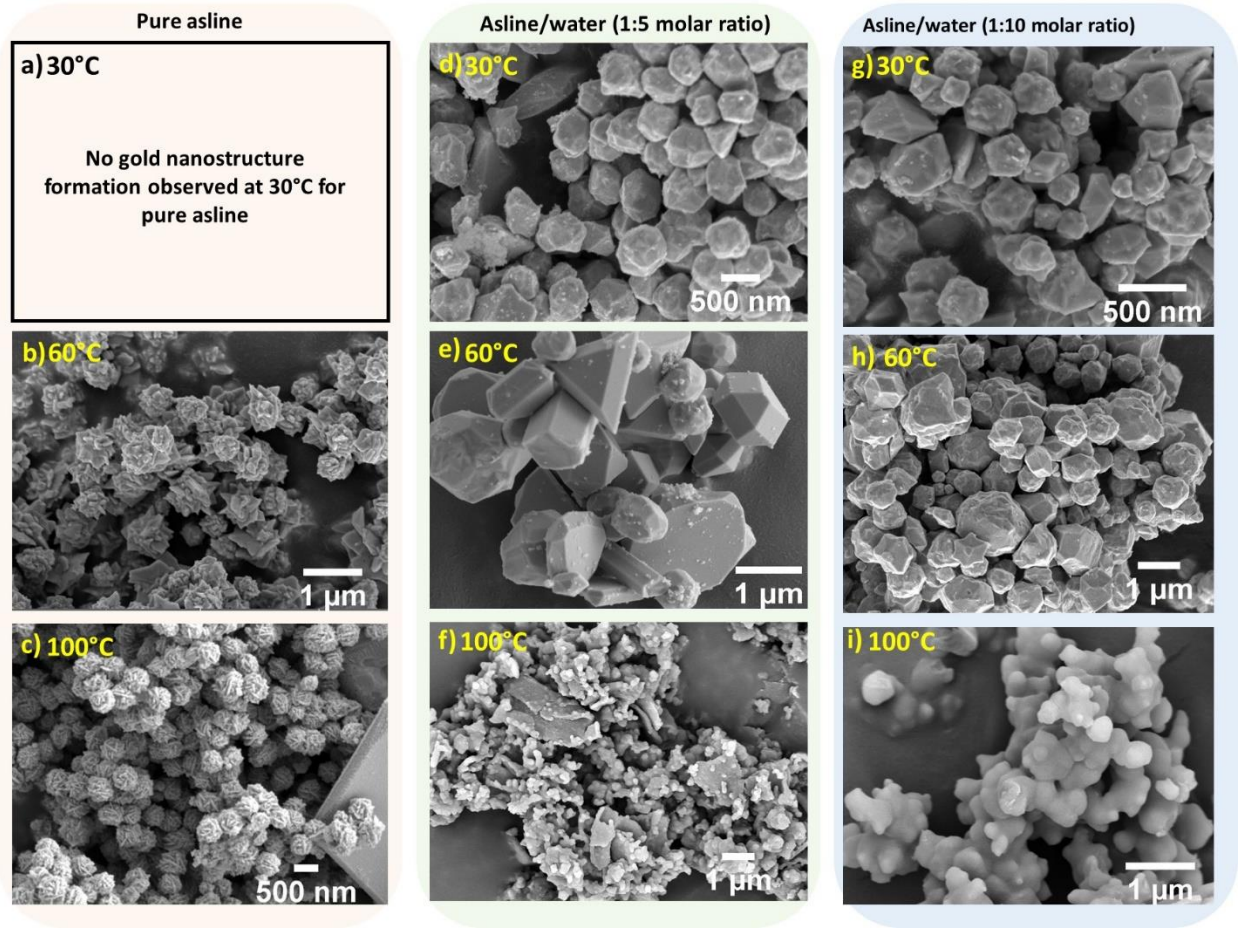

Figure 43: Effect of asline:water molar ratio and temperature in morphologies of gold nanomaterials; pure asline a) 30 ℃, b) 60 ℃, c) 100 ℃; asline/water (1:5 molar ratio) d) 30 ℃, e) 60 ℃, f) 100 ℃; asline/water (1:10) g) 30 ℃, h) 60 ℃, i) 100 ℃. All samples are synthesised for 1 h with a $HAuCl_4$ concentration of 48.2 mM.

In order to understand the formation of random gold morphologies in the presence of water in the asline system, another additional synthesis is performed in the asline/water mixtures 1:5 molar ratio at 100 ℃ to study the products obtained by quenching the reaction in ice-cold water when the solution turns red within 2-3 s just upon the addition of gold precursor. Corrugated nanoball like morphologies are observed in this reaction Figure 44 (which otherwise gives random structures after 1 h as shown in Figure 43f). It shows that initially in asline/water mixtures, flower like morphologies are formed but with time, these anisotropic flower like shapes evolve into random morphologies.

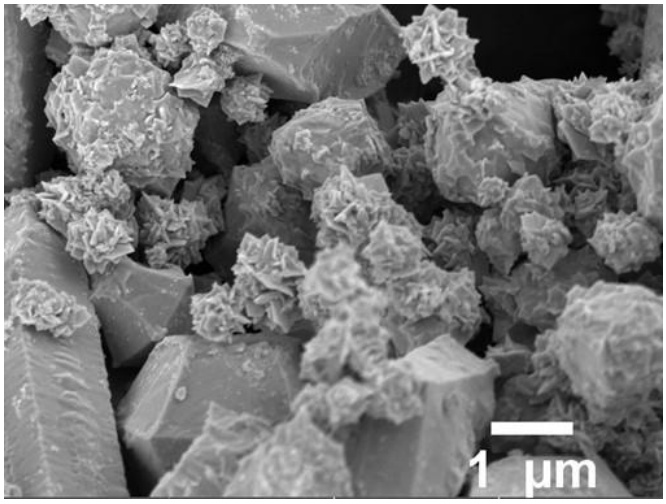

Figure 44: SEM micrograph of gold nanostructure synthesized in asline/water (1:5 by molar ratio) at 100 ℃ within 2-3 s when the solution turns red after the addition of gold precursor; $HAuCl_4$: 48.2 mM.

The gold nanowalnuts evolves rapidly into random morphologies in asline/water mixtures in 1 h in comparison to pure asline due to the following reasons: a) pure asline behaves as a weaker reducing agent than asline/water mixtures (which is also evident from the fact that asline/water solutions turn red within 2-3 s at all temperatures upon the addition of the gold precursor indicating faster reduction of $AuCl_4^-$ ions to Au^0 whereas pure asline turns red after 5 min even when the reaction temperature is 100 ℃). Presence of water in ascorbic acid is very important for the reducing action of ascorbic acid because the hydrated product of ascorbic acid (dehydroascorbic acid) is crucial in the reduction mechanism as discussed in Section 4.8.3 on the role of ascorbic acid and choline chloride and; b) The diffusivity of reactant ions in pure asline is lower than asline/water mixtures which in turn slows the reaction[266]. This is due to the high viscosity of pure asline (22.3968 Pa.s at 30 ℃) as seen from the viscosity values at different temperatures of 30 ℃, 60 ℃ and 80 ℃ for pure asline, asline/water (1:5) and asline/water (1:10) in Figure 45. The rheology experiments to determine the viscosities of asline and asline/water mixtures were performed by Dr Simon Butler, University of Cambridge.

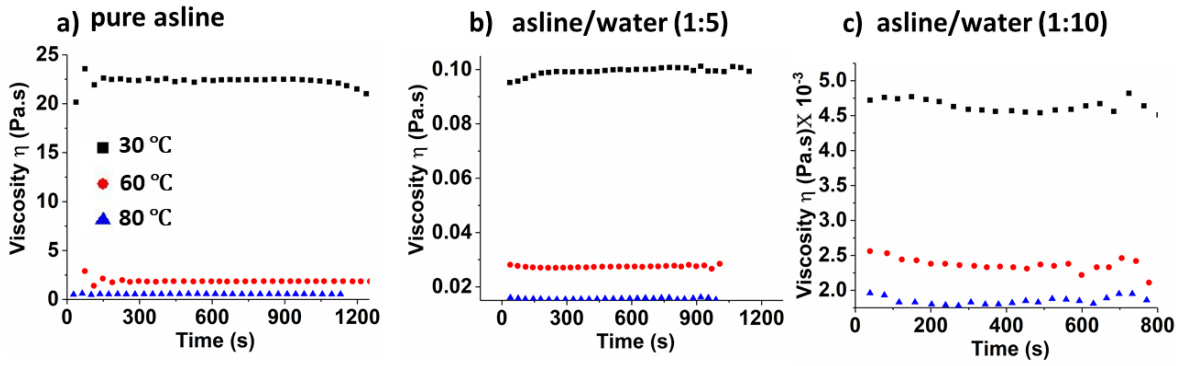

Figure 45: Viscosity-temperature measurements for a) pure asline, b) asline water (1:5 by molar ratio) and c) asline/water (1:10 by molar ratio) at 30 ℃, 60 ℃ and 80 ℃.

It is observed that appropriate reaction temperature is essential to tune the morphology of gold nanomaterials because it greatly affects the reduction kinetics[267]. For example, the growth of gold nanowalnuts occurs in pure asline at 60 ℃ and 100 ℃ but not at 30 ℃ indicating that the reaction temperature increases the reduction rate[268].

4.2.2 Role of ascorbic acid and choline chloride in asline to synthesize gold nanostructures

In order to understand the roles of ascorbic acid and choline chloride in asline in the synthesis of gold nanowalnuts, control experiments with $HAuCl_4$ are carried out. Gold precursor (48.2 mM) is added to the aqueous solution of choline chloride (formed by mixing water and choline chloride in 1:2 molar ratio similar to the composition between choline chloride and ascorbic acid in asline but without any ascorbic acid in this aqueous choline chloride solution) and the aqueous choline chloride solution is heated for 3 h under continuous stirring at 100 ℃. The solution colour remains unchanged from pale yellow indicating that no reduction of the gold precursor occurs in the absence of ascorbic acid. However, when the gold precursor (48.2 mM) is added to the aqueous solution of ascorbic acid (11 M) (formed by mixing water and ascorbic acid in 2:1 molar ratio similar to the composition between choline chloride and ascorbic acid in asline but without any choline chloride in this aqueous ascorbic acid solution), the colour of the aqueous ascorbic acid solution changes from pale yellow to red within 2-3 s upon adding the gold precursor

indicating the reduction of $AuCl_4^-$ ions to Au atoms. These studies show that ascorbic acid is the reducing agent in asline for the reduction of Au^{3+} to Au^0.

Non-uniform flower-shaped gold structures are observed when the reaction is stopped by quenching the reaction mixture in ice-water as soon as the solution turns red (Figure 46a). However within 1 h, these are randomly aggregated to form irregular random gold nanostructures as shown in Figure 46b.

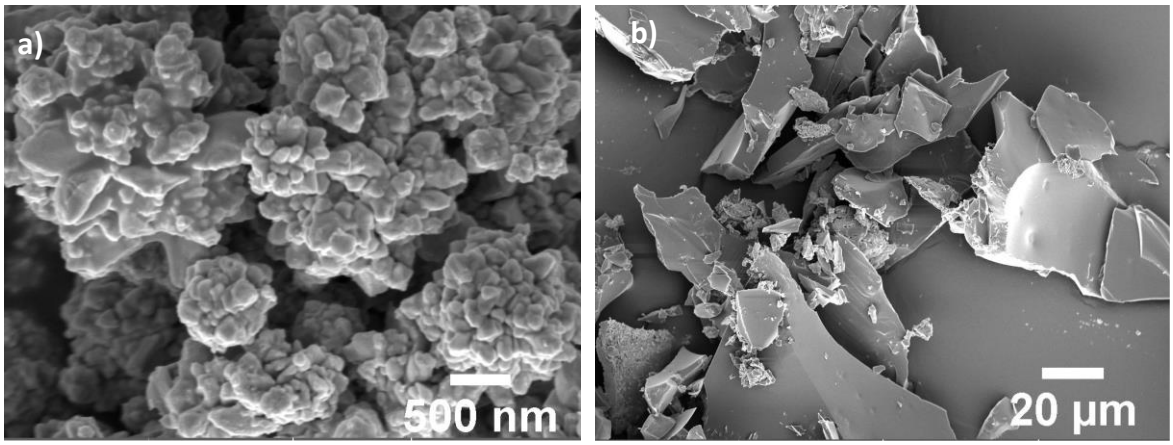

Figure 46: SEM micrographs for gold nanostructures at 100 °C, 48.2 mM $HAuCl_4$: a) Non-uniform irregular flower like shapes synthesized in aqueous solution of ascorbic acid (instantaneously), b) random nano gold structures observed in 1 h in aqueous ascorbic acid solution.

The reduction of gold by ascorbic acid is usually a two-step reduction process[269] as shown in eq. 20, 21 and 22 where ascorbic acid ($C_8H_8O_6$) is oxidized to dehydroascorbic acid (DHA) while $AuCl_4^-$ ions are reduced to $AuCl_2^-$ and then to Au atoms. DHA is extremely unstable being spontaneously converted to 2,3-diketogulonic acid (DGA)[270] as seen in eq. 22 on account of the hydrolysis of the lactone ring of DHA. Release of DGA is not possible in the absence of water and hence pure asline is a weak reducing agent than asline/water solutions. Ab-initio calculations show that the presence of sharp pointed features of the gold nanoflowers in the initial stages of product formation is due to the anchoring action of the –COOH groups from DGA molecules and it is shown to direct the growth of branched structures[271]. However it is important to note that although DGA is capable to produce branched structures, it is unable to prevent agglomeration or provide stability to these dendritic structures and thus capping ligands would be required to prevent

unwanted aggregation[272]. The generation of dislocations and kinks on the gold nanostructures due to the action of DGA produced as a by-product from the oxidation of ascorbic acid provide active sites for the adhesion of the DES asline to control the shape of these gold nanowalnuts[13].

$$[AuCl_4]^- + C_8H_8O_6 \rightarrow [AuCl_2]^- + DHA + 2Cl^- + 2H^+ \quad (20)$$

$$[AuCl_2]^- + C_8H_8O_6 \rightarrow Au + DHA + 2Cl^- + 2H^+ \quad (21)$$

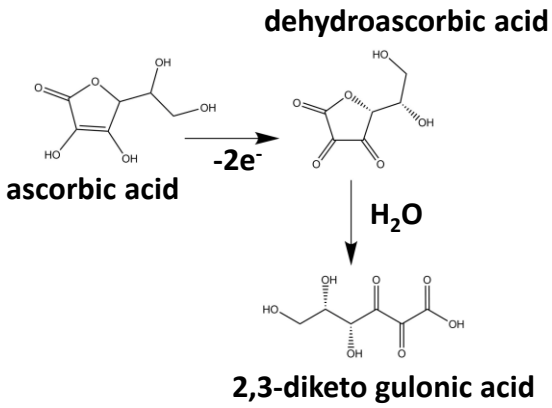

(22)

4.2.3 Effects of halide ions in choline chloride

Studying the influence of halide ions on the growth and morphology of nanomaterials is crucial for wet chemical synthesis as it is well documented that halide ions have strong affinities to the metal surfaces which in turn dictates the growth of nanostructures[273].

In order to study the effect of halide anions in the choline moiety present in asline, systematic studies are carried out by synthesizing gold nanostructures in another DES comprised of choline bromide instead of choline chloride in pure asline (choline bromide/ascorbic acid in the molar ratio of 2:1) at 100 °C for 1 h. As shown in Figure 47b, polydisperse gold nanoballs of sizes ranging from 500 nm to 1 µm are produced when choline bromide is used. These gold nanoballs are bigger in size than those synthesized with choline chloride which are of sizes 485 ± 45 nm. This indicates that upon changing the halide anion, there is little change in the overall morphology and it is still predominantly spherical in appearance but the size distribution is changed.

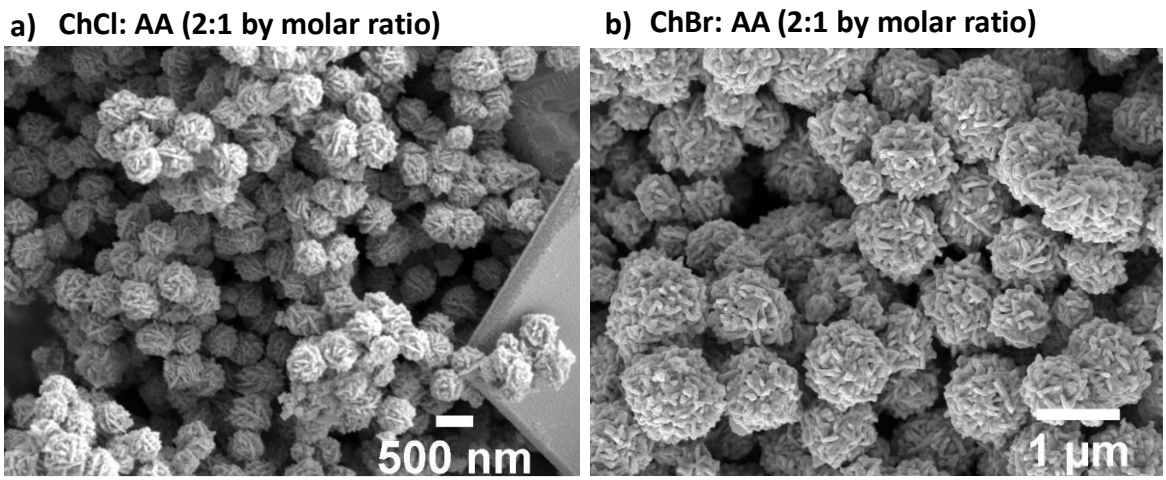

Figure 47: SEM micrographs to compare the effect of halide anion. All reactions are carried out at 100 °C, 1 h, $HAuCl_4$ (48.2 mM) a) ChCl:ascorbic acid (2:1); b) ChBr:ascorbic acid (2:1).

Halides are able to control the reaction kinetics and thus affect nucleation and growth factors in solution by complexing first with the gold ions as $[AuX_2]^-$ complexes, hence affecting the reduction potentials and solubility of gold ions in $[AuX_2]^-$ complexes and thus changing the reduction rates[274]. The addition of larger halide ions like Br^- to a solution containing the precursor $HAuCl_4$ (as in this case) leads to a slower growth of AuNP as the reduction kinetics of $[AuCl_2]^- > [AuBr_2]^-$ (1.154 V > 0.960 V) which means that Br^- would decrease the ability of Au^+ to be reduced by ascorbic acid[275,274]. The binding strengths of the halide ions are also different on Au surfaces for e.g. Br^- chemisorbs more strongly on the surface on Au than Cl^-[276]. This strong affinity of Br^- in comparison to Cl^- with Au can be explained by Pearson's theory of hard soft acid base (HSAB) according to which both Au and Br^- are soft acid and base respectively so their affinity for each other is stronger than Cl^-[277]. This explains the larger size of these gold nanowalnuts in the presence of choline bromide because lower reduction rates means weaker reducing agent and hence slower nucleation rates that lead to larger size particles[278].

Another experiment is carried out to study the synthesis of gold nanomaterials by combining choline iodide and ascorbic acid in the molar ratio of 2:1. However unlike choline chloride and choline bromide, choline iodide does not form any eutectic liquid with ascorbic acid.

4.2.4 Plasmonic applications of gold nanowalnuts

Plasmonic activities of the corrugated nanoballs or 'nanowalnuts' are tested for surface enhanced Raman spectroscopy (SERS) of the Rhodamine (R6G) dye by our collaborators at the Department of Material Science and Metallurgy, University of Cambridge (Ms Christina Boukouvala and Dr Emilie Ringe). R6G, a dye molecule commonly used to demonstrate SERS enhancement, is carried out to investigate the potential of the gold nanowalnuts as Raman signal enhancement factors. Figure 48 show the results of SERS detection. The characteristic Raman peaks for R6G are hard to distinguish in pure R6G but are considerably enhanced after the addition of the gold nanoballs, despite their large diameter which is bigger than what is commonly considered as optimum for SERS (40-50 nm)[279]. This enhancement is attributed to the corrugations/roughness on the surface of the gold nanowalnuts that act as hotspots and amplifies the local electromagnetic field. Note that the peak at 1000 cm^{-1} is present in both signals, due to second order Raman scattering from the silicon substrate[280] .

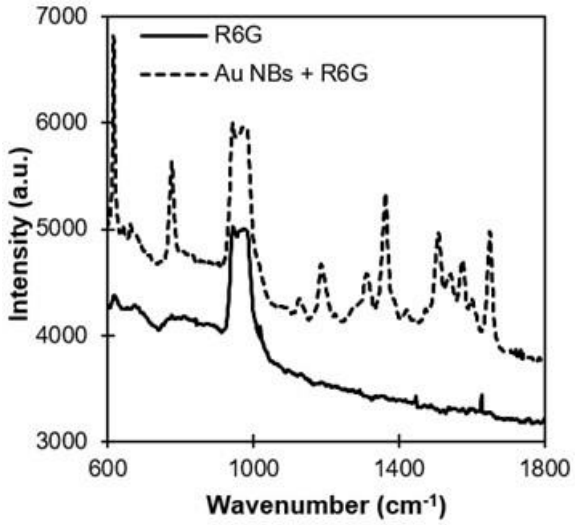

Figure 48: The Raman signal for R6G with and without the enhancement of gold spiky nanoballs. Acknowledgement: Ms Christina Boukouvala, University of Cambridge.

The plasmonic properties of the synthesised gold nanoballs seem promising for SERS enhancement applications and will attract a lot of attention being label-free and sensitive,

and potentially for other spectroscopy techniques such as plasmon enhanced fluorescence[281].

4.3 Conclusions

This chapter presents the synthesis and mechanistic understanding of a one-pot green solvent route method for the synthesis of gold nanoparticles using the deep eutectic solvents reline and asline which have the same quaternary ammonium salt choline chloride but different hydrogen bond donors (urea in reline and ascorbic acid in asline). There are no addition of any external additives in these methods.

In the case of pure reline and reline/water systems, release of ammonia due to the *in-situ* decomposition of reline and reline/water systems at high temperatures act as the reducing agent to produce small gold nanoparticles of size 1.6-3 nm. Neither choline chloride nor its decomposition product trimethylamine plays any role as a reducing agent. It is observed that the reduction of gold in pure reline is much quicker than aqueous solutions of reline or aqueous urea. This is attributed to the extensive hydrogen bonded framework available in pure reline which acts as catalysts to bring the reactants closer. However in the presence of water, the intermolecular hydrogen bonds are disrupted and the structure of reline is greatly altered. Reline systems also act as partial stabilizers due to the stabilization provided on account of the counter-ion layers (similar to the ionic liquids) and also urea/ammonia provide stabilities to the gold centres (Au^0 and Au^+). It is important to note that reline also provide stability to Au^+ centres which are usually unstable in water and rapidly disproportionates to Au^{3+} and Au^0.

The reline systems however produces only spherical gold nanoparticles because of the absence of any anisotropic agent in reline (neither choline chloride nor urea are anisotropic agents). In order to develop non-spherical morphologies such as branched or corrugated surfaces, asline which is another DES made of choline chloride and ascorbic acid combined in the molar ratio of 1:2 is employed.

It is observed that corrugated nanoballs or ‘nanowalnuts’ are synthesized in pure asline conditions within 1 h. The formation mechanism of these nanowalnuts are further

investigated by following the reaction at different time intervals of 5 min, 15 min and 30 min. It is observed that anisotropic growth of Au takes place within 5 min of starting the reaction. As time increases, these anisotropic morphologies evolve into increasingly spherical structures leading to monodisperse corrugated balls of sizes 405 nm (or nanowalnuts) within 1 h. A decrease in the yield of the solid product deposited at the bottom of the reaction vessel as the time increases, shows that morphology evolution takes place through digestive Ostwald ripening where the larger particles are re-dissolved to produce smaller particles that remain in supernatant.

Upon addition of water in asline, nanowalnuts are obtained within 2-3 s of the gold precursor addition but these nanowalnuts turn to random and irregular gold nanostructures within one h. This rapid change of nanowalnuts to irregular structures in asline/water systems is observed because of the high reducing nature of asline/water mixtures in comparison to pure asline and high viscosity of pure asline which slowers the ion diffusivity in the reaction.

Control experiments show that ascorbic acid moiety present in asline is responsible for the reducing the gold precursor because no reduction of the gold precursor is observed in the aqueous choline chloride solution. Diketogulonic acid (DGA) which is produced as a by-product of ascorbic acid hydrolysis is responsible for the growth of the branched/corrugated and pointed structures. However as DGA is unable to prevent agglomeration and hence asline act as capping ligand by binding to the kinks and corners of these corrugated structures to avoid aggregation.

The halide ion controls the reduction kinetics in the synthesis of gold nanomaterials because the size of the gold nanowalnuts changes upon varying the halide ion. Larger corrugated gold nanowalnuts are obtained when the quaternary ammonium salt is choline bromide due to the slower reduction rates meaning weaker reducing ability hence slower nucleation in solutions containing choline bromide in comparison to choline chloride in asline.

These gold nanowalnuts are further tested for SERS activities for R6G dyes by our collaborators, Ms Christina Boukouvala and Dr Emilie Ringe at the Department of Material Science and Metallurgy, University of Cambridge, UK. They show that there is an

enhancement of the Raman peaks of R6G dye on addition of the gold nanowalnuts which is otherwise difficult to observe in pure R6G dye due to the roughness and corrugated surface of the gold nanowalnuts.

Chapter 5: Elucidating the role of reline towards the synthesis of vanadium pentoxide

The objectives of Chapter 4 were to elucidate the role of DES towards the synthesis of gold nanomaterials and to underpin the mechanism for the reducing action of DES. In order to further develop our understanding on other multiple roles played by DES to control morphologies and size at the nanoscale, the synthesis of nanostructured metal oxide V_2O_5 (belonging to the transition metal oxide family) is carried out in reline assisted solvothermal synthesis. The interest to develop vanadium pentoxide nanomaterials is due to its applications in a wide range of areas like (photo)catalysis, electrochemical capacitors[199], sensors[200], Li-ion batteries[198,] etc[282]. The ability to synthesize tuneable and controllable nanostructured vanadium oxide has attracted the attention of the scientific community due to the strong morphology-activity relationships as mentioned previously in the literature review (Chapter 2)[7,8,6,283]. A rich class of nanoscale morphologies are developed for the above mentioned applications as nanofibers, nanotubes, nanosheets and hollow spheres[284].

This chapter is focused on understanding the mechanism and developing the solvothermal synthesis route for nanostructured V_2O_5 of different morphologies in reline by only varying the amount of water in the reaction medium, without the addition of auxiliary reagents. Several characterization techniques like XRD (X-ray diffraction), TEM (transmission electron microscopy), SEM (scanning electron microscopy) and ESI-MS (electrospray ionization-mass spectroscopy) are used in this chapter. The motivation to produce different nanostructures in reline upon changing the water ratio during the solvothermal synthesis for V_2O_5 stems from a previous publication reported by our group where different morphologies of nanostructured ceria such as nanorods and nanoparticles are synthesized in reline upon altering the water ratio[155].

These as-synthesized V_2O_5 nanostructured materials are tested as electrode materials for Li-ion batteries by our collaborators at the Institute for Manufacturing, University of Cambridge (Dr Changshin Jo and Dr Michael De Volder).

5.1 Screening of different precursors

Choice of precursor plays a vital role in determining the morphology of the nanomaterial as the nature of chelating ligand (or anion) influences the overall chemistry of the reaction[285]. Some of the most common vanadium precursors along with their reaction conditions to produce a range of different morphologies like 0D, 1D, 2D and 3D V_2O_5 nanostructures are shown in Table 10. For a particular precursor, e.g. V_2O_5 as the starting material, depending on the nature of the additional reagents such as Brij 30 or PEG, different morphologies such as nanowires and particles are synthesized[286,287] as these surfactants are excellent crystal growth modifiers to tune the formation of superstructures in solutions by their preferential adsorption to certain crystalline facets.

Table 10: Summary of the common vanadium precursors and their experimental conditions to produce different morphologies of nanostructured V_2O_5.

Precursor	Morphology	Solvent	Additional reagents	Conditions
V_2O_5	Particle[287]	H_2O, H_2O_2	PEG	200 °C, 30 min
	Nanowire[286]	H_2O	Brij 30	170 °C, 2 h
	Nanowire[288]	H_2O_2, H_2O	-	205 °C, 96 h
	Nanowire[289]	H_2O	$C_2H_2O_4$	Not given
	Nanosheet[290]	H_2O_2, H_2O	IPA	180 °C, 6 h
	Sphere[291]	H_2O_2, H_2O	$C_2H_2O_4$	170 °C, 24 h
$VO(O^iPr_3)$	Particle [292]	H_2O	pyridine, acetone	RT, -
	Sphere[293]	H_2O	CH_3COOH	200 °C, 1.5h
	Fibre[294]	IPA	Carbon fibre	200 °C, 10h
NH_4VO_3	Nanowire[295]	H_2O	Pluronic 123, HCl, HNO_3	120 °C, 24 h
	Nanobelt[296]	Ethylene glycol	-	190 °C, 2 h
	Nanosheet[297]	H_2O	$C_2H_2O_4$	180 °C, 24 h
	Octahedron[298]	H_2O	IPA	180 °C, 6 h
	Sphere[299]	H_2O	HCl, poly(styrenesulfonate)	180 °C, 24 h
VCl_3	Nanobelt[300]	H_2O	pyridine	160 °C, 12 h
$VO(acac)_2$	Sphere[301]	Ethylene glycol	-	220 °C, 17 h
	Spheres[198]	Ethylene glycol	PVP	140 °C, 12 h
	Nanorods[198]	Ethylene glycol	-	140 °C, 12 h
$VOSO_4$	Nanowires[302]	H_2O	$KMnO_4$	160 °C, 12 h

In order to decide the best starting material from Table 10, the solvothermal syntheses of four common vanadium precursors (V_2O_5, $VO(acac)_2$, $VOSO_4$ and NH_4VO_3) are carried out in reline water (1:2 and 1:10 molar ratio mixtures) and pure water. V_2O_5 as the starting precursor show the best results out of all the above precursors since diverse well-defined morphologies as 3D nanoballs, 2D nanosheets and nanounits arranged as nanofleece are obtained on changing the water ratio in the reaction mixture (Figure 49). For the other precursors, random morphologies are obtained in the presence of reline (Figure 50 and Figure 51).

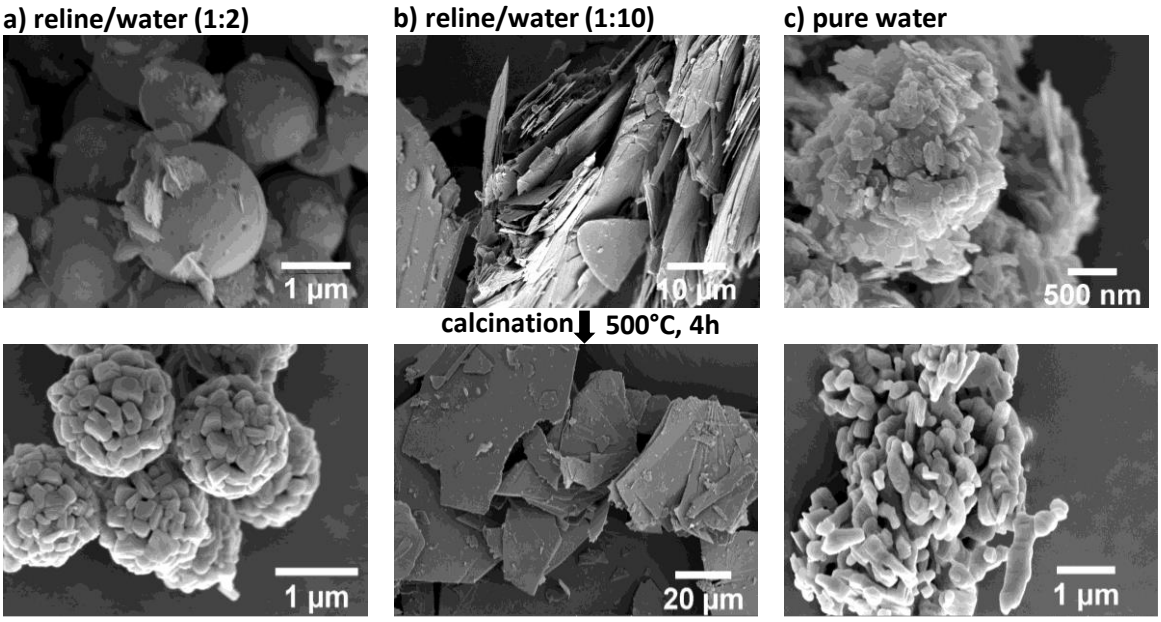

Figure 49: SEM micrographs of different morphologies of V_2O_5 under solvothermal synthesis conditions using V_2O_5 as the starting precursor (Temperature= 180 °C, time= 10 h); a) reline/water (1:2), b) reline/water (1:10) and c) pure water. Calcination conditions: Temperature= 500 °C, time=4 h, sweep rate= 10 °C/min.

Only when the reaction solvent is pure water, well-defined morphologies like micron sized sticks (about 2 µm) and nano-urchins of size approx. 1 µm are obtained with the starting precursors $VOSO_4$ and $VO(acac)_2$ as shown in Figure 50c and Figure 51c respectively.

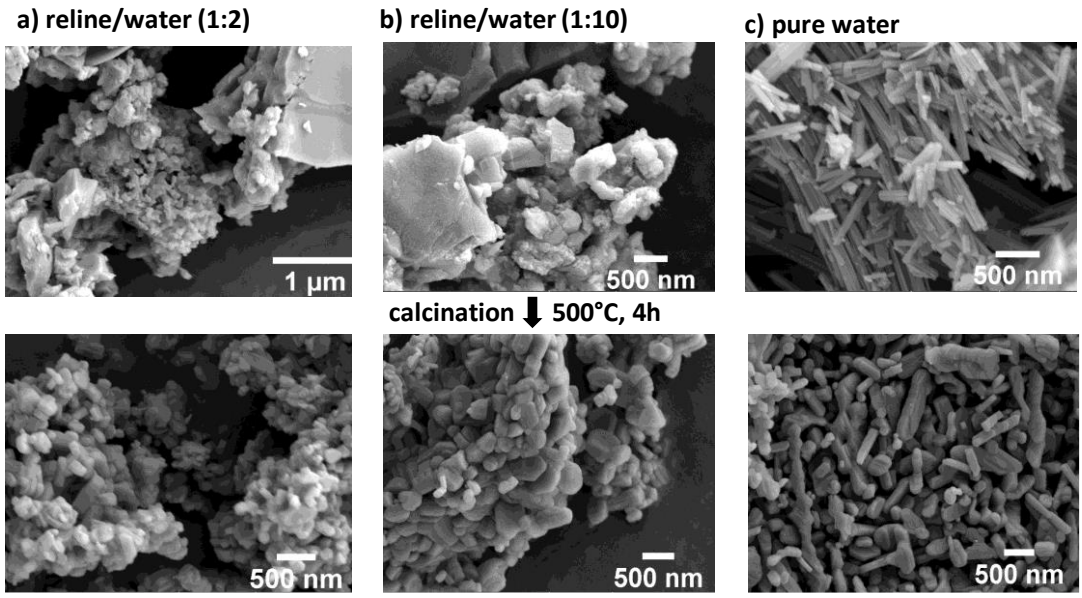

Figure 50: SEM micrographs of different morphologies of V_2O_5 under solvothermal synthesis conditions using $VOSO_4$ as the starting precursor (Temperature= 180 °C, time= 10 h); a) reline/water (1:2), b) reline/water (1:10) and c) pure water. Calcination conditions: Temperature= 500 °C, time=4 h, sweep rate= 10 °C/min.

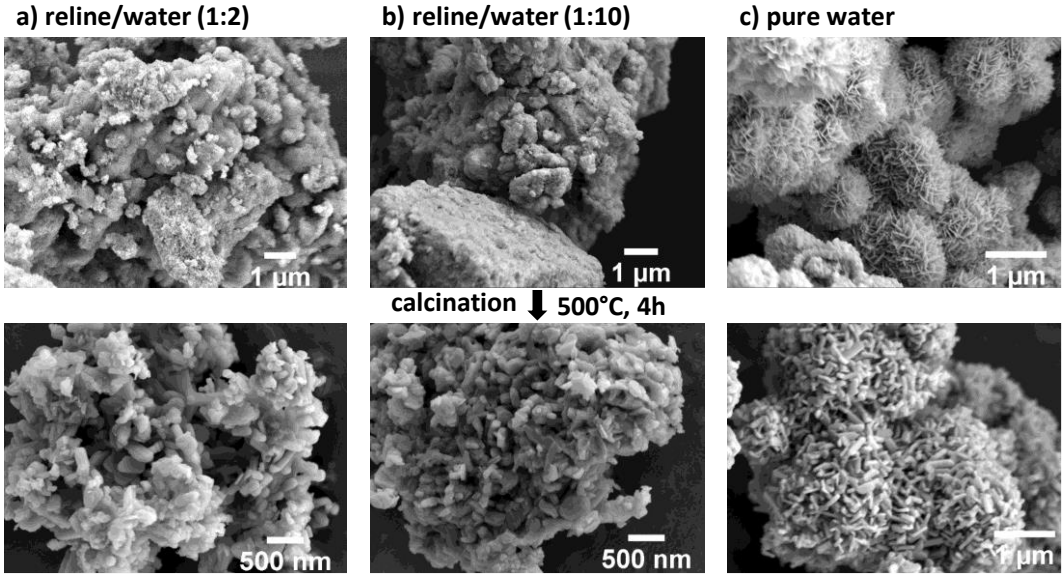

Figure 51: SEM micrographs of different morphologies of V_2O_5 under solvothermal synthesis conditions using $VO(acac)_2$ as the starting precursor (Temperature= 180 °C, time= 10 h); a) reline/water (1:2), b) reline/water (1:10) and c) pure water. Calcination conditions: Temperature= 500 °C, time=4 h, sweep rate= 10 °C/min.

As well-defined structures are obtained by using $VOSO_4$ and $VO(acac)_2$ in pure water for 10 h at 180 °C, the formation mechanism of these structures are investigated further by carrying out additional hydrothermal synthesis for shorter timescales of 2.5 and 5 h at 180 °C to study the morphology of the products formed as discussed in the Appendix section (A2).

No solid product is obtained when NH_4VO_3 is used as the starting precursor in water as the reaction solvent in hydrothermal synthesis (Figure 52).

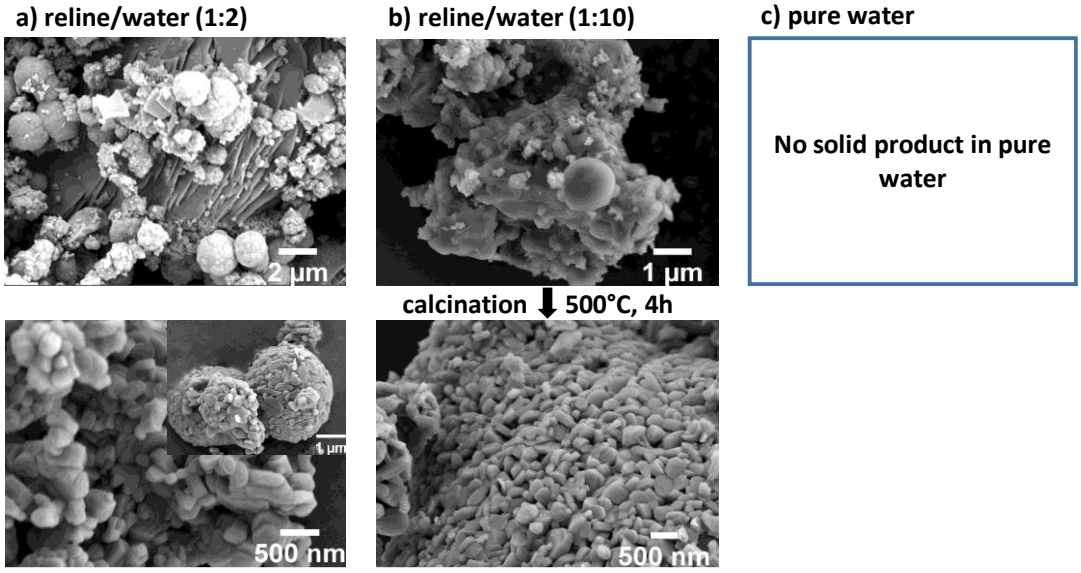

Figure 52: SEM micrographs of different morphologies of V_2O_5 under solvothermal synthesis conditions using NH_4VO_3 as the starting precursor (Temperature= 180 °C, time= 10 h); a) reline/water (1:2), b) reline/water (1:10) and c) pure water. Calcination conditions: Temperature= 500 °C, time=4 h, sweep rate= 10 °C/min.

The rest of this chapter is focussed on the mechanistic understanding of reline and reline/water mixtures using V_2O_5 as the precursor to synthesize nanostructured V_2O_5.

5.2 Synthesis of V_2O_5 nanostructures in reline

The deep eutectic solvent reline which is formed by combining choline chloride and urea in the molar ratio of 1:2 is used for the solvothermal synthesis of nanostructured V_2O_5 (using bulk V_2O_5 as the initial precursor) with its morphology being manipulated by simply increasing the molar ratio of water as shown by the SEM images in Figure 49. When pure water or pure reline are used as solvent, similar random morphologies are obtained after solvothermal synthesis which are converted into 1D nano-units randomly arranged crystals (nanofleece) after calcination. A 1:2 reline/water molar ratio mixture leads to the formation of well-defined and uniform V_2O_5 hemihydrate ($V_2O_5.xH_2O$) nanoballs which recrystallize during calcination but roughly retain a similar spherical shape. Due to the hygroscopic nature of pure reline[254], few 3D nanoballs are observed in pure reline because of the presence of trace amounts of water (Figure 53). When increasing the water content in reline (reline/water, 1:10 by molar ratio), nanosheets are synthesized. A further increase of the water content (e.g. reline/water, 1:20) leads to similar layered morphologies (Figure 53). Increasing the amount of water does not only vary the resulting morphology but also the V_2O_5 yield from < 0.5% in pure reline to 2.6%, 6.1% and 19.6% when the reline/water ratio is increased from 1:2, 1:10 and 1:20 respectively. A yield of 33.3% is obtained with pure water as solvent. These results suggest that the increase of yield can be associated to the decrease of viscosity as the water content increases[303] although water is also proposed to play an active role in the re-crystallisation process[304].

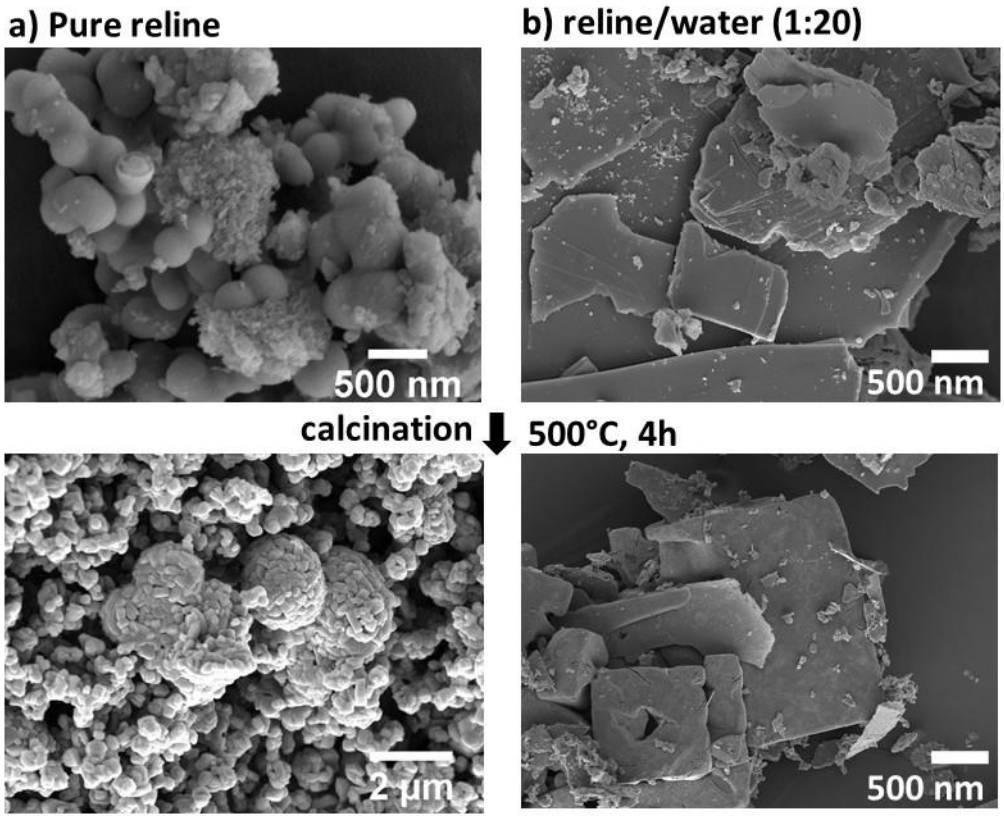

Figure 53: SEM micrographs of different morphologies of V_2O_5 under solvothermal synthesis conditions using V_2O_5 as the starting precursor (Temperature= 180 °C, time= 10 h); a) pure reline and b) reline/water 1:20.

Figure 54 shows a schematic representation of the different steps taking place during the solvothermal synthesis. A dark orange colour solution is obtained upon the dissolution of bulk V_2O_5 in pure reline, reline/water and pure water solutions characteristic of V(V). Upon heating the reactants at 80 °C for 2-3 h (prior solvothermal synthesis for the dissolution of the precursor), the colour of the solution turns green in the presence of reline, indicating its reduction to V(III). However, in the case of using pure water as solvent, no change in colour is observed, suggesting that reline, or one of its components, is responsible for the reduction of the vanadium precursor at relatively low temperature (80 °C) which is also shown in Chapter 4 on the reducing property of reline and reline/water solutions.

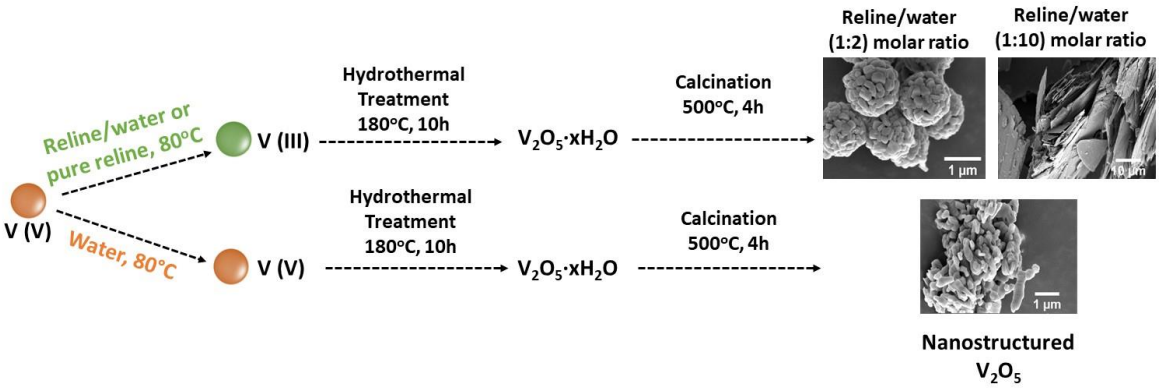

Figure 54: Schematic representation of the solvothermal synthesis of nanostructured V_2O_5 in reline and reline/water mixtures.

Independently of the initial solvent, solvothermal synthesis at 180 °C for 10 h leads to the formation of poorly crystalline vanadium oxide hemihydrate precipitates (black) as shown by the XRD patterns for reline/water (1:2), reline/water (1:10) and pure water uncalcined samples in Figure 55. The poor crystallinity of the vanadium oxide hemihydrate species is indicated by the broad peaks for the uncalcined samples for reline/water (1:2) and pure water samples. However the sample prepared in reline/water (1:10) is crystalline as shown by the sharp peaks in the XRD pattern (Figure 55). Different morphologies of vanadium oxide hemihydrate are produced depending on the chemical environment.

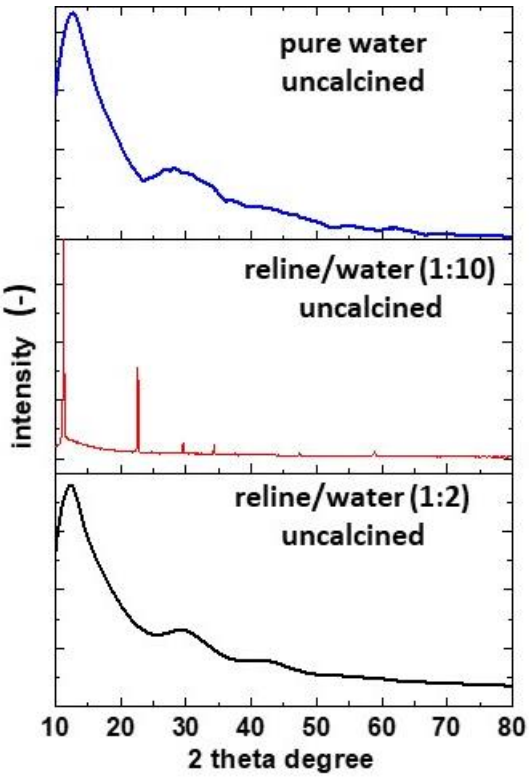

Figure 55: XRD pattern of uncalcined $V_2O_5.xH_2O$: nanoballs synthesized in reline/water molar ratio 1:2, nanosheets synthesized in reline/water molar ratio 1:10 and nanofleece in pure water. All the samples are prepared for 10 h at 180 °C under solvothermal conditions.

In the presence of oxygen rich atmosphere during calcination, $V_2O_5.xH_2O$ is converted to V_2O_5 after losing molecular water as shown below and in eq. 23.

$$V_2O_5.xH_2O \rightarrow V_2O_5 + xH_2O \qquad (23)$$

Upon calcination at 500 °C, the materials are then transformed into crystalized V_2O_5 phases. While the general morphology is still retained after calcination (Figure 49 and Figure 56), the smooth surface of the un-calcined samples are transformed into well-defined unit crystals of more than 100 nm sizes due to the release of coordinated water from the V_2O_5 hemihydrate materials[305]. Figure 56 shows the effect of calcination on the samples that are synthesized at 2.5 h and 5 h in reline/water (1:2 and 1:10 by molar ratio) and water solvent conditions to gain more mechanistic insights. It can be seen from Figure 56b, when the reaction is carried out at 2.5 h (in reline/water 1:10 molar ratio), smooth

blocks are produced pre-calcination but upon heat-treatment, cracks start appearing on the blocks.

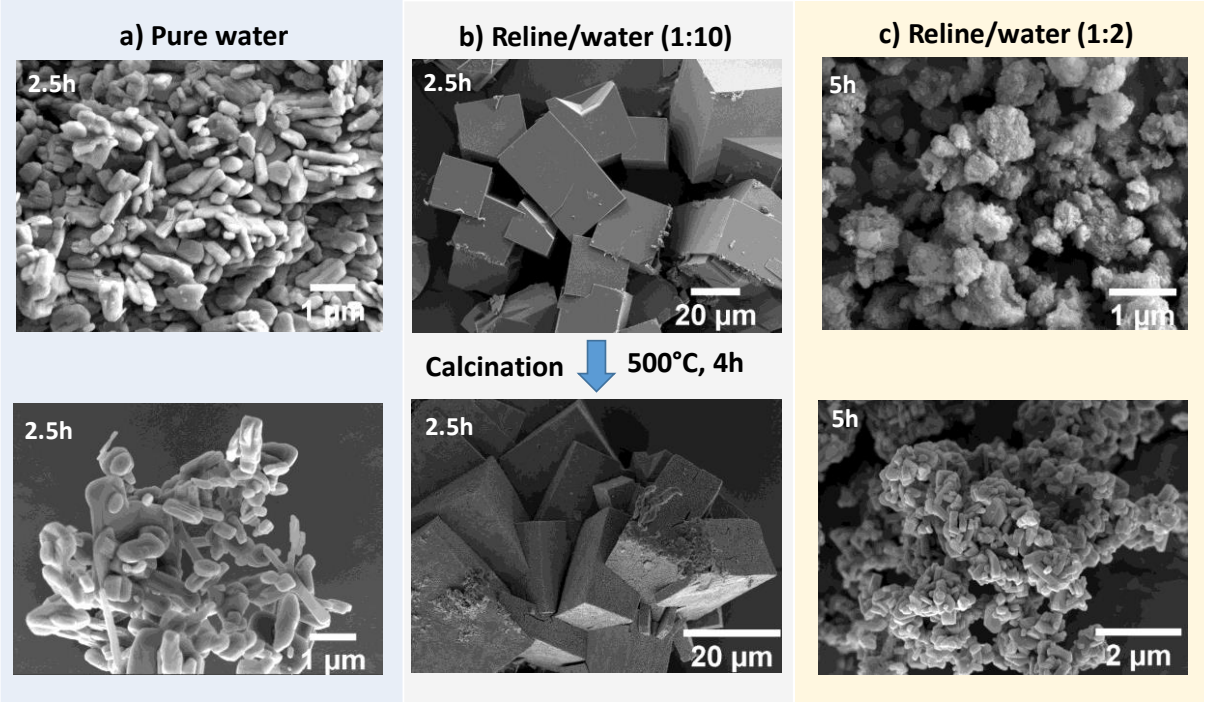

Figure 56: SEM micrographs of uncalcined and calcined V_2O_5 samples synthesised at 2.5 h and 5 h in a) pure water b) reline/water molar ratio 1:10 and c) reline/water molar ratio 1:2. All the samples are synthesised at 180 °C and calcined at 500 °C for 4 h at a rate of 10 °C/min.

The loss of smooth structures upon calcination of $V_2O_5.xH_2O$ nanomaterials and appearance of cracks is studied in greater detail by Liu *et al*. using thermogravimetric analysis[306]. The loss of adsorbed and weakly bound water occurs at 160 °C, followed by the release of more strongly bound water at 260 °C and finally chemically bond water is removed at 450 °C. Jiqi *et al*. also reports that calcination temperatures of more than 300 °C are required to remove coordinated water and amine species from the hydrated V_2O_5 to convert into V_2O_5[305].

^{51}V NMR studies are conducted after the addition of V_2O_5 precursor to the different solvents (pure reline, reline/water 1:2, reline/water 1:10 and pure water) prior to solvothermal synthesis to find out the different species present in the solution. These studies show the formation of decavanadate $[H_3V_{10}O_{28}^{3-}]$ species in the presence of water

(pure water and reline/water mixtures) in Figure 57. However when pure reline is used as a solvent, only [$V_4O_{12}^{4-}$] and [$V_5O_{15}^{5-}$] species are observed[307]. This is in agreement with the decrease of the pH of the reline/water and water solutions due to the release of protons H^+ associated to the formation of [$H_3V_{10}O_{28}^{3-}$] ions as shown in eq.24[308]. In pure reline (in the absence of water), decavanadate species are not formed and thus, no variation of pH is noticed (Table 11). The importance of the acidic environment has been discussed later in the text to explain the formation of nanosheets.

$$5V_2O_5 + 3H_2O \leftrightarrow [H_3V_{10}O_{28}^{3-}] + 3H^+ \quad (24)$$

Table 11: pH values of reline/water and pure water solutions before and after adding V_2O_5 initial precursor.

Solution	pH value [a]	pH value [b]
Pure reline	10.5	10.6
Reline/water (1:2)	9.1	6.1
Reline/water (1:10)	8.8	4.4
Pure water	8.4	4.0

pH values measured with ± 0.2 accuracy.

[a] pH value before the addition of V_2O_5 precursor.

[b] pH value after the addition of V_2O_5 precursor.

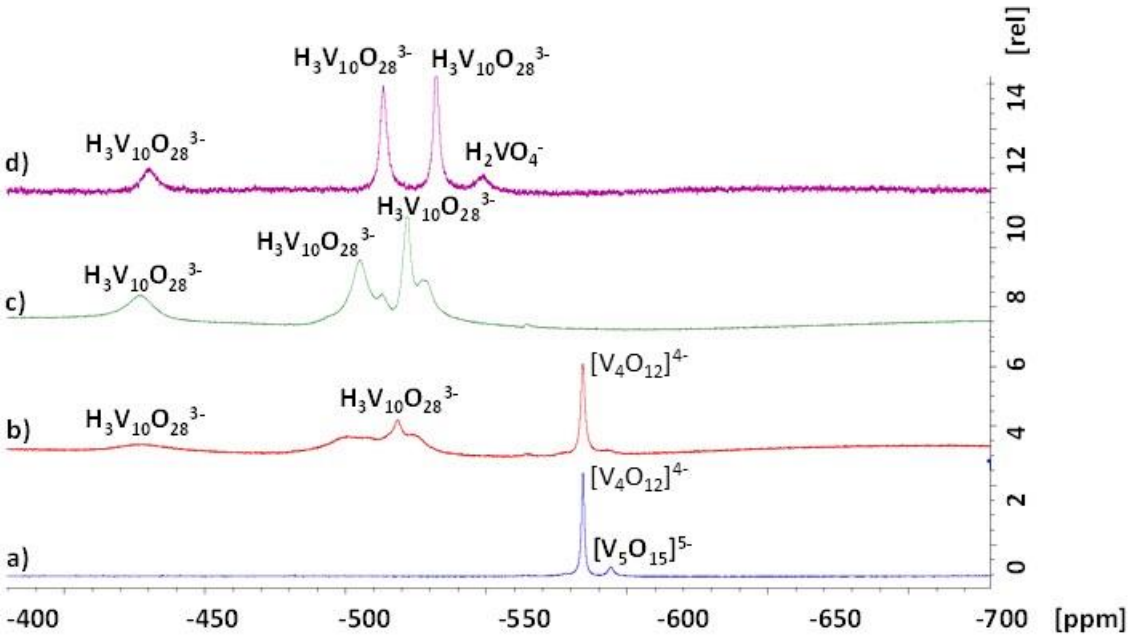

Figure 57: 51V NMR of V_2O_5 precursor dissolved in a) pure reline, b) reline/water molar ratio 1:2, c) reline/water molar ratio 1:10 and d) pure water. All the samples are diluted in D_2O prior to the 51V NMR studies.

Figure 58 shows the powder X-ray diffraction (pXRD) patterns of the three calcined nanostructured samples and bulk V_2O_5 (for reference). The diffraction peaks at 15.36°, 20.28°, 21.73°, 26.15°, 31.03°, 32.39°, 34.31° and 41.37° 2Θ angles are well indexed to the orthorhombic crystalline phase of V_2O_5 (space group: Pmmn 59) with lattice constant values of a= 11.516 Å, b= 3.5656 Å and c= 4.372 Å (JCPDS card number 41-1426) corresponding respectively to the {020}, {001}, {011}, {110}, {040}, {101}, {130} and {002} lattice planes[309]. In the case of V_2O_5 nanosheets, the diffraction peaks at 20.28° and 41.37° are considerably more intense indicating the dominant {001} and {002} planes[310] and the other peaks are relatively too small. It is previously reported that for V_2O_5 ultra-thin nanosheets, the {001} orientation phase is highly preferred and another minor diffraction peak could be indexed to {002}[310]. In the case of V_2O_5 nanoballs, intense diffraction peaks are observed at 15.36°, 20.28°, 26.15° and 31.03° which correspond to the crystal planes of {020}, {001}, {110} and {040} respectively. For V_2O_5 nanofleece, an intense diffraction peak is observed at 20.28° and a minor peak at 15.36° indicating the

dominant planes as {001} and {020} respectively. No other impurity peaks are observed in the samples.

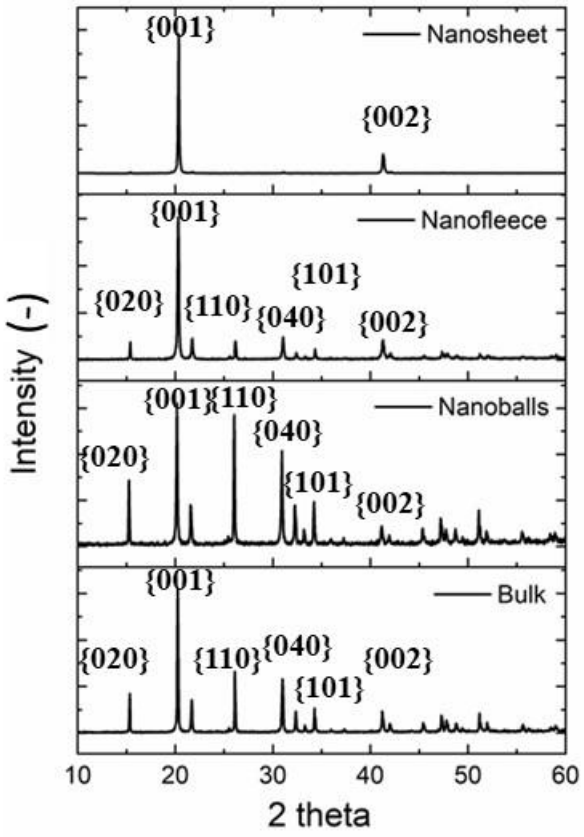

Figure 58: pXRD pattern of orthorhombic calcined V_2O_5 for nanosheets synthesized in reline/water molar ratio 1:10, nanofleece in pure water, nanoballs synthesized in reline/water molar ratio 1:2 and commercial V_2O_5. All the samples have been prepared for 10 h at 180 °C under solvothermal conditions. After preparation, the samples have been calcined in air at 500 °C for 4 h at a sweep rate of 10 °C/min.

HR-TEM micrographs of the different V_2O_5 materials (nanoballs, nanosheet and nanofleece) are shown in Figure 59a-c. All the samples exhibit good crystallinity and clear lattice fringes.

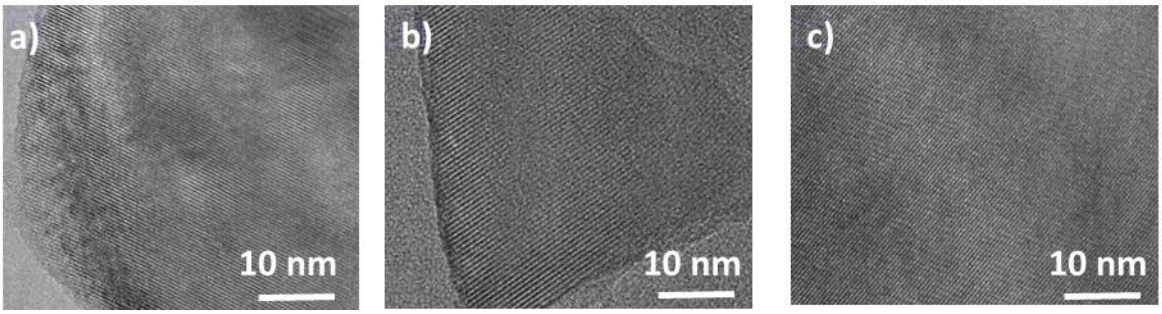

Figure 59: HRTEM micrographs of V_2O_5 calcined samples of a) nanoballs (reline/water 1:2), b) nanosheet (reline/water 1:10) and c) nanofleece (pure water). All the samples are prepared under solvothermal conditions for 10 h at 180 °C followed by calcination at 500 °C for 4 h.

5.3 Understanding the mechanism behind the synthesis of different morphologies of V_2O_5

The formation of the different V_2O_5 morphologies suggests a templating effect dependent on the reline/water content. Additional mechanistic insights are obtained by carrying out syntheses at shorter durations of 2.5 and 5 h. Figure 60 shows the morphology evolution as a function of solvothermal synthesis time.

Similar V_2O_5 nanocrystals of a few hundreds of nm in size are obtained in pure water and in the reline/water mixture with a 1:2 molar ratio at 2.5 and 5 h. Interestingly, nanoballs with 1.5-2 μm diameters are only formed in the 1:2 reline/water mixture after 10 h, suggesting that templating agents are formed during the solvothermal treatment of the reline components which interact with the V_2O_5 nuclei. On the other hand, well-defined V_2O_5 blocks with sizes ranging between 20-50 μm are formed in the 1:10 reline/water mixture after only 2.5 h of solvothermal treatment. These blocks swell and exfoliates into nanosheets as the solvothermal treatment time increases.

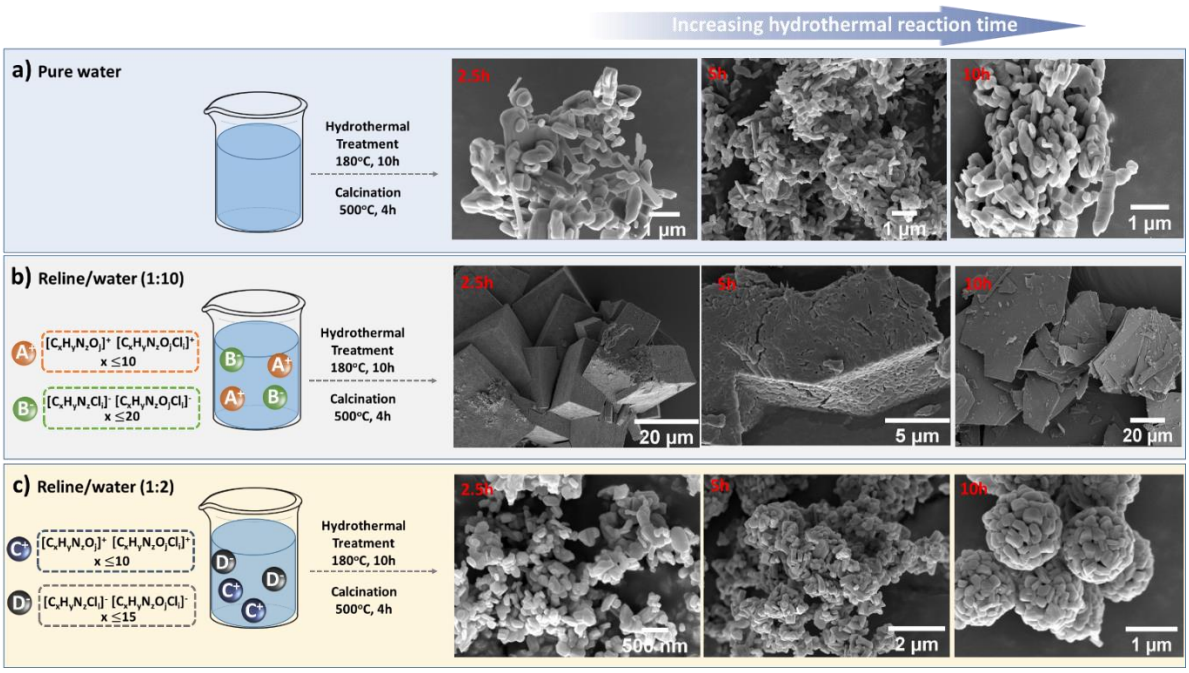

Figure 60: Morphology evolution of nanostructured V_2O_5 as a function of solvothermal time. Electrospray ionization-mass spectroscopy (ESI-MS) is used to identify the formation of alkyl based amine ionic species during the synthesis. a) In pure water, no formation of alkyl amine ionic species; b) In reline/water (1:10), formula of the alkyl amine ionic based species in ESI positive (A^+) and negative mode (B^-); c) In reline/water (1:2), formula of the alkyl amine ionic based species in ESI positive ion (C^+) and negative mode (D^-). SEM micrographs of calcined V_2O_5 samples synthesised in a) pure water, b) reline/water 1:10 molar ratio and c) reline/water 1:2 molar ratio as a function of time (2.5, 5 and 10 h). Samples synthesised under solvothermal conditions at 180 °C for 10 h and calcined at 500 °C for 4 h.

The occurrence of different morphologies of V_2O_5 upon changing the water ratio in reline indicates the potential formation of templating species due to the decomposition of the reline/water solutions at solvothermal conditions.

The thermal decomposition of DES (formed from 1,3 dimethyl urea as the hydrogen bond moiety) at higher temperatures to produce templating agents has been studied previously to synthesize zeolite based materials like aluminium phosphate[311] and open framework materials based on germanium phosphate family[312]. The decomposition of the hydrogen bond donor species like 1, 3 dimethyl urea, 2-imidazoline and tetrahydro-2-pyrimidione are responsible for the template activity of the DES[311]. The importance of water addition to the

DES is shown to accelerate the decomposition of organic templates which reduces the formation time of iron phosphate framework based compounds[313]. However detailed identification of the templating species by decomposing DES or the effect of increasing the water content has not been carried out before.

In order to understand the nature of the compounds formed in the different reline/water mixtures during their thermal treatment, electrospray ionization mass spectroscopy (ESI-MS) analyses are carried out on the reline/water mixtures as shown schematically in Figure 60. For this, reline/water mixtures (both 1:2 and 1:10 molar ratios) are treated at 180 °C for 10 h (without addition of V_2O_5 precursor) in an autoclave and then the solutions are analysed by ESI-MS. In both cases, a number of alkyl based amine ionic species (with the general formula of $[C_xH_yN_zO_jCl_i]^{\pm}$) are formed. Full identification of the formed species is shown in Table 12. The length of the hydrocarbon chain of these species varies with the reline/water molar ratio. With a reline/water molar ratio of 1:2, $C_{4\text{-}15}$ alkyl amines are formed while additional $C_{16\text{-}20}$ amines are also present when the reline/water molar ratio increases to 1:10. The alkyl chain length of the species plays a major role in deciding the morphology of the nanomaterials[314].

Alkyl amine based species are used as templating agents for gold nanomaterials where the length of the alkyl amine is shown to play a crucial role in deciding the final morphologies[315]. Shorter chain length fragments (C_8-C_{10}) give rise to 3D ball like aggregates whereas longer chains gives rise to more polyhedral shapes. In the case of vanadium oxide, nanotubes with tunable walls and cores are synthesized by varying the size of the alkyl amine chain because the chain length controls the inter-layer distance of 1.7-3.8 nm which is similar to the chain lengths of alkyl amines[316]. Nanotubes with thicker walls and smaller inner cores are synthesized with diamine templates in comparison to monoamine moieties. Theoretical calculations have previously suggested that the templating role of organic amines are due to their penetration inside the channel space or interlayers which helps them in playing important roles such as charge balancing and space filling[317,318].

Table 12: List of species from ESI-MS from the hydrothermal decomposition of reline/water solutions (1:2 and 1:10 by molar ratio).

Reline/water (1:2)	Reline/water (1:10)
$[C_4H_{12}NO]^+$	$[C_4H_{12}ON]^+$
$[C_4H_{12}NCl_2]^-$	$[C_4H_{17}NCl_2]^-$
$[C_5H_{14}NO]^+$	$[C_4H_{17}N_2O_5Cl]^-$
$[C_5H_{11}N_4Cl_3]^-$	$[C_5H_{13}NOCl]^-$
$[C_5H_{14}NOCl_2]^-$	$[C_5H_{14}NO]^+$
$[C_6H_{16}O_2N_3]^+$	$[C_5H_{14}NOCl_2]^-$
$[C_7H_{18}O_2N_3]^+$	$[C_6H_{16}NO_2]^+$
$[C_8H_{24}O_2N_2Cl]^+$	$[C_6H_{13}NO_3Cl]^-$
$[C_{10}H_{28}O_2N_2Cl]^+$	$[C_6H_{16}NO_4Cl_2]^-$
$[C_{10}H_{28}O_2N_2Cl_3]^-$ $[C_{10}H_{32}ON_3Cl_4]^-$	$[C_6H_{20}N_2OCl_3]^-$
$[C_{11}H_{34}O_2N_3Cl_4]^-$ $[C_{14}H_{40}O_2N_3Cl_4]^-$	$[C_7H_{26}N_3OCl_4]^-$
$[C_{15}H_{42}O_3N_3Cl_4]^-$	$[C_8H_{24}N_2O_2Cl]^+$
	$[C_{10}H_{27}N_2O_2Cl_2]$
	$[C_{10}H_{27}N_3O_2Cl_2]^+$
	$[C_{10}H_{28}N_2O_2Cl_3]^-$
	$[C_{10}H_{28}N_2O_2Cl]^+$
	$[C_{10}H_{32}N_3OCl_4]^-$
	$[C_{11}H_{34}N_3O_2Cl]^-$
	$[C_{12}H_{29}O_3Cl_2]^-$
	$[C_{14}H_{40}O_2N_3Cl_4]^-$ $[C_{15}H_{41}N_3O_3Cl_3]^-$
	$[C_{15}H_{37}N_3O_3Cl_4]^-$ $[C_{15}H_{42}N_3O_3Cl_4]^-$
	$[C_{18}H_{43}N_3O_3Cl_4]^-$ $[C_{19}H_{45}N_3O_4Cl_4]^-$
	$[C_{20}H_{55}N_4O_4Cl_4]^-$ $[C_{20}H_{51}N_4O_4Cl_5]^-$

Thermal treatment of the 1:2 reline/water molar ratio mixture leads to the formation of short chain alkyl based amine species originating from the choline chloride component of reline ($C_4H_{12}NO^+$/ $C_5H_{14}NO^+$). The formation of these species after 10 h of solvothermal treatment leads to the morphology evolution of V_2O_5 into nanoballs. It is reported that more longer chain lengths prefer less curved surfaces in comparison to shorter chain lengths[314]. This might be the reason that in our case, shorter alkyl chain lengths (less than C_{16}) favour the formation of spherical morphologies whereas the longer chain lengths favour the synthesis of nanosheets.

Interestingly, when the 1:2 reline/water mixture is thermally treated at 180 °C for 10 h prior the addition of the vanadium precursor, no nanoballs formation are observed after 2.5 h of solvothermal treatment (Figure 61a) indicating that along with the alkyl amine species detected by the ESI-MS analysis, the presence of the V_2O_5 precursor is required for the

effective templating effect. This observation shed light on the importance of the interaction of the templating agents with the vanadium nuclei to give the desirable morphologies.

Similar structures have been previously reported in the presence of poly(vinylpyrrolidone) (PVP)[198] with a similar chemical structure $(C_6H_9NO)_n$ which is well known to form micelle-type structures with a number of transition metallic precursor[319,320,321]. A polyol mediated process has been adopted to synthesize V_2O_5 hollow microspheres by using ethylene glycol in the presence of PVP[198]. The introduction of PVP in the synthesis is crucial because PVP (possessing hydrophobic vinyl group and hydrophilic carbonyl group) forms spherical micelles in ethylene glycol with the carbonyl groups on the outside.

Indeed, it is further demonstrated that in the presence of PVP, spherical aggregates of V_2O_5 are obtained in reline/water 1:2 mixtures after 2.5 h as seen in Figure 61b (one should note that V_2O_5 microballs are not formed after 2.5 h in fresh 1:2 reline/water mixtures otherwise). Whereas in the presence of PVP (polyvinyl pyrrolidone), non-uniform nanoballs are observed.

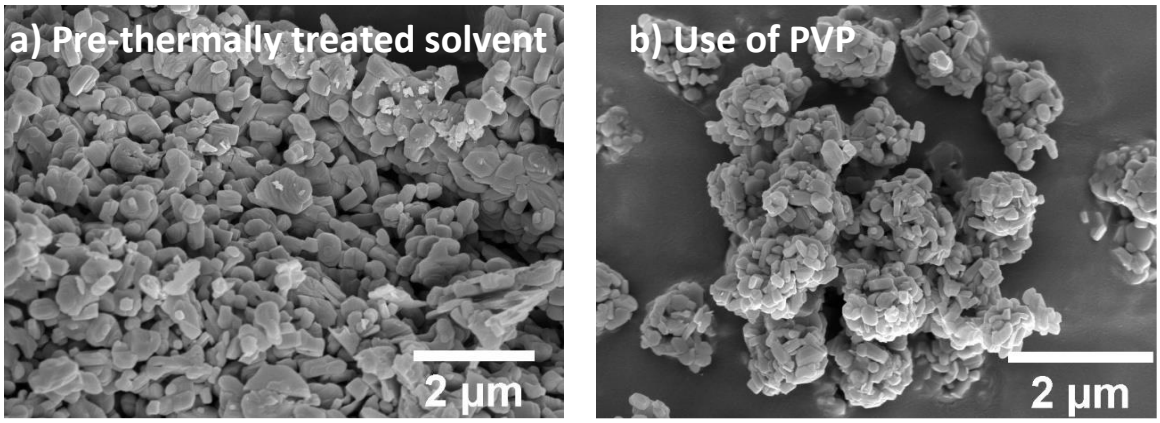

Figure 61: Representative SEM micrographs of calcined V_2O_5 samples to study the interaction of V_2O_5 nuclei with the solvent to control morphologies: a) reline/water (1:2 by molar ratio pre thermally treated for 10 h) followed by 2.5 h synthesis after adding V_2O_5; b) reline/water (1:2 by molar ratio) for 2.5 h with added PVP. All the samples are prepared at 180 °C for 10 h under solvothermal conditions. After preparation, the samples are calcined in air at 500 °C for 4 h at a sweep rate of 10 °C/min.

Similar alkyl amine based species are also formed in the reline/water mixture (1:10) as can be seen from Table 12. A range of short and long chain alkyl amine species are produced

as a result of decomposition of reline/water 1:10 molar ratio solution. The higher water ratio promotes the hydrolysis of urea (component of the DES reline), leading to the formation of V_2O_5 blocks. The subsequent formation of the V_2O_5 nanosheets as the solvothermal time increases, proceeds likely through the osmotic swelling of the V_2O_5 blocks followed by exfoliation. The acidic environment created in the presence of water, as shown above in the 51V NMR in Figure 57, is critical for the protonation of the thermally formed alkyl based amine species which has a high affinity for the vanadium species due to their Brønsted acid nature (NH+….O=V). Such acid-base reactions[322] enable the initial intercalation of short amine ionic species leading to the osmotic swelling of the vanadium blocks observed after 2.5 and 5 h of synthesis (Figure 60). Similar swelling effects are reported for other layered compounds like titanate and clay when a large volume of water (in presence of certain electrolytes) is introduced into the interlayer spacing[323].

Osmotic hydration or osmotic swelling is referred to the behaviour when a large volume of water (in presence of electrolytes) enters the crystal structure gallery resulting in an interlayer spacing of at least 2 nm and exceeding even 20 nm in certain cases[324]. The ultimate stage of this osmotic swelling process is followed by delamination of thin sheets. These thin nanosheets are observed to arrange themselves in a pile like manner because upon the removal of water from the colloidal solution, the most stable configuration for the anisotropic shapes of nanosheets is parallel piling[323]. Swelling of the V_2O_5 blocks causes their elastic deformation, creating inter-layer gaps where longer amines (e.g. $C_{16\text{-}20}$) penetrates leading to its exfoliation into nanosheets[322-325] such as those shown in Figure 62.

Similar morphologies are reported by hydrothermal synthesis of ammonium metavanadate (NH_4VO_3) in oxalic acid[326]. Thin nanosheets of V_2O_5 are produced from bulk VO_2 in a two-step process by liquid exfoliation method: a) intercalation of water molecules into the VO_2 crystals; b) cleavage of the covalent bonds holding the VO_2 layers together. Figure 62 shows the schematic representation of the exfoliation of VO_2 crystals to produce V_2O_5 nanosheets by intercalation of water molecules followed by the cleavage of the covalent bonds.

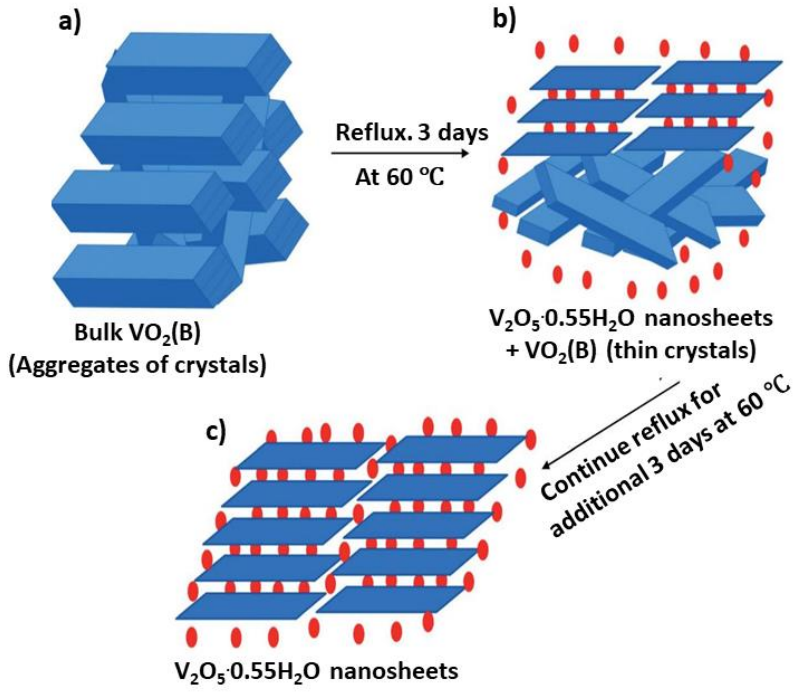

Figure 62: Schematic representation of the exfoliation of V_2O_5 nanosheets from VO_2 crystals (Directly reproduced with permission from reference [326] from the Royal Society of Chemistry). The alkylamine species are represented by the red dots.

Another similar concept known as 'tandem molecular intercalation (TMI)' is proposed to explain the formation of single layers of transition metal chalcogenides (TMCs) in solution phase[325]. According to the TMI concept, the alkyl amine species with shorter chain lengths (also called 'initiator' molecules) opens up the interlayer gap of the TMCs by an intercalation monolayer arrangement. With an increase in time, the long chain alkyl amines (known as 'primary' molecules), adopts a bilayer arrangement to overcome the interlayer forces and hence producing nanosheets ~~as shown in~~. The entry of the primary molecules increases the interlayer gaping.

A previously reported study investigated the role of sugar-based DES comprising of glucose, fructose and sucrose as exfoliating solvents to produce MoS_2 nanosheets[327]. It was found that the DES containing sucrose are the exfoliating solvents due to the larger molecular size in comparison to fructose and glucose and hence these bigger clusters are

able to prevent any van der Waals interactions taking place between the nanosheets on account of steric hindrance[327].

5.4 Effect of V_2O_5 morphologies on Li-ion battery applications

The effect of the different V_2O_5 nanostructured morphologies as cathode materials on Li-ion battery performance is tested by cyclic voltammetry, rate performance analysis and cycling stability at the Institute for manufacturing, University of Cambridge by Dr Changshin Jo and Dr Michael De Volder. All nanostructured V_2O_5 shows faster charge-discharge response than their bulk counterpart. The 2D V_2O_5 nanosheet electrodes exhibits the best cycling and rate performance according to the galvanostatic charge-discharge tests, likely this is due to its higher electrode density and its improved diffusion kinetic promoted by the {001} facet predominant in the 2D morphology.

The V_2O_5 nanosheet electrode shows the most stable cycle performance, with 170 mA h g^{-1} (73.8% retention) after 95 cycles at 250 mA h g^{-1}. The other two V_2O_5 nanomaterials (nanoballs: 141 mA h g^{-1}, 63.6% and nanofleeces: 139 mA h g^{-1}, 66.4%) also deliver better cycle performance compared with that of bulk V_2O_5 electrode (114 mA h g^{-1}, 61.4%). It is reported that fast ion insertion/extraction processes, resulting in fast charge-discharge performance are shown by the {001} phase dominant V_2O_5 nanosheets[328]. The rate performance and charge-discharge profiles of V_2O_5 materials are shown in the Appendix section (A3).

5.5 Conclusions

This chapter presents the development and understanding of a novel facile and surfactant-free green solvent platform for the solvothermal synthesis of nanostructured V_2O_5 using the deep eutectic solvent reline formed by combining choline chloride and urea in the molar ratio of 1:2 respectively.

Upon changing the amount of water in reline, different morphologies of V_2O_5 are obtained such as 3D nanoballs, 2D nanosheet and 1D randomly arranged nanofleece without the addition of any auxiliary reagents. Through advanced electrospray ionization mass spectroscopy, the mechanism of the formation of the different morphologies of V_2O_5 is elucidated. At low reline/water molar ratios (1:2), the *in-situ* formation of short-chain alkylamine species interacts with the vanadium precursor leading to the formation of 3D nanoballs through a templating effect similar to the one created by capping ligands such as polyvinylpyrrolidone (PVP). Increasing the reline water molar ratio (1:10) forms longer chain alkylamine species under solvothermal conditions and consequently, the formation of high quality thin 2D nanosheets by ionic intercalation, osmotic swelling and delamination into thin sheets. This work provides fundamental understanding of the role of DES reline as an exfoliating agent through the formation of alkylamine species rather than the previously hypothesised route of the decomposition of urea to produce ammonium ions, explaining the previously observed role of DES as exfoliating agents for the formation of thin graphene sheets and MoS_2.

Heat treatment at 500 °C also plays a role in the final morphology as the materials are then transformed into crystalized V_2O_5 phase. While the general morphology is still retained after calcination, the smooth surface of the un-calcined samples are transformed into well-defined unit crystals of more than 100 nm sizes due to the release of coordinated water from the V_2O_5 hemihydrate materials.

These nanostructured V_2O_5 materials are tested for Li-ion battery applications as cathode materials in collaboration with Dr Changshin Jo and Dr Michael De Volder at the Institute for Manufacturing, University of Cambridge and these show a faster charge-discharge response than the counterpart bulk-V_2O_5 electrode with V_2O_5 2D nanosheet presenting the highest improvement of the rate performance in galvanostatic charge-discharge tests with 170 mA h g^{-1} after 95 cycles at 250 mA h g^{-1}.

Chapter 6: Synthesis of ceria-zirconia nanomaterials in DES reline

The objective of the previous Chapter 5 was to elucidate the role of reline as a template agent in the synthesis of the transition metal oxide (V_2O_5) by solvothermal synthesis route. Similarly to the results from Chapter 5 for V_2O_5, the group has previously reported the role of reline on the synthesis of nanostructured ceria which provides us with the preliminary understanding on the DES assisted solvothermal synthesis of ceria[155].

In spite of the several advantages offered by nanoceria in areas like catalysis[151], ceramics[329] and photodynamic therapy in cancer treatment[2], ceria exhibits limited usage at higher temperatures such as 700 °C[330] due to sintering that lead to loss of oxygen storage capacity (OSC) and decrease in oxygen ion conductivity[331]. A number of approaches are presented during the last decades to alter the thermal stabilities of ceria, mainly doping it with yttrium and zirconium to enhance the OSC[332]. Indeed it is found that adding dopants into the ceria crystal structure increases the oxygen vacancies, oxygen mobilities and ionic conductivities[333]. Neutron diffraction studies have shown that the oxygen defects are largely responsible for the high OSC in pure ceria which deteriorates largely at higher temperatures. When zirconia is introduced as a dopant, these defects are preserved even at high temperatures of 700 °C[334].

This chapter is focussed on developing a green, eco-friendly solvothermal synthesis method of ceria-zirconia nanorods by using reline-water mixtures as the solvent. Detailed characterization techniques are discussed herein to study the structural properties of the ceria-zirconia samples. CO oxidation is employed as a model reaction to test the catalytic activities of the ceria-zirconia supports and also Au/ceria-zirconia materials.

6.1 Synthesis of nanostructured ceria in DES reline

It has been previously shown by the group that reline plays the role of a supramolecular catalyst in the autoclave based solvothermal synthesis to bring the reactants together by solvent driven pre-organization which facilitates the formation of nanostructured ceria under milder synthesis conditions in comparison to the conventional hydrothermal synthesis routes. Liquid phase neutron diffraction studies show the ready integration of cerium nitrate into the DES matrix to form chelated precursor complexes which offer alternative synthesis routes to produce nanostructured ceria that results in de-intensifying the overall synthesis process[155]. The template delivery roles of the DES to produce 1D structures is attributed to the breakdown of the components of the DES that delivers organic templates to tune the morphologies of the reaction as reported in the literature[335] and also shown in the previous chapters in this thesis.

Further investigations are carried out to understand the effect of DES decomposition to generate template directing species by conducting two synthesis reactions of ceria, one in a closed autoclave based solvothermal synthesis and the other one in an open atmosphere system with the help of a condenser under similar synthesis conditions of reline/water 1:10 molar ratio at 140 °C for 10 h. As can be seen from the TEM micrographs in Figure 63a, ceria nanorods grow as a result of oriented attachment from the ceria nanoparticles that align themselves in a rod like fashion in the solvothermal synthesis route whereas only ceria nanoparticles are obtained in the open atmosphere reactor (Figure 63b). The open atmosphere reactor is chosen to allow the decomposed products to escape. This result indicates the crucial role of the structure directing action of the decomposed products of reline that remains in the solution during the solvothermal method to produce ceria nanorods. In reline, neutron diffraction studies have shown that both the urea and the choline components are involved in hydrogen bonding with the nitrate anions of the cerium nitrate precursor[155]. The formation of the Ce-O bonds from the urea, choline molecules and the cerium nitrate precursor integrates the resulting complex ion product into the hydrogen bonded matrix. This integrated solvent structure is crucial to facilitate the hydrolysis of urea to produce products like CO_3^- and NH_4^+ which are crucial to direct 1D growth.

The use of another DES (known as ethaline formed between ethylene glycol and choline chloride) as the reaction medium have shown no formation of ceria nanorods because of the non-hydrolysability nature of ethylene glycol explaining the lack of decomposition products acting as template agents in the reaction medium. It has been previously proposed by Bakiz *et al.* that the hydrolysable products of urea CO_2 and NH_3 act as surfactants in the synthesis of 1D nanostructured ceria[336]. Hence in our open-atmosphere system, it is possible that CO_2 and NH_3 have escaped and hence there are no structure directing agents.

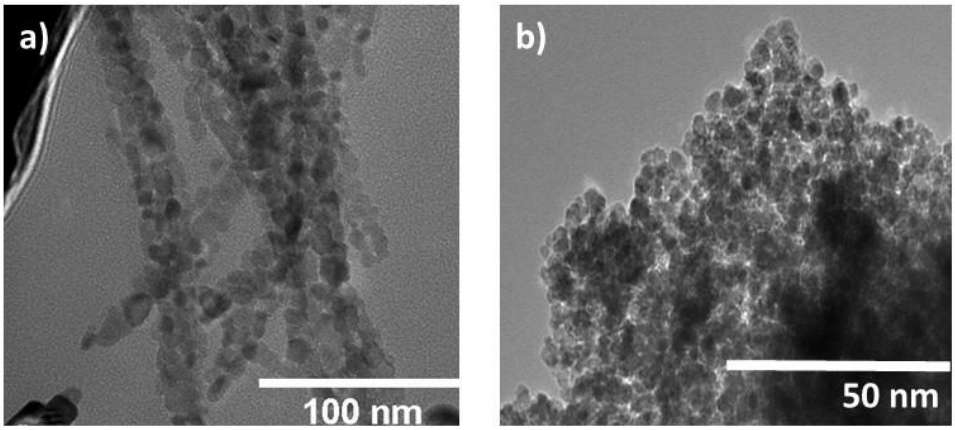

Figure 63: TEM micrographs of nanoceria in reline water 1:10 by molar ratio at 140 °C for 10 h in a) autoclave based solvothermal synthesis reaction and b) open atmosphere system setup. All the samples are calcined at 500 °C for 4 h at a sweep rate of 10 °C/min.

6.2 Synthesis of nanostructured ceria-zirconia materials in reline/water 1:10 systems

A range of ceria-zirconia (CZ) syntheses are carried out by the solvothermal synthesis approach in reline/water 1:10 by molar ratio using $Ce(NO_3)_2.6H_2O$ and $ZrO(NO_3)_2.6H_2O$ as the initial precursors at 140 °C in 10 h. Depending on the ratio of the precursors, these samples are referenced as pure ceria, CZ 80/20 (80% CeO_2 and 20% ZrO_2), CZ 60/40 (60% CeO_2 and 40% ZrO_2), CZ 50/50 (50% CeO_2 and 50% ZrO_2), CZ 20/80 (20% CeO_2 and 80% ZrO_2) and pure ZrO_2.

As can be seen from the TEM micrographs in Figure 64a-e, rod shaped nanomaterials are observed for reline/water 1:10 by molar ratio solvothermal synthesis for pure ceria and CZ samples and nanoparticles for pure ZrO_2. These rod shaped nanomaterials are believed to have grown by the mechanism of oriented attachment of nanoparticles arranged in a rod like order. Some theories are put forward to explain the anisotropic growth of nanorods as a result of oriented attachment of nanoparticles as discussed previously in literature review (Chapter 2): a) aligned nanoparticles collide in the solution; b) these collisions results in the growth of nanorods by restricting the growth in other crystallographic directions[337,338]. In the case of reline, metal oxycarbonates are produced as intermediate species due to the release of CO_3^- and NH_4^+ from the urea hydrolysis during the solvothermal reaction. Upon calcinating the metal oxycarbonates, the corresponding oxides are produced.

1D nano-morphologies of ceria-zirconia structures such as nanorods and nanotubes have been reported previously by other alkaline routes as well[339–342]. Ceria-zirconia nanorods/nanotubes are produced when a higher concentration of NaOH (6-15 M) is used as the solvent during the hydrothermal synthesis as the dissolution-recrystallization kinetics are favourable to drive the $Ce(OH)_3$ and $Zr(OH)_4$ nuclei to grow anisotropically into nanorods[343,342,340,339]. Unlike reline route, precipitation of metal ions as hydroxide species occur under solvothermal conditions when NaOH is employed[344]. Due to the similar values of solubility products for $Ce(OH)_4$ (pKsp= 47.7)[345] and $Zr(OH)_4$ (pKsp=48.2)[346], polynuclear species of ZrO^{2+} and Ce^{4+} ions are precipitated as hydroxides of formulas $[Ce(OH)_m(H_2O)_n]^{4-m}$ and $[Zr(OH)_p(H_2O)_q]^{4-p}$. During the process of solvothermal synthesis, these hydroxide species are further co-mingled to produce hydrated (Ce, Zr)-hydroxides ($[(Ce_{1-x}Zr_x)(OH)_y(H_2O)_z]^{4-y}$) which undergo dissolution-crystallization reactions to form ceria-zirconia complexes[347].

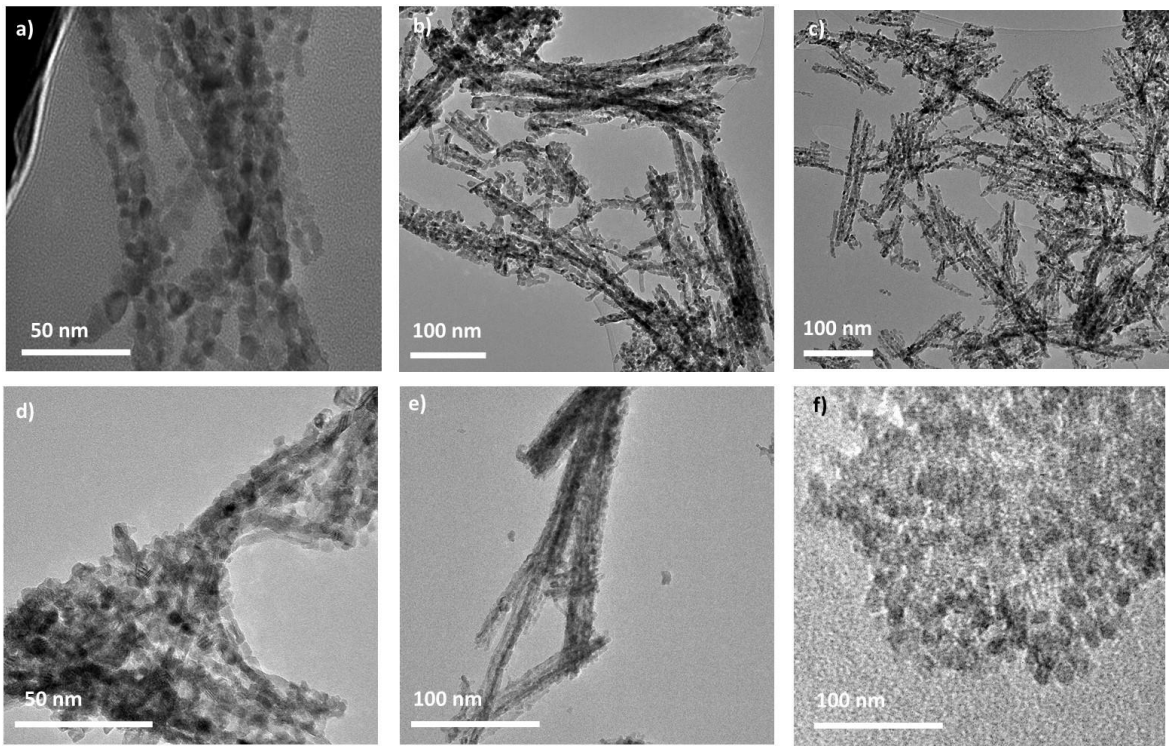

Figure 64: TEM micrographs of a) pure ceria, b) CZ 80/20, c) CZ 60/40, d) CZ 50/50, e) CZ 20/80 and f) pure zirconia. All the samples are prepared in reline/water 1:10 by molar ratio in solvothermal synthesis at 140 °C for10 h. The samples are calcined at 500 °C for 4 h at a sweep rate of 10 °C/min.

Previous reports show the growth of 1D nanorods of semiconductors[348], Co-Pt[349] and chalcogenide[350] based materials in imidazolium based IL and DES reline. The authors suggest the templating role of amines in the IL and DES to play an important role towards morphology control.

Qualitative elemental mapping using energy dispersive spectroscopy (EDS) technique is used to identify the distribution of ceria, zirconia and oxygen in one of the CZ sample (CZ 60/40) as shown in Figure 65. Detailed composition of the CZ samples are investigated by XPS studies (discussed in Section 6.2.1).

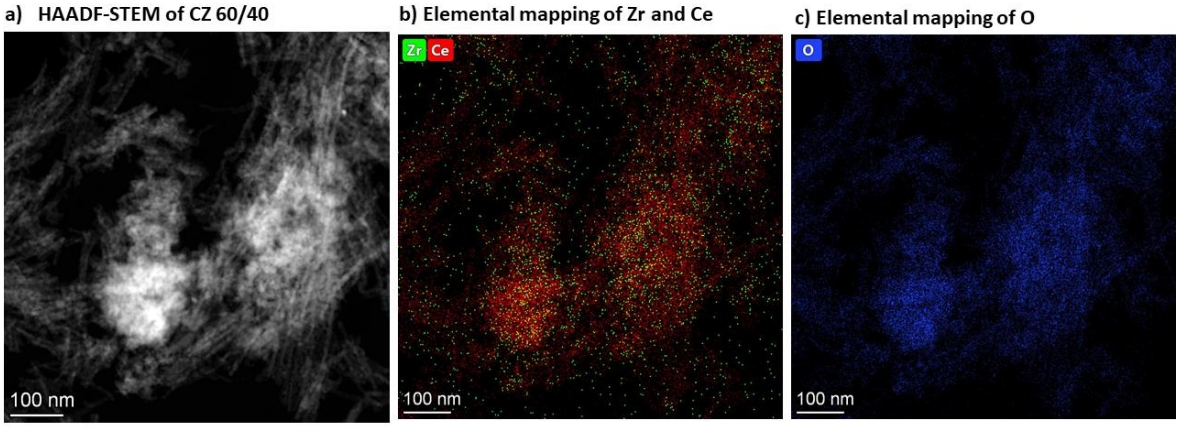

Figure 65: a) HAADF micrographs of CZ 60/40, b) elemental mapping using EDS for cerium and zirconium in CZ 60/40 and c) elemental mapping using EDS for oxygen in CZ 60/40. The sample is prepared in reline/water 1:10 by molar ratio in solvothermal synthesis at 140 ℃ for 10 h. The sample is calcined at 500 ℃ for 4 h at a sweep rate of 10 ℃/min.

6.2.1 Characterization of ceria-zirconia compounds

Several characterization techniques are employed to carry out detailed structural characterization of the as-synthesized ceria-zirconia samples.

XRD patterns of pure ceria, ceria-zirconia (CZ) and pure zirconia are shown in Figure 66a. The diffraction 2Θ peaks for pure ceria and all the CZ samples at 28.5°, 33.0°, 47.5°, 26.15° and 56.50° are well indexed to the lattice planes corresponding respectively to {111}, {200}, {220} and {311} of pure ceria with space group Fm3m (JCPDS database (75-0162)). The X-ray diffraction peaks for pure ZrO_2 in Figure 66a at 24.20°, 28.20°, 31.50°, 34.50°, 49.50° and 50.20° are well indexed to the monoclinic crystalline phase of ZrO_2 (JCPDS card number 37-1484) corresponding respectively to {110}, {111} and {002} lattice planes of monoclinic ZrO_2 respectively[161].

All the CZ samples exhibit XRD patterns corresponding to the cubic fluorite structure of pure ceria. None of the distinct XRD signature peaks for free ZrO_2 are observed in these CZ samples which are in accordance to the literature reports pertaining to the formation of well-defined homogeneous Zr-doped ceria structures[351,352]. It is believed that due to an intimate interaction between the Ce-oxide and Zr-oxide, free peaks of ZrO_2 are not observed in the CZ oxides[353]. Slight shifts in the peak positions towards higher 2Θ values

are observed in the XRD spectra upon Zr incorporation (zoomed spectra of the XRD peak for pure ceria and CZ samples positioned around 28° in Figure 66b). The diffraction lines for CZ-20/80 are slightly asymmetric at 28° (as the peak is slightly shifted towards lower theta values rather than higher values). This asymmetry has been attributed to the mixture of phases or phase segregation in CZ-20/80 previously[354].

Upon incorporation of zirconia in the ceria lattice, a decrease in the coherent diffraction domain size is observed as calculated from the Scherrer formula for the peak centred around 28.5°- Pure ceria (9.9 nm)> CZ 80/20 (7.3 nm)> CZ 60/40 (7.2 nm)> CZ 50/50 (6.8 nm) > CZ 20/80 (6.1 nm). This decrease in the coherent diffraction domain size is attributed due to the lattice shrinkage on account of the incorporation of the smaller Zr^{4+} cation (0.084 nm) in the ceria lattice compared to Ce^{4+} (0.097 nm)[355]. With an increase in the zirconia content, a decrease in the domain size is observed due to the greater number of smaller Zr^{4+} cations in the ceria lattice. By using the Scherrer equation, we obtain information about the coherent diffraction domain size, which is defined as the domain perpendicular to the diffraction peak being analysed instead of measuring the crystallite size (i.e. a combination of multiple domains)[232].

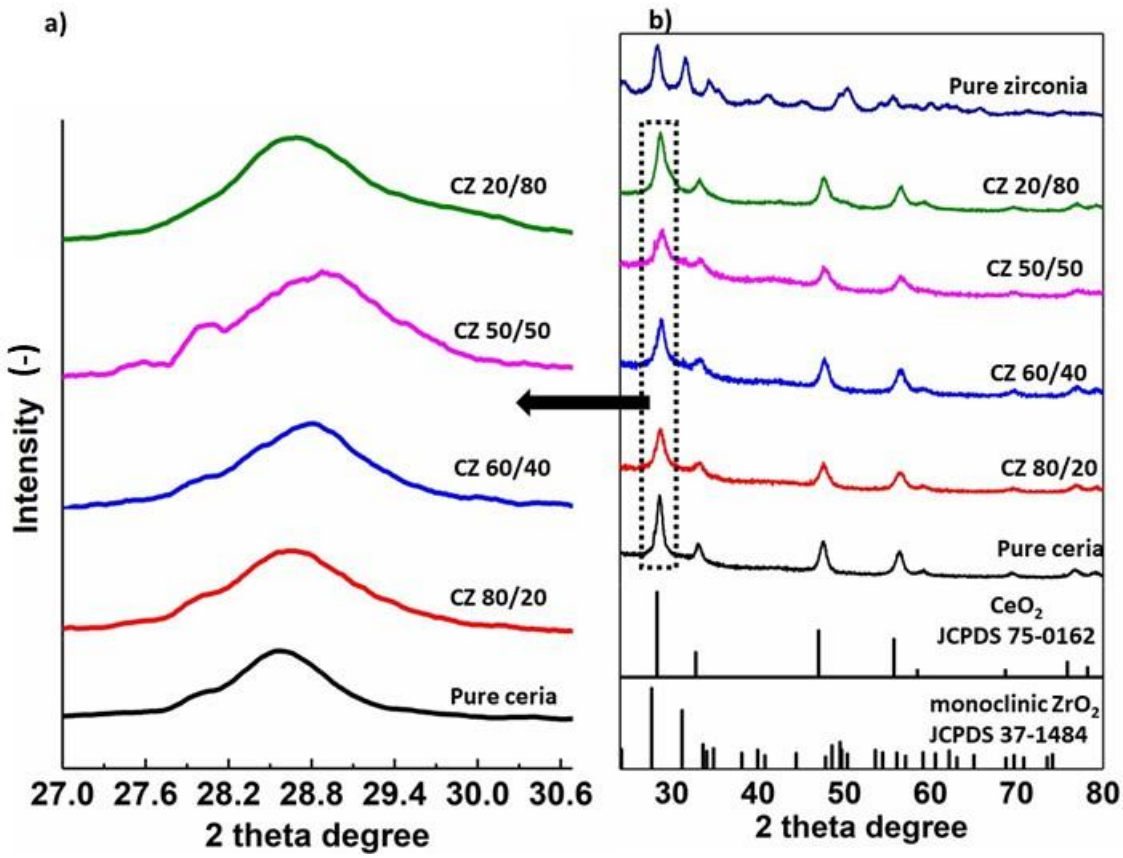

Figure 66: a) zoomed peak of XRD pattern of pure ceria and CZ samples centred at 28.5°; b) XRD patterns of pure ceria, CZ and pure zirconia samples. All the samples are prepared in reline/water 1:10 by molar ratio in solvothermal synthesis at 140 °C for 10 h. The samples are calcined at 500 °C for 4 h at a sweep rate of 10 °C/min.

Raman spectroscopy is a complementary tool in addition to XRD to study the crystal structures. Raman provides greater details regarding oxygen vacancies, lattice vibrations and anion positions by probing the vibrational bonds of the crystalline material which is otherwise not possible by XRD[356].

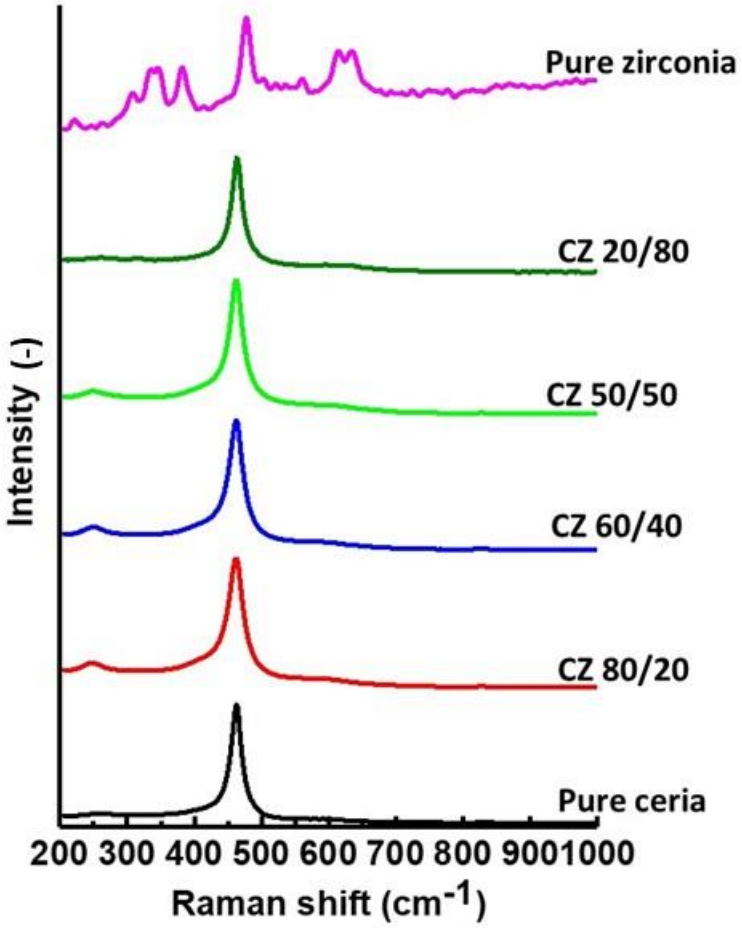

Figure 67: Raman spectra of pure ceria, CZ samples and pure zirconia samples. All the samples are prepared in reline/water 1:10 by molar ratio in solvothermal synthesis at 140 ℃ for 10 h. The samples are calcined at 500 ℃ for 4 h at a sweep rate of 10 ℃/min.

In pure ceria, the sharp peak at 465 cm^{-1} corresponds to the F_{2g} Raman mode of the fluorite structures attributed to the O-Ce-O stretching (Figure 67)[357,358]. The other CZ samples also exhibits a sharp peak at 465 cm^{-1} denoted for symmetric breathing mode of the oxygen atoms around cerium ions[359,360]. A small shoulder peak at 600 cm^{-1} is reported to be an indication of oxygen vacancies in the ceria lattice[361]. The slight peak at around 250 cm^{-1} for the CZ samples is due to the displacement of oxygen due to doping with zirconia in the ceria lattice[357]. For pure ZrO_2, the Raman band positions at 349, 383, 479, 507, 536, 569, 622 and 647 cm^{-1} corresponds to the monoclinic phase of ZrO_2[362].

The absence of free ZrO_2 peaks in Raman pattern for the CZ samples are in accordance to the previous literature findings that indicates homogeneous distribution of ceria and

zirconia in the CZ samples[363,364]. The Raman spectra also matches the XRD spectra (Figure 66a) which shows the lack of any ZrO_2 signature peaks in the CZ samples.

Information on surface area and porosity values for powder samples are usually obtained by carrying out nitrogen adsorption-desorption studies at liquid nitrogen temperatures (77 K). The surface areas calculated from the N_2 adsorption-desorption isotherms for pure ceria, CZ samples and pure zirconia are shown in Table 13.

Table 13: Nitrogen adsorption-desorption isotherms of pure ceria, CZ and pure zirconia samples. All the samples are prepared in reline/water 1:10 by molar ratio in solvothermal synthesis at 140 °C for 10 h. The samples are calcined at 500 °C for 4 h at a sweep rate of 10 °C/min.

Sample	Surface area (m^2/g)
Pure ceria	60
CZ- 80/20	51
CZ-60/40	57
CZ-50/50	68
CZ-20/80	45
Pure zirconia	51

All the samples are mesoporous in nature in accordance to the IUPAC type IV isotherms. Samples with pore sizes between 2-50 nm are commonly known as mesoporous. In these samples, the samples are thought to have inter-particle porosity. As the HR-TEM micrographs did not show any traces of pores, hence it is likely that intra-particle porosity is absent. A hysteresis is usually observed in the isotherms due to the dissimilarity in the nitrogen adsorption and desorption processes. Nitrogen adsorption occurs by the formation of a monolayer, then multilayer followed by capillary condensation of nitrogen in the pores. During desorption, some of the nitrogen may get trapped in the pores and hence the number of nitrogen molecules adsorbed is not similar to those desorbed. The highest surface area of 68 m^2/g is observed for CZ 50/50. No significant difference in surface area is observed as the Ce/Zr ratio varies.

The ceria-zirconia samples are characterized by temperature programmed reduction (TPR) technique from ambient temperature conditions till 1000 °C under hydrogen flow.

The TPR in Figure 68 shows two broad peaks centred around 500 ℃ and 750 ℃ for the ceria-zirconia solid samples corresponding to the reduction of surface oxygen and lattice oxygen respectively[151]. The mechanism of the ceria reduction occurs in two steps[365,151]. In the first step, surface oxygen is reduced by hydrogen to produce water. In the second step at higher temperature, sufficient energy is available for the lattice oxygen to migrate to the surface and get reduced by hydrogen to form water. These peaks comprise of several overlapping peaks (Gaussian is the line shape function) which are deconvoluted using Origin plotting software. The presence of non-uniform peaks within the surface oxygen reduction peak are due to the different crystal phases of ceria gradually reducing at different temperatures[366]. These peaks are further integrated to calculate the peak area to determine lattice and surface oxygen concentrations.

As the zirconia content increases in ceria, the peak associated to the reduction of lattice oxygen shifts to lower temperatures for example in pure ceria, the peak for reduction of lattice oxygen is observed at 760 ℃ and as the amount of zirconia increases in the CZ samples, the reduction temperature gradually shifts to lower values of 744 ℃ (CZ-80/20), 742 ℃ (CZ- 60/40), 732 ℃ (CZ- 50/50) and finally 736 ℃ (CZ- 20/80) (Table 14). Such findings on the shifting of the reduction peak for lattice oxygen in ceria-zirconia samples agree with previous observations[367]. The lowering in temperature of the lattice oxygen peak is due to the higher mobility and bulk diffusion of oxygen to the surface on account of the defects introduced in the ceria lattice by zirconia incorporation[368]. An increase in the oxygen mobilities is observed on increasing the zirconia content due to the smaller size of Zr^{4+} in comparison to Ce^{4+} leading to lattice shrinkage.

In order to quantify the hydrogen consumption for the samples, the area under the reduction peaks for surface and lattice oxygen are calculated by integration using the Origin software. Upon increasing the amount of zirconia in the ceria-zirconia samples, an increment in the ratio of surface oxygen to lattice oxygen is observed from 0.48 in pure ceria to 1.41 in CZ 20/80 (Table 14 and Figure 68). Incorporation of the Zr ions introduces more defects in the cubic fluorite structure of ceria that promotes the migration of lattice oxygen to the surface and hence the surface oxygen to the lattice oxygen ratio increases[369]. The TPR profile of CZ-20/80 sample (Figure 68e) is slightly different from the other CZ

samples and pure ceria as the relative intensity for hydrogen consumption of the second reduction peak (due to reduction of lattice oxygen) is lower than the first peak for surface oxygen reduction. This decrease in the intensity of the hydrogen consumption for the lattice oxygen is due to lower amounts of bulk ceria available compared to bulk zirconia in CZ- 20/80 sample[370].

Table 14: Reduction temperatures for surface oxygen and lattice oxygen for pure ceria and CZ samples obtained from temperature programmed reduction (TPR) technique.

Sample	Reduction temperature for surface oxygen (°C)[a]	Reduction temperature for lattice oxygen(°C)[a]	Ratio of surface oxygen to lattice oxygen[b]
Pure ceria	411, 485	760	0.48
CZ 80/20	432, 497	744	0.62
CZ 60/40	405, 486	742	0.64
CZ 50/50	407, 495	732	1.05
CZ 20/80	503, 542	736	1.41

[a] Reduction temperature calculated from temperature programmed reduction.

[b] Ratio calculated by integrating the area under the peaks for surface oxygen to lattice oxygen.

All the samples are prepared in reline/water 1:10 by molar ratio in solvothermal synthesis at 140 °C for 10 h. The samples are calcined at 500 °C for 4 h at a sweep rate of 10 °C/min.

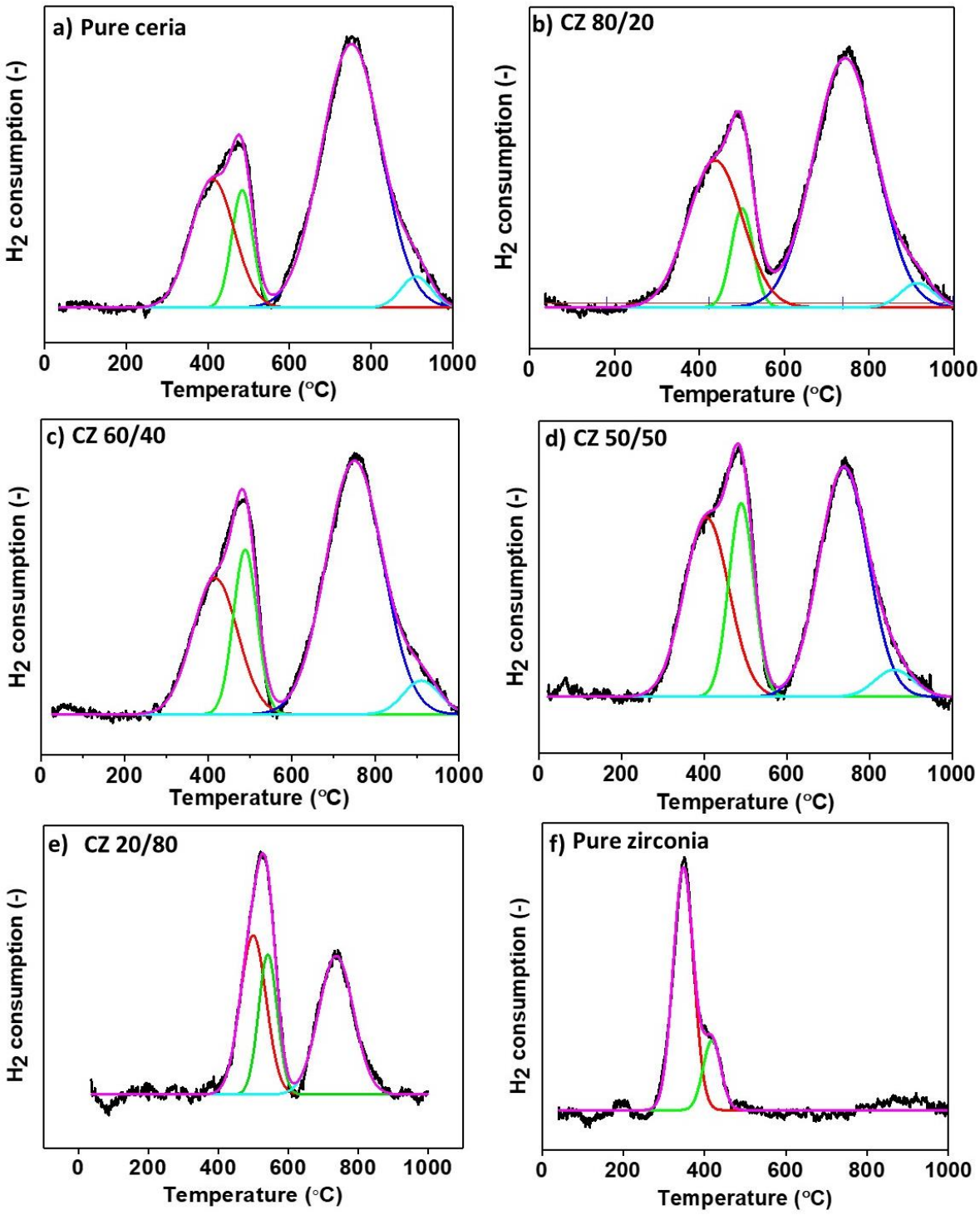

Figure 68: Temperature programmed reduction (TPR) profile of a) pure ceria, b) CZ 80/20, c) CZ 60/40, d) CZ 50/50, e) CZ 20/80 and f) pure zirconia. All the samples have been prepared in reline water 1:10 by molar ratio in solvothermal synthesis at 140 °C for 10 h. The samples are calcined at 500 °C for 4 h at a sweep rate of 10 °C/min.

X-ray photoelectron spectroscopy (XPS) studies are carried out to determine the oxidation state of cerium, phase homogeneities and the atomic ratios of Ce/Ce+Zr in the CZ samples. The XPS spectra is shown in Figure 69.

The XPS peaks of the CZ samples corresponds to the peaks of core level Ce3d, Zr3d and O1s as reported elsewhere[371]. As shown in Figure 69a-b, the complex XPS spectrum of Ce3d comprises of $Ce3d_{5/2}$ and $Ce3d_{3/2}$ peaks which are denoted by u and v respectively. The peaks labelled as u, u', u'' and u''' at 900.6 eV, 903.1 eV, 909.8 eV and 914.5 eV corresponds to the main peaks of $Ce3d_{3/2}$. Further the peaks labelled as v, v', v'' and v''' at 880.6 eV, 884.9 eV, 891.0 eV and 898.6 eV matches the main peaks of $Ce3d_{5/2}$. The $3d^{10}4f^0$ electronic state of Ce^{4+} is represented by the peaks of u''' and v''' whereas the $3d^{10}4f^1$ electronic state of Ce^{3+} is been shown by the u' and v' peaks. These spectra results show that both the +3 and +4 oxidation state of cerium is present. The peaks at 182.6 and 184.9 eV belongs to the $Zr3d_{5/2}$ and $Zr3d_{3/2}$ respectively of Zr^{4+} in Figure 69c. The peak at 529 eV corresponds to O1s of the pure ceria, CZ and pure zirconia samples (Figure 69d).

The relative surface content of Ce^{3+} to the total Ce content is calculated from the integrated peak areas of the Gaussian fitted peaks from the XPS data of Ce3d. The percentage of Ce^{3+} is highest for CZ 80/20 and CZ 60/40 (36.8% and 33.7% respectively) as shown in Table 15. In order to get an idea of the dispersion of Ce and Zr in the CZ samples, Ce/Ce+Zr ratios are calculated. The higher values of Ce/Ce+Zr samples is because the surface of CeO_2-ZrO_2 is CeO_2 enriched, which are also in accordance with the reports published elsewhere[355]. The surface enrichment of ceria maybe attributed due to the vaporization of $ZrCl_4$. Similar observations of ceria enrichment for CZ samples were reported by Masui *et al*. where the authors prepared CZ samples using ammonium chloride as the reducing agent[372]. $ZrCl_4$ has an extremely high vapour pressure at 327 °C and hence could be removed easily (as in our case the calcination temperature is 500 °C). Whereas $CeCl_3$ has a low vapour pressure and oxidizes to form CeO_2 at the same temperature. In our case, as reline contains chlorine (from choline chloride) and ammonia is release due to the decomposition of urea, we believe that a similar mechanism of Zr volatilization occurs that leads to ceria enrichment of the CZ samples. The atomic% of Zr and Ce are shown in Table 15.

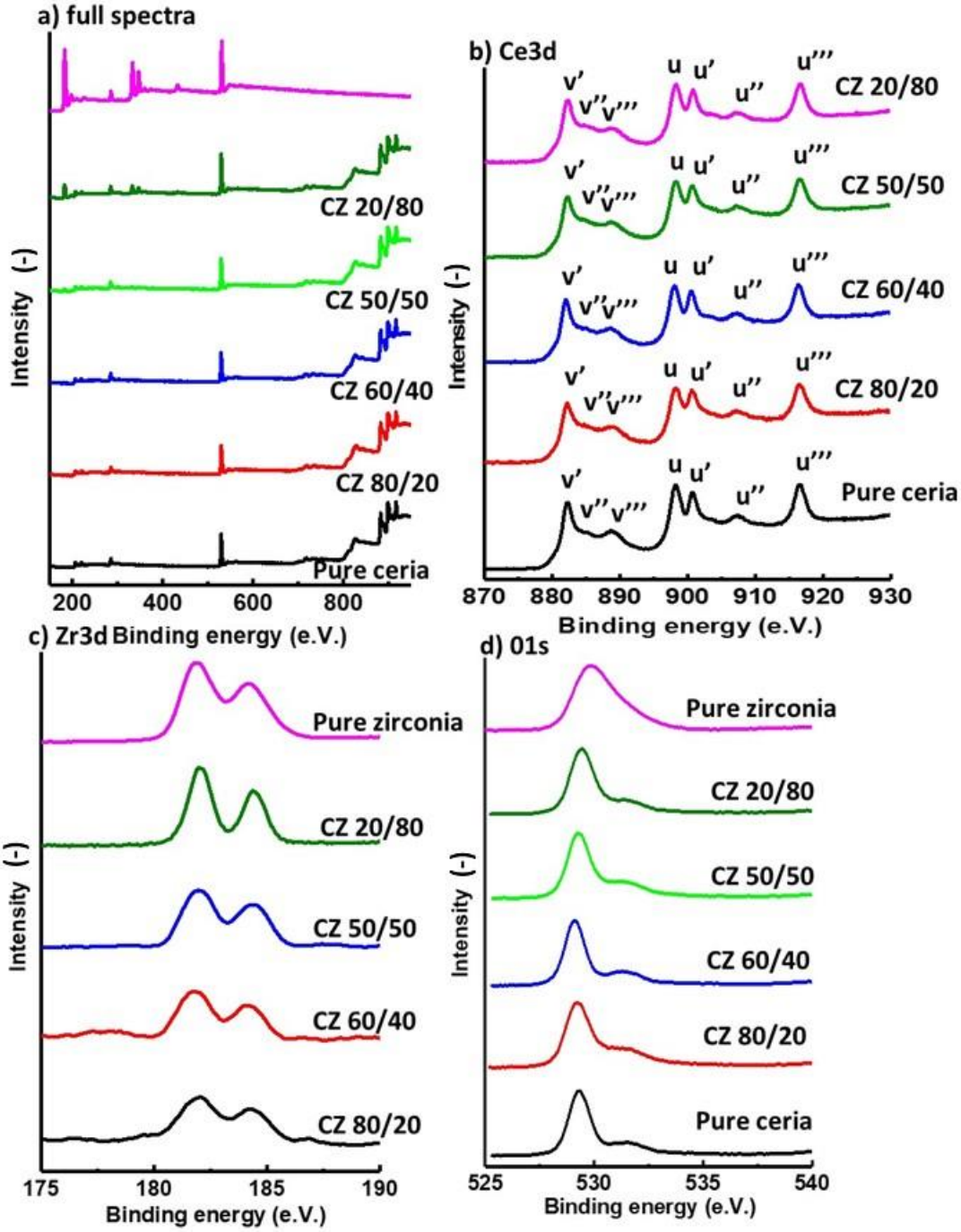

Figure 69: XPS spectra of a) full spectra of pure ceria, CZ and pure zirconia samples, b) Ce3d, c) Zr3d and d) O1s. All the samples are prepared in reline/water 1:10 by molar ratio in solvothermal synthesis at 140 ℃ for 10 h. The samples are calcined at 500 ℃ for 4 h at a sweep rate of 10 ℃/min.

Table 15: Summary of results from XPS data for pure ceria, CZ and pure zirconia samples.

Sample name	Zr $3d_{5/2}$ (at%)	Ce $3d_{5/2}$ (at%)	Ce/Ce+Zr[a]	$(Ce^{3+}/Ce^{3+}+Ce^{4+})$[b]
Pure ceria	-	12.54	1	14
CZ 80/20	0.67	12.58	0.97	37
CZ 60/40	0.51	12.21	0.97	34
CZ 50/50	1.54	12.29	0.92	29
CZ 20/80	8.56	8.75	0.61	11
Pure zirconia	27.24	-	0	-

[a] Calculated by multiplying the atomic ratios of Ce and Zr with their respective molecular weight.
[b] Calculated from the area under the curves.

All the samples have been prepared in reline/water 1:10 by molar ratio in solvothermal synthesis at 140 ℃ for 10 h. The samples are calcined at 500 ℃ for 4 h at a sweep rate of 10 ℃/min.

6.3 Ceria-zirconia as catalysts for CO oxidation

CO oxidation is used as a model reaction to test the catalytic activities of the ceria- zirconia samples that are prepared by the reline/water 1:10 by molar ratio assisted solvothermal synthesis route. All the samples are pre-reduced *in-situ* in the CO rig at 200 ℃ under hydrogen flow. The rate of CO conversion is calculated by monitoring the CO concentration at the outlet of the reactor. The experimental set-up, analysis conditions and data calculations are explained in detail in Chapter 3 (materials and methods).

6.3.1 Activities of the ceria-zirconia catalysts for CO oxidation

As can be seen in Figure 70a, the initial catalytic activity for all the samples except pure zirconia are observed to begin at 300 ℃. CZ-80/20 and CZ-60/40 exhibits the best catalytic activities as they show the highest rate in Table 16. Pure zirconia shows the poorest CO conversion rates of just 3% during the whole range of temperature tested till 625 ℃. Pure ceria, CZ-50/50 and CZ-20/80 supports exhibits 93%, 90% and 64% CO conversion respectively within the maximum temperature tested range of 625 ℃. The activation energies and temperature for 50% CO conversion achieved by the samples are shown in Table 16b.

The rates $mol_{CO2}g_{cat}^{-1}s^{-1}$ for pure ceria and CZ catalysts at 400 ℃ are calculated as follows: pure ceria (0.10×10^{-3}), CZ 80/20 (0.29×10^{-3}), CZ 60/40 (0.28×10^{-3}), CZ 50/50 (0.11×10^{-3})

and CZ 20/80 (0.03×10^{-3}) as shown in Table 16. It can be seen that CZ-80/20 and CZ-60/40 exhibits the highest rates.

Table 16: Summary of the temperatures for 50% CO conversion, activation energies and rate for the samples. All the samples are prepared in reline/water 1:10 by molar ratio in solvothermal synthesis at 140 °C for 10 h. The samples are calcined at 500 °C for 4 h at a sweep rate of 10 °C/min.

Sample type	T_{50} (°C)[a]	Activation energy (kJ/mol)[b]	$mol_{CO_2}g_{cat}^{-1}s^{-1}$ at 400 °C
Pure ceria	508	185	0.10×10^{-3}
CZ- 80/20	445	88	0.29×10^{-3}
CZ-60/40	451	94	0.28×10^{-3}
CZ-50/50	512	121	0.11×10^{-3}
CZ-20/80	589	151	0.03×10^{-3}
Pure zirconia	-	-	-

[a] Temperature at which 50% CO conversion is achieved,
[b] Activation energies as calculated from the Arrhenius plot.

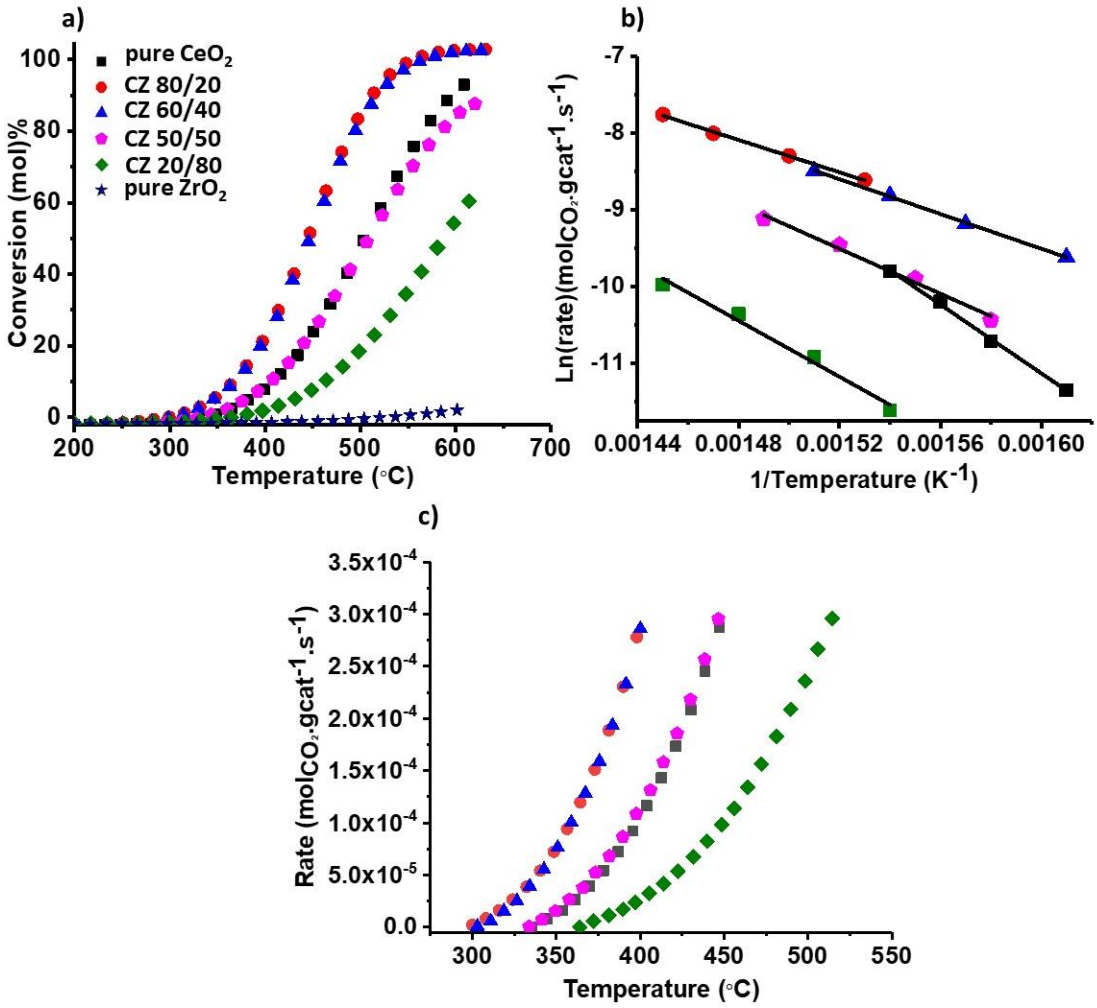

Figure 70: a) CO conversion (mol)% as a function of temperature for ceria-zirconia supports: pure ceria, CZ 80/20, CZ 60/40, CZ 50/50, CZ 20/80 and pure zirconia, b) Arrhenius plots to calculate the activation energies for different samples: pure ceria, CZ 80/20, CZ 60/40, CZ 50/50 and CZ 20/80 and c) rate vs temperature plot. All the samples are prepared in reline/water 1:10 by molar ratio in solvothermal synthesis at 140 ℃ for 10 h. The samples are calcined at 500 ℃ for 4 h at a sweep rate of 10 ℃/min.

The activation energies are calculated for the different samples with the help of the Arrhenius equation in Figure 70b. CZ 80/20 and CZ 60/40 exhibits the lowest activation energies of 88 KJ/mol and 94 KJ/mol respectively of all the materials. The high rates and lower activation energies of CZ 80/20 and CZ 60/40 can be explained on the basis of results from XPS and Raman studies. Oxygen vacancies are considered to be crucial for CO oxidation as these act as active sites for oxygen (diamagnetic) activation by the

formation of superoxide (O^-_2 is paramagnetic) and peroxide (O^{2-}_2 are diamagnetic) species as detected by the electron paramagnetic resonance (EPR) studies[373,374]. The adsorption of O_2 on ceria surface leads to the formation of superoxide species[375]. Superoxide species have been shown to be quite reactive for CO oxidation as CO could be directly oxidized to CO_2 by superoxide without an activation barrier. Superoxides usually transform to peroxides and the peroxide species initiates the formation of carbonates when CO reacts with peroxides. The role of oxygen vacancies in the CO oxidation mechanism has been discussed previously in the literature review (Section 2.7). As mentioned previously from the XPS data in Section 6.2.1 that the highest fraction of Ce^{3+} cations is available for CZ 80/20 and CZ 60/40 of 37% and 34% respectively (Table 17). This implies that CZ 80/20 and CZ 60/40 has the highest oxygen vacancies on their surface as it is shown in the literature that the presence of Ce^{3+} is associated to the oxygen vacancies formation[376,377]. According to energetic calculations, formation of an oxygen vacancy in pure ceria requires 4.55 eV in comparison to just 0.26 eV next to a pair of Ce^{3+} atoms[378]. The concentration of the oxygen species in the CZ samples is also calculated from the two peaks as seen in the O1s XPS spectra. The high binding energy peak centred around 531-532 eV (O_β) corresponds to oxygen vacancies and the low binding energy peak at 529.0-530.5 eV (O_α) is ascribed to lattice oxygen[7]. It is possible to assess the amount of oxygen vacancies by calculating O_β/O_α. The samples which exhibit the highest O_β/O_α are CZ 80/20 (57%) and CZ 60/40 (39%) as seen in Table 17.

Information on the concentration of oxygen vacancies is also obtained from the full width half maximum (FWHM) of the main Raman band[379] centred at 426 cm^{-1}. An increase in the value of FWHM is an indication of the higher oxygen vacancies available. CZ 80/20 and CZ 60/40 exhibits the highest value of FWHM of 46 and 31 cm^{-1} respectively (Table 17). Additionally, the intensity ratios of the peak at 600 cm^{-1} and 460 cm^{-1} (I_{600}/I_{460}) from the Raman spectra also provides the concentration of oxygen vacancies in the samples[379]. This is because the shoulder at 600 cm^{-1} is an indication of the oxygen vacancies available in the crystal lattice[361]. The highest values of I_{600}/I_{460} is observed for CZ 80/20 and CZ 60/40 (Table 17). These results from XPS and Raman show that the highest concentration of oxygen vacancies is available in CZ 80/20 and CZ 60/40.

Table 17: Summary of the characterization results from XPS and Raman spectra.

Sample name	Ce^{3+} (at%)[a]	O_α (at%)[a]	O_β (at%)[a]	O_β/O_α (at%)[a]	FWHM(cm^{-1})[b]	I_{600}/I_{460} (at%)[b]
Pure ceria	14%	77	22	28	29	0.029
CZ 80/20	37%	63	36	57	46	1.73
CZ 60/40	34%	67	26	39	31	1.16
CZ 50/50	29%	86	14	16	30	0.822
CZ 20/80	11%	75	24	32	18	0.018

[a] Determined from XPS spectra.
[b] Calculated from Raman spectra.

Linsebigler *et al.* explained that during CO oxidation reactions over metal oxide supports, the O moiety of CO interacts with the anion vacancy site whereas binding of C from CO on the metal oxide lattice sites facilitates primary adsorbate binding[380]. Ab-initio calculations point that the availability of extra electron density in an oxygen vacancy site (due to the removal of oxygen) increases the back-donation to the empty π* orbitals of CO adsorbed at these sites[381]. The creation of the structural defects are enhanced upon the incorporation of Zr^{4+} in the ceria lattice which increases the mobilities of oxygen sites[382].

For the same amount of catalyst, the CO conversion might have intuitively being expected to increase with the surface area because this is a surface reaction. However catalytic activities does not only depend on surface areas but on several other factors like stoichiometry and oxygen vacancies[379].

The rate $mol_{CO2}g_{cat}^{-1}s^{-1}$ for our catalysts are also compared with the other ceria-zirconia catalysts in the literature in Table 18.

Table 18: Comparison of the catalytic activities for CO oxidation of the different ceria-zirconia catalysts reported in the literature with respect to our sample.

Ref	Sample	Conversion%	$mol_{CO2}g_{cat}^{-1}s^{-1}$	Temperature (°C)[a]
Our work	Pure ceria	8	0.10×10^{-3}	400
	CZ 80/20	20	0.29×10^{-3}	400
	CZ 60/40	22	0.28×10^{-3}	400
	CZ 50/50	9	0.11×10^{-3}	400
	CZ 20/80	2	0.03×10^{-3}	400
[383]	Pure ceria	70	0.22×10^{-5}	400
	CZ 80/20	38	0.55×10^{-5}	400
	CZ 50/50	28	0.42×10^{-5}	400
	CZ 15/85	18	0.27×10^{-5}	400

[363]	CZ 75/25	80	0.27×10^{-5}	400
	CZ 50/50	70	0.24×10^{-5}	400
	CZ 25/75	18	0.06×10^{-5}	400
[384]	Pure ceria	18	0.22×10^{-5}	300
	CZ 10/90	22	0.27×10^{-5}	300
	CZ 25/75	25	0.30×10^{-5}	300
	CZ 50/50	21	0.26×10^{-5}	300
[385]	CZ 75/25	20	0.81×10^{-7}	351

[a] Reaction temperature.

Table 18 presents a summary of the catalytic activities of ceria-zirconia nanostructured materials reported in the literature for CO oxidation reaction. Despite of the different reaction conditions or synthesis procedures in the preparation of these CZ samples, ~~yet~~ there seems to be a general consensus on the reactivity trends of the samples i.e. the highest activities are shown when the ceria ratios in the CZ samples are between 50-80% (samples labelled in Table 18 as CZ50/50 to CZ 80/20). It is clear from the rates that incorporation of zirconia up to a certain extent (about 20-50%) is hence beneficial to increase the CO oxidation activities of the CZ sample in comparison to pure ceria. Boaro *et al.* proposed that a higher concentration of oxygen vacancies in the CZ material is beneficial for CO oxidation due to the increase in the diffusion of oxygen in ceria[383]. Although there is a lack of general agreement in the literature about the right content of zirconia in ceria in order to achieve the highest rates for CO oxidation activities[386], still Trovarelli *et al.*[387] established CZ 80/20 as the most stable composition for CO oxidation which also matches with our findings. Masahiro explained the influence of cation coordination of cerium ions via oxygen ions in CZ materials on the oxygen storage capacities[388]. For pure ceria, under reductive environment, even if Ce^{4+} changes to Ce^{3+} but due to the bigger size of Ce^{3+}, any further valence change is limited. Whereas if the cerium ions are surrounded by the Zr^{4+} ions via oxygen ions, expansion of the crystal lattice resulting in a higher oxygen storage capacity is possible due to the smaller ionic radii of Zr^{4+}(0.084 nm) in comparison to Ce^{3+}(0.114 nm). In this work, the TPR results discussed in the previous Section 6.2.1 also show that the ratio of surface oxygen to lattice oxygen increases as the concentration of Zr increases in the CZ samples which supports Masahiro's argument. The activity rates of the CZ catalysts prepared in this work by the reline assisted solvothermal synthesis routes shows higher rates than other reported in the

literature till date. Although the activity rates are higher for our samples than the other catalysts, yet the conversion is lower. The lower conversion rates are due to different flow rates of CO and hence different concentrations of CO for our reaction when compared with others. Usually 1D morphologies of CZ samples have been shown to be catalytically active due to the preferential exposure of surface active planes ({110} and {100}) than other morphologies which may contribute to the high activities of our CZ samples[6]. However due to the different morphologies of CZ samples prepared in the literature and different reaction conditions, it is difficult to compare the activities of the as-prepared samples with other materials.

6.3.2 Thermal stability of the ceria-zirconia catalysts

Catalyst poisoning due to the formation of carbonates upon the interaction of CO with the materials is one of the prime reasons for the deactivation of the catalysts[373]. In this regard, it is important to carry out stability studies to assess the quality of the catalysts at higher temperatures and over consecutive cycles.

The stability studies for pure ceria, CZ 80/20, CZ 60/40, CZ 50/50 and CZ 20/80 and pure zirconia in CO oxidation reactions is carried out by performing three consecutive runs by increasing the temperature from 300 ℃ till 625 ℃ and then returning back to 300 ℃. As can be seen from Figure 71, all the catalysts are stable and do not degrade over the consecutive cycle runs including pure ceria. To the best of our knowledge, stability studies for CZ samples over few weeks or months have not been reported so far. The only claim reported so far for the stability of ceria nanoparticles is for six months by Cerion nanomaterial company.

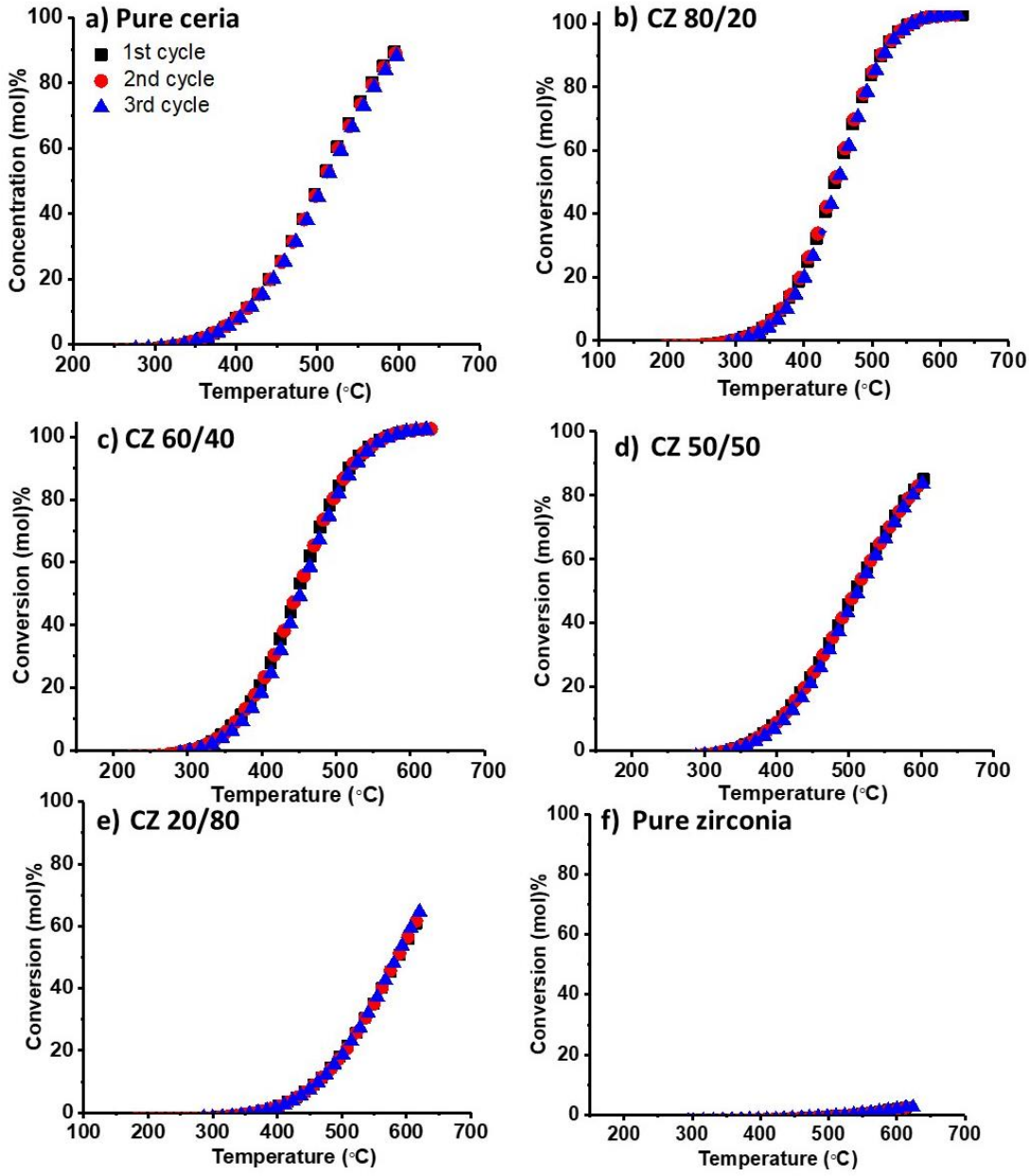

Figure 71: CO conversion (mol)% plots as a function of temperature for different supports to assess thermal stabilities: a) pure ceria, b) CZ 80/20, c) CZ 60/40, d) CZ 50/50, e) CZ 20/80 and f) pure zirconia. All the samples are prepared in reline/water 1:10 by molar ratio in solvothermal synthesis at 140 °C for 10 h. The samples are calcined at 500 °C for 4 h at a sweep rate of 10 °C/min.

6.3.3 Au/CeO_2-ZrO_2 catalysts for CO oxidation

Chapter 4 shows the synthesis of small Au nanoparticles of size 1.6-3 nm in the reline system without the addition of any external additives. However formation of agglomerates is also observed due to the weak stabilization of reline. In this section, the use of as-synthesized ceria-zirconia nanomaterial to stabilize the gold nanoparticles is shown and hence the catalytic activities of the Au/CZ materials are tested. In order to prepare Au/CZ catalysts, commercial ceria is used as a test material instead of ceria-zirconia to optimize the protocol of the catalyst preparation. For the catalyst synthesis, the gold precursor $HAuCl_4$ is added in pure reline containing the commercial ceria powder and the reaction is continuously stirred under batch conditions for 3 h at 80 ℃. After this, these solutions are washed alternately with ethanol and water to remove any traces of reline. The products are then dried under vacuum. In this syntheses, two kinds of theoretical Au loadings are used 5.8 wt% (Figure 72 a-e) and 2.8 wt% (Figure 72 g-k) on commercial ceria supports.

The AC-STEM in Figure 72 show no agglomerations of gold with both the gold loadings on commercial ceria support. The particle size increases as the gold loading increases because for 2.8 wt%, the gold particles seem to be very small (1.0 ± 0.4 nm) in Figure 72l, rather clusters than nanoparticles. In the case of 5.6 wt% Au loading, the particle size distribution is 1.9 ± 0.4 nm (Figure 72f).

Atomic resolution of single gold atoms can be seen as well in the AC-STEM micrographs. These micrographs show that gold nanoparticles are stabilized in reline in the presence of a suitable support like ceria in this case.

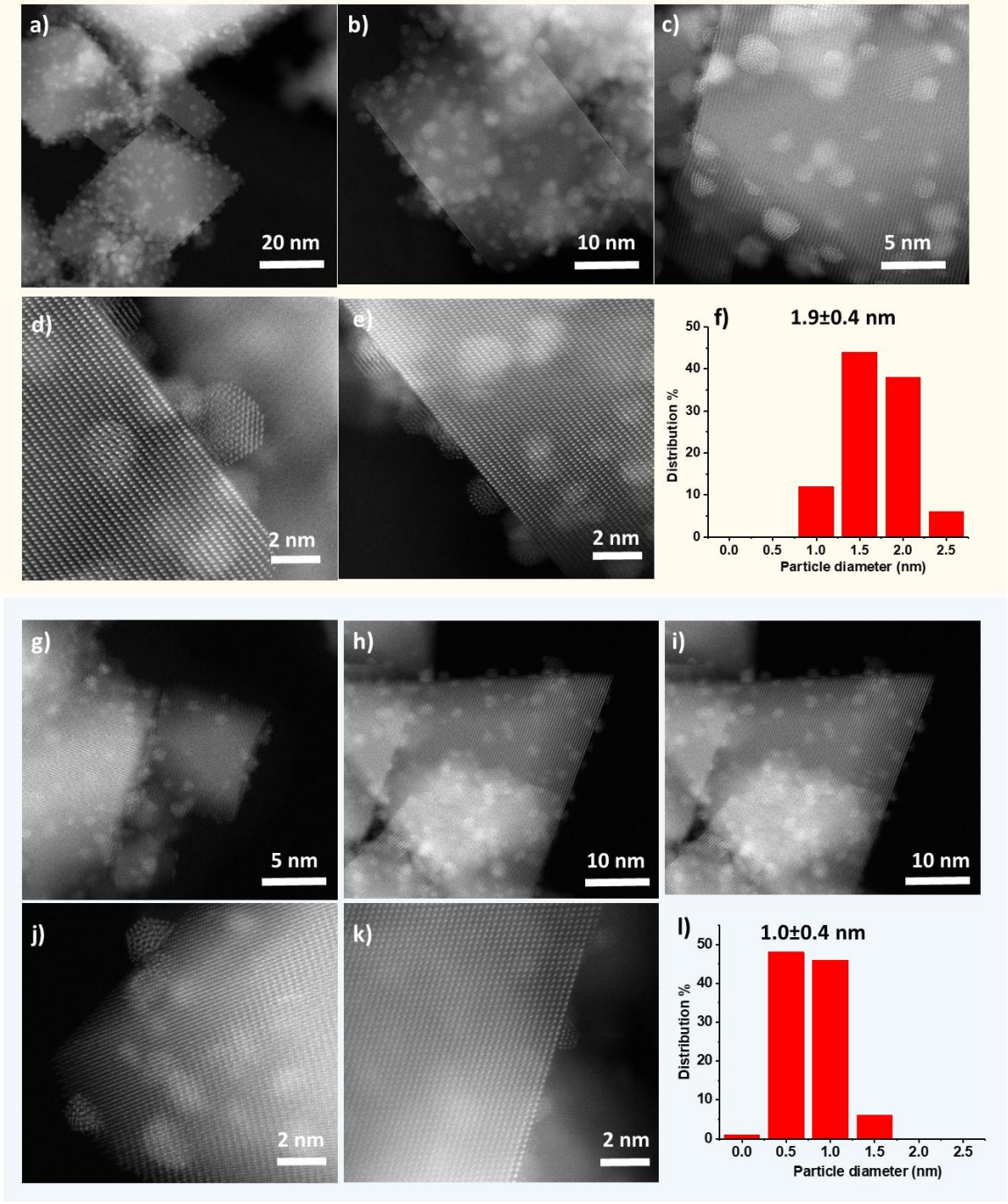

Figure 72: AC-STEM images of Au/CeO_2; a-e) 5.6 wt% theoretical gold loading on CeO_2; f) particle size distribution of 5.6 wt% theoretical gold loading on CeO_2; g- k) 2.8 wt% theoretical gold loading on commercial CeO_2; l) particle size distribution of 2.8 wt% theoretical gold loading on CeO_2. The supports in this case is commercial ceria. The catalyst is prepared by the addition of gold precursor to the support in pure reline and heating at 80 °C for 3 h. Acknowledgement: Dr Emanuela Liberti.

Based on the pre-screening results of the catalytic activities of the ceria-zirconia supports discussed in the previous section, CZ 80/20 and CZ 60/40 are chosen as the choice of supports to synthesize Au/ceria-zirconia catalysts as these two supports show the highest rate in comparison to the other CZ materials. Au/CZ catalysts with two different theoretical gold loadings of 2.8 wt% and 5.6 wt% are prepared as catalysts for the CO-oxidation activities. Inductively coupled plasma (ICP) technique is used to determine the actual gold loading on the supports. ICP results show that the actual gold loading on the supports are lower than the theoretical loading indicating that the gold is lost during the washing step of the catalysts (except for 5.6% Au loading on CZ 60/40 support) or may not have been attached to the support in the first place. The summary of the properties of the gold/ceria zirconia catalysts are shown in Table 19. All the Au/CZ samples looks pale yellow after the addition of gold and no change in colour of the sample is observed before and after gold addition.

Table 19: Summary of the properties of the Au/ceria-zirconia catalysts prepared in reline for CO oxidation reactions.

Catalyst	Theoretical loading (wt%)	Actual loading (wt%)[a]	Reduction temperature (°C)[b]	Particle size[c]
Au-CZ 80/20	2.8	1.1	148	9.88 nm
Au-CZ 80/20	5.6	4.0	163	7.46 nm
Au-CZ 60/40	2.8	1.5	139	1.26 nm
Au-CZ 60/40	5.6	5.6	141	-

[a] Actual loading as determined by ICP.

[b] Reduction temperature as calculated from TPR.

[c] Particle size as determined from CO chemisorption studies at -80 °C after *in-situ* pre-reduction at 200°C.

The HAADF-STEM micrographs of 4.0 wt% Au-CZ 80/20, is shown in Figure 73. There is a discrepancy in the size distribution results of gold nanoparticles between CO chemisorption data and TEM as from the HAADF micrographs, it is clear that the gold nanoparticles are not larger than 2 nm in size. The size distribution of gold nanoparticles from CO chemisorption carried out under cryogenic conditions is estimated to have errors because CO chemisorption provides the average size distribution whereas TEM is a localized technique [234]. The other sources of error in particle size distribution by CO chemisorption technique is discussed in Chapter 3 (Section 3.10.12).

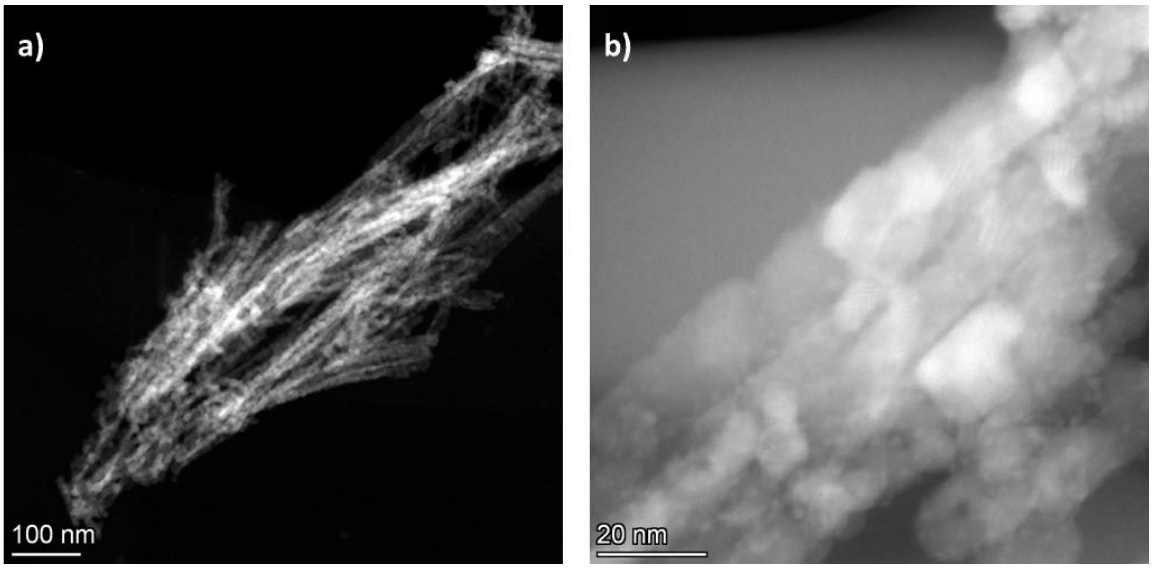

Figure 73: HAADF-STEM micrograph of 4.0 wt% Au- CZ 80/20 a) dark field and b) HAADF-STEM image-bright field. The catalyst is prepared by the addition gold precursor to the support in pure reline and heating at 80 ℃ for 3 h.

The temperature programmed reduction (TPR) profiles of all the Au/CZ catalysts shows a reduction peak below 200 ℃ (which are absent in the CZ supports) and additional broad peaks at temperatures above 600 ℃ related to the supports (lattice oxygen reduction of the ceria-zirconia supports) in Figure 74. The low temperature peak (LTP) for Au/CZ samples below 200 ℃ is attributed to the surface oxygen reduction of ceria at lower temperatures as Au enhances the reducibility of the supports[389]. Some reports have also proposed that the LTP appears due to the reduction of oxygen species on the fine gold nanoparticles[390] or reduction of any remaining cationic gold in the samples[389]. The lattice oxygen reduction peaks above 600 ℃ are also present in the TPR spectra for the CZ samples (without any gold) as seen in Figure 68. TPR studies are essential to determine the reduction temperature of the Au/CZ catalysts prior to CO oxidation in order to obtain the metal nanoparticle free of any oxide layer. The interface between gold and the support is considered to be the most active site for CO oxidation reaction (though some reports also mention that Au^{+} is the active centre)[391]. *In-situ* techniques reveal that the contribution of metallic gold in clusters or particles (sizes less than 5 nm) are much more active towards CO oxidation than single Au atoms on reducible supports such as CeO_2[392].

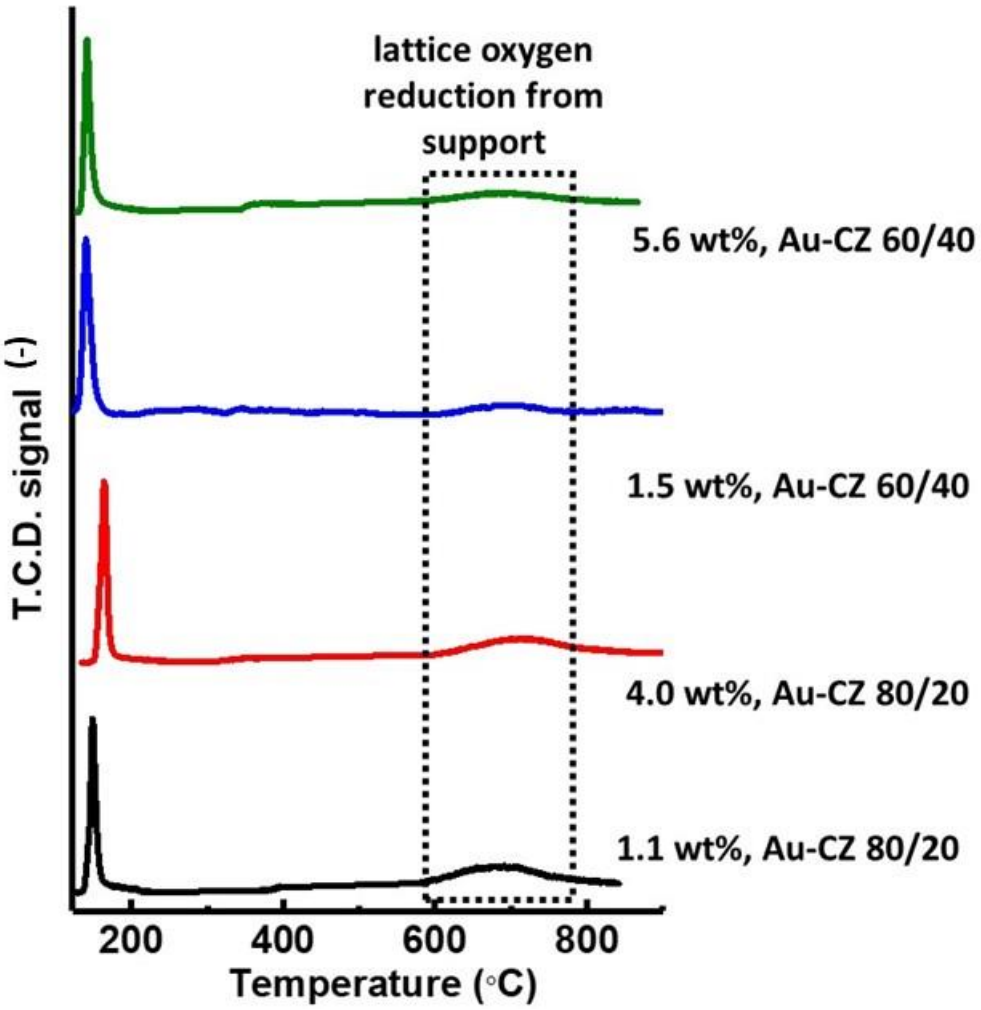

Figure 74: TPR profiles of Au/CZ samples representing the reduction peaks for Au^0 and lattice oxygen reduction of the parent supports. The actual loadings detected by ICP studies is reported here. The catalyst is prepared by the addition of the gold precursor to the support in pure reline and heating at 80 ℃ for 3 h.

6.3.4 CO oxidation catalytic activities of the Au/ceria-zirconia catalyst

In order to determine the catalytic activities of the Au/CZ catalysts, the first cycle for each CO conversion (mol)% of the Au/CZ catalyst are plotted as a function of temperature in Figure 75a. The initial catalytic activity for all the samples begins at around 45 ℃. All the catalysts reach 100% CO conversion within 220 ℃. Out of all the four samples, 1.1 wt% Au-CZ 80/20 and 1.5 wt% Au-CZ 60/40 shows the best catalytic activity with the highest

rates of reaction as 4.4×10^{-3} and 3.6×10^{-3} respectively at 75 °C (Figure 75c). The activation energies for the Au/CZ samples are calculated by the Arrhenius equation in Figure 76b. The temperature for 50% CO oxidation activities, rates of reaction and the activation energies exhibited by Au/CZ samples are shown in Table 20. The catalytic activities of the Au supported samples are much better than the bare supports as seen in Figure 75a.

Table 20: Activation energies calculated from Arrhenius plots and temperatures for 50% CO conversion of the Au-CZ catalysts.

Catalyst	T_{50} (°C) [a]	Activation energy kJ/mol [b]	Rate $mol_{CO_2}.mol_{Au}^{-1}.s^{-1}$ @ 75 °C
1.1 wt% Au-CZ 80/20	110	48	4.4×10^{-3}
4.0 wt% Au-CZ 80/20	92	52	2.2×10^{-3}
1.5 wt% Au-CZ 60/40	103	50	3.6×10^{-3}
5.6 wt% Au-CZ 60/40	97	48	1.3×10^{-3}

[a] Temperature at which 50% CO conversion is achieved.

[b] Activation energies as calculated from the Arrhenius plot.

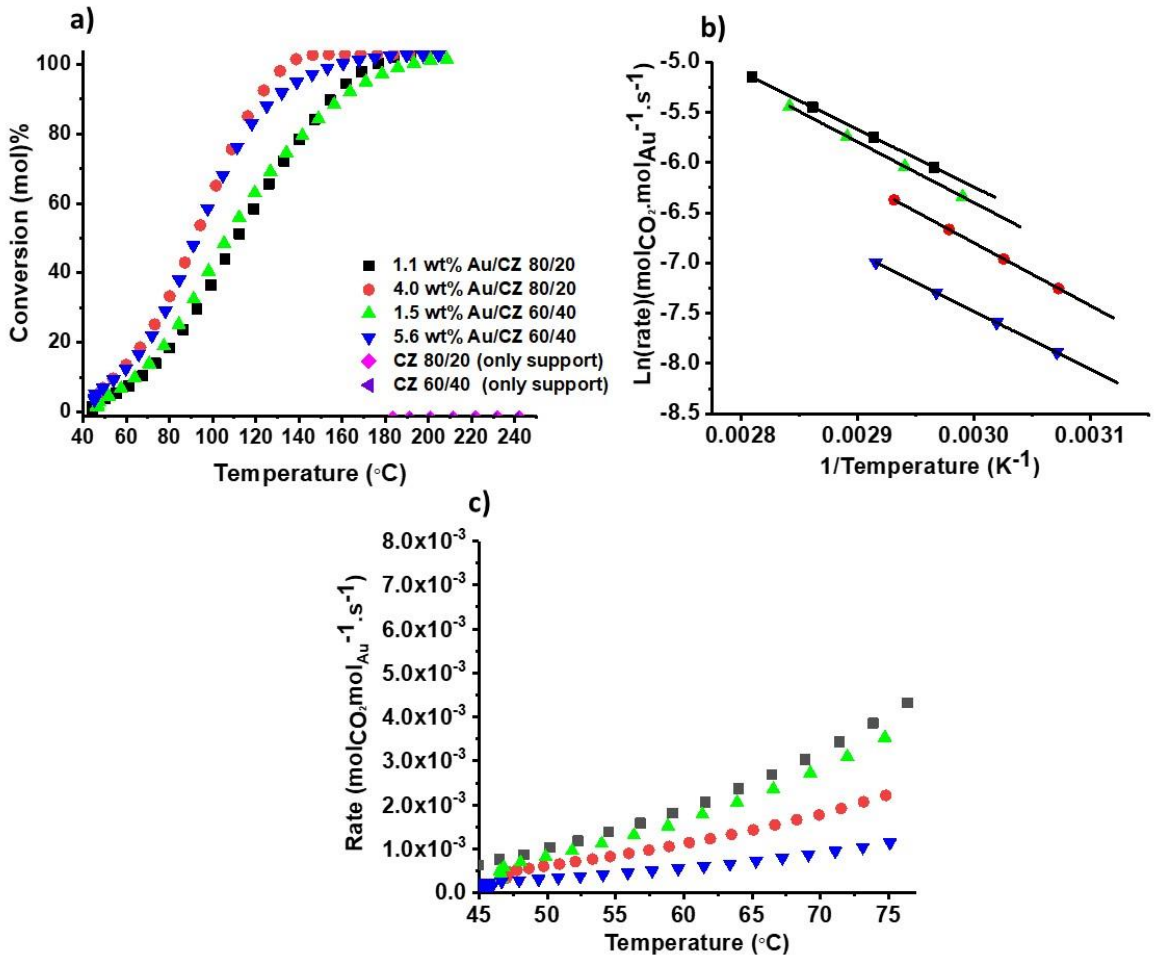

Figure 75: a) CO conversion mol% plots as a function of temperature for the first cycle of Au/CZ catalysts and the bare supports (CZ-80/20 and CZ-60/40), b) Arrhenius plots for the calculation of activation energies for the Au/CZ samples: 1.1% Au/CZ 80/20, 4% Au/CZ, 1.5% Au/CZ 60/40 and 5.6% Au/CZ 60/40 and c) rates of reaction for the Au/CZ samples. All the catalysts are pre-reduced *in-situ* under hydrogen at 200 °C before the CO oxidation reaction. The catalyst is prepared by the addition of gold precursor to the support in pure reline and heating at 80 °C for 3 h.

A significant improvement in the activation energies are observed upon Au addition for e.g. the activation energy of bare CZ 80/20 support is 88 KJ/mol (Figure 71) but upon gold addition the activation energy decreases to 48 KJ/mol. The use of reducible supports like ceria are attractive to support metal nanoparticles because these provide reactive oxygen to the gold nanoparticles, enhances metal dispersion and prevents sintering upon heating to a large extent due to its structure stability[393]. The presence of zirconium ions in ceria, stabilizes the oxygen defects in the ceria lattice and density functional theory (DFT)

calculations show that these defects surrounding the metal nanoparticles play an important role in the reaction mechanism[394]. In our case, the addition of zirconia in materials CZ 80/20 and CZ 60/40 is able to show a better activity due to enhanced oxygen vacancies as evident from the Raman and XPS studies.

There is a vast literature available on the role of gold to improve CO oxidation of supports and some of the main proposals include presence of active sites at the gold/support boundary, quantum effects due to small gold clusters, surface steps and strain defects[391]. Laguna *et al.* have reported improved CO oxidation activities for Au/CZ complexes in comparison to Au/pure ceria due to the interaction between Au and the increased surface oxygen vacancies due to incorporation of zirconia[395]. Enhancement of CO oxidation catalytic activities with an increase in surface oxygen vacancies for gold supported systems has also been attributed due to the high electron density of vacancy-Au bonding as vacancies are usually electron-rich sites[396]. DFT calculations previously showed that a single oxygen vacancy has the capability to bind to 3 Au atoms and the Au-vacancy cluster is found to be stable at room temperatures[397]. A high concentration of Ce^{3+} in the materials is usually considered to be beneficial for CO oxidation on Au supported catalysts because time-resolved resonant X-ray emission spectroscopy studies showed that Ce^{3+} act as active centres to supply electrons for the activation of oxygen[398]. The XPS data for the CZ materials indicate that the % of Ce^{3+} is highest for CZ 80/20 and CZ 60/40 (Table 17). As seen from the HAADF-STEM micrographs of the gold nanoparticles on the surface of commercial ceria and CZ 80/20, the sizes are less than 2 nm (Figure 72 and Figure 73). The size of the gold nanoparticle is crucial in the CO oxidation reaction as Lopez *et al.* have calculated that the adsorption energies for CO and O considerably decreases by 1 eV while coordinating with a small sized gold nanoparticle than a larger one. Size plays an enormous effect in the CO oxidation as the authors also show that CO oxidation is 2 orders more in magnitude for 2-4 nm size gold nanoparticles than 20-30 nm because of the availability of low coordinated atoms on the steps and corners of small nanoparticles[83].

A summary of the catalytic rates ($mol_{CO2}mol_{Au}^{-1}s^{-1}$) of the CO oxidation of gold supported ceria-zirconia catalysts is presented in Table 21. Despite of the different reaction routes to prepare Au/CZ catalysts, there is a general consensus that a synergistic role plays when

gold supported catalysts are employed for CO oxidation rather than mere supports. Upon doping the ceria lattice with cations like Zr^{4+}, the doping ions distort the crystal lattice and these distortions in turn provides anchoring sites for gold nanoparticles resulting in better dispersions and smaller sizes of gold nanoparticles[389]. Increase in the concentration of oxygen vacancies upon introducing zirconia in the ceria crystal structure also exhibits a beneficial role on the Au-CZ catalyst as discussed above towards the CO oxidation[399]. Although a direct comparison is not possible between the rates of reaction for our catalysts and those reported in the literature due to differences in gold loading amount and post-treatment of the catalysis, yet the catalyst produced by Dobrosz *et al.* exhibits the highest activities[400]. The authors attribute the higher activities of their catalyst to the preparation procedure of the Au/CZ materials synthesized by direct anionic exchange method (anions of the gold precursor exchanged with the hydroxyl groups of the support). Our catalysts display intermediate rates when compared with other Au/CZ catalysts (Table 21).

Table 21: Comparison of the catalytic activities for CO oxidation of the different Au/ceria-zirconia catalysts reported in the literature with respect to our sample.

Ref	Sample	Au (wt%)	Conversion %	$Mol_{CO2}mol_{Au}^{-1}s^{-1}$	Temperature (°C)
Our work	Au-CZ 80/20	1.1	15	4.4×10^{-3}	75
	Au-CZ 80/20	4.0	27	2.2×10^{-3}	75
	Au-CZ 60/40	1.5	21	3.6×10^{-3}	75
	Au- CZ60/40	5.6	33	1.3×10^{-3}	75
[400]	Au-CZ 75	1.68	90	0.133	75
	Au-CZ 50	1.74	30	0.127	75
	Au-CZ 25	1.71	30	0.130	75
[401]	Au-CZ 80	2	50	5.89×10^{-2}	75
[402]	Au-CZ 62	2.6	90	0.19×10^{-6}	75
[399]	Au-CZ 62	0.94	50	0.7×10^{-5}	56
[386]	Au-CZ 90	1	65	2.5×10^{-3}	75

6.3.5 Thermal stability studies of Au/ceria-zirconia catalysts

Deactivation of the catalysts during subsequent CO oxidation catalytic cycles is a common phenomenon due to the sintering of the active metal nanoparticles at high temperatures[403]. Thus stability studies for CO oxidation activities over consecutive cycle runs gives an indication of the stabilities of the catalyst.

The stability studies of all the Au/CZ catalysts are carried out under CO oxidation reactions by performing three consecutive runs by increasing the temperature from 40 ℃ till 220 ℃ and then returning back to 40 ℃. As can be seen from Figure 76, the catalysts are quite stable and do not degrade over the consecutive cycle runs indicating a strong Au-support interactions.

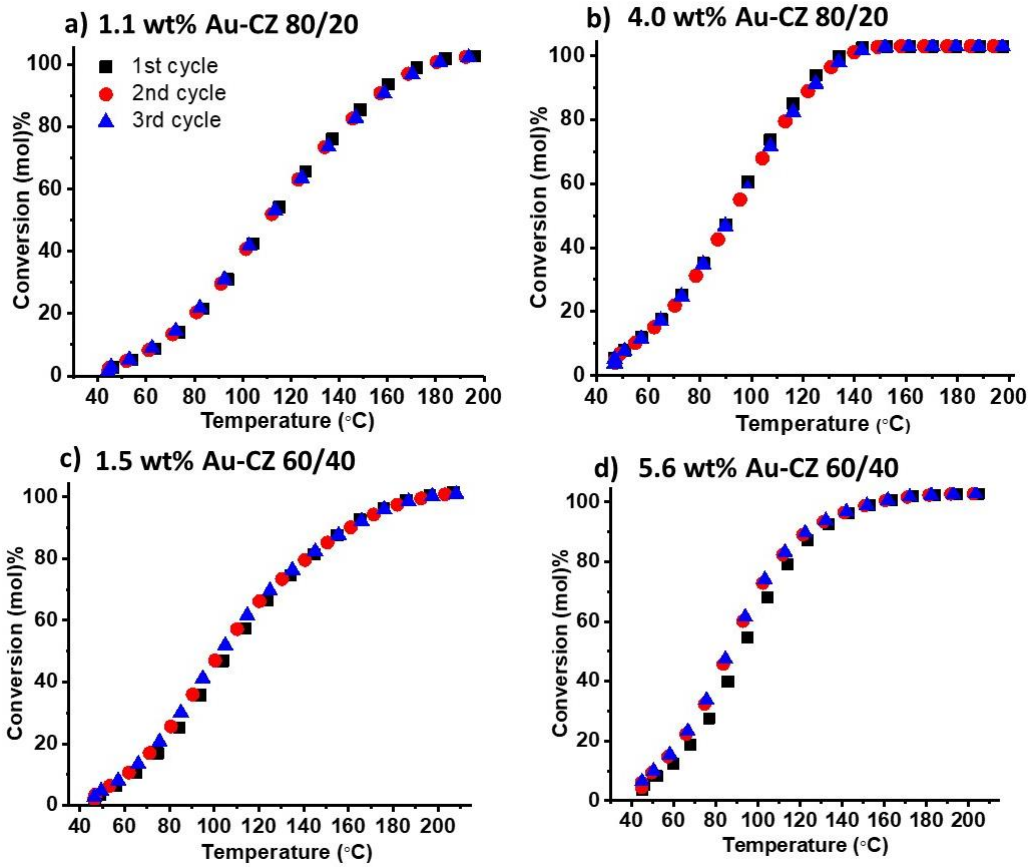

Figure 76: CO conversion mol% plots as a function of temperature for Au/CZ catalysts: a) 1.1 wt% Au/CZ 80/20, b) 4 wt% Au/CZ 80/20, c) 1.5 wt% Au/CZ 60/40 and d) 5.6 wt% Au/CZ 60/40. All the catalysts are pre-reduced *in-situ* under hydrogen at 200 ℃ before the CO oxidation reaction. The catalyst is prepared by the addition of gold precursor to the support in pure reline and heating at 80 ℃ for 3 h.

6.4 Conclusions

This chapter presents the synthesis of a novel facile and surfactant-free green solvent platform for the solvothermal synthesis of ceria-zirconia nanorods using the deep eutectic solvent reline without the addition of any external additives in the reaction medium. In the past, few groups report the synthesis of 1D structures of ceria-zirconia nanorods/nanotubes by using corrosive bases like NaOH or by employing surfactants like CTAB. Herein it is shown that the reline/water solution itself is able to produce 1D nanorod structures of ceria-zirconia by the mechanism of oriented attachment of nanoparticles promoted by the presence of water in reline.

Advanced characterization techniques like X-ray diffraction, Raman spectroscopy and X-ray photoelectron spectroscopy techniques are carried out to investigate the structural properties of the ceria-zirconia samples. The incorporation of the smaller ion of Zr^{4+} in the cubic fluorite lattice of ceria is demonstrated by the peak shift in XRD as lattice shrinkage is observed upon calculation of the crystallite size. Absence of free ZrO_2 peaks in Raman also indicates homogeneity in the ceria-zirconia samples.

The concentration of the oxygen vacancies in the ceria-zirconia samples are calculated from the XPS and Raman measurements. In Raman, an increase in the FWHM band is primarily observed due to higher concentration of oxygen vacancies. In XPS, from the O1s peak of oxygen, the ratio of oxygen vacancies to lattice oxygen (O_β/O_α) and the % of Ce^{3+} is an indication of the presence of oxygen vacancies. Both the XPS and Raman data indicates a higher percentage of oxygen vacancies in CZ 80/20 and CZ 60/40 samples.

Temperature programmed reduction data show that reduction of ceria and ceria-zirconia samples exhibits two reduction peaks at around 500 °C and 800 °C to reduce surface oxygen and lattice oxygen respectively. Upon increasing the content of zirconia in the ceria-zirconia samples, the reduction peak for lattice oxygen shifts to lower temperatures as mobility of oxygen species increases due to the decrease in the crystallite size upon zirconia incorporation on account of lattice shrinkage due to the smaller size of the Zr^{4+} (0.084 nm) in comparison to Ce^{4+} (0.097 nm).

CO oxidation catalytic activity is used as a model reaction to elucidate the structure-property relationship of the CZ supports. It is observed that CZ 80/20 and CZ 60/40 exhibits the best CO oxidation activity due to the highest percentage of surface oxygen vacancies as indicated by the Raman and XPS data. Oxygen vacancies are crucial for CO oxidation as these vacancy sites are believed to responsible for oxygen activation through the formation of superoxide and peroxide species as intermediate complexes. Oxygen vacancy sites also enhances the mobility of oxygen in the ceria crystal lattice.

As seen in Chapter 4, small sized gold nanoparticles of sizes 1.6-3nm are produced in reline but the nanoparticles agglomerate due to the weak stabilization provided by reline. Ceria-zirconia supports are added in pure reline to provide stability to the gold nanoparticles and prevent them for agglomeration. AC-STEM studies show that gold nanoparticles of sizes 2 nm are deposited on the supports and no agglomerations are observed. These results indicate that the ceria zirconia supports are able to stabilize the gold nanoparticles in reline in addition to the TPR results which also indicate adsorption of Au. These as-synthesized Au/CZ catalysts are tested for CO oxidation activities. There is an improvement in the catalytic activities such as lower activation energies in the presence of gold and enhancement in the reducibility of the supports due to the appearance of low temperature peak in the TPR profiles for Au based catalysts. 1.1 wt% Au/CZ 80/20 exhibits the highest rate and is the best catalyst within this study. Although it is difficult to directly compare the activities of the Au/CZ catalysts due to different gold loadings however it is plausible that as the support CZ 80/20 shows the highest percentage of oxygen vacancies, hence the Au/CZ 80/20 behaves as a better catalyst because CO oxidation reaction is closely related to the active sites present between the metal/support interface and oxygen vacancies. Overall, both the support and the Au/ CZ catalysts exhibits good thermal stabilities as no significant degradation in the catalytic behaviour is observed upon subsequent cycle runs. The as-synthesized CZ supports synthesized here exhibits the highest rates amongst other CZ materials reported so far and the Au/CZ shows comparable reaction rates.

Potential future work may involve investigating the use of zirconia to improve thermal stabilities of CZ samples by modifying the sintering behaviour. The samples maybe

calcined at higher temperatures and could be possibly tested for thermal stabilities to identify the temperatures up to which CZ samples are stabilized compared to pure ceria.

Chapter 7: Synthesis of nano-structured ZrO_2 in deep eutectic solvent reline

The objectives of the previous chapters 4, 5 and 6 were to elucidate the roles played by the deep eutectic solvents towards the synthesis of nanomaterials from different families like Au, V_2O_5, CeO_2 and CeO_2-ZrO_2. It is found that DES fulfils multiple roles in these syntheses such as reducing and capping agent for Au, template delivery roles for vanadium oxide and ceria-zirconia and exfoliating agents for vanadium oxide nanosheets. However, there are no reports in the literature yet to study the effect of DES on the crystal phases of nanomaterials. As discussed previously in Chapter 2 (literature review), proper control over different crystal phases of ZrO_2 is important as it is shown that different crystallographic phases exhibit different catalytic activities due to variations in the cation/anion pairs and Brønsted acid/base sites on their surface[183]. In this chapter, zirconia is chosen as the material to study the effect of DES on crystal phase because ZrO_2 is used extensively in a wide range of applications such as nanoceramics, (photo)catalysis, reinforced ceramic composites, biomaterial for dental implants and coatings for ceramic fibres[159,404]. This wide range of applications has been related to its intrinsic properties such as high melting point, resistance to acids and alkali, hardness and shock wear to name a few[405]. Other factors like low thermal conductivity and high thermal coefficient expansion has made ZrO_2 a suitable candidate to be used for thermal coatings[406]. It is also known that ZrO_2 exists in three crystallographic phases: monoclinic, tetragonal and cubic phase. In the absence of any stabilizers, the monoclinic phase is stable under room temperature conditions unlike the tetragonal and cubic phases which are unstable under room temperature[180]. In the literature review, solvent conditions are shown to influence the crystal phase due to variations in the recrystallization/dissolution kinetics.

The purpose of this chapter is to investigate the role of DES reline on the crystal phase of ZrO_2. In order to understand the influence of solvent environment on crystal phase, another synthesis is carried out by NaOH route. Au/ZrO_2 catalysts are prepared to study the effect of the crystal phase on the CO oxidation.

7.1 Comparison between solvothermal and hydrothermal route in the synthesis of nanostructured ZrO_2

A comparison between the hydrothermal and solvothermal route to synthesize nanostructured ZrO_2 is carried out. For this purpose, the DES reline is used as the solvent for the solvothermal synthesis and the hydrothermal synthesis is carried out in aqueous NaOH (15 M) as a solvent (using $ZrO(NO_3)_2.6H_2O$ as the initial precursor).

Figure 77 shows a schematic representation of the different steps taking place during the solvothermal syntheses. A milky white colour solution is initially obtained upon the dissolution of $ZrO(NO_3)_2.6H_2O$ in reline/water (1:10 by molar ratio) and aqueous NaOH (15 M). After solvothermal treatment at 140 °C for 10 h, a white product is obtained at the end of syntheses in both cases. When NaOH is used as the solvent, pure cubic phase of nanostructured ZrO_2 is obtained (Figure 77). However when reline/water (1:10 by molar ratio) is used as the solvent, pure monoclinic phase of ZrO_2 is produced at the end of the synthesis (Figure 77).

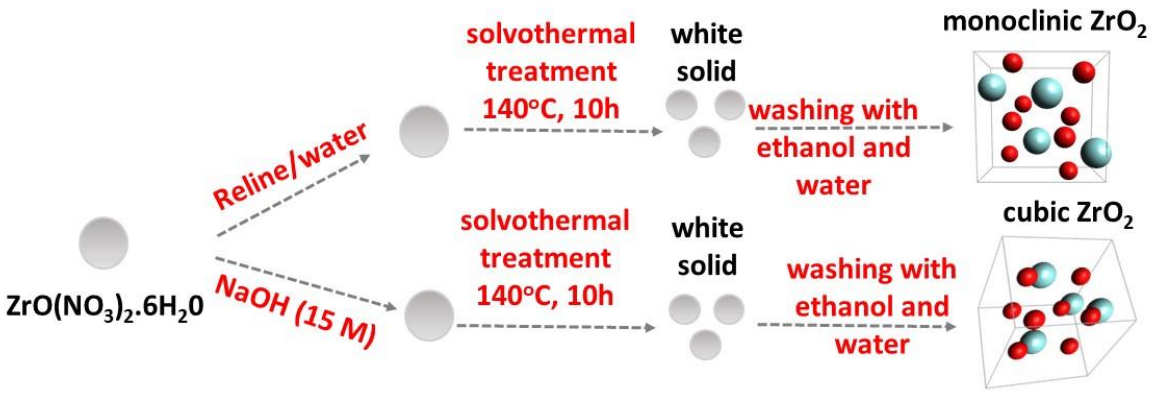

Figure 77: Schematic representation of the solvothermal and hydrothermal synthesis of nanostructured ZrO_2 in reline/water 1:10 molar ratio solution and aqueous NaOH respectively.

The X-ray diffraction pattern of the nanostructured ZrO_2 synthesized in aqueous NaOH (15 M) at 140 ℃ for 10 h is shown in Figure 78a. The peaks at 30.20°, 35.00°, 50.40°, 60.00° and 62.70° are well indexed to the lattice planes of cubic phase of ZrO_2 {101}, {110}, {200}, {211} and {202} respectively[407] (JCPDS card number 27-0997). The coherent diffraction domain size as calculated from the Scherrer equation is 4.1 nm.

The X-ray diffraction peaks of the nanostructured ZrO_2 synthesized in reline/water (1:10 by molar ratio) at 140 ℃ for 10 h is shown in Figure 78b. The peaks at 24.20°, 28.20°, 31.50°, 34.50°, 49.50°, and 50.20° are well indexed to the monoclinic crystalline phase of ZrO_2 (JCPDS card number 37-1484) corresponding respectively to {110}, {111} and {002} lattice planes[161]. The coherent diffraction domain size as calculated from the Scherrer equation is 6.3 nm.

Figure 79 presents the HR-TEM micrographs of the nanostructured ZrO_2 synthesized by reline/water 1:10 molar ratio and aqueous NaOH (15 M) in 10 h. All the samples exhibit good crystallinity and clear lattice fringes. Particle size distribution for the ZrO_2 nanoparticles is not possible from HR-TEM due to very small particle size.

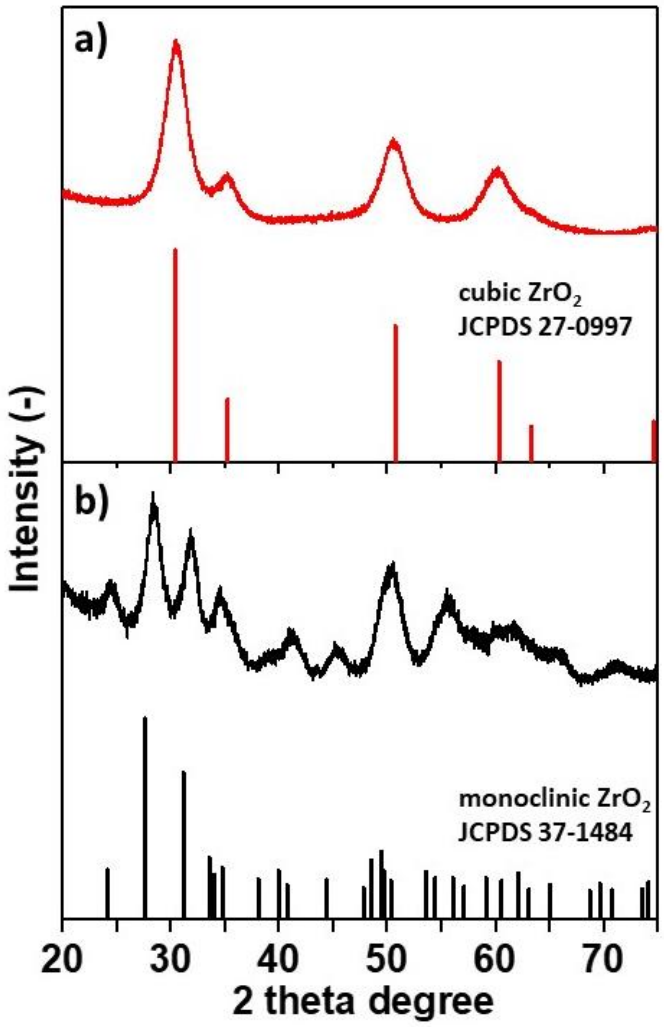

Figure 78: XRD patterns of nano ZrO_2 synthesized in a) aqueous NaOH (15 M) and b) reline/water 1:10 by molar ratio. Both the samples are prepared under hydrothermal and solvothermal conditions respectively at 140 °C for 10 h.

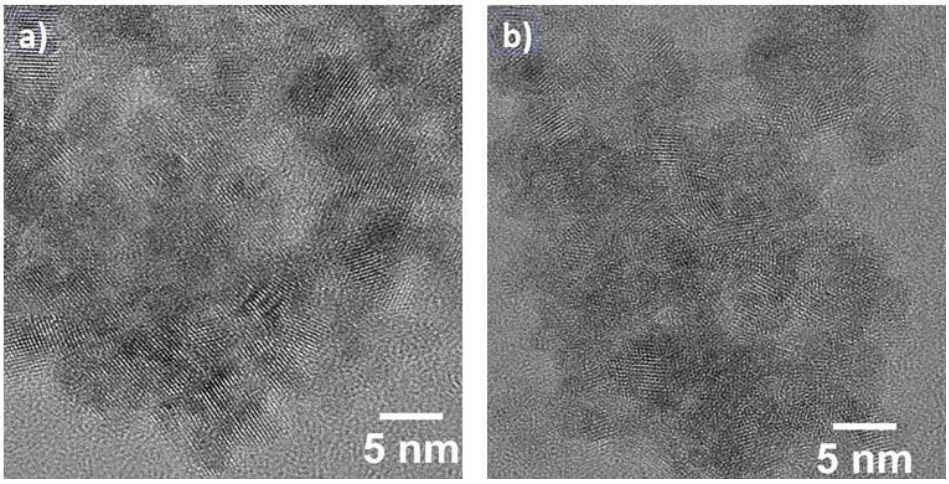

Figure 79: HR-TEM images of ZrO_2 nanoparticles synthesized under solvothermal and hydrothermal conditions respectively at 140 °C for 10 h in a) reline/water 1:10, b) aqueous NaOH (15 M).

From the XRD pattern of both ZrO_2 samples, it is clear that the thermodynamically unstable cubic phase is stabilized by aqueous NaOH solution but not in reline/water mixture in the solvothermal synthesis. Earlier studies report similar findings on the stabilization of the cubic phase of ZrO_2 by the Na^+ ions present in NaOH[408,409]. Kinetic studies on the crystallization process of ZrO_2 under hydrothermal condition in pure water at 250 °C, 70 MPa shows that clusters comprises of mainly nuclei of cubic ZrO_2 in the hydroxo complexes which are present during the initial stages of primary crystallization phase[410].

The smaller crystallite size of cubic ZrO_2 (4.1 nm) in comparison to monoclinic ZrO_2 (6.3 nm) are in agreement with the reports of Matsuoke *et al.* that as the monoclinic phase grows from the cubic phase instead of the initial true solution, hence the size of the zirconia nanoparticles in the monoclinic phase is greater than the cubic phase [411].

Electron probe micro-analysis studies have shown that the stabilization of the cubic phase is provided by the incorporation of the alkali cations due to the heterovalent substitution of some Zr^{4+} ions by Na^+ ions ($Zr^{4+}_{1-x}Me_x^{n+}O_{2-(2-n/2)x}$) in the hydroxo complex formed during the hydrothermal synthesis due to similarities in the ionic radii i.e. 84 pm and 102 pm for Zr^{4+} and Na^+ respectively[410,411]. The role of NaOH to stabilize the cubic phase was made clear by Benedetti *et al.* by replacing NaOH with NH_4OH and obtaining a mixture of

monoclinic and tetragonal phase instead of any cubic phase. This is due to the larger ionic radii of NH^{4+} ion (148 pm) that makes the incorporation of NH^{4+} in the hydroxo complexes difficult[408].

The absence of the monoclinic phase in NaOH (15 M) is attributed due to the similarities between the cubic phase and the polymeric hydroxo complexes present during the early stages of the synthesis[412].

Cubic ZrO_2 synthesized in aqueous NaOH exhibits a higher surface area of 270 m^2/g in comparison to the monoclinic ZrO_2 synthesized by reline/water 1:10 molar ratio route which gives a surface area of 163 m^2/g as calculated from the nitrogen adsorption-desorption isotherms in Figure 80. A 'kink' type feature is observed in the desorption arm of the hysteresis loop in the cubic zirconia sample. This kink feature is due to occurrence of cavitation rather than capillary desorption[413]. Usually samples with a network of 'ink-bottle' pores exhibit cavitation where the wide cavities are filled with condensate at relative high vapour pressure. But pore emptying is difficult during desorption due to the curved necks of the pores that creates difficulty for evaporation. The pore sizes are usually smaller for these 'ink-bottle' shaped pores and the standard BJH (Barrett, Joyner, and Halenda) method for pore size distribution may lead to errors. These nitrogen adsorption-desorption isotherms for both the nanostructured ZrO_2 samples corresponds to IUPAC Type IV shape, characteristic of mesoporous materials.

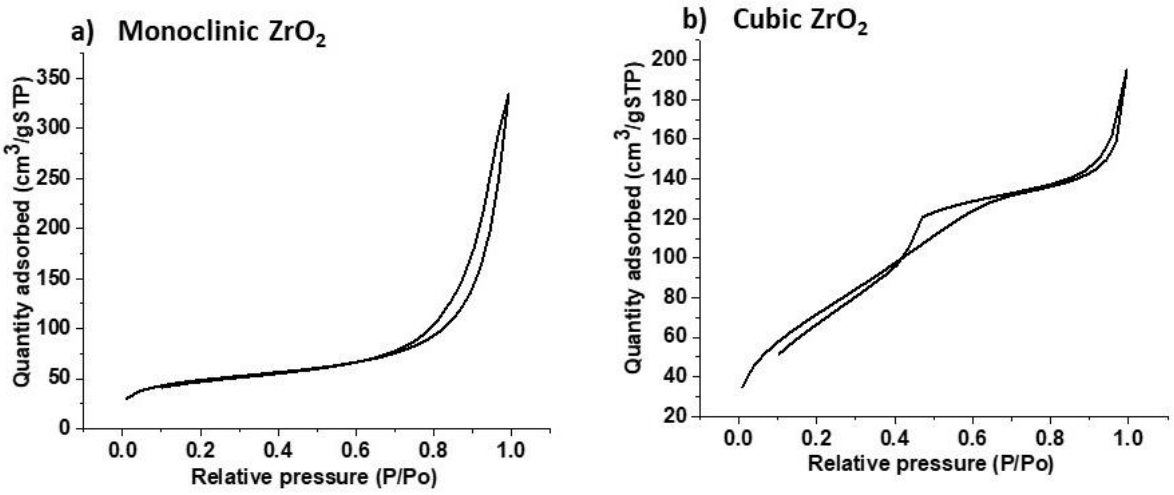

Figure 80: BET surface areas of the ZrO_2 samples calculated by the nitrogen adsorption-desorption isotherms: a) monoclinic ZrO_2, b) cubic ZrO_2. Both the samples are prepared under solvothermal conditions at 140 °C for 10 h. Monoclinic ZrO_2 is prepared in reline/water 1:10 by molar ratio and cubic ZrO_2 in aqueous NaOH (15 M) as the solvent.

The optical spectra to calculate the band gap as determined by the solid UV-vis absorption spectroscopy as shown in Figure 81 for monoclinic and cubic zirconia are relatively similar to each other in agreement to previous report[414]. Band gap is defined as the energy gap or the energy difference between the valence band and the conduction band where no other electronic states exist and provides important information on the electronic properties of nanomaterials[415]. In addition to electronic properties, it is also possible to obtain information on the structural defects and oxygen vacancies present in the material[416]. The transition from valence band to conduction band for both the samples occurs at ~220 nm and another absorption band is observed at 280-320 nm due to the defects present in ZrO_2[417]. ZrO_2 is a well-known direct band gap material with two band-band transitions as also indicated by our results[418]. The higher absorbance of the band centred around 300 nm for cubic zirconia than the monoclinic counterpart is due to increased transitions on account of a higher concentration of oxygen vacancies and defects which is also observed earlier for the cubic phase[418]. The band gap of the monoclinic ZrO_2 and cubic ZrO_2 are 5.08 eV and 5.16 eV as seen in Figure 81. Band-gap calculations for the monoclinic and cubic ZrO_2 are carried out by the Tauc plot between hν and $(\alpha h\nu)^2$ as seen in the inset in Figure 81, where hν is the photon energy and α is the absorption coefficient. Direct band

gap transition is taken into account for the Tauc plot calculation. Similar band gap values in the range of 3.1-5.1 eV for nanostructured ZrO_2 are reported in the literature[416].

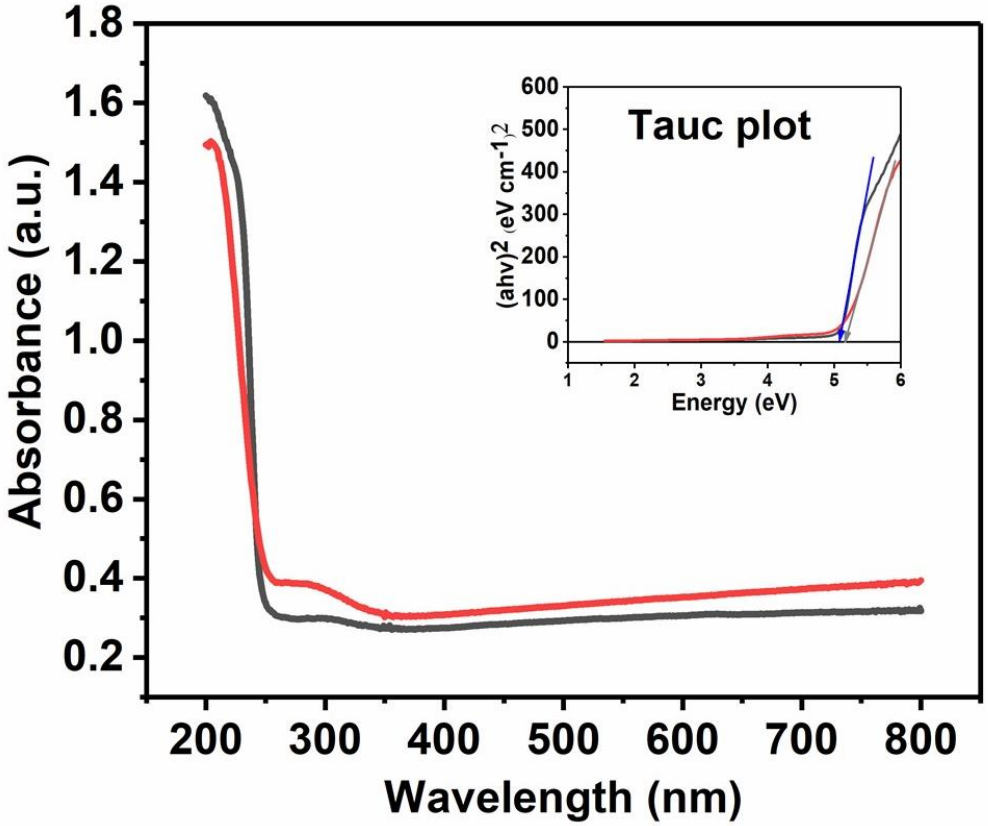

Figure 81: Solid UV-vis absorbance spectrum of monoclinic ZrO_2 (black) and cubic ZrO_2 (red colour). The inset represented the Tauc plot to calculate the energy band gap of monoclinic ZrO_2 and cubic ZrO_2. Both the samples are prepared under solvothermal conditions at 140 °C for 10 h. Monoclinic ZrO_2 is prepared in reline/water 1:10 by molar ratio and cubic ZrO_2 in aqueous NaOH (15M) as the solvent.

In addition to XRD analysis, Raman spectroscopy is carried out due to the sensitivity of the Raman technique to distinguish the ZrO_2 polymorphs. Figure 82 presents the Raman spectra of monoclinic and cubic ZrO_2. Raman pattern for monoclinic ZrO_2 displays peaks at 326, 387, 479, 553, 613, 757 and 880 cm^{-1} that are in agreement with the spectral values reported in literature[416]. The peak at 326 cm^{-1} is shown to have no dependence on the oxygen atoms and is designated for Zr-Zr vibrations[419]. The other peaks correspond to Zr-O and O-O vibrational modes. The Raman pattern for cubic ZrO_2 is characterized by broad

peaks at 396 and 560 cm^{-1} along with peaks at 765, 880 and 927cm^{-1} in accordance with reports published elsewhere[420]. It is clear from the Raman spectra of cubic zirconia that there are no traces of tetragonal zirconia due to the absence of sharp peaks at 292 and 636 cm^{-1} characteristic of tetragonal phase. The broad and asymmetric peak in cubic ZrO_2 centred at 560 cm^{-1} is attributed ~~due~~ to the oxygen vacancies that leads to lattice distortions[421].

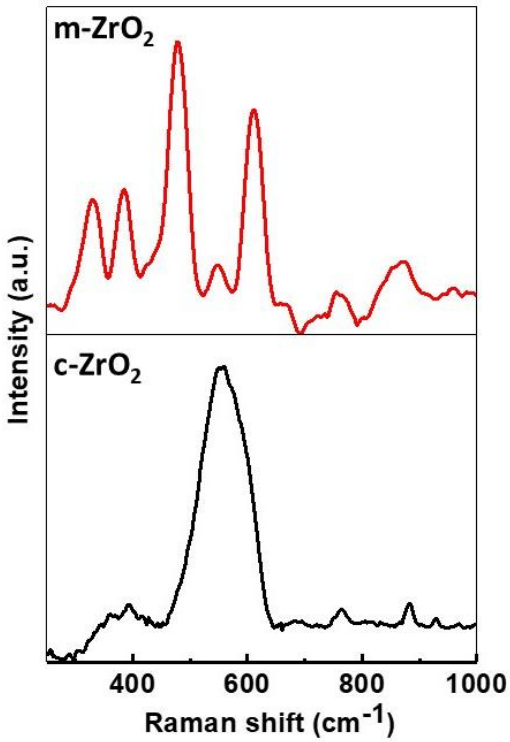

Figure 82: Raman pattern of monoclinic ZrO_2 and cubic ZrO_2. Monoclinic ZrO_2 is prepared in reline/water 1:10 by molar ratio and cubic ZrO_2 in aqueous NaOH (15M) as the solvent at 140 °C for 10 h.

The presence of oxygen vacancies in cubic ZrO_2 is hence clear from the solid UV-vis absorption spectroscopy and Raman studies. It is possible to acquire some idea on oxygen vacancies from solid UV-vis absorption spectroscopy as these vacancies alter the crystal structure and change the electronic properties which in affects the absorbance.

7.2 Effect of changing the water ratio in reline in the synthesis of nanostructured ZrO_2

In order to understand the effect of water present in reline on the synthesis of nanostructured ZrO_2, additional syntheses are carried out in pure reline, reline/water 1:2 by molar ratio, reline/water 1:10 by molar ratio and pure water. As can be seen from the XRD pattern of nanostructured ZrO_2 in Figure 83, monoclinic phase of ZrO_2 is obtained whenever pure reline, reline/water mixtures and pure water is used as the solvent. Due to the absence of any alkali cations in reline solutions or pure water, stabilization of any other phase except monoclinic is not possible as it is the most thermodynamically stable phase[422]. Effective substitution in the hydroxo complexes of zirconium by the ammonium cations present in the quaternary ammonium salt in reline to stabilize cubic phase is also not possible due to the large ionic radii of NH_4^+ (148 pm) in comparison to Zr^{4+} (84 pm) as discussed in Section 7.1.

When pure reline is used as the solvent, tiny crystallites of size 1.3 nm are obtained as calculated from the Scherrer formula (Figure 83a). As the amount of water increases in reline, the crystallite size grows from 4.3 nm in reline/water 1:2 molar ratio to 6.3 nm in reline/water 1:10 by molar ratio. The product yield also increases with an increase in the amount of water in reline such as 41% (pure reline) < 58% (reline/water 1:2 by molar ratio) < 72% (reline/water 1:10 by molar ratio). These results indicate that the increase of the product yield can be associated to the decrease of viscosity as the water content increases[303] although water is also proposed to play an active role in the re-crystallisation process due to which the size of the nanoparticulate changes[304]. These results are in accordance with previous reports where water has been shown to influence the energetics of a reaction during early stages of cluster growth in the formation of nanoparticles which in turn affects the various growth pathways in the solution[423]. Molecular dynamic simulation studies showed that strong water interaction is present with the nanoparticle surface that affects the size of the nanoparticle and overall structural stabilization energies[424].

When pure water is used as the solvent, nano ZrO_2 of size 4.3 nm is produced and the product yield is 21% which is lower than those obtained with reline solutions (Figure 83c). The higher yield% in reline solutions in comparison to pure water shows that reline exhibits catalytic behaviour to increase the product yield[155].

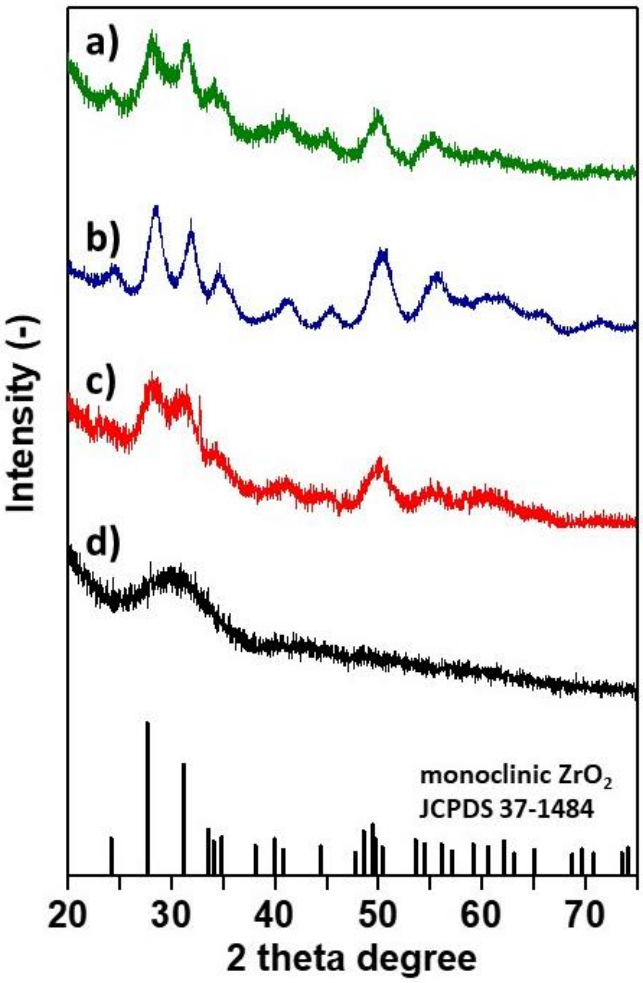

Figure 83: XRD pattern of nano ZrO_2 in a) pure water, b) reline/ water 1:10 by molar ratio c) reline/ water 1:2 by molar ratio and d) pure reline. All the samples are synthesized under solvothermal conditions at 180 °C for 10 h.

7.3 Effect of temperature in reline on the synthesis of nanostructured ZrO_2

Temperature plays a crucial role towards the synthesis of nanomaterials as it affects the formation, growth and size of the nanoparticles[425]. A series of syntheses to study the effect of temperature on nanostructured ZrO_2 is carried out at 70 ℃, 100 ℃, 120 ℃, 140 ℃ and 180 ℃ with reline/water 1:10 molar ratio solution. The XRD patterns shown in Figure 84 corresponds to monoclinic phase of ZrO_2. An increment in the crystallite size of nanostructured ZrO_2 is observed upon increasing the temperature from 70 ℃ to 180 ℃. Coherent diffraction domain of size 1.9 nm are obtained at 70 ℃ which increases to 2 nm (100 ℃), 4.5 nm (120 ℃), 5.1 nm (140 ℃) and 5.6 nm (180 ℃) as calculated from the Scherrer equation.

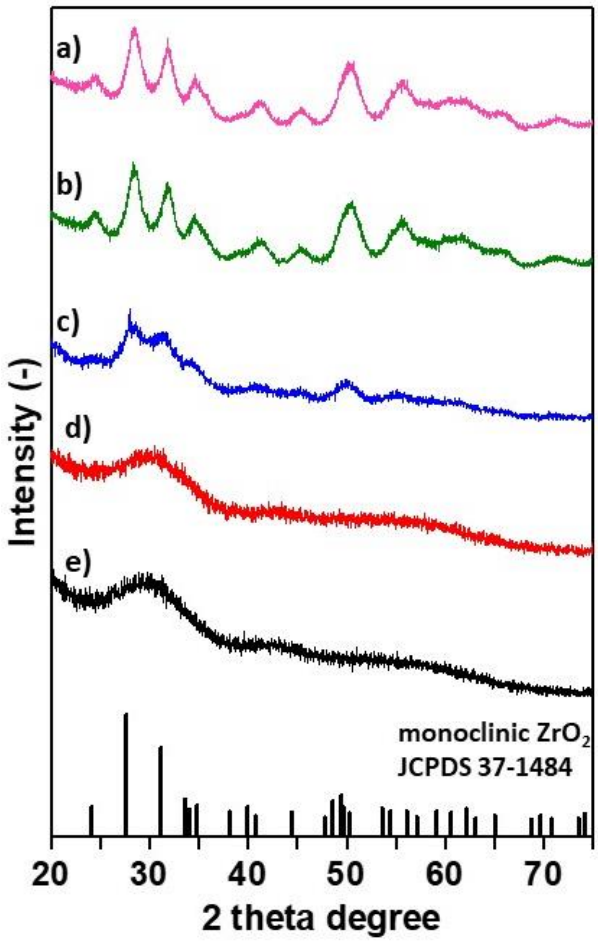

Figure 84: XRD pattern of nano ZrO_2 synthesized in reline/water 1:10 by molar ratio at a) 180 °C, b) 140 °C, c) 120 °C, d) 100 °C and e) 70 °C. All the samples have been prepared by solvothermal synthesis for 10 h.

The growth of the nanoparticles on increasing the reaction temperature is explained on the basis of an increase in the rates of aggregation which is enhanced as the temperature increases due to decrease in the viscosity of the solvent[426].

A summary of the observed crystal phase and corresponding experimental conditions is shown in Table 22.

Table 22: Different synthesis conditions used to synthesize nano ZrO_2.

Solvent	Phase[a]	Synthesis temperatures[b]
Pure reline	-	180 °C
Reline/water (1:2)	m	180 °C
Reline/water (1:10)	m	180 °C
	m	140 °C
	m	120 °C
	m	100 °C
	m	70 °C
Pure water	m	180 °C
	m	140 °C
NaOH (15M)	c	180 °C
	c	140 °C

[a] Phase identification by XRD, [b] Synthesis conditions for a time duration of 10 h.

[m] monoclinic, [c] cubic.

7.4 Effect of NaOH concentration on the hydrothermal synthesis of nanostructured ZrO_2

Different concentrations of aqueous NaOH (1 M, 5 M and 15 M) are used to study the effect of base concentration on the synthesis of nanosized zirconia at 140 °C. It is observed that pure cubic ZrO_2 is obtained in all the cases as shown by the XRD patterns in Figure 85a-c. These results indicate that NaOH stabilizes the cubic phase of ZrO_2 for the above mentioned concentrations.

In addition to the cubic phase, minor peaks of monoclinic zirconia crystal phase are seen around 28°, 40° and 55° in 1M aqueous NaOH (Figure 85c). NaOH (<1 M) is known to provide a mixture of cubic and monoclinic phase because of the lower concentration of NaOH that is unable to stabilize the cubic phase completely due to lesser number of Na^+ ions[411]. A decrease in the coherent diffraction domain size of ZrO_2 is observed upon increasing the concentration of aqueous NaOH from 1 M to 15 M as calculated from the Scherrer equation from the XRD pattern in Figure 85. The crystallite size decreases from 5.3 nm in 1 M aqueous NaOH to 4.3 nm (5 M) and 3.8 nm (15 M). The highest crystallite size is obtained for 1 M aqueous NaOH solution due to the presence of crystallites in

monoclinic phase in addition to the cubic phase as discussed in Section 7.1[411]. There is a decrease in the product yield from 85% in 1 M aqueous NaOH solution to 77% in 5 M and 15 M NaOH. The solvothermal synthesis of $M(NO_3)_x$ precursor (as in our case $ZrO(NO_3)_2.6H_2O$) to form MO_2 proceeds through the formation of a hydroxide species $M(OH)_x$ as explained previously in Section 2.3.2 in the literature review. It is a possibility that a mixture of $Zr(OH)_4$ and ZrO_2 is produced in the 1 M NaOH route as the solid product due to incomplete oxidation of $Zr(OH)_4$ to ZrO_2. If some amounts of $Zr(OH)_4$ is present in the product during the synthesis in 1 M NaOH, the product yield will increase due to the higher molecular weight of $Zr(OH)_4$ (159 g/mol) when compared to ZrO_2 (123 g/mol). Whereas in 5 M and 15 M, only ZrO_2 is produced. Kanade *et al.* have suggested the possibility of the formation of Zr-OH complexes during the hydrothermal synthesis of ZrO_2 in aqueous NaOH. Literature findings show that it is difficult to ascribe XRD pattern for $Zr(OH)_4$ due to it amorphous nature[427,428].

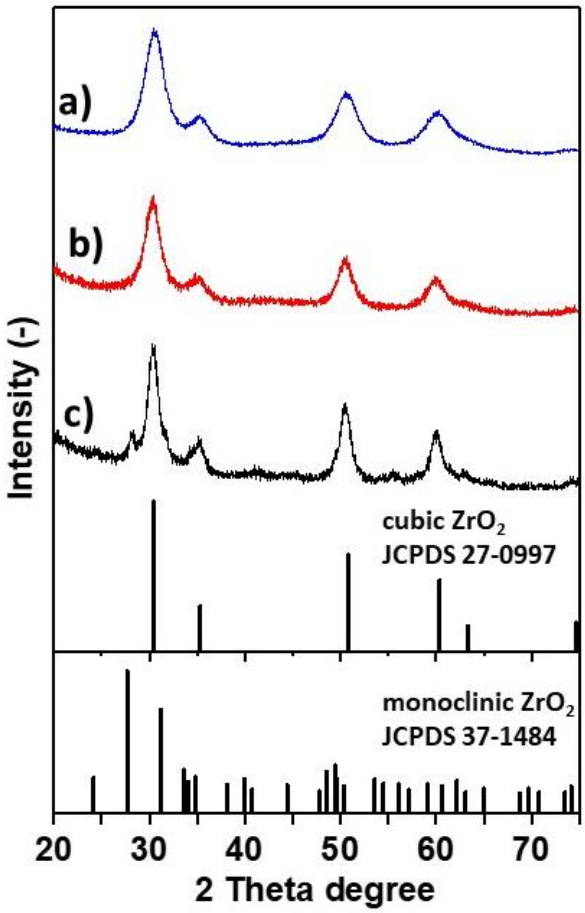

Figure 85: XRD patterns of nano ZrO_2 synthesized in different concentrations of NaOH solutions: a) 15 M, b) 5 M and c) 1 M. All the samples are prepared under hydrothermal conditions at 140 ℃ for 10 h.

The effect of temperature on the aqueous NaOH assisted solvothermal synthesis is studied by carrying out reactions at 140 ℃ and 180 ℃ for 10 h in aqueous NaOH (15 M). As seen from the XRD pattern in Figure 86, cubic phase of ZrO_2 is obtained under both temperature conditions. Larger coherent diffraction domain size of 7 nm is obtained at a higher temperature of 180 ℃ and ZrO_2 particle of size 3.8 nm is obtained under reaction conditions of 140 ℃. Similar observation of increase in particle size upon increasing the reaction temperature is also observed in reline/water synthesis (Section 7.3) and can be explained on the basis of increase in aggregation upon temperature increase.

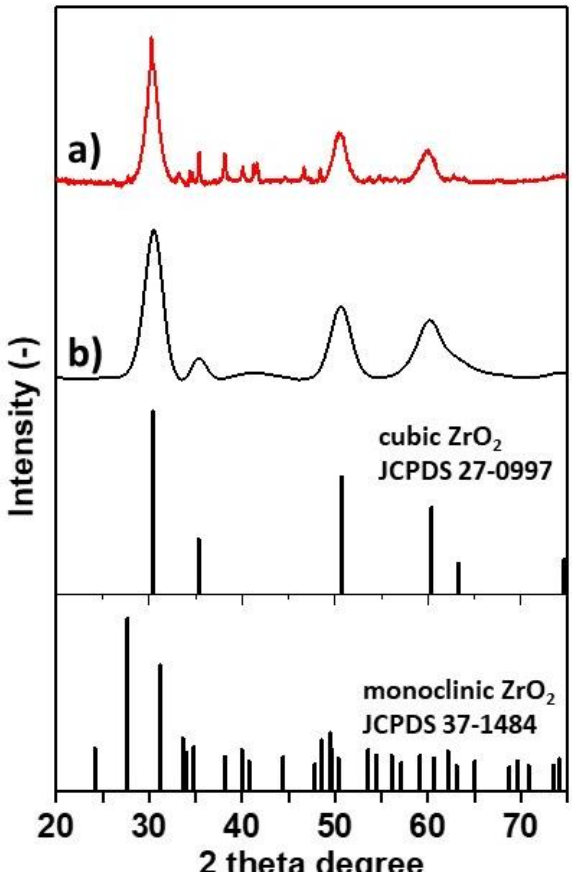

Figure 86: XRD patterns of nano ZrO_2 synthesized in different temperature conditions of NaOH solutions: a) 180 °C and b) 140 °C. All the samples are prepared under hydrothermal conditions for 10 h.

7.5 ZrO_2 as a catalytic support for CO oxidation

In the CO oxidation of gold supported catalyst, the interface between the gold nanoparticle and the metal oxide support plays a crucial role[429]. The increased catalytic activities at the interface is due to occurrence of CO oxidation at the metal/support border with a small energy barrier and adsorption of oxygen at the interface sites[430]. The interface activity between the metal nanoparticle and metal oxide greatly depends on the nature of the metal oxide support (such as reducible or non-reducible supports) and the crystal phase of the supports. For example in the case of Au/Al_2O_3 catalyst, the γ crystal phase of Al_2O_3 exhibits higher CO oxidation catalytic activity than the α phase due to better reducibility and redox properties[431]. The effect of zirconia crystal phase on the applications is already

discussed in the literature review (Chapter 2). In this section, CO oxidation of gold supported on monoclinic (prepared in reline/water 1:10 molar ratio at 140 °C for 10 h) and cubic ZrO_2 (aqueous NaOH 15 M at 140 °C for 10 h) is carried out to understand the effect of crystal phase of ZrO_2 on CO oxidation catalytic activities. The zirconia polymorphs have different surface environments due to difference in acidity-basicity sites and coordination numbers[187] hence it is crucial to investigate the influence of the crystal phase towards CO oxidation. Unlike ceria and ceria based materials which are used as active supports for CO oxidation in Chapter 6, zirconia is considered as a non-reducible support but zirconia becomes much more reducible at the nanoscale[432] in accordance to previous experimental studies[433]. Density functional theory calculations (DFT) have shown that at the nanoscale, zirconia turns from a non-reducible oxide to a reducible oxide due to the lower coordination number of Zr and O on the zirconia surface that introduces defective gaps and thus the reduction of Zr^{4+} species is easier due to these low-lying acceptor states[432]. For example, due to the higher coordination number of Zr and O ions in bulk zirconia, a higher energy value of +5.74 eV is required for hydrogen incorporation to reduce Zr^{4+} in comparison to +1.12 eV for nanostructured zirconia[432].

Puigdollers *et al.* have shown that in Au/ZrO_2 catalysts, Au is the active site for CO oxidation because Au further enhances the reducibility of the nano ZrO_2 and promotes the formation of surface oxygen vacancies[224]. The cost to remove oxygen from the zirconia surface is much lower in the presence of gold (+2.43 eV) in comparison to without gold (+5.79 eV) because of two key reasons: a) the stabilization of oxygen vacancies upon introducing Au in ZrO_2 is primarily due to the rearrangements in the local atomic environment on account of lattice strain mismatch between Au and ZrO_2; and b) ease in transfer of extra electrons to Au due to the creation of the oxygen vacancies[224]. Previous reports indicated the promising role of comparable small sized Au and ZrO_2 nanoparticles (both the metal and support in the size range of 2-5 nm) are advantageous towards catalytic activity in comparison to the bigger ZrO_2 nanoparticles (50 nm)[434,435]. This is due to the results from the electron paramagnetic resonance studies that shows the presence of crystal defects on the zirconia surface where the electrons are trapped in the oxygen vacancies and are readily available to supply electrons to the gold centres in Au/ZrO_2 samples when the ZrO_2 supports are smaller than 50 nm[433,436].

It is clear from the literature findings that the preparation method to synthesize Au/ZrO_2 catalysts is extremely crucial to ensure a monodisperse size distribution of small Au nanoparticles in the range of 2-4 nm. Based on our results on the synthesis of gold nanoparticles of size 1.6-3 nm in reline (Chapter 4) and using the preparation methodology of Au/ ceria-zirconia catalyst in chapter 6, Au supported on monoclinic ZrO_2 and cubic ZrO_2 are synthesized.

7.5.1 Characterization of Au/ZrO_2 catalysts

Catalysts with a theoretical gold loading of 5.6 wt% are prepared for both these supports and the preparation of the Au/ZrO_2 catalysts is carried out in pure reline as the solvent as described in the experimental section in Chapter 3. Inductively coupled plasma (ICP) technique is used to determine the actual gold loading on the supports by acid digestion of the catalysts itself. ICP results show that the actual gold loading on the supports are lower than the theoretical loading indicating that the gold is lost during the washing step of the catalysts or it is even possible that Au was not attached to the ZrO_2 surface in the first place (Table 23). The Au/m-ZrO_2 appears very pale pink in colour in comparison to the Au/c-ZrO_2 which is white. Pale-pink colour has been observed for Au supported catalysts due to the overlap of the 5d orbital of Au with the cationic orbitals of the support[437]. The properties of the gold support catalysts such as the colour, size and reduction temperatures are summarized in Table 23.

Table 23: Properties of the Au/ZrO_2 catalysts for different loadings of gold.

Catalyst	Colour	Theoretical loading % wt	Actual loading % wt[a]	Reduction temperature (°C)[b]	Au^0 size[c]
Au-m ZrO_2	pale pink	5.6%	0.73%	196	0.79 nm
Au-c ZrO_2	white	5.6%	0.27%	Centred around 200	0.052 nm

[a] Determined from ICP of the acid digested solid.

[b] Calculated from the TPR profiles.

[c] Calculated by pulse CO chemisorption at -80 °C after *in-situ* reduction at 200 °C.

The HR-TEM and HAADF-STEM micrographs of 0.73 wt% Au/m-ZrO_2 and 0.27 wt% Au/c-ZrO_2 are shown in Figure 87. Particle size distribution calculation of the Au

nanoparticles on the ZrO_2 supports is not possible due to the difficulty to observe the distinct gold nanoparticles. CO pulse chemisorption technique is used as a complementary tool in addition to electron microscopy to obtain more information on the size distribution for the samples. CO chemisorption usually provides the average size distribution of all the particles unlike electron microscopy measurements which provide only localized images. Details of particle size calculation by CO chemisorption technique and the possible sources of errors have been provided in Chapter 3 (Section 3.10.12). Very small gold nanoparticles of sizes less than 1 nm in the Au/ZrO_2 catalysts are recorded by CO pulse chemisorption after the catalysts are reduced *in-situ* at 200 ℃ as seen in Table 23. For particle diameters < 1.6 nm, the CO chemisorption technique approaches a limiting value[438].

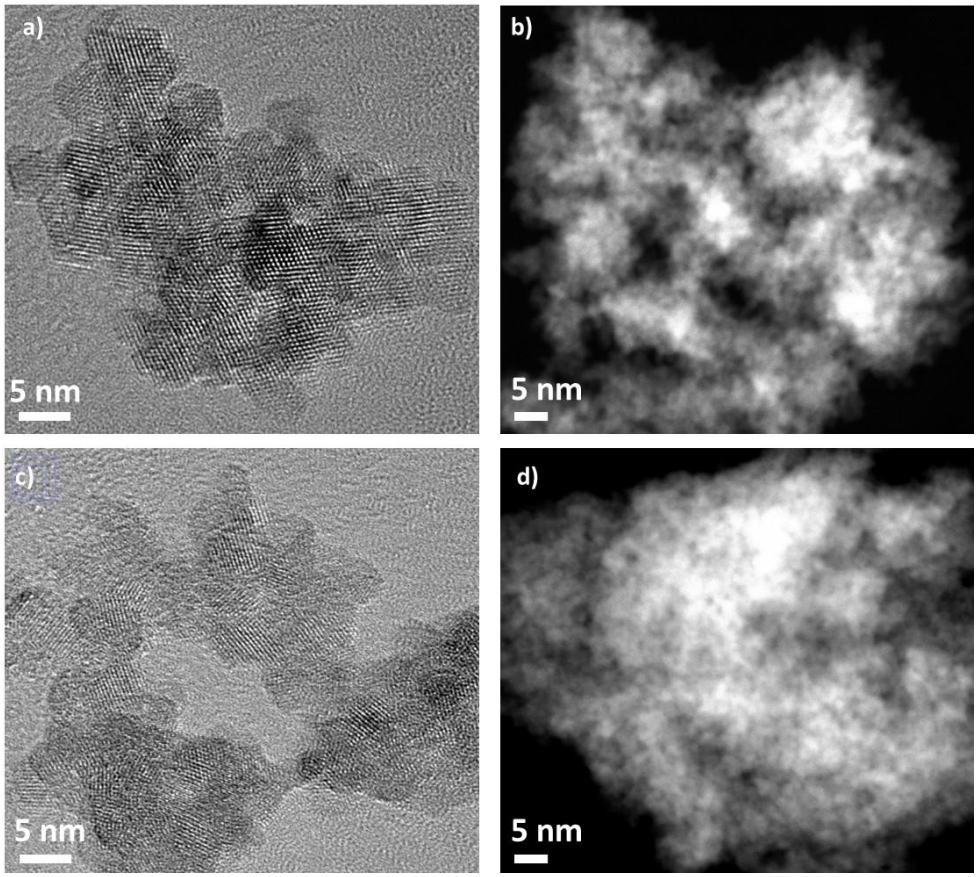

Figure 87: Electron microscopy micrographs of Au/ZrO_2 catalysts; 0.73 wt% Au/m-ZrO2, a) HR-TEM, b) HAADF-STEM; 0.27 wt% $Au/c-ZrO_2$, c) HR-TEM and d) HAADF-STEM. Monoclinic ZrO_2 is prepared in reline/water 1:10 by molar ratio and cubic ZrO_2 in aqueous NaOH (15 M) as the solvent at 140 ℃ for 10 h. The Au supported catalysts are prepared by combining the gold precursor and the supports in pure reline and stirring at 80 ℃ for 3 h.

The temperature programmed reduction (TPR) profiles of all the Au/ZrO_2 catalysts shows a reduction peak below 200 ℃ upon gold addition and additional broad peaks at temperatures beyond 200 ℃ are related to the reduction of Zr^{4+} to Zr^{3+} of the supports (Table 23 and Figure 88) in accordance to previous reports published elsewhere[187]. The low temperature peak observed below 200 ℃ upon gold addition is attributed to the reduction of oxygen species on the gold nanoparticles along with the shift in the surface reduction peaks of the supports towards lower temperature due to enhancement of the removal of surface oxygen by gold addition[439]. TPR studies are essential to determine the reduction temperature of the Au/ZrO_2 catalysts. In 0.27 wt% Au/cubic ZrO_2, the gold reduction peak is not clearly visible due to the low loading amounts on the support.

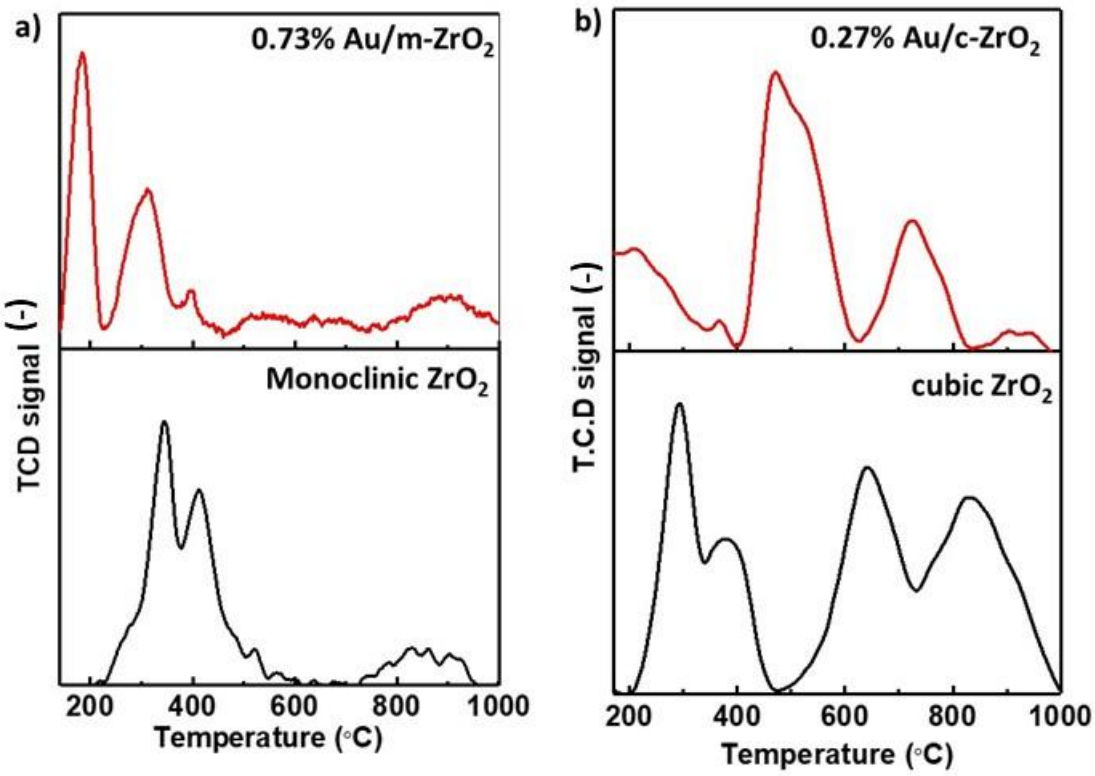

Figure 88: Temperature programmed reduction (TPR) profiles of Au/ZrO_2 catalysts; a) monoclinic ZrO_2 and Au/m-ZrO_2, b) cubic ZrO_2 and Au/c-ZrO_2. Monoclinic ZrO_2 is prepared in reline/water 1:10 by molar ratio and cubic ZrO_2 in aqueous NaOH (15 M) as the solvent at 140 ℃ for 10 h. The Au supported catalysts are prepared by combining the gold precursor and the supports in pure reline and stirring at 80 ℃ for 3 h.

7.5.2 Catalytic testing of Au/ZrO_2 catalysts

In order to assess the catalytic activities of the Au/ZrO_2 catalysts, the first catalytic cycle for CO oxidation and activation energy plots (from Arrhenius equation) is shown in Figure 89a comparing the two Au supported catalysts on monoclinic and cubic zirconia. 0.27 wt% $Au/c\text{-}ZrO_2$ exhibits a higher rate ($mol_{CO2}.mol_{Au}^{-1}.s^{-1}$) than 0.73 wt% $Au/m\text{-}ZrO_2$ (Table 24 and Figure 89c). In order to compare the reaction rates of the two catalysts, a set temperature of 280 °C is chosen to determine the values. The catalysts are pre-reduced *in-situ* in hydrogen at 200 °C prior to the CO oxidation reactions. 0.27 wt% $Au/c\text{-}ZrO_2$ shows the highest reaction rate with the lowest activation energy of 56 KJ/mol (Table 24).

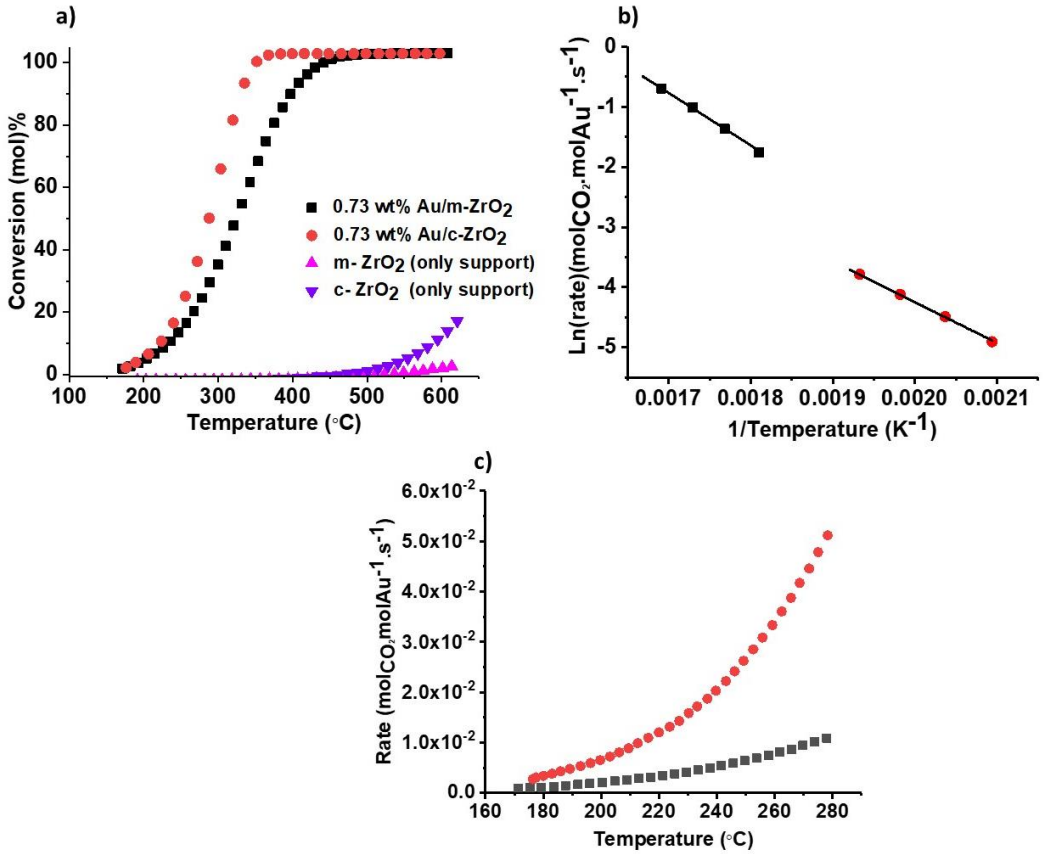

Figure 89: CO conversion mol% plots as a function of temperature for Au/ZrO_2 catalysts: a) 0.73% $Au/m\text{-}ZrO_2$ and 0.27% $Au/c\text{-}ZrO_2$, b) Arrhenius plots for 0.73% $Au/m\text{-}ZrO_2$ and 0.27% $Au/c\text{-}ZrO_2$ and c) rate of reaction for 0.73% $Au/m\text{-}ZrO_2$ and 0.27% $Au/c\text{-}ZrO_2$. All the catalysts are pre-reduced *in-situ* at 200 °C before the CO oxidation reaction. The Au supported catalysts are prepared by combining the gold precursor and the supports in pure reline and stirring at 80 °C for 3 h.

Table 24: Activation energies and temperatures for 50% CO conversion of the Au-ZrO_2 catalysts.

Catalyst[a]	T_{50} (°C)[b]	Activation energy[c] KJ/mol	$mol_{CO2}.mol_{Au}^{-1}.s^{-1}$ @ 280 °C
0.73% Au/m-ZrO_2	409	72	1.1×10^{-2} [d]
0.27%Au/c- ZrO_2	288	56	5.3×10^{-2} [e]

[a] Catalyst description with actual gold loading as determined from ICP studies.

[b] Temperature at which 50% CO conversion is observed.

[c] Activation energy as calculated from Arrhenius equation.

[d] 25% CO conversion achieved at 280 °C.

[d] 44% CO conversion achieved at 280 °C.

It is well known that CO oxidation for a gold supported metal oxide catalyst occurs at the Au particle-ZrO_2 boundary[440]. A scheme is proposed by Konova *et al.* to explain the CO oxidation occurring at the interface between Au and ZrO_2 border as explained in Figure 90[441]. The first step includes the 1) adsorption of CO on the gold nanoparticle to form an intermediate species that is comprised of CO adsorbed as a surface carbonyl on gold nanoparticle surface and lattice oxygen at the gold-ZrO_2 boundary; 2) If this intermediate complex decomposes, CO oxidation occurs readily by releasing CO_2; 3) However formation of carbonate ($Zr(CO_3)_2$) also occurs that depletes the availability of lattice oxygen at the border of gold-zirconia support; 4) The oxygen present in the gas phase adsorbs on the surface oxygen vacancy sites and undergoes a series of oxidation forms: $O_{2(g)}$-O_2-$_{(ads)}$-$2O^-_{(ads)}$-$2O^{2-}_{(ads)}$ that helps in replenishing oxygen into the active sites that can participate again in the CO oxidation reaction. The mechanism of CO oxidation on Au/ZrO_2 proposed by Konova et al. is also supported by the DFT calculations carried out by Puigdollers *et al.* where the key message is the increase in oxygen vacancies at the Au/ZrO_2 interface on account of Au incorporation in zirconia.

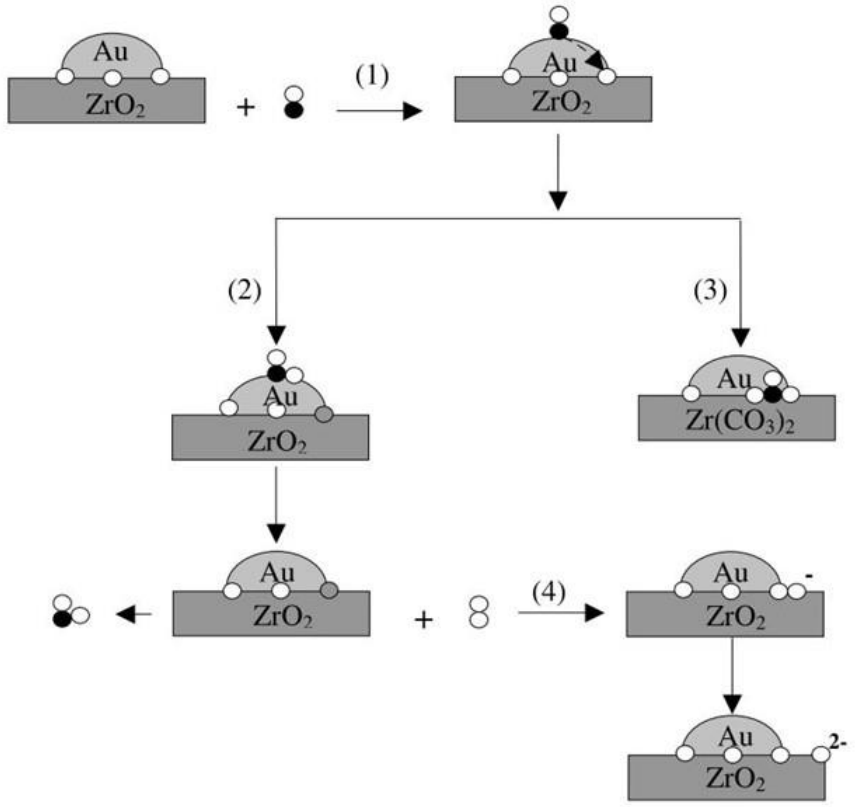

Figure 90: Reaction mechanism to explain CO oxidation on Au/ZrO_2 catalyst system (Directly reproduced from Ref [441] with permission from Elsevier).

In our case, Au supported on cubic ZrO_2 exhibits better catalytic activities which match the DFT predictions of Wang *et al.* on better CO oxidation activities at the Au/c-ZrO_2 surface. The presence of a higher concentration of oxygen vacancies in cubic ZrO_2 as shown from UV-vis absorption spectroscopy (Figure 81) and raman measurements (Figure 82) also supports the better reaction rates of gold supported on cubic zirconia catalyst due to the beneficial role of oxygen vacancies in the CO oxidation reactions in the catalyst as discussed in Chapter 6. Extensive DFT calculations are carried out by Wang *et al.* for CO oxidation on Au supported on monoclinic and tetragonal/cubic supports to show that crystal phase and structural defects greatly affect the reaction kinetics[442]. DFT results showed that the activation energies required for CO oxidation is lower on tetragonal/cubic phase (0.23 eV) in comparison to the monoclinic phase (0.39 eV). The interaction of the zirconia d states in tetragonal/cubic phase with oxygen is stronger (5.88 eV) than the

monoclinic phase (1.80 eV) and higher energy value of d states indicates higher activity of Zr cation sites.

However due to the different gold loadings on the monoclinic and cubic ZrO_2 support, it is difficult to conclude on the structure-functionality role for CO oxidation.

The reaction rates of our as-synthesized Au/ZrO_2 catalysts are compared with the literature reports on CO oxidation for $Au\text{-}ZrO_2$ catalysts (Table 25). A direct comparison of the crystal phase-activity relationship is not possible because all the ZrO_2 supports reported so far for CO oxidation reaction in Au/ZrO_2 samples is a mixture of monoclinic and tetragonal phase. The highest reaction rates are shown by the $Au\text{-}ZrO_2$ catalysts prepared by Zhang *et al.* where the authors demonstrated that a proper tuning of the Au^{3+}/Au^0 ratio is crucial to increase the catalytic performance[443]. In another work of Zhang *et al.*, the importance of small particle size of ZrO_2 (4-5 nm) in Au/ZrO_2 catalyst due to increase in the number of oxygen vacancies with small size was considered crucial for high rates of CO oxidation. Karwacki *et al.* have reported the role played by the surface hydroxyl groups on ZrO_2 surface for CO oxidation and showed there is an increase in the charge transfer at the nanoparticle-zirconia interface due to the formation of surface terminal and bridged hydroxyl species[444]. The reaction rates of our catalysts are comparable to the rates reported to the other catalysts in the literature.

Table 25: Summary of the activities of Au/ZrO_2 catalyst reported in literature.

Ref	Sample	Au wt%	Conversion %	Rate $mol_{CO2}.mol_{Au}^{-1}.s^{-1}$	Temperature(°C)
Our work	$Au\text{-}ZrO_2^{m}$	0.73	25	1.1×10^{-2}	280
	$Au\text{-}ZrO_2^{c}$	0.27	44	5.3×10^{-2}	280
[434]	$Au\text{-}ZrO_2$ $^{m+t}$	0.74	5	2.8×10^{-3}	69
	$Au\text{-}ZrO_2$ $^{m+t}$	0.63	13	9.2×10^{-3}	69
	$Au\text{-}ZrO_2$ $^{m+t}$	0.77	32	18.5×10^{-3}	69
[443]	$Au\text{-}ZrO_2$ $^{m+t}$	0.05	5	0.45	69
	$Au\text{-}ZrO_2$ $^{m+t}$	0.08	8	0.46	69
	$Au\text{-}ZrO_2$ $^{m+t}$	0.76	39	0.74	69
[444]	$Au\text{-}ZrO_2$ $^{m+t}$	2	-	24×10^{-3}	100
[445]	$Au\text{-}ZrO_2$ $^{m+t}$	1	< 15	0.34×10^{-3}	0

$^{m+t}$ mixture of monoclinic and tetragonal, c is cubic phase.

7.5.3 Thermal stabilities of Au/ZrO_2 catalysts

In the case of gold supported metal oxide catalysts, two of the most common causes of catalyst deactivation are due to increase in particle size upon sintering[446] and carbonate formation (due to adsorption of CO and CO_2 during CO oxidation reaction) at the gold-metal oxide interface that covers all the surface of the catalyst depleting obstructing the access of new oxygen to carry out oxidation reaction[441]. The stability checks for the 0.73 wt% Au/m-ZrO_2 and 0.27 wt% Au/c-ZrO_2 is carried out by performing three consecutive CO oxidation catalytic runs by increasing the temperature from 300 ℃ till 625 ℃ and then returning back to 300 ℃. A set temperature of 320 ℃ is chosen to study the changes in CO conversion percentage over three cycles. The changes in stabilities of the three catalysts are expressed in terms of change in the CO conversion % over the three cycles at 320 ℃. For 0.73 wt% Au/m-ZrO_2, there is a decrease in the thermal stability of 28% from the first cycle to the third cycle and for 0.27 wt% Au/c-ZrO_2, a decrease of 17% is observed between the 1st and third cycle (Figure 91 and Table 26). This result shows that 0.27 wt% Au/c-ZrO_2 is thermally more stable than 0.73 wt% Au/m-ZrO_2.

Due to the different surface acid-base properties of zirconia polymorphs, the strength of the interaction of CO and CO_2 is different for monoclinic and cubic zirconia[447]. As both CO_2 and CO are acidic in nature hence stronger surface adsorption of these occur on monoclinic zirconia due to the higher concentration of basic centres (hydroxyl groups and O^{2-} centres)[448]. Thus it is likely that carbonate formation occurs readily on monoclinic zirconia surface in comparison to cubic zirconia subsequently blocking the active sites and thus higher deactivation of Au/m-ZrO_2 catalyst in observed.

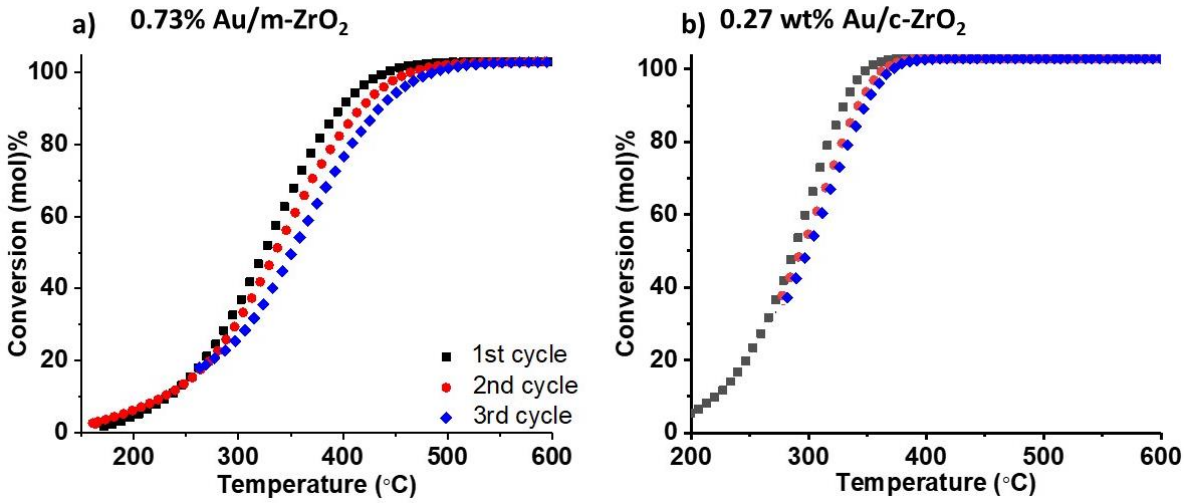

Figure 91: Consecutive CO conversion cycles to assess the thermal stabilities of the catalysts: a) 0.73 wt% Au/m-ZrO_2 and b) 0.27 wt% Au/c-ZrO_2. Monoclinic ZrO_2 is prepared in reline/water 1:10 by molar ratio and cubic ZrO_2 in aqueous NaOH (15M) as the solvent at 140 °C for 10 h.

Table 26: Thermal stabilities of the Au/m-ZrO_2 and Au/c-ZrO_2 at 320 °C over three consecutive cycles.

Catalyst	% CO conversion[a]	% CO conversion[b]	% CO conversion[c]
0.73% Au/m-ZrO_2	47	41	34
0.27% Au/c-ZrO_2	82	72	68

[a] 1st cycle, [b] 2nd cycle, [c] 3rd cycle.

7.6 Conclusions

This chapter presents the development and understanding of a novel facile and surfactant-free green solvent platform for the solvothermal synthesis of nanostructured zirconia ZrO_2 using the deep eutectic solvent reline without the addition of any external additives in the reaction medium.

The importance of the solvent environment to control and tune the crystalline phase of ZrO_2 has been explained. It is observed that whenever pure water or reline/water solutions are used as the solvent in the solvothermal synthesis, pure monoclinic phase is obtained. However the use of aqueous NaOH as the solvent produces pure cubic phase. Upon the dissolution of the zirconium precursor, the nuclei are in its cubic phase during the early stages of nucleation due to similarities between the precursor and the cubic crystal phase.

This cubic phase is stabilized by the Na^+ ions in NaOH by the heterovalent substitution of some Zr^{4+} ions by Na^+ ions ($Zr^{4+}_{1-x}Me_x^{n+}$ $O_{2-(2-n/2)x}$) in the hydroxo complex formed during the hydrothermal synthesis due to similarities in size between the Na^+ and Zr^{4+} ion. Whereas in pure water or reline water solutions, due to the absence of any alkali cation, the cubic phase is not stabilized and pure monoclinic phase is obtained.

Other factors such as effect of temperature and water addition in reline system on the synthesis of nanostructured ZrO_2 is reported herein. Irrespective of the water content and reaction temperatures in the reline system, pure monoclinic phase of ZrO_2 is always obtained. With an increase in the water content and temperature in the reline system, the size of nanocrystalline ZrO_2 grows indicating the active role played by water in the re-crystallization process. The influence of different concentrations of aqueous NaOH on the crystal phase of ZrO_2 is also studied. In lower concentration of aqueous NaOH like 1 M, traces of monoclinic phase appear due to the lack of Na^+ ions to stabilize the hydroxo complex for the cubic phase.

In order to study the crystal phase-activity relationship of nanostructured ZrO_2, CO oxidation catalytic reaction is carried out as model reaction for gold supported on monoclinic and cubic phase of ZrO_2 synthesized by the reline and NaOH route respectively. DFT calculations have shown that at the nanoscale, due to the presence of under-coordinated Zr and O ions, the non-reducible zirconia turns into reducible zirconia. The incorporation of Au in zirconia enhances the formation of surface oxygen vacancies as the energy cost to remove oxygen from the zirconia surface is lower in presence of Au than in the absence of Au. This lowering of energy cost is due to the residual lattice strain mismatch and charge transfer to Au as a result of vacancy creation by removing oxygen.

CO oxidation catalysis results show that 0.27 wt% Au/c-ZrO_2 exhibits higher catalytic activities per mol of Au than 0.73 wt% Au/ m-ZrO_2. The surface atom configuration and the oxygen vacancy sites present at the gold-zirconia interface plays a crucial role in determining the activities of the crystal phases of ZrO_2 towards CO oxidation. The catalytic activities of the as-synthesized Au-ZrO_2 catalysts are comparable to the other Au-ZrO_2 catalysts reported in the literature. The reaction rates of our as-synthesized Au/ZrO_2 catalysts are comparable with the other Au/ZrO_2 reported so far.

Thermal stability studies for CO oxidation over three consecutive cycles to assess the deactivation of catalysts showed that 0.27 wt% Au/c-ZrO_2 (17% deactivation between 1st and 3rd cycle) is more stable than 0.73 wt% Au/ m-ZrO_2 (28% deactivation between 1st and 3rd cycle). Due to the larger number of basic sites present on the surface of monoclinic zirconia in comparison to the cubic counterpart, adsorption of CO and CO_2 (being acidic molecules) is higher on monoclinic zirconia. This strong interaction of CO/CO_2 with the monoclinic surface leads to the formation of carbonates which blocks the active sites responsible for CO oxidation.

In addition to the influence of the crystal phase towards CO oxidation catalysis, other factors like actual metal loading on the supports and the active sites present between the interface between the metal nanoparticle and the support are equally important to assess the catalytic activities.

Chapter 8: Conclusions and future work

In this chapter, key conclusions from the whole thesis is presented along with the scientific evidences to validate the PhD research aim.

The overall aim of this thesis is to elucidate the various roles played by deep eutectic solvents in the synthesis of nanomaterials. The purpose of this work is to develop the understanding on the use of deep eutectic solvents as an 'all in one' platform to develop nanomaterials without the addition of any external additives in the system in order to reduce the overall chemical wastage and decrease the ecological footprint. In this thesis, two kinds of deep eutectic solvents are studied: i) reline which is formed by combining choline chloride and urea in the molar ratio of 1:2 and ii) asline which is formed between choline chloride and ascorbic acid in the molar ratio of 2:1. To achieve this aim, the main objective is to develop and understand the synthesis of nanomaterials from different families such as noble metals (Au), transition metal oxides (V_2O_5) and ceramic oxides (CeO_2 and ZrO_2) in DES to study the interaction of DES with a variety of materials.

In addition to playing versatile roles in the synthesis of nanomaterials, DES are eco-friendly and biodegradable and thus provides more greener ways to synthesize nanomaterials than the conventional harsh and corrosive bases like NaOH to prepare such materials.

In this work, the different chapters shed light on the different properties of the DES that plays the key role to synthesize a particular kind of nanomaterial. For e.g. Chapter 4 unravels the reducing and capping ligand properties of reline and asline to produce gold nanomaterials. Chapter 5 elucidates the templating action of reline to synthesize different morphologies of V_2O_5. Chapter 6 focusses on the synthesis of ceria-zirconia nanomaterials in reline and finally Chapter 7 throws light on the role of reline to produce a particular

crystalline phase (monoclinic) of ZrO_2. These nanomaterials are also tested for applications like plasmonics, Li-ion batteries and CO oxidation as model reactions.

8.1 Role of DES as a reducing and capping ligand

A one-pot synthesis method of gold nanomaterials in reline and asline systems separately are presented without the addition of any external additives. These results show that reline and asline present a platform to synthesize gold nanomaterials with significant effects on size and morphology. In the case of reline and reline/water systems, release of ammonia/ammonium ions are the in-situ reducing agents to reduce Au^{3+} to Au^0. As the reaction proceeds slowly (in the order of minutes for pure reline and hours for reline/water solution), each oxidation state of gold is identified upon observing the solution colour such as pale yellow, colourless and ruby red state for +3, +1 and 0 oxidation state respectively. Small gold nanoparticles of sizes 1.6-3 nm are produced in the reline and reline/water systems due to the stability provided by reline to prevent the agglomeration of the gold nanoparticles partially on account of the counter-ion layers. The intermolecular hydrogen bonded framework in reline plays a crucial catalytic role in the synthesis of gold nanoparticles because gold nanoparticles are formed much quicker in reline than in reline/water 1:10 by molar ratio system. In reline/water 1:10 solution, the hydrogen bonded framework is disrupted and hence the reline structure is altered upon the addition of water. Spherical gold nanoparticles are produced in pure reline and reline/water systems due to the absence of any anisotropic agents in reline.

In addition to these spherical gold nanoparticles, anisotropic morphologies like corrugated nanoballs or ‘nanowalnuts’ are synthesized in asline which plays dual roles as the solvent and template directing agent to synthesize nanowalnuts which exhibits surface enhanced Raman spectroscopy activities of Rhodamine B dye. The ascorbic acid moiety in asline is responsible for the reduction of gold precursor and the DGA (diketogulonic acid) component of ascorbic acid produces the corrugations on the nanowalnuts. The DES asline acts as the capping ligand to prevent the agglomeration of the gold nnaowalnuts.

8.2 Use of DES reline as template and exfoliating agent

The template property of reline and reline/water systems is elucidated when different morphologies of V_2O_5 such as nanoballs, nanosheets and nanofleece are synthesized on changing the water ratio in reline during the solvothermal synthesis. The generation of the different chain lengths of alkyl amine species produced from the decomposition of reline and reline/water mixtures during the solvothermal synthesis at 180 ℃ plays a key role in tuning the morphologies. The interaction between the vanadium crystallites and the solvent has been of importance to control the morphologies.

Reline/water 1:10 by molar ratio plays the role of exfoliating agent to produce ultra-thin V_2O_5 nanosheets by ionic intercalation, osmotic swelling and delamination into thin sheets due to the formation of long chain alkylamine species under solvothermal synthesis conditions. The interaction between the solvent environment and vanadium nuclei is also vital in shape control.

Nanoballs are produced due to the formation of short chain alkylamine species under solvothermal conditions for reline/water 1:2 by molar ratio solutions.

Ceria-zirconia nanorods are produced in reline/water solutions (1:10 by molar ratio) without the addition of any external additives in the reaction medium or high concentration corrosive bases followed by the detailed characterization of these nanostructures. The hydrolysis of urea in reline produces the template directing agent that aids the growth of 1D structures. The ability to synthesize small gold nanoparticles (1.6-3 nm) in reline systems is used to produce Au/ZrO_2 and Au/CeO_2-ZrO_2 catalysts in reline for CO oxidation reaction. Due to the weak stabilizing nature of reline, agglomeration of nanoparticles occurs and hence ceria-zirconia and zirconia materials are added as supports to prevent the aggregation of gold nanoparticles in reline. AC-STEM micrographs taken at different magnifications show that the agglomeration of gold nanoparticles is prevented in the presence of a support. Incorporation of zirconia in the ceria supports increases oxygen vacancies.

8.3 Importance of the solvent environment on the crystal phase of ZrO_2

The final crystal phase of ZrO_2 is shown to depend on the nature of the solvent. In the presence of NaOH, pure cubic phase of ZrO_2 is produced but in reline and reline/water solutions, pure monoclinic phase is always produced. This is observed due to the absence of any stabilizing ion in the reline/water mixtures which could stabilize the cubic phase of ZrO_2. Upon increasing the water concentrations and temperature of the reline system, pure monoclinic phase of zirconia is always obtained. The stability of the cubic phase by NaOH route is due to the stabilization offered by Na^+ ions in the hydroxo complexes.

The effect of crystal phase on the final applications is studied by preparing Au/ZrO_2 catalysts for CO oxidation studies. At the nanoscale, zirconia turns from a non-reducible support to a reducible support due to the presence of under-coordinated ions. The addition of gold enhances the reducibility of nano-zirconia further and stabilizes the oxygen vacancy sites.

8.4 Structure-activity relationship studies

The applications that are carried out in this thesis for the as-synthesized nanomaterials unequivocally emphasize the importance of a suitable synthesis route to obtain nanomaterials of desirable morphology and size. There is a strong relationship between the final applications shown by the materials and their underlying physico-chemical properties due to the resulting morphologies and sizes. An enhancement in the SERS signals of the Rhodamine B dye has been observed due to the corrugations on the surface of the nanowalnuts. Based on the distinct morphologies of V_2O_5, different activities are exhibited as cathode electrodes for Li-ion battery applications. V_2O_5 nanosheets show the best activities due to improved diffusion kinetics. In the synthesis of ceria-zirconia and bare zirconia materials followed by Au supported metal oxide catalyst preparation, a correlation between the oxygen vacancies and CO oxidation is undermined. Hence, these results show

that a proper control over the nanoparticle morphology and size is crucial for any desirable application.

8.5 Future work

The unique properties of DES have tremendous potential to act as a sustainable medium for the synthesis of nanomaterials as shown in this thesis. In order to scale-up the manufacturing of nanomaterials, there is an urgent need for low-viscosity DES options that could be used in the continuous synthesis processes. In comparison to the research done on IL, limited number of DES are known so far that are liquid at (or below) room temperatures. In this digital era, in order to save chemicals and resources, tools like machine learning could be possibly employed to carry out pre-screening analysis to devise suitable combinations of salts and hydrogen bond donors to form DES that have low viscosities and are liquid at room temperature conditions to utilize the capabilities of DES effectively for nanomaterial fabrication.

With the growing demands of batteries for several consumer electrical goods, it is extremely important to find ways in order to effectively recycle battery electrodes. As the earth has limited resources, it is vital to recycle and reuse the strategic and critical elements such as rare earth and platinum group metals. Due to the high solubilities of metals and metal oxides in DES, sustainable recycling of battery electrodes to extract valuable metals is a very promising application. As the DES also act as reducing agents, hence alternative routes to replace current energy intensive processes like hydrometallurgy to extract metals is possible. In this way, the recovered precursors from the batteries can be again used to grow nanomaterials in the DES to ensure minimum wastage.

Exploring the use of DES for electrodeposition techniques as they have exceptional advantages in comparison to aqueous medium such as wide electrochemical window and negligible vapour pressure (hence enabling deposition techniques even at higher temperatures). A solid fundamental understanding on the physical and electrochemical properties of the DES will accelerate and open more directions to use them for different applications.

As shown in this work, morphologies of nanomaterials play a crucial role in driving successful applications. Depending on the experimental parameters, it is possible to tune different morphologies and sizes of the materials at the nanoscale. However there are still challenges in the use of tunable morphologies for clinical applications due to several factors like biocompatibility issues, loss of material to reach the active sites and lack in precise control of the targets *in-situ*.

It is extremely important to synthesize nanomaterials of tunable shapes using techniques that are scalable, economical and feasible. Novel shapes like development of assembly of nanorods with space domains between nanorods are proposed in the literature to be effective towards plasmonic properties due to enhancement in electric fields. There is a need to develop morphologies tailored to respective applications with a better knowledge and understanding on the growth of nanomaterials. In addition to experimental paraneters, concepts in theory and computer simulation may provide answers and key guidelines in predicting the shape and growth mechanistics of nanomaterials in the near future.

Bibliography

(1) Roco, M. *J.Nanoparticle research* **2011**, 13 (2), 427-445.

(2) B. Shcherbakova, N. M. Zholobaka, N. Y. S. and V. K. I. *Russ. J. Inorg. Chem.* **2014**, *59* (13), 1556–1575.

(3) Polte, J. *CrystEngComm* **2015**, *17*, 6809–6830.

(4) Yamada, T.; Hayamizu, Y.; Yamamoto, Y.; Yomogida, Y.; Izadi-Najafabadi, A.; Futaba, D. N.; Hata, K. *Nat. Nanotechnol.* **2011**, *6* (5), 296–301.

(5) Baruah, S.; Dutta, J. *Environmental Chemistry Letters*. **2009**, 7(3), 191–204.

(6) Datta, S.; Torrente-Murciano, L. *Curr. Opin. Chem. Eng.* **2018**, *20*, 99–106.

(7) Torrente-Murciano, L.; Gilbank, A.; Na Puertolas, B.; Garcia, T.; Solsona, B.; Chadwick, D. *Appl. Catal. B Environ.* **2013**, *132* (133), 116–122.

(8) Bell, T. E.; González-Carballo, J. M.; Tooze, R. P.; Torrente-Murciano, L. *RSC Adv.* **2017**, *7* (36), 22369–22377.

(9) Abbott, A. P.; Capper, G.; Davies, D. L.; Munro, H. L.; Rasheed, R. K.; Tambyrajah, V. *Chem. Commun.* **2001**, *1* (19), 2010–2011.

(10) Wagle, D. V.; Zhao, H.; Baker, G. A. *Acc. Chem. Res.* **2014**, *47* (8), 2299–2308.

(11) Chavali, M. S.; Nikolova, M. P. *SN Appl. Sci.* **2019**, *1* (6), 607.

(12) Nikam, A. V.; Prasad, B. L. V.; Kulkarni, A. A. *CrystEngComm* **2018**, *20* (35), 5091–5107.

(13) Bakshi, M. S. *Cryst. Growth Des.* **2016**, *16* (2), 1104–1133.

(14) Duan, H.; Wang, D.; Li, Y. *Chem. Soc. Rev* **2015**, *44*, 5778–5792.

(15) Wu, K. J.; Torrente-Murciano, L. *React. Chem. Eng.* **2018**, *3* (3), 267–276.

(16) Welton, T. *Proc. R. Soc. A* **2015**, *471* (2183), 1–26.

(17) Wall, M. A.; Harmsen, S.; Pal, S.; Zhang, L.; Arianna, G.; Lombardi, J. R.; Drain, C. M.; Kircher, M. F. *Adv. Mater.* **2017**, *29* (21), 1605622–1605630.

(18) Kharissova, O. V.; Kharisov, B. I.; González, C. M. O.; Méndez, Y. P.; López, I. *R. Soc. Open Sci.* **2019**, *6* (11), 1–41.

(19) Smith, E. L.; Abbott, A. P.; Ryder, K. S. *Chem. Rev.* **2014**, *114* (21), 11060–11082.

(20) Zhang, Q.; De, K.; Vigier, O.; Royer, S.; Jeoe, F. *Chem. Soc. Rev. Chem. Soc. Rev* **2012**, *41* (41), 7108–7146.

(21) Walden, V. P. *Bull. l'Académie Impériale des Sci. St.-pétersbg.* **1914**, 405–422.

(22) Plechkova, N. V.; Seddon, K. R. *Chem. Soc. Rev.* **2007**, *37* (1), 123–150.

(23) Kudłak, B.; Owczarek, K.; Namieśnik, J. *Environ. Sci. Pollut. Res.* **2015**, *22* (16), 11975–11992.

(24) Pena-Pereira, F.; Namieśnik, J. *ChemSusChem* **2014**, *7* (7), 1784–1800.

(25) Petrucci, R. H. *J. Chem. Educ.* **1959**, *36* (12), 603–604.

(26) Christopher, R.; Mchem, H. Physical Properties of Alcohol Based Deep Eutectic Solvents (Doctoral dissertation), University of Leicester, 2008.

(27) Zhekenov, T.; Toksanbayev, N.; Kazakbayeva, Z.; Shah, D.; Mjalli, F. S. *Fluid Phase Equilib.* **2017**, *441*, 43–48.

(28) Abbott, A. P.; Barron, J. C.; Ryder, K. S.; Wilson, D. *Chem. - A Eur. J.* **2007**, *13* (22), 6495–6501.

(29) Florindo, C.; Oliveira, F. S.; Rebelo, L. P. N.; Fernandes, A. M.; Marrucho, I. M. *ACS Sustain. Chem. Eng.* **2014**, *2* (10), 2416–2425.

(30) Carriazo, D.; Serrano, M. C.; Gutiérrez, M. C.; Ferrer, L. M.; del Monte, F. *Chem.soc.rev.* **2015**, *41*, 23–45.

(31) Araujo, C. F.; Coutinho, J. A. P.; Nolasco, M. M.; Parker, S. F.; Ribeiro-Claro, P. J.

A.; Rudić, S.; Soares, B. I. G.; Vaz, P. D. *Phys. Chem. Chem. Phys.* **2017**, *19* (27), 17998–18009.

(32) Abbott, A. P.; Boothby, D.; Capper, G.; Davies, D. L.; Rasheed, R. K. *J. Am. Chem. Soc.* **2004**, *126* (29), 9142–9147.

(33) Zahn, S.; Kirchner, B.; Mollenhauer, D. *ChemPhysChem* **2016**, *17* (21), 3354–3358.

(34) Perkins, S. L.; Painter, P.; Colina, C. M. *J. Phys. Chem. B* **2013**, *117* (35), 10250–10260.

(35) Liu, W.; Zhang, K.; Chen, J.; Yu, J. *J. Mol. Liq.* **2018**, *260*, 173–179.

(36) Mjalli, F. S.; Ahmed, O. U. *Asia-Pacific J. Chem. Eng.* **2016**, *11* (4), 549–557.

(37) Yadav, A.; Pandey, S. *J. Chem. Eng. Data* **2014**, *59* (7), 2221–2229.

(38) Shah, D.; Mjalli, F. S. *Phys. Chem. Chem. Phys.* **2014**, *16* (43), 23900–23907.

(39) Abbott, A. P.; Capper, G.; Davies, D. L.; McKenzie, K. J.; Obi, S. U. *J. Chem. Eng. Data* **2006**, *51* (4), 1280–1282.

(40) Abo-Hamad, A.; Hayyan, M.; AlSaadi, M. A. H.; Hashim, M. A. *Chem. Eng. J.* **2015**, *273*, 551–567.

(41) Liao, H.-G.; Jiang, Y.-X.; Zhou, Z.-Y.; Chen, S.-P.; Sun, S.-G. *Angew. Chemie* **2008**, *120* (47), 9240–9243.

(42) Dreaden, E. C.; Austin, L. A.; Mackey, M. A.; El-Sayed, M. A. *Ther. Deliv.* **2012**, *3* (4), 457–478.

(43) Yeh, Y. C.; Creran, B.; Rotello, V. M. *Nanoscale*. Royal Society of Chemistry March 21, 2012, pp 1871–1880.

(44) Roduner, E. *Chem. Soc. Rev.* **2006**, *35* (7), 583–592.

(45) Kenneth J. Klabunde, Jane Stark, Olga Koper, Cathy Mohs, Dong G. Park, Shawn Decker, Yan Jiang, Isabelle Lagadic, and D. Z. *J.Phys.Chem.* **1996**, *100*, 12142–12153.

(46) Li, Y.; Shen, W. *Chem. Soc. Rev.* **2014**, *43* (5), 1543–1574.

(47) Grzelczak, M.; Pérez-Juste, J.; Mulvaney, P.; Liz-Marzán, L. M. *Chem. Soc. Rev.* **2008**, *37* (9), 1783–1791.

(48) Faraday, M. *Philos. Trans. R. Soc. London* **1857**, *147*, 145–181.

(49) Guerrero-Martínez, A.; Barbosa, S.; Pastoriza-Santos, I.; Liz-Marzán, L. M. *Curr. Opin. Colloid Interface Sci.* **2011**, *16*, 118–127.

(50) Vincent, B. *J. Colloid Interface Sci.* **1973**, *42* (2), 270–285.

(51) Hotze, E. M.; Phenrat, T.; Lowry, G. V. *J. Environ. Qual.* **2010**, *39* (6), 1909–1924.

(52) Park, S. J.; Seo, M. K. In *Interface Science and Technology*; 2011; Vol. 18, pp 1–57.

(53) Greenwood, B. M. Gold Nanoparticle Synthesis Turkevich method, 2006.

(54) Goel, A.; Rani, N. *Open J. Inorg. Chem.* **2012**, *2*, 67–73.

(55) Mayer, A. B. R. *Polym. Adv. Technol.* **2001**, *12* (1–2), 96–106.

(56) Viswanatha, R.; Sarma, D. D. *Growth of Nanocrystals in Solution*; 2007.

(57) Mer, V. K. La. *Ind. Eng. Chem.* **1952**, *44* (6), 1270–1277.

(58) Thanh, N. T. K.; Maclean, N.; Mahiddine, S. *Chem. Rev.* **2014**, *114* (15), 7610–7630.

(59) Bastús, N. G.; Comenge, J.; Puntes, V. *Langmuir* **2011**, *27* (17), 11098–11105.

(60) Ten Hove, J. B.; Schijven, L. M. I.; Wang, J.; Velders, A. H. *Chem. Commun.* **2018**, *54* (95), 13355–13358.

(61) Koczkur, K. M.; Mourdikoudis, S.; Polavarapu, L.; Skrabalak, S. E. *Dalt. Trans.* **2015**, *44* (41), 17883–17905.

(62) Piella, J.; Bastús, N. G.; Puntes, V. *Chem. Mater.* **2016**, *28* (4), 1066–1075.

(63) Liu, Y.; Male, K. B.; Bouvrette, P.; Luong, J. H. T. *Chem. Mater.* **2003**, *15* (22), 4172–4180.

(64) John Turkevich, B.; Cooper Stevenson, P.; Hillier, J. *A study of the nucleation and growth processes in the synthesis of colloidal gold*; Turkevich and Hillier, 1941; Vol. 47.

(65) Frens, G. *Nat. Phys. Sci.* **1973**, *241* (105), 20–22.

(66) Brust, M.; Walker, M.; Bethell, D.; Schiffrin, D. J.; Whyman, R. *J. Chem.Soc.Chem.Commun.* **1994**, 801–802.

(67) Xia, Y.; Xiong, Y.; Lim, B.; Skrabalak, S. E. *Angew. Chemie - Int. Ed.* **2009**, *48* (1), 60–103.

(68) Kim, F.; Connor, S.; Song, H.; Kuykendall, T.; Yang, P. *Angew. Chemie - Int. Ed.* **2004**, *43* (28), 3673–3677.

(69) Sánchez-Iglesias, A.; Pastoriza-Santos, I.; Pérez-Juste, J.; Rodríguez-González, B.; García De Abajo, F. J.; Liz-Marzán, L. M. *Adv. Mater.* **2006**, *18* (19), 2529–2534.

(70) John Turkevich, B.; Cooper Stevenson, P.; Hillier, J. *J. Phys. Chem.* **1951**, *57* (7), 670–673.

(71) Frens, G. *Nat. Phys. Sci.* **1973**, *241* (105), 20–22.

(72) Smitha, S. L.; Gopchandran, K. G.; Smijesh, N.; Philip, R. *Prog. Nat. Sci. Mater. Int.* **2013**, *23* (1), 36–43.

(73) Baumberg, J. J. *Faraday Discuss.* **2019**, *214*, 501.

(74) Chen, S.; Wang, Z. L.; Ballato, J.; Foulger, S. H.; Carroll, D. L. *J. Am. Chem. Soc.* **2003**, *125* (52), 16186–16187.

(75) Sau, T. K.; Murphy, C. J. *J.Am.Chem.Soc.* **2004**, *126*, 8648–8649.

(76) Kuo, C. H.; Huang, M. H. *Langmuir* **2005**, *21* (5), 2012–2016.

(77) Xu, J.; Zhao, T.; Liang, Z.; Zhu, L. *Chem. Mater.* **2008**, *20*, 1688–1690.

(78) Pastoriza-Santos, I.; Liz-Marzán, L. M. *Adv. Funct. Mater.* **2009**, *19* (5), 679–688.

(79) Zhang, H.; Cao, P.; Dou, J.; Cheng, L.; Niu, T.; Zhang, G. *RSC Adv.* **2018**, *8* (3),

1700–1705.

(80) Jia, W.; Li, J.; Jiang, L. *ACS Appl. Mater. Interfaces* **2013**, *5* (15), 6886–6892.

(81) Chen, H.; Kou, X.; Yang, Z.; Ni, W.; Wang, J. *Langmuir* **2008**, *24* (10), 5233–5237.

(82) Kettemann, F.; Witte, S.; Birnbaum, A.; Paul, B.; Clavel, G.; Pinna, N.; Rademann, K.; Kraehnert, R.; Jörg Polte. *ACS Catal.* **2019**, *13*, 5.

(83) Lopez, N.; Janssens, T. V. W.; Clausen, B. S.; Xu, Y.; Mavrikakis, M.; Bligaard, T.; Nørskov, J. K. *J. Catal.* **2004**, *223*, 232–235.

(84) Liao, H.-G.; Jiang, Y.-X.; Zhou, Z.-Y.; Chen, S.-P.; Sun, S.-G. *Angew. Chemie Int. Ed.* **2008**, *47* (47), 9100–9103.

(85) Mota-Morales, P. J. D.; Luna-Bárcenas, G.; Kumar-Krishnan, S.; Prokhorov, E.; Arias De Fuentes, O.; Ra Irez, M.; Bogdanchikova, N.; Sanchez, I. C.; Mota-Morales, J. D.; Luna-Arcenas, G. *J. Mater. Chem. A* **2015**, *3* (31), 15771–16362.

(86) Chirea, M.; Freitas, A.; Vasile, B. S.; Ghitulica, C.; Pereira, C. M.; Silva, F. *Langmuir* **2011**, *27*, 3906–3913.

(87) Stassi, S.; Cauda, V.; Canavese, G.; Manfredi, D.; Pirri, C. F. *Eur. J. Inorg. Chem.* **2012**, *2012* (16), 2669–2673.

(88) Lee, J. S. *Nanotechnol. Rev.* **2017**, *6* (3), 271–278.

(89) Li, A.; Chen, Y.; Zhuo, K.; Wang, C.; Wang, C.; Wang, J. *RSC Adv.* **2016**, *6* (11), 8786–8790.

(90) Mahyari, F. A.; Tohidi, M.; Safavi, A. *Mater. Res. Express* **2016**, *3* (9), 095006.

(91) Shen, G.; Chen, P. C.; Ryu, K.; Zhou, C. *J. Mater. Chem.* **2009**, *19* (7), 828–839.

(92) Wang, C.; Yin, L.; Zhang, L.; Xiang, D.; Gao, R. *Sensors* **2010**, *10* (3), 2088–2106.

(93) Wang, T. X.; Li, Y. G.; Liu, H. R.; Li, H.; Chen, S. X. *Mater. Lett.* **2014**, *124*, 148–150.

(94) Rodrigues, T. S.; Zhao, M.; Yang, T. H.; Gilroy, K. D.; da Silva, A. G. M.;

Camargo, P. H. C.; Xia, Y. *Chem. - A Eur. J.* **2018**, *24* (64), 16944–16963.

(95) Adschiri, T.; Hakuta, Y.; Arai, K. *Ind. Eng. Chem. Res.* **2000**, *39* (12), 4901–4907.

(96) Hayashi, H.; Hakuta, Y. *Materials (Basel).* **2010**, *3* (7), 3794–3817.

(97) van der Put, P. J.; van der Put, P. J. *Synthesis of Inorganic Materials*; 1998.

(98) Demazeau, G. *J. Mater. Sci.* **2008**, *43* (7), 2104–2114.

(99) Aliofkhazraei, M. *Handbook of nanoparticles*; 2015.

(100) Li, J.; Q Wu, W. *Synthesis of Nanoparticles via Solvothermal and Hydrothermal Methods*; 2015.

(101) Komarneni, S. *Curr. Sci.* **2003**, *85* (12), 1730–1734.

(102) Rimer, J. D.; Trofymluk, O.; Navrotsky, A.; Lobo, R. F.; Vlachos, D. G. *Chem. Mater.* **2007**, *19* (17), 4189–4197.

(103) Vogelsberger, W.; Schmidt, J.; Roelofs, F. *Colloids Surfaces A Physicochem. Eng. Asp.* **2008**, *324* (1–3), 51–57.

(104) Dinh, C.; Nguyen, T.; Kleitz, F.; Do, T. *Controlled Nanofabrication: advances and applications*; 2012, 327–367.

(105) Zhang, J.; Huang, F.; Lin, Z. *Nanoscale* **2010**, *2* (1), 18–34.

(106) Lee, E. J. H.; Ribeiro, C.; Longo, E.; Leite, E. R. *J. Phys. Chem. B* **2005**, *109* (44), 20842–20846.

(107) Ribeiro, C.; Vila, C.; Stroppa, D. B.; Mastelaro, V. R.; Bettini, J.; Longo, E.; Leite, E. R. *J. Phys. Chem. C* **2007**, *111* (16), 5871–5875.

(108) Jun, Y. W.; Casula, M. F.; Sim, J. H.; Kim, S. Y.; Cheon, J.; Alivisatos, A. P. *J. Am. Chem. Soc.* **2003**, *125* (51), 15981–15985.

(109) Feng, X.; Sayle, D. C.; Wang, Z. L.; Paras, M. S.; Santora, B.; Sutorik, A. C.; Sayle, T. X. T.; Yang, Y.; Ding, Y.; Wang, X.; Her, Y.-S. *Science* **2006**, *312* (5779), 1504–1508.

(110) Chen, D.; Wang, Y.; Zhao, G.; Fang,X.Y.; Jin, H.B.; Gao, P.; Zhu, C.L.; Cao, M.S.; Xiao, G. *J. Phys. Chem. C* **2010**, 114 (20), 9239-9244 .

(111) Nguyen, T. D.; Do, T. O. *J. Phys. Chem. C* **2009**, *113* (26), 11204–11214.

(112) Pinna, N.; Niederberger, M. *Angew. Chemie - Int. Ed.* **2008**, *47* (29), 5292–5304.

(113) Garnweitner, G.; Niederberger, M. *J. Am. Ceram. Soc.* **2006**, *89* (6), 1801–1808.

(114) Pinna, N.; Garnweitner, G.; Antonietti, M.; Niederberger, M. *J. Am. Chem. Soc.* **2005**, *127* (15), 5608–5612.

(115) Kongwudthiti, S.; Praserthdam, P.; Silveston, P.; Inoue, M. *Ceram. Int.* **2003**, *29* (7), 807–814.

(116) Inoue, M.; Kominami, H.; Inui, T. *Appl. Catal. A, Gen.* **1993**, *97* (2), 25–30.

(117) Zhang, D.; Zhang, X.; Ni, X.; Zheng, H.; Song, J. *Chem. Lett.* **2005**, *34* (2), 240.

(118) Emily R. Cooper, Christopher D. Andrews, Paul S. Wheatley, P. B. W.; Philip Wormald & Russell E. Morris. *Nature* **2004**, *430*, 1012–1015.

(119) Duan, X.; Ma, J.; Lian, J.; Zheng, W. *CrystEngComm* **2014**, *16*, 2550.

(120) Janiak, C. *Z. Naturforsch* **2013**, *68*, 1059–1089.

(121) Rao, G. R.; Mishra Braja Gopal. *Bull. Catal. Soc. India* **2003**, *2*, 122–134.

(122) Table 4.2.2. Lonic Radii (in Pm)* With Coordinatio... | Chegg.com https://www.chegg.com/homework-help/questions-and-answers/table-422-lonic-radii-pm-coordination-number-6-ion-radius-ion-radius-lorn-radius-ion-radiu-q32715704 (accessed Dec 23, 2019).

(123) Li, P.; Chen, X.; Li, Y.; Schwank, J. W. *Catal. Today* **2019**, 90–115.

(124) Alessandro Trovarelli; Carla de Leitenburg, Marta Boaro, G. D. *Catal. Today* **1999**, *50*, 535–367.

(125) Zhang, F.; Chan, S. W.; Spanier, J. E.; Apak, E.; Jin, Q.; Robinson, R. D.; Herman, I. P. *Appl. Phys. Lett.* **2002**, *80* (1), 127–129.

(126) Yamaguchi, I.; Watanabe, M.; Shinagawa, T.; Chigane, M.; Inaba, M.; Tasaka, A.; Izaki, M. *ACS Appl. Mater. Interfaces* **2009**, *1* (5), 1070–1075.

(127) Zhaolin Liu, Bing Guo, Liang Hong, H. J. *J. Phys. Chem. Solids* **2005**, *66*, 161–167.

(128) Sun, C.; Li, H.; Zhang, H.; Wang, Z.; Chen, L. *Nanotechnology* **2005**, *16* (9), 1454–1463.

(129) Song, Y.; Wei, J.; Yang, Y.; Yang, Z.; Yang, H. *J. Mater. Sci.* **2010**, *45* (15), 4158–4162.

(130) Kempaiah, D. M.; Yin, S.; Sato, T. *CrystEngComm* **2011**, *13* (3), 741–746.

(131) Fu, C.; Li, R.; Tang, Q.; Li, C.; Yin, S.; Sato, T. *Res. Chem. Intermed.* **2011**, *37* (2–5), 319–327.

(132) Arul, N. S.; Mangalaraj, D.; Kim, T. W. *J. Sol-Gel Sci. Technol.* **2013**, *66* (1), 15–21.

(133) Wang, H.; Zhu, J. J.; Zhu, J. M.; Liao, X. H.; Xu, S.; Ding, T.; Chen, H. Y. *Phys. Chem. Chem. Phys.* **2002**, *4* (15), 3794–3799.

(134) Sun, C.; Li, H.; Zhang, H.; Wang, Z.; Chen, L. *Nanotechnology* **2005**, *16* (9), 1454–1463.

(135) Vantomme, A.; Yuan, Z. Y.; Du, G.; Su, B. L. *Langmuir* **2005**, *21* (3), 1132–1135.

(136) Zhang, D.; Niu, F.; Li, H.; Shi, L.; Fang, J. *Powder Technol.* **2011**, *207* (1–3), 35–41.

(137) Hosokawa, S.; Shimamura, K.; Inoue, M. *Mater. Res. Bull.* **2011**, *46* (11), 1928–1932.

(138) Chen, G.; Xu, C.; Song, X.; Xu, S.; Ding, Y.; Sun, S. *Cryst. Growth Des.* **2008**, *8* (12), 4449–4453.

(139) Yang, Z.; Han, D.; Ma, D.; Liang, H.; Liu, L.; Yang, Y. *Cryst. Growth Des.* **2010**, *10* (1), 291–295.

(140) Zhang, D.; Niu, F.; Yan, T.; Shi, L.; Du, X.; Fang, J. *Appl. Surf. Sci.* **2011**, *257* (23),

10161–10167.

(141) Arul, N. S.; Mangalaraj, D.; Han, J. I. *Phys. status solidi - Rapid Res. Lett.* **2014**, *8* (7), 643–647.

(142) Zhou, F.; Zhao, X.; Xu, H.; Yuan, C. *J. Phys. Chem. C* **2007**, *111* (4), 1651–1657.

(143) Zhang, D.-E.; Zhang, X.-J.; Ni, X.-M.; Song, J.-M.; Zheng, H.-G. *ChemPhysChem* **2006**, *7* (12), 2468–2470.

(144) Guo, Z.; Du, F.; Li, G.; Cui, Z. *Inorg. Chem.* **2006**, *45* (10), 4167–4169.

(145) Si, R.; Flytzani-Stephanopoulos, M. *Angew. Chemie - Int. Ed.* **2008**, *47* (15), 2884–2887.

(146) Nolan, M.; Watson, G. W. *J. Phys. Chem. B* **2006**, *110* (33), 16600–16606.

(147) Sayle, T. X. T.; Parker, S.; Catlow, C. R. A. *Surf. Sci.* **1994**, *316*, 329–336.

(148) Conesa, J. C. *Surf. Sci.* **1995**, *339*, 337–352.

(149) Mai, H. X.; Sun, L. D.; Zhang, Y. W.; Si, R.; Feng, W.; Zhang, H. P.; Liu, H. C.; Yan, C. H. *J. Phys. Chem. B* **2005**, *109* (51), 24380–24385.

(150) Esch, F.; Fabris, S.; Zhou, L.; Montini, T.; Africh, C.; Fornasiero, P.; Comelli, G.; Rosei, R. *Science (80-.).* **2005**, *309* (5735), 752–755.

(151) Xu, J.; Harmer, J.; Li, G.; Chapman, T.; Collier, P.; Longworth, S.; Tsang, S. C. *Chem. Commun.* **2010**, *46* (11), 1887.

(152) Wu, Z.; Li, M.; Overbury, S. H. *J. Catal.* **2012**, *285* (1), 61–73.

(153) Alammar, T.; Noei, H.; Wang, Y.; Grünert, W.; Mudring, A.-V. *ACS Sustain. Chem. Eng.* **2015**, *3* (1), 42–54.

(154) Li, Z. X.; Li, L. Le; Yuan, Q.; Feng, W.; Xu, J.; Sun, L. D.; Song, W. G.; Yan, C. H. *J. Phys. Chem. C* **2008**, *112* (47), 18405–18411.

(155) Hammond, O. S.; Edler, K. J.; Bowron, D. T.; Torrente-Murciano, L. *Nat. Commun.* **2017**, *8*, 14150.

(156) Iqbal, J.; Shah, N. S.; Sayed, M.; Muhammad, N.; Rehman, S. ur; Khan, J. A.; Haq Khan, Z. U.; Howari, F. M.; Nazzal, Y.; Xavier, C.; Arshad, S.; Hussein, A.; Polychronopoulou, K. *J. Water Process Eng.* **2020**, *33*, 101012.

(157) Hannink, R. H. J.; Kelly, P. M.; Muddle, B. C. *J. Am. Ceram. Soc.* **2004**, *83* (3), 461–487.

(158) Brog, J. P.; Chanez, C. L.; Crochet, A.; Fromm, K. M. *RSC Adv.* **2013**, *3* (38), 16905–16931.

(159) Kaya, C.; He, J. Y.; Gu, X.; Butler, E. G. *Microporous Mesoporous Mater.* **2002**, *54*, 37–49.

(160) Reddy Channu, V.; Kalluru, R. R.; Schlesinger, M.; Mehring, M.; Holze, R. *Physicochem. Eng. Asp.* **2011**, *386*, 151–157.

(161) K. Geethalakshmi, T. P. and J. H. *Int. J. Mater. Metall. Eng.* **2012**, *6* (4), 256–259.

(162) Kumari, L.; Li, W. Z.; Xu, J. M.; Leblanc, R. M.; Wang, D. Z.; Li, Y.; Guo, H.; Zhang, J. *Cryst. Growth Des.* **2009**, *9* (9), 3874–3880.

(163) Behbahani, A.; Rowshanzamir, S.; Esmaeilifar, A. *Procedia Eng.* **2012**, *42*, 908–917.

(164) Shevchenko, A. V.; Ruban, A. K.; Dudnik, E. V.; Mel'nikova, V. A. *Powder Metall. Met. Ceram.* **1997**, *36* (7–8), 420–424.

(165) Taguchi, M.; Nakane, T.; Matsushita, A.; Sakka, Y.; Uchikoshi, T.; Funazukuri, T.; Naka, T. *J. Supercrit. Fluids* **2014**, *85*, 57–61.

(166) Li, W.; Huang, H.; Li, H.; Zhang, W.; Liu, H. *Langmuir* **2008**, *24* (15), 8358–8366.

(167) Zhu, H.; Yang, D.; Xi, Z.; Zhu, L. *J. Am. Ceram. Soc.* **2007**, *90* (4), 1334–1338.

(168) Jiao, X.; Chen, D.; Xiao, L. *J. Cryst. Growth* **2003**, *258* (1–2), 158–162.

(169) Espinoza-González, R. A.; Diaz-Droguett, D. E.; Avila, J. I.; Gonzalez-Fuentes, C. A.; Fuenzalida, V. M. *Mater. Lett.* **2011**, *65* (14), 2121–2123.

(170) Khan, S. A.; Fu, Z.; Rehman, S. S.; Asif, M.; Wang, W.; Wang, H. *Powder Technol.*

2014, *256*, 71–74.

(171) Wang, Z.; Lu, Y.; Yuan, S.; Shi, L.; Zhao, Y.; Zhang, M.; Deng, W. *J. Colloid Interface Sci.* **2013**, *396*, 9–15.

(172) Reddy, C. V.; Babu, B.; Reddy, I. N.; Shim, J. *Ceram. Int.* **2018**, *44* (6), 6940–6948.

(173) Dell'Agli, G.; Colantuono, A.; Mascolo, G. *Solid State Ionics* **1999**, *123* (1–4), 87–94.

(174) Mottet, B.; Pichavant, M.; Bény, J. -M; Alary, J. -A. *J. Am. Ceram. Soc.* **1992**, *75* (9), 2515–2519.

(175) Kolen'ko, Y. V.; Maximov, V. D.; Burukhin, A. A.; Muhanov, V. A.; Churagulov, B. R. *Mater. Sci. Eng. C* **2003**, *23* (6–8), 1033–1038.

(176) Zhang, J.; Song, B.; Peng, W.; Feng, Y.; Xu, B. *Mater. Chem. Phys.* **2010**, *123*, 606–609.

(177) Ji, X.; Liu, C.; Liu, C.; Li, J.; Yu, X.; Su, P.; Huang, J.; Jia, J.; Wu, J.; Chen, L.; Chen, C.; Wu, Y.; Fan, Y.; Lin, J.; Cheng, B.; Tang, C. *Mater. Lett.* **2014**, *122*, 309–311.

(178) Liu, C.; Zhao, S.; Ji, X.; Wang, B.; Ma, D. *Mater. Chem. Phys.* **2012**, *133*, 579–583.

(179) Xie, S.; Iglesia, E.; Bell, A. T. *Chem. Mater.* **2000**, *12* (8), 2442–2447.

(180) Murase, Y.; Kato, E. *J. Am. Ceram. Soc.* **1983**, *66* (3), 196–200.

(181) Kelly, J. R.; Denry, I. *Dent. Mater.* **2008**, *24* (3), 289–298.

(182) Xie, H.; Lu, J.; Shekhar, M.; Elam, J. W.; Delgass, W. N.; Ribeiro, F. H.; Weitz, E.; Poeppelmeier, K. R. *ACS Catal.* **2013**, *3* (1), 61–73.

(183) Bumajdad, A.; Nazeer, A. A.; Al Sagheer, F.; Nahar, S.; Zaki, M. I. *Sci. Rep.* **2018**, *8*, 3695.

(184) Zhong-Yi Ma, Cheng Yang, Wei Wei, Wen-Huai Li, Y.-H. S. *J. Mol. Catal. A* **2005**, *227*, 119–124.

(185) Basahel, S. N.; Ali, T. T.; Mokhtar, M.; Narasimharao, K. *Nanoscale Res. Lett.* **2015**, *10* (1).

(186) Taek Jung, K.; Bell, A. T. *Catal. Letters* **2002**, *80*, 63–68.

(187) Li, J.; Chen, J.; Song, W.; Liu, J.; Shen, W. *Appl. Catal. A Gen.* **2008**, *334* (1–2), 321–329.

(188) Chary, K. V. R.; Ramesh, K.; Naresh, D.; Rao, P. V. R.; Rao, A. R.; Rao, V. V. *Catal. Today* **2009**, *141* (1–2), 187–194.

(189) Zhou, G.; Liu, J.; Tan, X.; Pei, Y.; Qiao, M.; Fan, K.; Zong, B. *Ind. Eng. Chem. Res* **2012**, *51*, 12205–12213.

(190) Ma, Z.-Y.; Yang, C.; Wei, W.; Li, W.-H.; Sun, Y.-H. *J. Mol. Catal. A Chem.* **2005**, *231*, 75–81.

(191) Althues, H.; Kaskel, S. *Langmuir* **2002**, *18* (20), 7428–7435.

(192) Dong, W.-S.; Lin, F.-Q.; Liu, C.-L.; Li, M.-Y. *J. Colloid Interface Sci.* **2009**, *333*, 734–740.

(193) Li, N.; Dong, B.; Yuan, W.; Gao, an; Zheng, L.; Huang, Y.; Wang, S. *J. Dispers. Sci. Technol.* **2007**, *287*, 1030–1033.

(194) Liu, L.; Chen, Z.-F.; Wei, H.-B.; Li, Y.; Fu, Y.-C.; Xu, H.; Li, J.-P.; Slawin, A. M. Z.; Dong, J.-X. *Inorg. Chem* **2010**, *49*, 8270–8275.

(195) Wang, W.; Liu, L.; Yang, J.; Li, S.; Li, J.; Dong, J. *Dalt. Trans.* **2012**, *41* (41), 12915–12919.

(196) Liu, L.; Yang, J.; Li, J.; Dong, J.; Šišak, D.; Luzzatto, M.; McCusker, L. B. *Angew. Chemie Int. Ed.* **2011**, *50* (35), 8139–8142.

(197) Smeets, S.; Liu, L.; Dong, J.; McCusker, L. B. *Inorg. Chem.* **2015**, *54* (16), 7953–7958.

(198) Cao, A.-M.; Hu, J.-S.; Liang, H.-P.; Wan, L.-J. *Angew . Chem . Int . Ed* **2005**, *44*, 4391–4395.

(199) Zhang, Y.; Zheng, J.; Zhao, Y.; Hu, T.; Gao, Z.; Meng, C. *Appl. Surf. Sci.* **2016**, *377*, 385–393.

(200) Mao, C.-J.; Pan, H.-C.; Wu, X.-C.; Zhu, J.-J.; Chen, H.-Y. *J.Phys.Chem.B* **2006**, *110*, 14709–14713.

(201) Wang, S.; Lu, Z.; Wang, D.; Li, C.; Chen, C.; Yin, Y. *J.Mater.Chem.* **2011**, *21*, 6365–6369.

(202) Sucharitakul, S.; Ye, G.; Lambrecht, W. R. L.; Bhandari, C.; Gross, A.; He, R.; Poelman, H.; Gao, X. P. A. *ACS Appl. Mater. Interfaces* **2017**, *9*, 9.

(203) Beke, S. *Thin Solid Films* **2011**, *519*, 1761–1771.

(204) Enjalbert, R.; Galy, J. *Bull. Soc. Fr. Mindr. Cristal.* **1970**, *24*, 1467–1469.

(205) Minić, D. M.; Blagojević, V. A. *CrystEngComm* **2013**, *15* (33), 6617–6624.

(206) Avansi, W.; Ribeiro, C.; Leite, E. R.; Mastelaro, V. R. *Cryst. Growth Des.* **2009**, *9* (8), 3626–3631.

(207) Zeng, M.; Yin, H.; Yu, K. *Chem. Eng. J.* **2012**, *188*, 64–70.

(208) Juyi Mu, J. W.; Jinghua Hao, Pin Cao, Shuoqing Zhao, Wen Zeng, Bin Miao, S. *Ceram. Int.* **2015**, *41*, 12626–12632.

(209) Kim, Y. B.; Shin, W. *Mater. Lett.* **2014**, *132*, 247–250.

(210) Wu, Z.; Yang, S.; Wu, W. *Nanoscale* **2015**, *8*, 1237.

(211) Li, B.; Xu, Y.; Rong, G.; Jing, M.; Xie, Y. *Nanotechnology* **2006**, *17* (10), 2560–2566.

(212) Pan, A.; Wu, H. Bin; Yu, L.; Lou, X. W. D. *Angew. Chemie* **2013**, *125* (8), 2282–2286.

(213) Al, M.; Ae, Z.; Farag, H. K.; Endres, A. F. *J. Mater. Sci* **2009**, *44*, 1363–1373.

(214) Manjunath, K.; D'Souza, V.; Dupont, J.; Ramakrishnappa, T.; Nagaraju, G. *Ionic liquid intercalated V2O5 nanorods: Synthesis and characterization*; 2015; Vol. 38.

(215) Patil, H. R.; Murthy, Z. V. P. *Chem. Eng. Process. Process Intensif.* **2016**, *102*, 130–140.

(216) Li, G.; Zhang, Q.; Fang, W.; Zhao, Y. *Energy Environ. Focus* **2015**, *4*, 301–306.

(217) Aidoudi, F. H.; Byrne, P. J.; Allan, P. K.; Teat, S. J.; Lightfoot, P.; Morris, R. E. *Dalt. Trans.* **2011**, *40* (16), 4324–4331.

(218) Soubaihi, R. M. Al; Saoud, K. M.; Dutta, J. *Catalysts*. MDPI AG December 1, 2018.

(219) Haruta, M. *J. Catal.* **1989**, *115* (2), 301–309.

(220) Hutchings, G. J.; Brust, M.; Schmidbaur, H. *Chem. Soc. Rev.* **2008**, *37* (9), 1759–1765.

(221) Landman, U.; Yoon, B.; Zhang, C.; Heiz, U.; Arenz, M. *Top. Catal.* **2007**, *44* (1–2), 145–158.

(222) Haruta, M. *Catal. Today* **1997**, *36* (1), 153–166.

(223) Lohrenscheit, M.; Hess, C. *ChemCatChem* **2016**, *8* (3), 523–526.

(224) Puigdollers, A. R.; Pacchioni, G. *ChemCatChem* **2017**, *9* (6), 1119–1127.

(225) Liu, B.; Li, W.; Song, W.; Liu, J. *Phys. Chem. Chem. Phys* **2018**, *20*, 16045.

(226) Zeng, M.; Liu, J.; Ding, Y.; He, W.; Lan, R.; Tang, Y.; Zhou, M.; Yu, X. *CrystEngComm* **2019**, *21* (19), 3056–3063.

(227) Chen, M.; Zou, Y.; Wu, L.; Pan, Q.; Yang, D.; Hu, H.; Tan, Y.; Zhong, Q.; Xu, Y.; Liu, H.; Sun, B.; Zhang, Q. *Adv. Funct. Mater.* **2017**, *27* (23), 1701121.

(228) Brewster, D. A.; Bian, Y.; Knowles, K. E. *Chem. Mater.* **2020**, *32* (5), 2004–2013.

(229) Preciado-Flores, S.; Wang, D.; Wheeler, D. A.; Newhouse, R.; Hensel, J. K.; Schwartzberg, A.; Wang, L.; Zhu, J.; Barboza-Flores, M.; Zhang, J. Z. *J. Mater. Chem.* **2011**, *21* (7), 2344–2350.

(230) Famengo, A.; Anantharaman, S.; Ischia, G.; Causin, V.; Natile, M. M.; Maccato, C.; Tondello, E.; Bertagnolli, H.; Gross, S. *Eur. J. Inorg. Chem.* **2009**, *2009* (33), 5017–

5028.

(231) Balzar, D.; Ledbetter, H. *J. Appl. Crystallogr.* **1993**, *26*, 97–103.

(232) Hargreaves, J. S. J. *Catalysis, Structure & Reactivity*, **2016**, 2, 33-37.

(233) Atribak, I.; Bueno-López, A.; García-García, A. *J. Mol. Catal. A Chem.* **2009**, *300*, 103–110.

(234) Torrente-Murciano, L. *J. Nanoparticle Res.* **2016**, *18* (4).

(235) Ren, J.; Tilley, R. D. *J. Am. Chem. Soc.* **2007**, *129*, 3287–3291.

(236) Huang, H.; Toit, H. du; Besenhard, M. O.; Ben-Jaber, S.; Dobson, P.; Parkin, I.; Gavriilidis, A. *Chem. Eng. Sci.* **2018**, *189*, 422–430.

(237) Halder, A.; Ravishankar, N. *Adv. Mater.* **2007**, *19* (14), 1854–1858.

(238) Bir, D.; Tutin, K. *J. Chromatogr. Sci.* **2002**, *40* (6), 337–342.

(239) Okabayashi, K.; Alvi, N.; Than, A.; Saulys, D.; Safvi, S. A.; Gaines, D. F.; Kuech, T. F. *The Finite Element Method in Thermo-mechanics*; Allen & Uniwin, 1997; Vol. 144.

(240) Haerens, K.; Matthijs, E.; Binnemans, K.; Van Der Bruggen, B. *Green Chem.* **2009**, *11* (9), 1357.

(241) Duyuan Yuea,b, Yongzhong Jiaa, Ying Yaoa, Jinhe Suna, Y. J. *Electrochim. Acta* **2012**, *65*, 30–36.

(242) Dragerwerk. *Detect chlorine gas more efficiently and safely*.

(243) Rangel-Vazquez, N. A.; Sánchez-López, C.; Rodríguez Felix, F. *Polimeros* **2014**, *24* (4), 453–463.

(244) D'Agostino, C.; Gladden, L. F.; Mantle, M. D.; Abbott, A. P.; Ahmed, E. I.; Al-Murshedi, A. Y. M.; Harris, R. C. *Phys. Chem. Chem. Phys.* **2015**, *17* (23), 15297–15304.

(245) Udert, K. M.; Larsen, T. A.; Biebow, M.; Gujer, W. *Water Res.* **2003**, *37* (11),

2571–2582.

(246) Lau, K. T.; Edwards, S.; Diamond, D. *Sensors Actuators, B Chem.* **2004**, *98* (1), 12–17.

(247) Wakeland, S.; Martinez, R.; Grey, J. K.; Luhrs, C. C. *Carbon N. Y.* **2010**, *48* (12), 3463–3470.

(248) Debbarma, M.; Das, S.; Saha, M. *Adv. Manuf.* **2013**, *1* (2), 183–186.

(249) Kasapoğlu, N.; Baykal, A.; Köseoğlu, Y.; Toprak, M. S. *Scr. Mater.* **2007**, *57* (5), 441–444.

(250) Danwanichakul, P.; Suwatthanarak, T.; Suwanvisith, C.; Danwanichakul, D. *J. Nanosci.* **2016**, *2016*, 1–6.

(251) Lousa, D.; Baptista, A. M.; Soares, C. M. *Physical Chemistry Chemical Physics*. 2013, pp 13723–13736.

(252) Kim, H. S.; Ha, S. H.; Sethaphong, L.; Koo, Y. M.; Yingling, Y. G. *Phys. Chem. Chem. Phys.* **2014**, *16* (7), 2944–2953.

(253) Kaur, S.; Sharma, S.; Kashyap, H. K. *J. Chem. Phys* **2017**, *147*, 194507.

(254) Kumari, P.; Kaur, S.; Kashyap, H. K. *ACS Omega* **2019**, *3*, 15246–15255.

(255) Hammond, O. S.; Bowron, D. T.; Edler, K. J. *Angew. Chemie* **2017**, *56*, 9782–9785.

(256) Wang, Y.; He, J.; Liu, C.; Chong, W. H.; Chen, H. *Angew. Chemie Int. Ed.* **2015**, *54* (7), 2022–2051.

(257) Jose, M.; Sakthivel, M. *Mater. Lett.* **2014**, *117*, 78–81.

(258) Gorup, L. F.; Longo, E.; Leite, E. R.; Camargo, E. R. *Journal of Colloid and Interface Science*. 2011, pp 355–358.

(259) Dupont, J.; Scholten, J. D. *Chem. Soc. Rev.* **2010**, *39* (5), 1780–1804.

(260) Astruc, D.; Lu, F.; Aranzaes, J. R. *Angew. Chemie - Int. Ed.* **2005**, *44* (48), 7852–7872.

(261) Vollmer, C.; Janiak, C. *Coord. Chem. Rev.* **2011**, *255* (17–18), 2039–2057.

(262) Janiak, C; Hardacre, C.; Parvulescu, V. Metal Nanoparticle synthesis in ionic liquids; RSC, 2014; Vol. 51, pp 537-577. Online link: https://doi.org/10.1039/9781849737210-00537

(263) Gammons, C. H.; Yu, Y.; Williams-jones, A. E. *The disproportionation of gold(I) chloride complexes at 25 to 200°C*; 1997; Vol. 61.

(264) Motl, N. E.; Smith, A. F.; Desantis, C. J.; Skrabalak, S. E. *Chem. Soc. Rev.* **2014**, *43* (11), 3823–3834.

(265) Tadros, T. In *Encyclopedia of Colloid and Interface Science*; Springer Berlin Heidelberg, 2013; pp 820–820.

(266) Qin, Y.; Song, Y.; Sun, N.; Zhao, N.; Li, M.; Qi, L. *Chem. Mater.* **2008**, *20* (12), 3965–3972.

(267) Zhang, H.; Lu, Y.; Liu, H.; Fang, J. *RSC Adv.* **2014**, *4* (69), 36757–36764.

(268) Kim, D. Y.; Yu, T.; Cho, E. C.; Ma, Y.; Park, O. O.; Xia, Y. *Angew. Chemie - Int. Ed.* **2011**, *50* (28), 6328–6331.

(269) Luty-Błocho, M.; Wojnicki, M.; Fitzner, K. *Int J Chem Kinet* **2017**, *49*, 789–797.

(270) Ann M.Bode, Lane Cunningham, R. C. R. *Clin. Chem.* **1990**, *36* (10), 1807–1809.

(271) Wang, L.; Hu, C.; Nemoto, Y.; Tateyama, Y.; Yamauchi, Y. *Cryst. Growth Des.* **2010**, *10* (8), 3454–3460.

(272) Huang, D.; Bai, X.; Zheng, L. *J. Phys. Chem. C* **2011**, *115*, 14641–14647.

(273) Ghosh, S.; Manna, L. *Chem. Rev.* **2018**, *118* (16), 7804–7864.

(274) Langille, M. R.; Personick, M. L.; Zhang, J.; Mirkin, C. A. *J. Am. Chem. Soc.* **2012**, *134* (35), 14542–14554.

(275) Bard, A. J.; Parsons, R.; Jordan, J. *Standard Potentials in Aqueous Solution*; Routledge, 2017.

(276) Rai, A.; Singh, A.; Ahmad, A.; Sastry, M. *Langmuir* **2006**, *22* (2), 736–741.

(277) Pearson, R. G. *J. Chem. Educ.* **1968**, *45* (9), 581.

(278) Agnihotri, S.; Mukherji, S.; Mukherji, S. *RSC Adv.* **2014**, *4* (8), 3974–3983.

(279) Starowicz, Z.; Wojnarowska-Nowak, R.; Ozga, P.; Sheregii, E. M. *Colloid Polym. Sci.* **2018**, *296* (6), 1029–1037.

(280) Parker, J. H.; Feldman, D. W.; Ashkin, M. *Raman scattering by silicon and germanium*; 1967; Vol. 155.

(281) Li, J. F.; Li, C. Y.; Aroca, R. F. *Chemical Society Reviews*. Royal Society of Chemistry July 7, 2017, pp 3962–3979.

(282) Liu, M.; Su, B.; Tang, Y.; Jiang, X.; Yu, A. *Adv. Energy Mater.* **2017**, *7* (23), 1700885.

(283) E.A. Flugel, A.; Ranft, A.; Haase, F.; Lotsch, B. V. *J.Mater.Chem.* **2012**, *22*, 10119–10133.

(284) Li, Z.; Zhang, H.; Liu, Q.; Stanciu, L.; Li, Z.-F.; Liu, Y.; Xie, J. *ACS Appl. Mater. Interfaces* **2018**, *6*, 18894–18900.

(285) Barreto, G. P.; Morales, G.; Quintanilla, M. L. L. *J. Mater.* **2013**, *2013* (1), 1–11.

(286) Chou, S. L.; Wang, J. Z.; Sun, J. Z.; Wexler, D.; Forsyth, M.; Liu, H. K.; MacFarlane, D. R.; Dou, S. X. *Chem. Mater.* **2008**.

(287) Pan, J.; Li, M.; Luo, Y. Y.; Wu, H.; Zhong, L.; Wang, Q.; Li, G. H. *Appl. Surf. Sci.* **2015**, *333*, 34–38.

(288) Zhai, T.; Liu, H.; Li, H.; Fang, X.; Liao, M.; Li, L.; Zhou, H.; Koide, Y.; Bando, Y.; Golberg, D. *Adv. Mater.* **2010**, *22* (23), 2547–2552.

(289) De Jesus, L. R.; Horrocks, G. A.; Liang, Y.; Parija, A.; Jaye, C.; Wangoh, L.; Wang, J.; Fischer, D. A.; Piper, L. F. J.; Prendergast, D.; Banerjee, S. *Nat. Commun.* **2016**, *7*, 1–9.

(290) Liang, S.; Hu, Y.; Nie, Z.; Huang, H.; Chen, T.; Pan, A.; Cao, G. *Nano Energy*

2015, *13*, 58–66.

(291) Pan, A.; Wu, H. Bin; Yu, L.; Zhu, T.; Lou, X. W. *ACS Appl. Mater. Interfaces* **2012**, *4* (8), 3874–3879.

(292) Sun, B.; Huang, K.; Qi, X.; Wei, X.; Zhong, J.; Sun, B.; Huang, K.; Qi, X.; Wei, X.; Zhong, J. X. *Adv. Funct. Mater.* **2015**, *25*, 5633–5639.

(293) Zhang, C.; Chen, Z.; Guo, Z.; Lou, X. W. *Energy Environ. Sci.* **2013**, *6* (3), 974–978.

(294) Li, L.; Peng, S.; Wu, H. Bin; Yu, L.; Madhavi, S.; Lou, X. W. *Adv. Energy Mater.* **2015**, *5* (17).

(295) Xiong, C.; Aliev, A. E.; Gnade, B.; Balkus, K. J. *ACS Nano* **2008**, *2* (2), 293–301.

(296) Ragupathy, P.; Shivakumara, S.; Vasan, H. N.; Munichandraiah, N. *J. Phys. Chem. C* **2008**, *112* (42), 16700–16707.

(297) Song, H.; Zhang, C.; Liu, Y.; Liu, C.; Nan, X.; Cao, G. *J. Power Sources* **2015**, *294*, 1–7.

(298) An, Q.; Zhang, P.; Xiong, F.; Wei, Q.; Sheng, J.; Wang, Q.; Mai, L. *Nano Res.* **2015**, *8* (2), 481–490.

(299) Bai, H.; Liu, Z.; Sun, D. D.; Chan, S. H. *Energy* **2014**, *76*, 607–613.

(300) Su, D.; Wang, G. *ACS Catal* **2013**, *7* (12), 11218–11226.

(301) Dong, Y.; Wei, H.; Liu, W.; Liu, Q.; Zhang, W.; Yang, Y. *J. Power Sources* **2015**, *285*, 538–542.

(302) Zhou, F.; Zhao, X.; Yuan, C.; Li, L.; Xu, H. *Chem. Lett.* **2007**, *36* (2), 310–311.

(303) Xie, Y.; Dong, H.; Zhang, S.; Lu, X.; Ji, X. *J. chem Engg. data* **2014**, *59*, 3344–3352.

(304) Nguyen, T.-D.; Do, T.-O. *Langmuir* **2009**, *25* (9), 5322–5332.

(305) Zheng, J.; Hu, T.; Zhang, Y.; Lv, T.; Tian, F.; Meng, C. *Colloids Surfaces A*

Physicochem. Eng. Asp. **2018**, *553*, 317–326.

(306) Liu, J.; Wang, X.; Peng, Q.; Li, Y. *Adv. Mater.* **2005**, *17* (6), 764–767.

(307) Aureliano, M.; Ohlin, C. A.; Vieira, M. O.; Marques, M. P. M.; Casey, W. H.; Batista De Carvalho, L. A. E. *Dalt. Trans.* **2016**, *45* (17), 7391–7399.

(308) Livage, J. *Materials (Basel).* **2010**, *3* (8), 4175–4195.

(309) Chan, Y.-L.; Pung, S.-Y.; Sreekantan, S. *J. Catal.* **2014**, *2014*, 1–7.

(310) Rui, X.; Lu, Z.; Yu, H.; Yang, D.; Hng, H. H.; Lim, T. M.; Yan, Q. *Nanoscale* **2013**, *556* (5), 556–560.

(311) Parnham, E. R.; Morris, R. E. *Acc. Chem. Res.* **2007**, *40*, 1005–1013.

(312) Wang, W.; Li, Y.; Liu, L.; Dong, J. *Dalt. Trans.* **2012**, *41* (35), 10511–10513.

(313) Yonemoto, B. T.; Lin, Z.; Jiao, F. *Chem. Commun.* **2012**, *48* (73), 9132–9134.

(314) Prasad, B. L. V.; Stoeva, S. I.; Sorensen, C. M.; Klabunde, K. J. *Langmuir* **2002**, *18* (20), 7515–7520.

(315) Sun, Y.; Jose, D.; Sorensen, C.; Klabunde, K.; Sun, Y.; Jose, D.; Sorensen, C.; Klabunde, K. J. *Nanomaterials* **2013**, *3* (3), 370–392.

(316) Krumeich, F.; Muhr, H. J.; Niederberger, M.; Bieri, F.; Schnyder, B.; Nesper, R. *J. Am. Chem. Soc.* **1999**, *121* (36), 8324–8331.

(317) Zhao, N.; Yang, L.; Xie, B.; Han, J.; Pan, Q.; Li, X.; Liu, M.; Wang, Y.; Wang, X.; Zhu, G. *Chem. Commun.* **2018**, *54* (80), 11264–11267.

(318) Fang, Q.; Zhu, G.; Xue, M.; Wang, Z.; Sun, J.; Qiu, S. *Cryst. Growth Des.* **2008**, *8* (1), 319–329.

(319) Koczkur, K. M.; Mourdikoudis, S.; Polavarapu, L.; Skrabalak, S. E. *Dalt. Trans.* **2015**, *44* (41), 17883–17905.

(320) Naseri, M. G, Saion, E. B., Shaari, A. H. *Int. Nano Lett.* **2013**, *3*, 1–19.

(321) Reddy, C. V. S.; Jin, A.-P.; Han, X.; Zhu, Q.-Y.; Mai, L.-Q.; Chen, W. *Electrochem.*

commun. **2006**, *8*, 279–283.

(322) Chen, Y.; Yang, G.; Zhang, Z.; Yang, X.; Hou, W.; Zhu, J.-J. *Nanoscale* **2010**, *2*, 2131–2138.

(323) Sasaki, T.; Watanabe, M. *J. Am. Chem.Soc* **1998**, *120*, 4682–4689.

(324) Sasaki, T.; Watanabe, M. *J. Am. Chem. Soc* **1998**, *120*, 4682–4689.

(325) Jeong, S.; Yoo, D.; Ahn, M.; Miró, P.; Heine, T.; Cheon, J. *Nat. Commun.* **2014**, *6*, 5763.

(326) Etman, A. S.; Asfaw, H. D.; Yuan, N.; Li, J.; Zhou, Z.; Peng, F.; Persson, I.; Zou, X.; Torbj¨, T.; Gustafsson, T.; Edström, K. E. E.; Sun, J. *J.Mater.Chem.A* **2016**, *4*, 17988–18001. Online link: https://doi.org/10.1039/C6TA06571F

(327) Mohammadpour, Z.; Abdollahi, S. H.; Safavi, A. *ACS Appl. Energy Mater.* **2018**, *1* (11), 5896–5906.

(328) Zhu, K.; Zhang, C.; Guo, S.; Yu, H.; Liao, K.; Chen, G.; Wei, Y.; Zhou, H. *ChemElectroChem* **2015**, *2* (11), 1660–1664.

(329) Lu, X.; Zheng, D.; Zhang, P.; Liang, C.; Liu, P.; Tong, Y. *Chem. Commun* **2010**, *46*, 7721–7723.

(330) Kleinlogel, C.; Gauckler, L. J. *Solid State Ionics* **2000**, *135* (1–4), 567–573.

(331) Devaiah, D.; Reddy, L. H.; Kuntaiah, K.; Reddy, B. M. *Indian J. Chem. - Sect. A Inorganic, Phys. Theor. Anal. Chem.* **2012**, *51* (1–2), 186–195.

(332) Atribak, I.; Bueno-López, A.; García-García, A. *J. Mol. Catal. A Chem.* **2009**, *300* (1–2), 103–110.

(333) Bueno-López, A.; Krishna, K.; Makkee, M.; Moulijn, J. A. *J. Catal.* **2005**, *230* (1), 237–248.

(334) Mamontov, E.; Egami, T.; Brezny, R.; Koranne, M.; Tyagi, S. *J. Phys. Chem. B* **2000**, *104* (47), 11110–11116.

(335) Parnham, E. R.; Drylie, E. A.; Wheatley, P. S.; Slawin, A. M. Z.; Morris, R. E.

Angew. Chemie **2006**, *118* (30), 5084–5088.

(336) Bakiz, B.; Guinneton, F.; Dallas, J. P.; Villain, S.; Gavarri, J. R. *J. Cryst. Growth* **2008**, *310* (12), 3055–3061.

(337) Ribeiro, C.; Lee, E. J. H.; Giraldi, T. R.; Longo, E.; Varela, J. A.; Leite, E. R. *J. Phys. Chem. B* **2004**, *108* (40), 15612–15617.

(338) Ribeiro, C.; Lee, E. J. H.; Longo, E.; Leite, E. R. *ChemPhysChem* **2005**, *6* (4), 690–696.

(339) Chen, Y. C.; Chen, K. B.; Lee, C. S.; Lin, M. C. *J. Phys. Chem. C* **2009**, *113* (13), 5031–5034.

(340) Liu, X.; Ding, J.; Lin, X.; Gao, R.; Li, Z.; Dai, W. L. *Appl. Catal. A Gen.* **2015**, *503*, 117–123.

(341) Zhang, Y.; Zhang, L.; Deng, J.; Dai, H.; He, H. *Inorg. Chem.* **2009**, *48* (5), 2181–2192.

(342) Chen, A.; Zhou, Y.; Ta, N.; Li, Y.; Shen, W. *Catal. Sci. Technol.* **2015**, *5* (8), 4184–4192.

(343) Mai, H. X.; Sun, L. D.; Zhang, Y. W.; Si, R.; Feng, W.; Zhang, H. P.; Liu, H. C.; Yan, C. H. *J. Phys. Chem. B* **2005**, *109* (51), 24380–24385.

(344) Yu, J. C.; Zhang, L.; Lin, J. *J. Colloid Interface Sci.* **2003**, *260* (1), 240–243.

(345) Hirano, M.; Kato, E. *J. Am. Ceram. Soc.* **2004**, *82* (3), 786–788.

(346) Muha, G. M.; Vaughan, P. A. *J. Chem. Phys.* **1960**, *33* (1), 194–199.

(347) Si, R.; Zhang, Y. W.; Li, S. J.; Lin, B. X.; Yan, C. H. *J. Phys. Chem. B* **2004**, *108* (33), 12481–12488.

(348) Biswas, K.; Rao, C. N. R. *Chem. - A Eur. J.* **2007**, *13* (21), 6123–6129.

(349) Wang, Y.; Yang, H. *J. Am. Chem. Soc.* **2005**, *127* (15), 5316–5317.

(350) Zhang, J.; Chen, J.; Li, Q. *Mater. Res. Bull.* **2015**, *63*, 88–92.

(351) Zhou, G.; Shah, P. R.; Kim, T.; Fornasiero, P.; Gorte, R. J. *Catal. Today* **2007**, *123* (1–4), 86–93.

(352) Ren, Z.; Wang, P.; Kong, J.; Wang, M.; Chang, L. *J. Energy Chem.* **2017**, *26* (4), 647–654.

(353) Reddy, B. M.; Saikia, P.; Bharali, P. *Catal. Surv. from Asia* **2008**, *12* (3), 214–228.

(354) Bozo, C.; Gaillard, F.; Guilhaume, N. *Appl. Catal. A Gen.* **2001**, *220* (1–2), 69–77.

(355) Damyanova, S.; Pawelec, B.; Arishtirova, K.; Huerta, M. V. M.; Fierro, J. L. G. *Appl. Catal. A Gen.* **2008**, *337* (1), 86–96.

(356) Atribak, I.; Bueno-López, A.; García-García, A. *J. Mol. Catal. A Chem.* **2009**, *300* (1–2), 103–110.

(357) Sánchez Escribano, V.; Fernández López, E.; Panizza, M.; Resini, C.; Gallardo Amores, J. M.; Busca, G. *Solid State Sci.* **2003**, *5* (10), 1369–1376.

(358) Guo, M.; Lu, J.; Wu, Y.; Wang, Y.; Luo, M. *Langmuir* **2011**, *27* (7), 3872–3877.

(359) Jian, L.; Zhen, Z.; Chunming, X.; Aijun, D.; Guiyuan, J. *J. Rare Earths* **2010**, *28* (2), 198–204.

(360) Reddy, B. M.; Khan, A.; Yamada, Y.; Kobayashi, T.; Loridant, S.; Volta, J. C. *J. Phys. Chem. B* **2003**, *107* (22), 5162–5167.

(361) McBride, J. R.; Hass, K. C.; Poindexter, B. D.; Weber, W. H. *J. Appl. Phys.* **1994**, *76* (4), 2435–2441.

(362) Pezzotti, G.; Porporati, A. A. *J. Biomed. Opt.* **2004**, *9* (2), 372.

(363) Thammachart, M.; Meeyoo, V.; Risksomboon, T.; Osuwan, S. *Catal. Today* **2001**, *68* (1–3), 53–61.

(364) Vinodkumar, T.; Durgasri, N.; Maloth, S.; Reddy, B. M. *J. Chem. Sci* **2015**, *127* (7), 1145–1153.

(365) Perrichon, V.; Laachir, A.; Abouarnadasse, S.; Touret, O.; Blanchard, G. *Appl. Catal. A, Gen.* **1995**, *129* (1), 69–82.

(366) Piumetti, M.; Bensaid, S.; Russo, N.; Fino, D. *Appl. Catal. B Environ.* **2015**, *165*, 742–751.

(367) Kim, J. R.; Myeong, W. J.; Ihm, S. K. *Appl. Catal. B Environ.* **2007**, *71* (1–2), 57–63.

(368) Terribile, D.; Trovarelli, A.; De Leitenburg, C.; Primavera, A.; Dolcetti, G. *Catal. Today* **1999**, *47* (1–4), 133–140.

(369) Ren, Z.; Wang, P.; Kong, J.; Wang, M.; Chang, L. *J. Energy Chem.* **2017**, *26* (4), 647–654.

(370) Shah, P. M.; Burnett, J. W. H.; Morgan, D. J.; Davies, T. E.; Taylor, S. H. *Catalysts* **2019**, *9* (5), 475.

(371) Tsoncheva, T.; Ivanova, R.; Henych, J.; Dimitrov, M.; Kormunda, M.; Kovacheva, D.; Scotti, N.; Santo, V. D.; Štengl, V. *Appl. Catal. A Gen.* **2015**, *502*, 418–432.

(372) Masui, T.; Nakano, K.; Ozaki, T.; Adachi, G. Y.; Kang, Z.; Eyring, L. *Chem. Mater.* **2001**, *13* (5), 1834–1840.

(373) Bozo, C.; Guilhaume, N.; Herrmann, J. M. *J. Catal.* **2001**, *203* (2), 393–406.

(374) Li, C.; Domen, K.; Maruya, K. I.; Onishi, T. *J. Am. Chem. Soc.* **1989**, *111* (20), 7683–7687.

(375) Zhao, Y.; Teng, B. T.; Wen, X. D.; Zhao, Y.; Chen, Q. P.; Zhao, L. H.; Luo, M. F. *J. Phys. Chem. C* **2012**, *116* (30), 15986–15991.

(376) Li, J.; Liu, X.; Zhan, W.; Guo, Y.; Guo, Y.; Lu, G. *Catal. Sci. Technol.* **2016**, *6* (3), 897–907.

(377) Wang, Q.; Li, G.; Zhao, B.; Zhou, R. *Appl. Catal. B Environ.* **2010**, *100* (3–4), 516–528.

(378) Skorodumova, N. V.; Simak, S. I.; Lundqvist, B. I.; Abrikosov, I. A.; Johansson, B. *Phys. Rev. Lett.* **2002**, *89* (16), 166601.

(379) López, J. M.; Gilbank, A. L.; García, T.; Solsona, B.; Agouram, S.; Torrente-

Murciano, L. *Appl. Catal. B Environ.* **2015**, *174175*, 403–412.

(380) Linsebigler, A.; Lu, G.; Yates, J. T. *J. Chem. Phys.* **1995**, *103* (21), 9438–9443.

(381) Kobayashi, H.; Yamaguchi, M. *Surf. Sci.* **1989**, *214* (3), 466–476.

(382) Markaryan, G. L.; Ikryannikova, L. N.; Muravieva, G. P.; Turakulova, A. O.; Kostyuk, B. G.; Lunina, E. V.; Lunin, V. V.; Zhilinskaya, E.; Aboukais, A. *Colloids Surfaces A Physicochem. Eng. Asp.* **1999**, *151* (3), 435–447.

(383) Boaro, M.; De Leitenburg, C.; Dolcetti, G.; Trovarelli, A. *J. Catal.* **2000**, *193* (2), 338–347.

(384) Laguna, O. H.; Pérez, A.; Centeno, M. A.; Odriozola, J. A. *Appl. Catal. B Environ.* **2015**, *176–177*, 385–395.

(385) Benjaram, M. R.; Gode, T.; Katta, L. *Chinese J. Catal.* **2011**, *32* (5), 800–806.

(386) Laguna, O. H.; Romero Sarria, F.; Centeno, M. A.; Odriozola, J. A. *J. Catal.* **2010**, *276* (2), 360–370.

(387) A. Trovarelli, C. D. L. and G. D. *Chemtech* **1997**, *27* (6), 32–37.

(388) Sugiura, M. *Catal. Surv. from Asia* **2003**, *7* (1), 77–87.

(389) Laguna, O. H.; Romero Sarria, F.; Centeno, M. A.; Odriozola, J. A. *J. Catal.* **2010**, *276* (2), 360–370.

(390) Andreeva, D. *Gold Bull.* **2002**, *35* (3), 82–88.

(391) Costello, C. K.; Kung, M. C.; Oh, H. S.; Wang, Y.; Kung, H. H. *Appl. Catal. A Gen.* **2002**, *232* (1–2), 159–168.

(392) Guo, L.-W.; Du, P.-P.; Fu, X.-P.; Ma, C.; Zeng, J.; Si, R.; Huang, Y.-Y.; Jia, C.-J.; Zhang, Y.-W.; Yan, C.-H. *Nat. Commun.* **2016**, *7* (1), 13481.

(393) Centeno, M. Á.; Portales, C.; Carrizosa, I.; Odriozola, J. A. *Catal. Letters* **2005**, *102* (3–4), 289–297.

(394) Tibiletti, D.; Amieiro-Fonseca, A.; Burch, R.; Chen, Y.; Fisher, J. M.; Goguet, A.;

Hardacre, C.; Hu, P.; Thompsett, D. *J. Phys. Chem. B* **2005**, *109* (47), 22553–22559.

(395) Laguna, O. H.; Pérez, A.; Centeno, M. A.; Odriozola, J. A. *Appl. Catal. B Environ.* **2015**, *176–177*, 385–395.

(396) Hernández, W. Y.; Romero-Sarria, F.; Centeno, M. A.; Odriozola, J. A. *J. Phys. Chem. C* **2010**, *114* (24), 10857–10865.

(397) Wahlström, E.; Lopez, N.; Schaub, R.; Thostrup, P.; Rønnau, A.; Africh, C.; Lægsgaard, E.; Nørskov, J. K.; Besenbacher, F. *Phys. Rev. Lett.* **2003**, *90* (2), 4.

(398) Kopelent, R.; van Bokhoven, J. A.; Szlachetko, J.; Edebeli, J.; Paun, C.; Nachtegaal, M.; Safonova, O. V. *Angew. Chemie Int. Ed.* **2015**, *54* (30), 8728–8731.

(399) Sudarsanam, P.; Mallesham, B.; Reddy, P. S.; Großmann, D.; Grünert, W.; Reddy, B. M. *Appl. Catal. B Environ.* **2014**, *144*, 900–908.

(400) Dobrosz-Gómez, I.; Kocemba, I.; Rynkowski, J. M. *Appl. Catal. B Environ.* **2008**, *83* (3–4), 240–255.

(401) Wang, S. P.; Zhang, T. Y.; Wang, X. Y.; Zhang, S. M.; Wang, S. R.; Huang, W. P.; Wu, S. H. *Journal of Molecular Catalysis A: Chemical*. July 2, 2007, pp 45–52.

(402) Del Río, E.; Blanco, G.; Collins, S.; Haro, M. L.; Chen, X.; Delgado, J. J.; Calvino, J. J.; Bernal, S. *Top. Catal.* **2011**, *54* (13–15), 931–940.

(403) Della Pina, C.; Falletta, E.; Rossi, M.; Sacco, A. *J. Catal.* **2009**, *263* (1), 92–97.

(404) Hisbergues, M.; Vendeville, S.; Vendeville, P. *J. Biomed. Mater. Res. - Part B Appl. Biomater.* **2009**, *88* (2), 519–529.

(405) Bansal, V.; Rautaray, D.; Ahmad, A.; Sastry, M. *J. Mater. Chem.* **2004**, *14* (22), 3303.

(406) Mueller, R.; Jossen, R.; Pratsinis, S. E.; Watson, M.; Akhtar, M. K. *J. Am. Ceram. Soc.* **2004**, *87* (2), 197–202.

(407) Wang, J.; Yin, W.; He, X.; Wang, Q.; Guo, M.; Chen, S. *Sci. Rep.* **2016**, *6*.

(408) Benedetti, A.; Fagherazzi, G.; Pinna, F.; Polizzi, S. *J. Mater. Sci.* **1990**, *25* (2),

1473–1478.

(409) Benedetti, A.; Fagherazzi, G.; Pinna, F. *J. Am. Ceram. Soc.* **1989**, *72* (3), 467–469.

(410) Pozhidaeva, O. V.; Korytkova, E. N.; Romanov, D. P.; Gusarov, V. V. *Russ. J. Gen. Chem.* **2002**, *72* (6), 849–853.

(411) Nishizawa, H.; Yamasaki, N.; Matsuoka, K.; Mitsushio, H. *J. Am. Ceram. Soc.* **1982**, *65* (7), 343–346.

(412) Esmaeilifar, A.; Rowshanzamir, S.; Behbahani, A. *Iran. J. Hydrog. Fuel Cell* **2014**, *3*, 163–173.

(413) Eslava, S.; Baklanov, M. R.; Neimark, A. V.; Iacopi, F.; Kirschhock, C. E. A.; Maex, K.; Martens, J. A. *Adv. Mater.* **2008**, *20* (16), 3110–3116.

(414) Gionco, C.; Paganini, M. C.; Giamello, E.; Burgess, R.; Di Valentin, C.; Pacchioni, G. *Chem. Mater.* **2013**, *25* (11), 2243–2253.

(415) Singh, M.; Goyal, M.; Devlal, K. *J. Taibah Univ. Sci.* **2018**, *12* (4), 470–475.

(416) Basahel, S. N.; Ali, T. T.; Mokhtar, M.; Narasimharao, K. *Nanoscale Res. Lett.* **2015**, *10* (1), 73.

(417) Gionco, C.; Paganini, M. C.; Giamello, E.; Sacco, O.; Vaiano, V.; Sannino, D. *J. Energy Chem.* **2017**, *26* (2), 270–276.

(418) Rashad, M. M.; Baioumy, H. M. *J. Mater. Process. Technol.* **2008**, *195* (1–3), 178–185.

(419) Kim, B.-K.; Hamaguchi, H. *Phys. status solidi* **1997**, *203* (2), 557–563.

(420) Morell, G.; Katiyar, R. S.; Torres, D.; Paje, S. E.; Llopis, J. *J. Appl. Phys.* **1997**, *81* (6), 2830–2834.

(421) Ghosh, A.; Suri, A. K.; Pandey, M.; Thomas, S.; Rama Mohan, T. R.; Rao, B. T. *Mater. Lett.* **2006**, *60* (9–10), 1170–1173.

(422) Kurapova, O. Y.; Konakov, V. G. *Rev. Adv. Mater. Sci.* **2014**, *36* (2), 177–190.

(423) Mpourmpakis, G.; Vlachos, D. G. *Langmuir* **2008**, *24* (14), 7465–7473.

(424) Finne, A. P.; Araki, T.; Blaauwgeers, R.; Eltsov, V. B.; Kopnin, N. B.; Krusius, M.; Skrbek, L.; Tsubota, M.; Volovik, G. E. *Nature* **2003**, *424* (6952), 1022–1025.

(425) Madras, G.; McCoy, B. J. *Chem. Eng. Sci.* **2004**, *59* (13), 2753–2765.

(426) Vorkapic, D.; Matsoukas, T. *J. Am. Ceram. Soc.* **2005**, *81* (11), 2815–2820.

(427) Štefanić, G.; Popović, S.; Musić, S. *Thermochim. Acta* **1995**, *259* (2), 225–234.

(428) Guo, G. Y.; Chen, Y. L. *J. Mater. Sci.* **2004**, *39* (12), 4039–4043.

(429) Kim, H. Y.; Henkelman, G. *J. Phys. Chem. Lett.* **2013**, *4* (1), 216–221.

(430) Liu, Z. P.; Gong, X. Q.; Kohanoff, J.; Sanchez, C.; Hu, P. *Phys. Rev. Lett.* **2003**, *91* (26).

(431) Zhao, K.; Tang, H.; Qiao, B.; Li, L.; Wang, J. *ACS Catal.* **2015**, *5* (6), 3528–3539.

(432) Ruiz Puigdollers, A.; Tosoni, S.; Pacchioni, G. *J. Phys. Chem. C* **2016**, *120* (28), 15329–15337.

(433) Claus, P.; Bruckner, A.; Mohr, C.; Hofmeister, H. *J. Am. Chem. Soc.* **2000**, *122* (46), 11430–11439.

(434) Zhang, X.; Wang, H.; Xu, B. Q. *J. Phys. Chem. B* **2005**, *109* (19), 9678–9683.

(435) Schüth, F. *Phys. status solidi* **2013**, *250* (6), 1142–1151.

(436) Liu, H.; Feng, L.; Zhang, X.; Xue, Q. *J. Phys. Chem.* **1995**, *99* (1), 332–334.

(437) Bond, G. C.; Thompson, D. T. *Catal. Rev. - Sci. Eng.* **1999**, *41* (3–4), 319–388.

(438) Yang, C. H.; Goodwin, J. G. *Particle size dependence for CO chemisorption on supported Ru catalysts*; 1982; Vol. 20.

(439) Idakiev, V.; Tabakova, T.; Naydenov, A.; Yuan, Z. Y.; Su, B. L. *Appl. Catal. B Environ.* **2006**, *63* (3–4), 178–186.

(440) Haruta, M.; Tsubota, S.; Kobayashi, T.; Kageyama, H.; Genet, M. J.; Delmon, B. *J. Catal.* **1993**, *144* (1), 175–192.

(441) Konova, P.; Naydenov, A.; Tabakova, T.; Mehandjiev, D. *Catal. Commun.* **2004**, *5* (9), 537–542. Online link: https://doi.org/10.1016/j.catcom.2004.06.010

(442) Wang, C. M.; Fan, K. N.; Liu, Z. P. *J. Am. Chem. Soc.* **2007**, *129* (9), 2642–2647.

(443) Zhang, X.; Shi, H.; Xu, B. Q. *Catal. Today* **2007**, *122* (3–4), 330–337.

(444) Karwacki, C. J.; Ganesh, P.; Kent, P. R. C.; Gordon, W. O.; Peterson, G. W.; Niu, J. J.; Gogotsi, Y. *J. Mater. Chem. A* **2013**, *1* (19), 6051–6062.

(445) Hong, Y.-C.; Sun, K.-Q.; Han, K.-H.; Liu, G.; Xu, B.-Q. *Catal. Today* **2010**, *158* (3–4), 415–422.

(446) Costello, C. K.; Guzman, J.; Yang, J. H.; Wang, Y. M.; Kung, M. C.; Gates, B. C.; Kung, H. H. *J. Phys. Chem. B* **2004**, *108* (33), 12529–12536.

(447) Pokrovski, K.; Jung, K. T.; Bell, A. T. *Langmuir* **2001**, *17* (14), 4297–4303.

(448) Bachiller-Baeza, B.; Rodriguez-Ramos, I.; Guerrero-Ruiz, A. *Langmuir* **1998**, *14* (13), 3556–3564.

(449) Wang, J.; Cui, C.; Gao, G.; Zhou, X.; Wu, J.; Yang, H.; Li, Q.; Wu, G. *RSC Adv.* **2015**, *5* (59), 47522–47528.

(450) O'Dwyer, C.; Navas, D.; Lavayen, V.; Benavente, E.; Santa Ana, M. A.; González, G.; Newcomb, S. B.; Sotomayor Torres, C. M. *Chem. Mater.* **2006**, *18* (13), 3016–3022.

Appendix

A1- Calibration chart for the IR gas analyser for real CO ppm values vs theoretical CO ppm values (as read in the IR detector) in Figure 93. The sample CZ (60/40) is chosen as an example to show the calibration data curve.

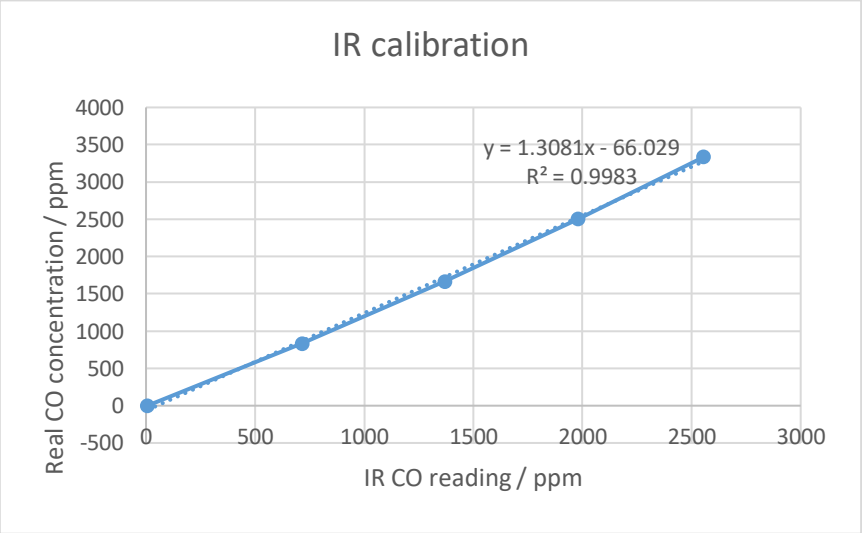

Figure 92: Calibration chart to correlate real CO concentration (in ppm) vs theoretical CO reading (as seen in the IR detector)

The calibration of the mass flow controllers for He, CO and O_2 by bubble flow meters are shown in Figure 93.

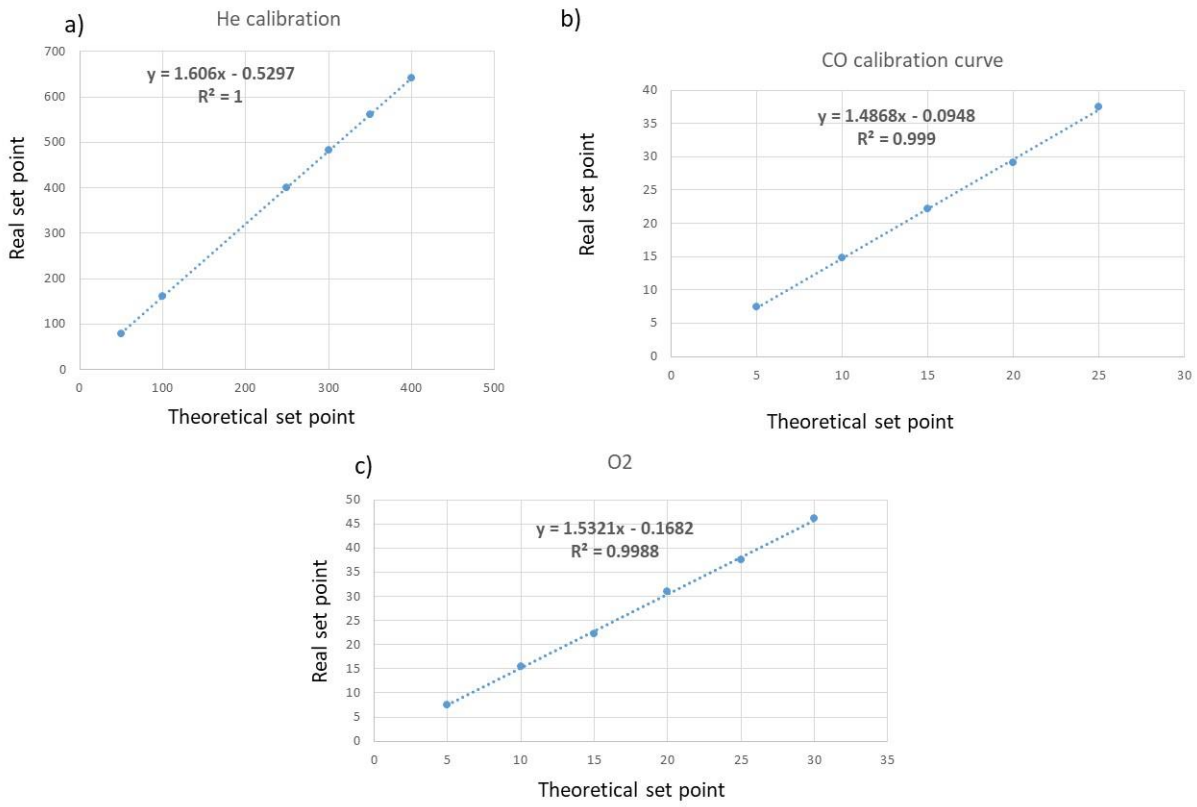

Figure 93: Calibration of the gases used in the CO oxidation rig using bubble flow meter in a) He, b) CO and c) O_2.

A2 Formation mechanism of the nanostructures in water using $VOSO_4$ and $VO(acac)_2$ as the precursor (Chapter 5)-

As seen from Figure 94(a-c), when $VOSO_4$ is used as the precursor, after 2.5 h, nanosticks are stacked together as nanoballs of sizes 5 µm. After calcination step, the spherical morphologies of similar sizes are still retained but the nanosticks are broken into nano-units subjected to the heat treatment. After 5 h, these balls disintegrate into nanosticks. Previous studies report the formation of 1D vanadium oxide (VO_2) based nanostructures like nanobelts, nanoribbons and nanowires under hydrothermal synthesis conditions when $VOSO_4$ is employed as the precursor[202,290,430,431,432]. The formation of 1D structures is attributed due to the crystallization of the 1D based VO_2 structures from the VO^{2+} ions released from $VOSO_4$[205]. However the exact reason of the crystallization of VO_2 nanoribbon like structures from the VO^{2+} cations is not clear yet.

When $VO(acac)_2$ is used as the precursor (Figure 94d-f), oval shaped structures of 1 µm composed of numerous lamellae are formed after 2.5 h. After calcination, these structures lose their uniformity. After 5 h, these oval like structures start evolving into branched structures. In 10 h, these grow as well defined nanourchins of sizes 1 µm. The formation of vanadium oxide nanourchins are also reported previously where the authors see the growth of lamellae in radially outwards direction to develop as a cluster of nanotubes giving rise to a nanourchin like appearance[449,450].

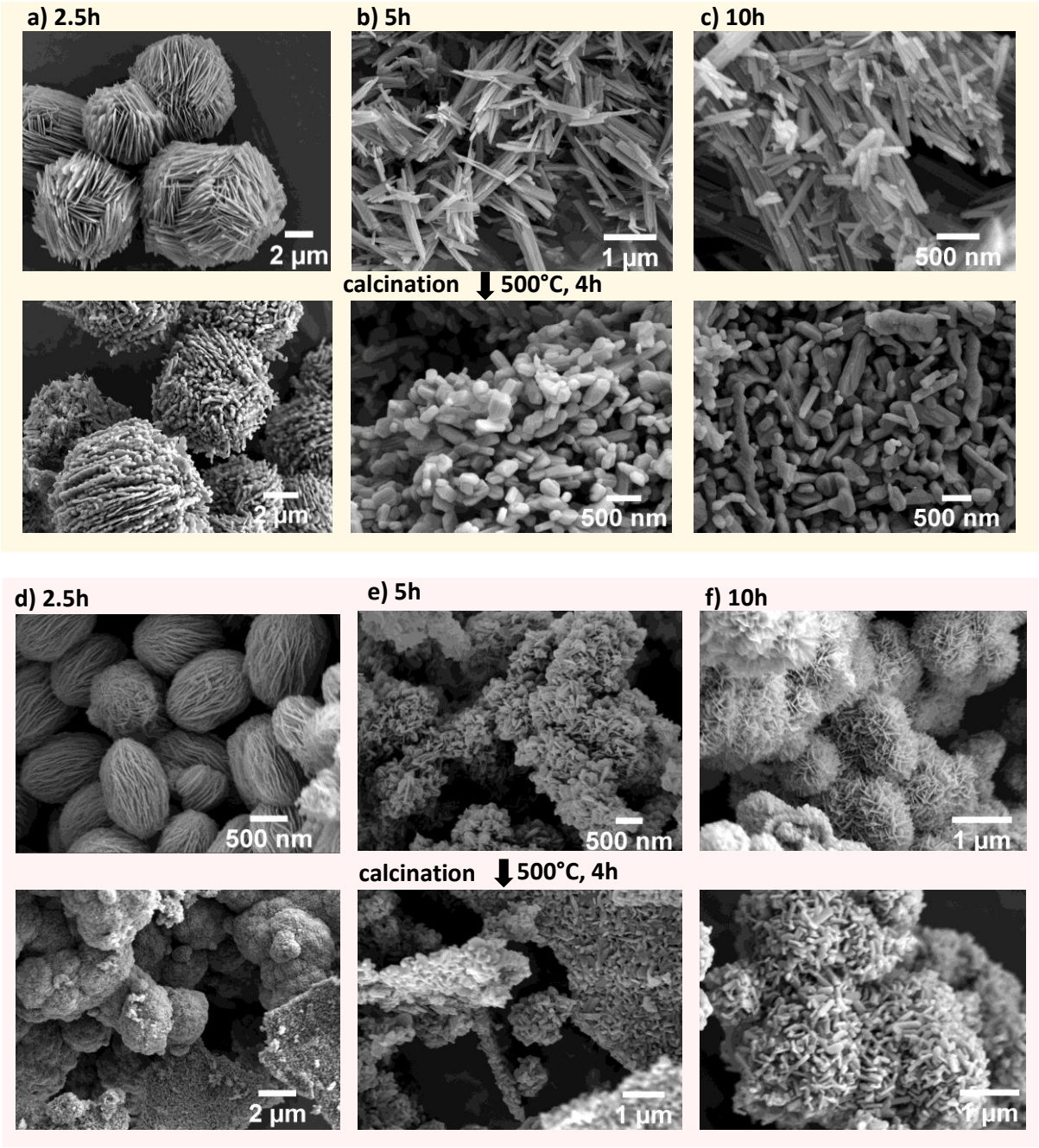

Figure 94: SEM micrographs of uncalcined and calcined V_2O_5 nanostructures synthesized using $VOSO_4$ as the initial precursor (a-c) and $VO(acac)_2$ (d-f) in water at a temperature of 180 °C for different time durations. Calcination conditions: Temperature= 500 °C, time=4 h, sweep rate= 10 °C/min.

A3 Performance of Li-ion battery electrodes (provided by Dr Changshin Jo, Institute for manufacturing, Cambridge)-

Nanostructured V_2O_5 electrodes show faster charge-discharge response than the bulk-V_2O_5 electrode (Figure 95b and c). When varying the current densities from 25 to 800 mA g^{-1}, the nanosheet electrode delivers 172 mA h g^{-1} at 800 mA g^{-1}, which corresponds to 64.5 % of its maximum capacity. In comparison, V_2O_5 nanobeads, nanofleece and bulk electrodes retain 45.3%, 50.0 %, and 12.5% of their initial capacity at 800 mA h g^{-1}, respectively. Finally, the cycling stability of all the electrodes is measured at 250 mA g^{-1} current density (Figure 95 d). The V_2O_5 nanosheet electrode exhibits the most stable cycling performance, with 170 mA h g^{-1} (73.8% retention) after 100 cycles. The other two V_2O_5 nanomaterials (nanobeads: 141 mA h g^{-1}, 63.6% and nanofleeces: 139 mA h g^{-1}, 66.4%) also deliver better cycle performance compared with that of bulk-V_2O_5 electrode (114 mA h g^{-1}, 61.4%).

To better understand the differences in performance between different V_2O_5 structures, cyclic voltammetry was measured with varying scan rates between 0.2 and 1.5 mV s^{-1} (Figure 96 a-d). The Li^+ charge-discharge mechanisms can be analysed by correlating scan rates with peak currents.

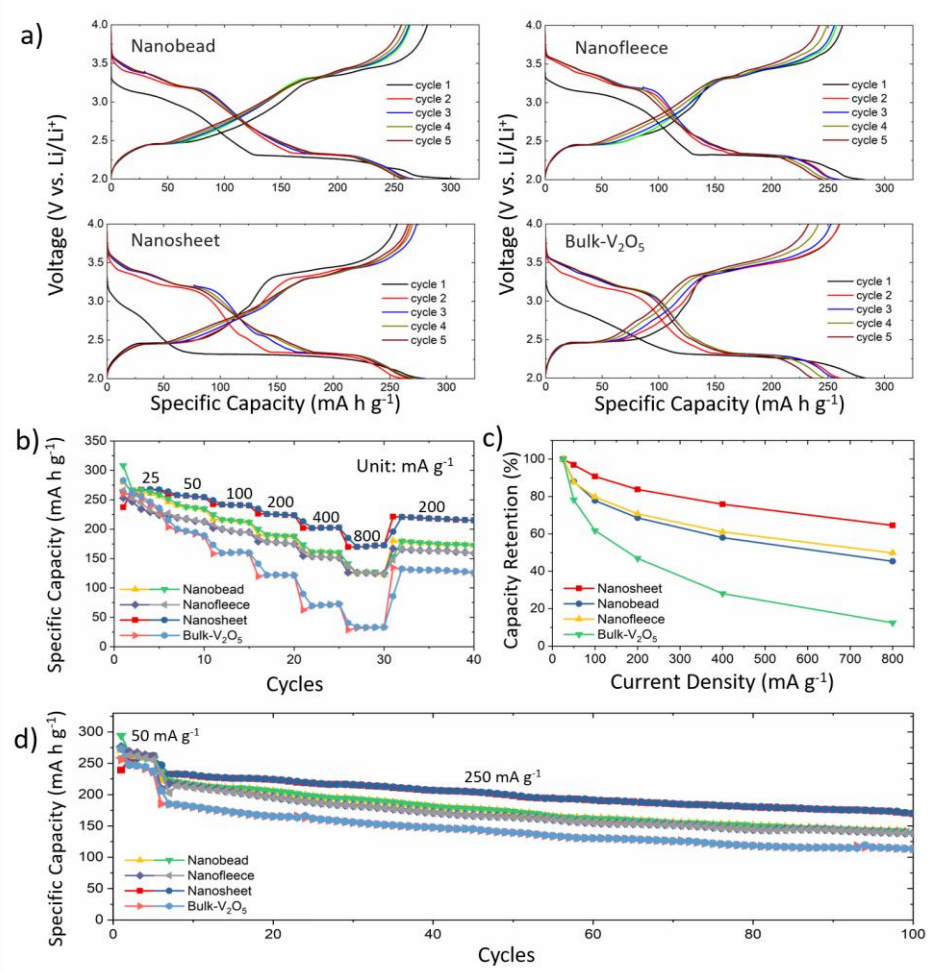

Figure 95: a) Charge-discharge profiles of V_2O_5 electrodes under 25 mA g^{-1} current density. b) rate performance of V_2O_5 electrodes and c) capacity retention plots under different current densities (25 to 800 mA g^{-1}). d) Cycle performance of all V_2O_5 electrodes.

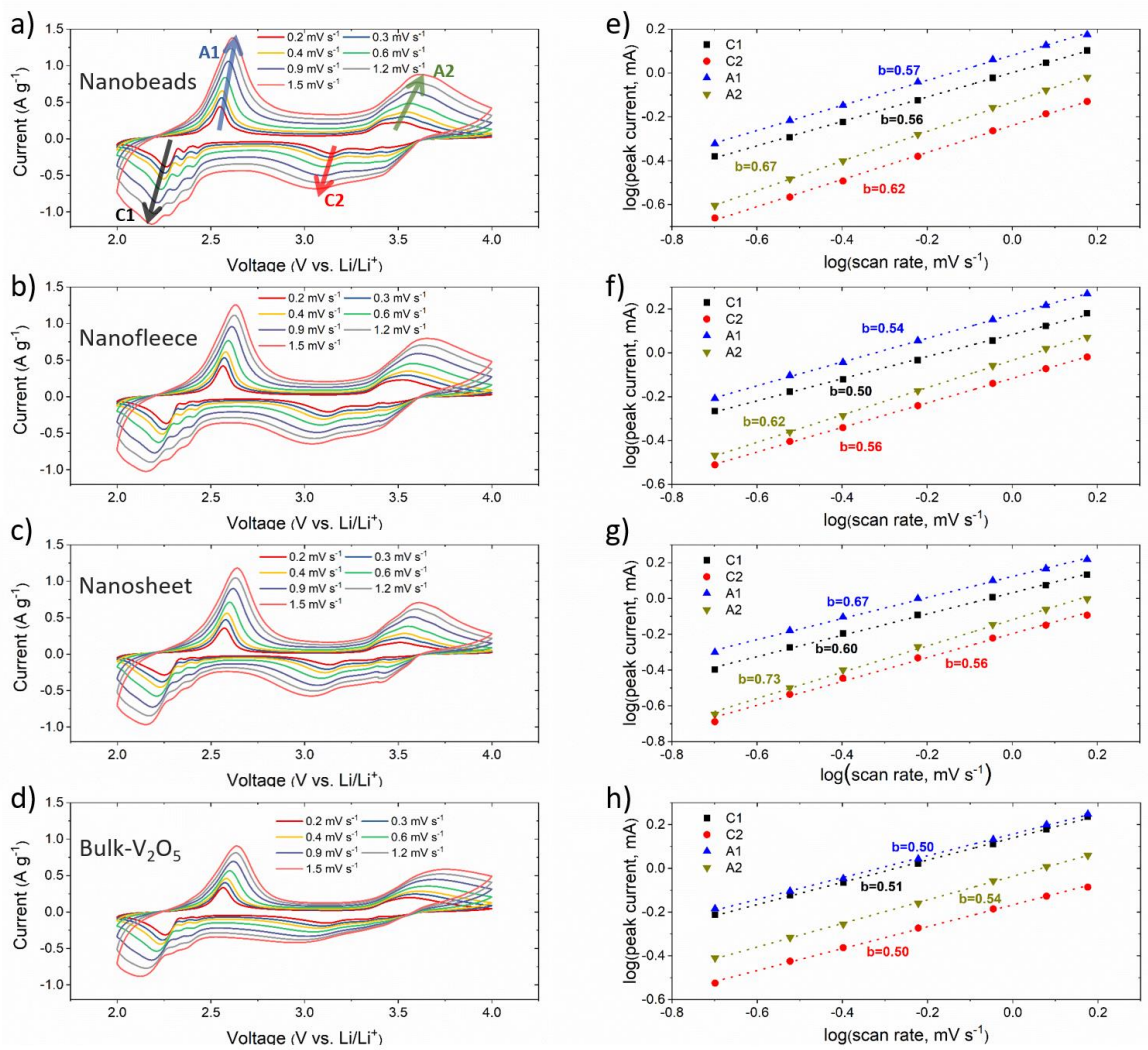

Figure 96: Cyclic voltammetry curves of a) nanobeads, b) nanofleece, c) nanosheet and d) bulk-V_2O_5 electrodes (C and A indicate the cathodic and anodic peaks, respectively. C1: 2.2~2.4 V, C2: 3.0~3.2 V, A1: 2.5~2.7 V, and A2: 3.4~3.7 V). Scan rate and peak current relationships of a) nanobeads, b) nanofleece, c) nanosheet and d) bulk-V_2O_5 electrodes obtained from CV curves with different scan rates (a-d, 0.2 – 1.5 mV s^{-1}).